5-2018

CONTROL OF GRAIN STRUCTURE IN SELECTIVE-ELECTRON BEAM MELTING OF NICKEL-BASED SUPERALLOYS

Curtis Lee Frederick
University of Tennessee

To the Graduate Council:

I am submitting herewith a dissertation written by Curtis Lee Frederick entitled "CONTROL OF GRAIN STRUCTURE IN SELECTIVE-ELECTRON BEAM MELTING OF NICKEL-BASED SUPERALLOYS." I have examined the final electronic copy of this dissertation for form and content and recommend that it be accepted in partial fulfillment of the requirements for the degree of Doctor of Philosophy, with a major in Materials Science and Engineering.

Sudarsanam Suresh Babu, Major Professor

We have read this dissertation and recommend its acceptance:

Ryan R. Dehoff, Easo P. George, Claudia J. Rawn

Accepted for the Council:
Dixie L. Thompson

Vice Provost and Dean of the Graduate School

(Original signatures are on file with official student records.)

CONTROL OF GRAIN STRUCTURE IN SELECTIVE-ELECTRON BEAM MELTING OF NICKEL-BASED SUPERALLOYS

A Dissertation Presented for the

Doctor of Philosophy

Degree

The University of Tennessee, Knoxville

Curtis Lee Frederick

May 2018

To my parents,

Greg and Kathy

Acknowledgements

I must first thank Suresh Babu for inviting me to join his amazing team and giving his relentless support for the past 4 years. His desire to connect the fundamental science to the surrounding world has changed my life. Ryan Dehoff for sharing his excitement for research on Additive Manufacturing while I worked at the Manufacturing Demonstration Facility. Michael Kirka for passing on his knowledge of the Arcam process and Nickel Alloys. Alex Plotkowski for countless conversations breaking down the theory of solidification and heat transfer. It has been a pleasure to work with Eddie Schwalbach and the team at the Air Force Research Laboratory with their constant feedback and insight in Additive Manufacturing. Niyanth Sridharan for teaching me the theory and application of EBSD. Narendran Raghavan for all the exciting conversations about new experiments that could be tried in the Arcam process. Michael Haines for his dedication and consistency in finding new answers to problems. Jacob Raplee for creating and passing on his amazing tools to analyze in-situ IR video. Running the Arcam system and making alterations to the MiniVat would not have been possible without the input of Larry Lowe and Scott Marlow. My committee members Claudia Rawn and Easo George for their inspiring conversations about life and research. Austin Staub for his excellent work and help in characterization. Grant Helmreich for setting the standard of what a postdoc should be. Danny Galicki and Michael Massey for their perseverance in designing the MiniVat. In addition, there are countless others who have contributed to my work through conversations or critiques of my work. Thank you all.

I would like to thank Ralph Dinwiddie for helping set up the IR Video used and give credit to him and SPIE for giving permission to reprint Figure 27 from Thermographic in-situ process monitoring of the electron-beam melting technology used in additive manufacturing by R.B. Dinwiddie, R.R. Dehoff, P.D. Lloyd, L.E. Lowe, J.B. Ulrich, SPIE, Vol. 8705 (2013).

Funding for this project was provided by contract FA8650-15-C-5205 issued by AFRL/RXCM.

Abstract

The powder bed additive manufacturing process of selective-electron beam melting can produce near net shape parts with nickel based superalloys. Control of grain structure is the next step in research as site specific columnar or equiaxed grain structure can give the process further advantage over traditional processing. Previous work has used alloys that were designed for casting processes and have not tried to control the columnar to equiaxed transition (CET) by changing the composition. To determine if alloying for the CET is possible, two custom high gamma prime nickel alloys were designed using CALPHAD software and a CET model. After processing the custom alloys alongside traditional alloys using the Selective Electron Beam Melting (S-EBM) process multi-scale characterization was performed to determine the resulting grain and precipitate structure. From our findings, the process parameters and class of alloy have more control over the CET than expected. Alloying for the CET, without the context of final geometry and processing, is not recommended due to composition having a greater effect on precipitant structure than grain structure.

Table of Contents

List of Tables

Table **Page**

List of Figures

Figure **Page**

1. INTRODUCTION

The science and technology of Alloying for Additive Manufacturing (AM) was explored for the Selective Electron Beam Melting (S-EBM) process for nickel-based alloys. The goal was to developed alloy design rules for controlling the Columnar to Equiaxed transition (CET) during processing of complex parts, while maintaining the requisite solid-state microstructure.

Controlling the CET is an important aspect of additive manufacturing, as the resulting columnar or equiaxed microstructure of Nickel based alloys leads to anisotropic and isotropic mechanical properties, respectively. Furthermore, having the ability to design parts with site specific microstructure would give AM a unique advantage over traditional processing techniques. Therefore, it is crucial to develop design rules that allow for creation of columnar grain structure aligned with the loading direction in regions with uniaxial loading and creation of equiaxed grain structure in areas of multiaxial loading. To take advantage of this phenomenon, we must understand the spatial and temporal variation of thermal gradient, *G*, and solidification velocity, *R*, which control the solidification grains structure. In this research, two approaches for describing the variations of *G* and *R* were undertaken: (1) A Semi-Analytical Heat Transfer Model (SAHTM) was used to describe the variations on the layer-scale; (2) In-situ Infrared (IR) video was used to record the top surface of the build to estimate *G* and *R.* Macroscopic and microscopic characterization of the resulting grain structure is then performed on select cross sections to verify the above.

A CET model, based on previous welding and solidification models and computational thermodynamics, was used to select two alloys for experimentation. Traditional Nickel Alloys and two custom alloys were processed by S-EBM for comparison. Standard raster and spot melt approaches were used to test a wide range of solidification conditions (weld pool size, G and R) using cuboids and right triangular prism geometry. Microscopic characterization of the resulting precipitants was performed to confirm the extent of gamma prime precipitation.

This research revealed that there is a strong interdependency between process parameters, geometry, and composition. The variations in G and R due to changes in process parameters and beam scanning strategies have the greatest control on grain structure and controlling the CET, for a given part geometry and composition. Regions that are in contact with powder have randomly oriented nucleation sites that can disrupt the predominate columnar grain structure. The changes

to composition does modify the tendency for CET transition, but cannot move it to a drastic extent to obtain all columnar or all equiaxed microstructure within a complex build geometry.

During S-EBM, the local thermal gradient and liquid-solid interface velocity can vary by many orders of magnitude. This conclusion appears to be consistent based on results from analytical modeling, as well as, estimations from in-situ IR measurements. However, the variations repeat across the surface of each layer with no macro scale gradient achieved across the layer. A limitation of the body of current experimental work includes being unable to obtain the gradients in solidification conditions along the depth direction.

Due to the elevated temperatures of the S-EBM process, the gamma prime precipitate structure evolution either occurs during cooling or during the build processing stage and is related to the composition and build temperature, with minor influence from the part geometry.

1.1 The Arcam Electron Beam Additive Manufacturing Process

The S-EBM process has been used to produce near net shape parts from materials such as Titanium, Copper, Tungsten, and Nickel Alloys. The defining features of the process include processing in a controlled vacuum environment and using and electron beam as a heat/melting source. Figure 1 gives examples of the variation of the process temperature and power used during processing as well as a schematic This combination allows the starting plate to be heated prior to build start by rapidly rastering a defocused electron beam over baseplate. Funding for my work and school was provided by AFRL contract FA8650-15-C-5205. For nickel alloys, a baseplate temperature between 800 and 1200 °C have been used. Layer heights range between 50 and 100 µm using a powder size distribution mean diameter near 75 µm [1]. During the process, each layer begins by lowering the build plate, raking powder from the side mounds, preheating/sintering of the new powder, melting using a beam speed ranging from 0.5 to 3 m/s, and finishing with a post heating period.

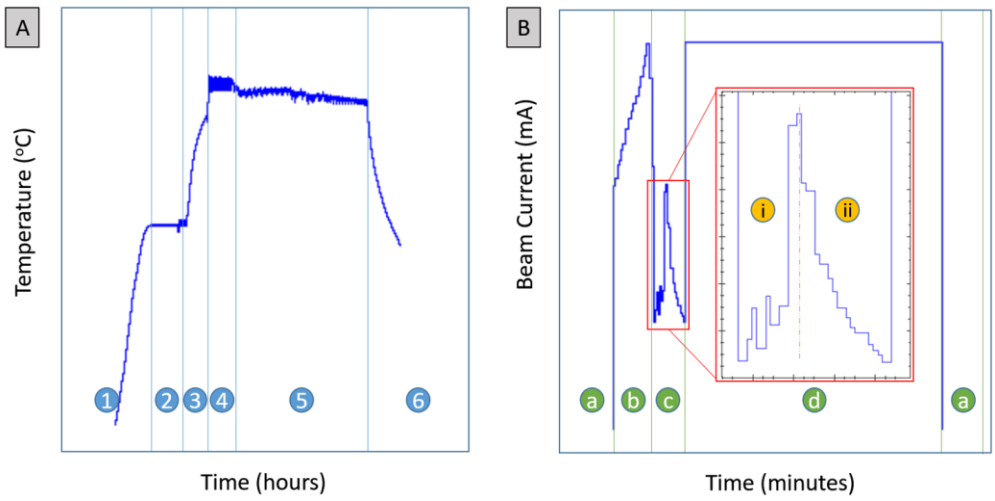

Figure 1. (A) Substrate Temperature Plot, (B) Layer Steps.

Figure 1A shows a generalized plot of the temperature during preheat, melting, and cool down; Figure 1B gives the variation in beam current taken during each layer, preheat, melt, and post heat. Arc Tripping is the most common cause of build failure and occurred in Figure 1A at the end of step 5. Arc Tripping can occur for various reasons (fine powder distribution, oxide coating, etc.) and leads to powder being thrown into the air which disrupts the build process. The Arcam build chamber made up of the powder hoppers, heat shield, rake, and build platform is an open space which can be modified for experimental purposes. Due to the simple feeding mechanism that is gravity fed, the chamber can be completely removed and replaced in one day allowing new materials to be run with little down time.

1.2Nickel Superalloys

The elevated processing temperatures of the Arcam process is well suited for processing of nickel-based superalloys. The nickel superalloy strength at high temperatures comes from the two-phase microstructure of FCC (gamma, γ) and the L12 phase (gamma prime, γ'), which precipitates above 800 °C (alloy dependent). Superalloys tend to have compositions which contain eight or more alloy additions as highlighted in Figure 2, with additions being made to meet targeted properties for a given application (Adapted from [2]). When moving to higher gamma prime volume fractions with increasing titanium and aluminum concentrations, better creep properties are achieved, but processability decreases. Cracking during processing becomes more common as the solidification range increases and as the γ' solidus temperature increases.

Improvements in superalloy creep strength occurred due to advances in the science and technology of characterizing and processing [3]. For example, better understanding of the microstructure property relations was brought about by rapid progress in electron microscopy tools. Similarly, advances in vacuum arc melting (VAM) and vacuum induction melting (VIM) reduced impurities that lead to brittle phase formation elements and ensured quality control. Furthermore, introduction of casting methods, including directional solidification and single crystal allowed us to leverage the anisotropic properties of nickel alloys [4].

In this regard, S-EBM parts primarily show grain growth in the build direction following the FCC <001> preferred growth direction like directionally solidified grain structure. A complex geometry experiencing multi-directional loading conditions in service could take advantage of both highly oriented columnar grains and randomly oriented equiaxed grains, giving isotropic properties [5]. Adding this tool to designers' toolbox would require better understanding of the CET with relation to part geometry. Obtaining control of CET with complex geometries could lead to the next jump in creep life.

1.3Columnar to Equiaxed Transition (CET)

Modelling of the columnar to equiaxed transition (CET) began in order to better understand the microstructure to processing relations of casting alloys [6]. The solidification front of alloys occurs in a planar fashion for low and high velocities with dendritic or cellular growth at intermediate velocities for a given thermal gradient. The dendrites at the solid liquid interface

arise due to the instability at the liquid/solid interface at these intermediate velocities and stabilization of the same through diffusion of solute. Spacing, curvature, and the interaction of diffusion fields with neighboring arms play a role in defining the solidification front [7]. Dendrite arms grow epitaxially from existing partially melted grains at the solid-liquid interface, as soon as a positive temperature gradient is established allowing for growth into the liquid. As solute is ejected from the extending dendrite arms, constitutional undercooling can may set in. The extent of supercooling can reach a critical point at which the homogeneous nucleation of equiaxed grains may be favored in the liquid ahead of the solid-liquid interface [6]. This can be seen schematically in Figure 3 as the equiaxed nucleated sites are incorporated into the advancing front. Once a critically defined volume fraction of equiaxed grains, ϕ, are formed ahead of the dendritic front the structure is considered equiaxed [8].

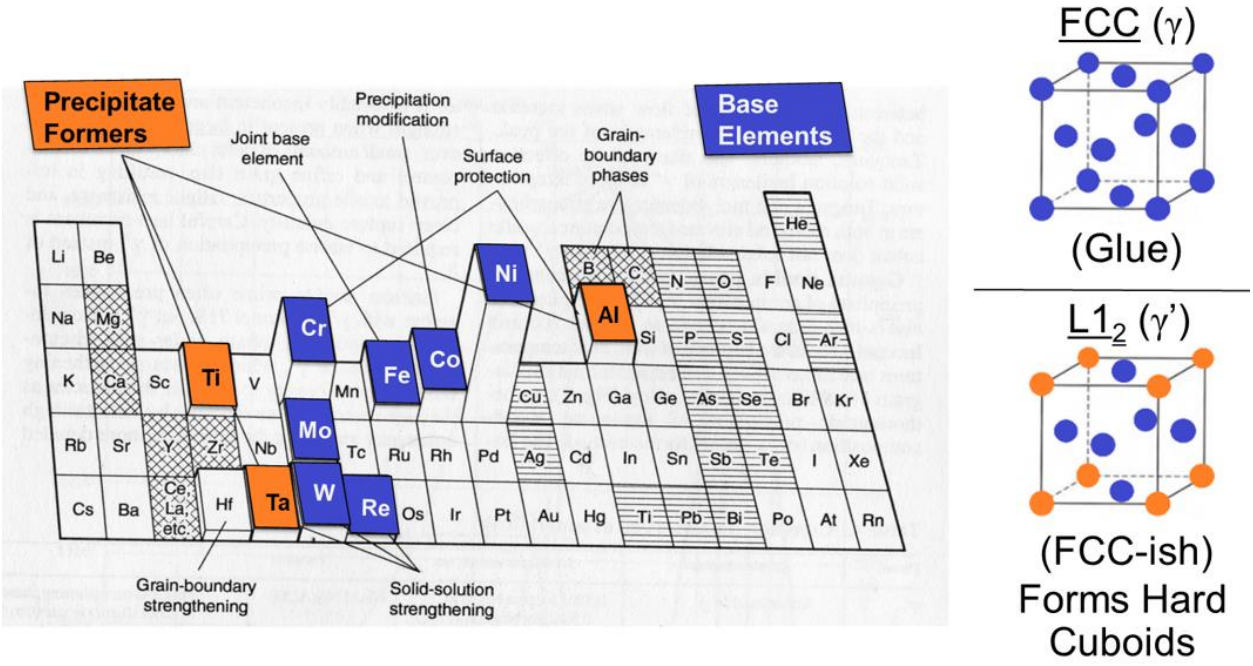

Figure 2. Common Nickel superalloy elemental additions (Adapted from [2]**).**

The CET defined by Hunt [9] for casting was applied to rapid solidification by Kurz [10] and later by M. Gäumann to laser deposition of single crystal superalloys [8]. These theories were extended to early additive processes including laser metal forming. For laser remelting a zero feed rate was assumed (i.e., ignoring powder properties and only remelting solid material). The important conditions for determining when the columnar to equiaxed transition (CET) include the temperature gradient at the interface, G, and the solidification velocity of the columnar front, R. In Gäumann's work on tip repair of CMSX-4 blades, he showed the difficulty of relating process parameters directly to the most critical parameters of the CET equations. To address this challenge, a few process and material constants were introduced and calibrated based on

experimental measurements. In Gäumann's work, the nucleation undercooling was set to be constant for a given material, but it could be expanded as shown by Babu et al [11].

Experimentally it is difficult to obtain solidification conditions, G and R, and the solid-liquid interface. In Gäumann's work it was possible to use a simplified steady state melt pool for a single pass welding experiment. However, the complex beam path of a melted layer in S-EBM does not produce a steady melt pool. To overcome this, in-situ IR video and a SAHTM were used to obtain trends in solidification conditions for this work.

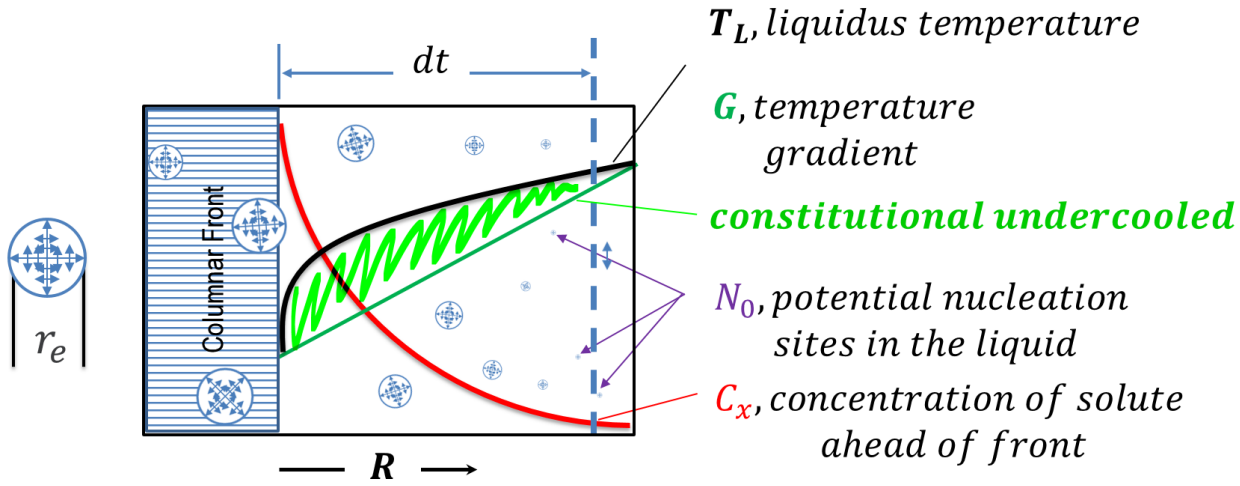

Figure 3. Schematic of equiaxed nucleation ahead of a cellular front (Adapted from [12]**).**

2. LITERATURE REVIEW

2.1 Experiments in the Arcam to Control the CET

When it comes to the columnar to equiaxed transition in SEBM there are two lines of thought for the formation of equiaxed grains and both have only been demonstrated in Inconel 718: (1) Created by standard line scan strategy; (2) Created by spot melting. The first case comes from Carolin Körner's group at the University of Erlangen-Nuremberg, Germany and their work with changing the grain aspect ratio in cuboidal geometries [13]. They observed a transition from the columnar grains, commonly found in SEBM with large aspect ratios, to a near equiaxed structure (the term equiaxed should be reserved to indicate full random traditional CET) caused by a tilting of the thermal gradient on each layer. Their design of experiment (DOE) includes a relatively small cube (15 x 15 x 10 mm^3) that keeps the time to return relatively short and a low energy input giving a small remelt depth but enough to prevent a lack of fusion. While increasing speed, the return time is increased, and a reduction in aspect ratio is observed from 3:1 for the slower beam velocity to near 1.5:1 for the fastest beam velocity. They conclude that the grains are misoriented away from the <001> direction due to the scan strategy causing a change in thermal gradient direction (orienting it toward the raster traverse direction and away from the build direction) on each layer. They then predict the G and R for their experiment using a heat transfer model developed by the group [14–16]. The resulting G and R values for their process do not predict a columnar to equiaxed transition through the traditional mechanism of constitutional undercooling. It is clear with further experiments that it is not a traditional CET and it is interesting that they do not evaluate the effect of geometry in their discussion.

The second method for obtaining an equiaxed grain structure in SEBM has been carried out at ORNL by Ryan Dehoff's Deposition Science & Technology Group [17,18] including Narendran Raghavan [19] and Michael Kirka [20]. In their work the CET has been observed in parts where a modified melting strategy was applied controlling the beam on time, spacing, and time to return. They concluded that when the spot pattern used creates an area melt (which remelts ~5 layers) the thermal gradient is reduced greatly across the entire layer allowing a traditional CET to occur. In their work it is important to note that even though a CET was obtained in complex geometries of published work, for example the DOE block [17] and in the IR Nature paper [21], scaling up the technique to non-cuboidal shapes has not been perfected.

The difficulty of changing the process parameters to complex geometries stems from the numerous process variables in additive manufacturing. The most of important according to Narendran [19] is preheat temperature. A variable that is difficult to measure experimentally as only a thermocouple on the bottom of the baseplate is used during normal operation. Energy input calculated from beam speed, process power, and hatch spacing stem from welding literature [22] for predicting weld defects when the geometry is the same on each pass. Many have attempted to apply them to additive manufacturing [14,23,24] but each will be ruined once the geometry used to calibrate them is changed. This goes for preventing porosity as well as predicting grain structure because in AM the geometry of the melt pool will change with the geometry of the part if the input is not changed accordingly. Arcam® acknowledges this is in two cases (1) Turning Function (2) Speed function. The turning function increases the speed of the beam as it changes direction and moves away from the edge of a part and is done to prevent overheating at the edges. The speed function can be used to change the current and speed based on the line length of each pass, in an attempt to keep the melt pool consistent for complex geometries.

2.2SEBM on Complex Geometry

Little research has been done on the effect of geometry on microstructure but the research that has been done points to edge effects or a vertical gradient. None have seen a gradient horizontally through the build. Yihong Kok et al. [25,26] built parts with curved and straight fins of varying wall thicknesses (1, 5, 10, 20 mm) with Ti-6Al-4V. The chosen geometry simulates impeller walls that can be more easily characterized. An increase in hardness for the 1 mm thin wall was observed which they attributed to a presence of martensitic α' lathes in the 1 mm fins but not larger fins. A decrease in β width as wall thickness decreased was observed in the flat walls but not in the curved walls. The cause for varied microstructure and hardness was attributed to the in-fill hatch strategy and change in heat transfer caused by the different geometries.

Another study in Ti-6Al-4V by Antonysamy, Meyer, and Prangnell [27] characterized a variety of thin wall structures stepping in smaller intervals (1, 2, 3, 4, and 5 mm) and discovered a change in texture. They indicated 5 unique regions from the wall of the structure toward the center, with the thickness of the part determining if all 5 regions will form. Additionally, it was shown that if a "V" shaped base was built then the random grains growing off the powder particles could prevent a single crystal grain from being selected from the base plate. This is because the edge grain orientations are closer to the melt pools thermal gradient direction than the <001> grains oriented with the build direction in the bulk of the part.

In a different approach to geometry, Ramsperger et al [28] used inverted pyramids in a process parameter developing experiment to determine the maximum size achievable before cracking would occur in CMSX-4. An OM image was produced showing how the columnar grains in the center grew from the base plate and new grains grew off the part walls epitaxially from powder grains. Controlling this microstructure was not the focus of their experiment. However, the OM images showed similar behavior and stages of grain growth to the prior β grains in Ti-6Al-4V.

2.3Cracking of Nickel-Based Super Alloys

High gamma prime Nickel alloys tend to crack along stray grains during welding due to the thermomechanical stresses that the process creates. The mechanism is referred to as solidification cracking, which occurs between grain boundaries during solidification and the likelihood of occurring is increased by stray grain formation. J.W. Park et al [29] showed how this can be avoided with reduction of weld speed, v, over power, q, of laser welds and electron beam single remelt passes. From this they created a v/q process map differentiating between (non)cracked welds and recommending a v/q relationship be observed when welding single crystal high gamma prime alloys.

SEBM is a form of multi-pass welding and thus suffers from crack susceptibility when manufacturing high gamma prime nickel alloys. Recently it has been shown as a viable process for producing alloys which are considered difficult to weld using a similar rule setting. Ramsperger's experiments on CMSX-4 [28] has shown this with cuboids 15 x 15 x 20 mm^3 that were produced crack free. In their experiment, process speeds and powers were varied per a DOE grid, finding that a reduction in v/q reduces crack tendencies similar to J.W. Park's findings. Another factor found to reduce cracking was to raise the base plate temperature to reduce thermal stresses during processing.

2.4Precipitation and Growth of Gamma Prime in Arcam Process

Due to the high holding temperature and layer wise process of the Arcam, a gradient has been observed from top to bottom in precipitate size as each layer has seen a slightly different heat treatment [1,30]. The heat treatment cycle is more complicated than traditional processing as layers are formed by rapid solidification, experience remelting on the next few layers, then reheat above the solvus for the next few layers, before being held at an elevated temperature (900-1200 ^{o}C). Builds in the Arcam process can take about 2 minutes for each 50 μm layer adding up to over 13 hours for a 20 mm tall part. This results in a long holding time for the bottom layers before the beam turns off and a slow cooling in a vacuum environment occurs. The feasibility of in-situ heat treating during the Arcam process for Inconel 718 was found detrimental to the tensile properties and unsuccessful overall. Cracking along grain boundaries was observed as well as oversized grains and large delta needles that had formed in the bulk. Other detrimental effects of attempting in-situ heat treating include over-sintering of surrounding powder which prevents recycling and increases the post processing required [30]. No further work has considered in-situ heat treating but solution heat treating of removed parts has shown success and prevents this need. In CMSX-4 it is possible to quickly homogenize the microstructure and retain the as built columnar grain size in only 4 minutes at 1320 ^{o}C [31]. Due to a strong correlation between build height and precipitate size and the ability to easily homogenize SEBM parts regardless of build height, post heat treating is a much more viable approach.

3. METHODS AND PROCEDURES

The Arcam S12 and Arcam A2 with a modified build chamber were used to process traditional and custom nickel-based alloy powders. During processing, our specific objective was to target conditions that could trigger a Columnar to Equiaxed Transition (CET). A FLIR ® IR camera was used to monitor the process and a semi-analytical heat transfer model was used to verify and validate the wide range of solidification conditions. The estimated solidification conditions, thermal gradient (G) and solidification velocity (V), were then coupled with a CET model which considers the elemental composition of the alloy.

3.1 Arcam Modifications, Process Control, and Geometry Selection

Due to small batches of custom alloys being produced, we modified the internal build chamber for processing a smaller volume of powder per build. This modification, referred to as the MiniVat, is incorporated inside the existing build column and requires a few changes to the process settings. In addition, an understanding of process parameters and the methodologies to control the same is required to process new alloy chemistries. During processing of new alloys, unique geometries are also desired that may create a wide range of solidification conditions in contrast to cuboidal shapes commonly reported in the literature.

3.1.1 Arcam Build Chamber Modifications.

A schematic of the MiniVat is shown in Figure 4. The first two iterations of the MiniVat, Figure 4 A and B, designs used a double blade seen in Figure 4 C and D. The double blades systems kept a powder mound in-between the two blades. However, this design was unable to produce parts taller than ~1 mm and therefore this design was discontinued. This limitation is due to the high flowability of powder, the large traverse distance of each raking, and the limited clearance of the heat shield (not shown in the schematic). The third version combined the original Arcam build table with the MiniVat column and shortened blade seen in Figure 5. The final design, returned to the full-length blade and removed the “Front Mod Single Piece.” The decision was made to reduce the hopper size instead of the shortening the blade.Figure 6 shows how the various components come together to make up the MiniVat as an insert to the main build chamber. Figure 6 (a) is the first addition, a piston that will go inside of the reduced build column seen in (b) with the build table set on top of the chamber. Figure 6 (c) includes the addition of the build cover and insulation rope seal.

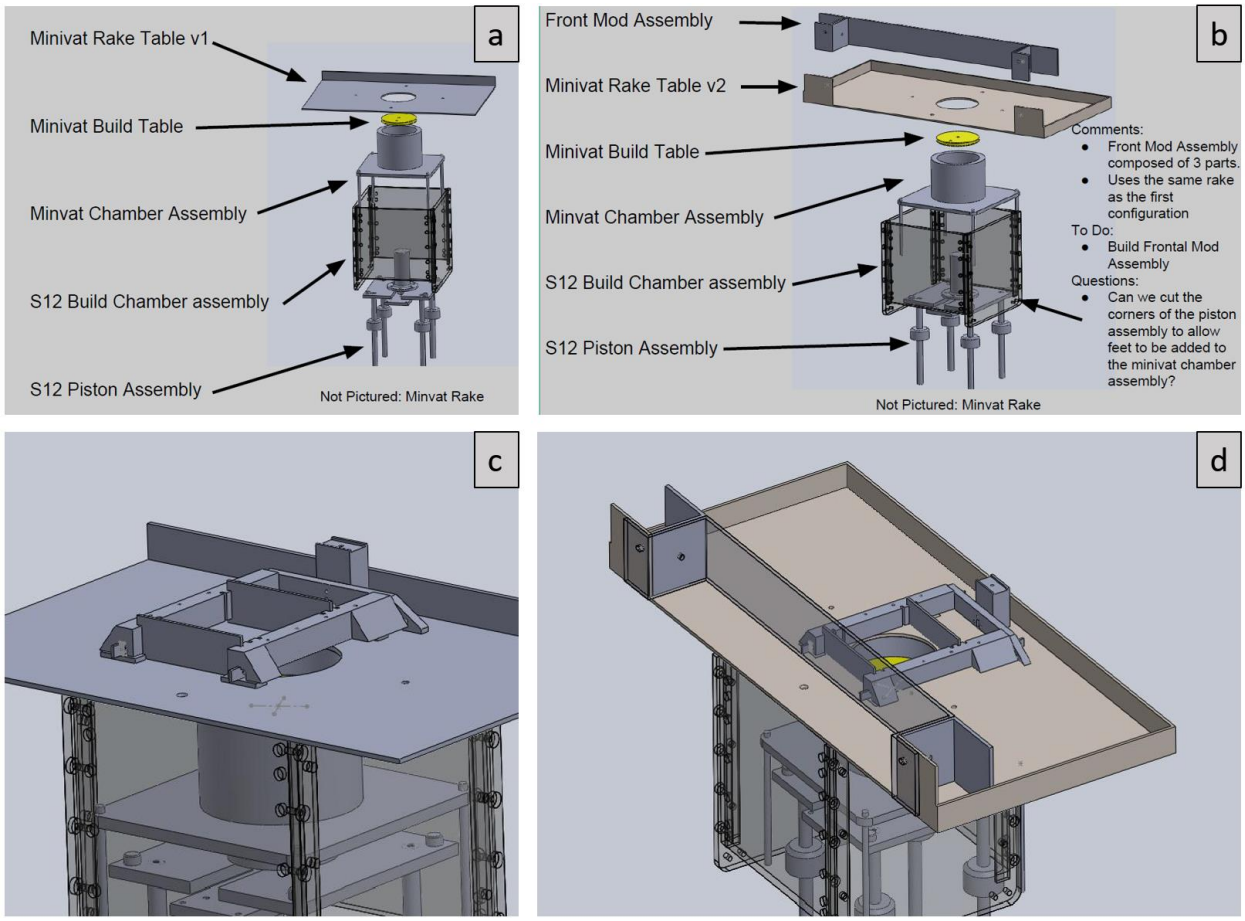

Figure 4. Schematic and rendering of early MiniVat insert Version 1 and 2.

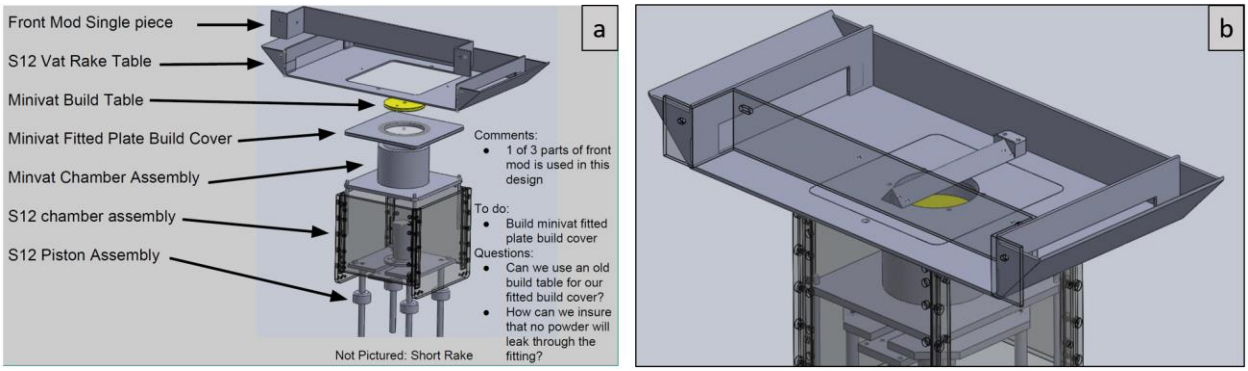

Figure 5. Assembly of MiniVat Version 3.

The MiniVat after a completed build using a 1-sided sweep is seen in Figure 6 (d). The final version could be improved further as the build cover was manually aligned with the rake table after each build. This lead to powder falling in between the build cover and the rake table seen in Figure 6 (d). The 'single rake' setting in the Arcam is not sustainable for taller builds as a mound begins to form on the opposite side and will eventually impede the raking motion.

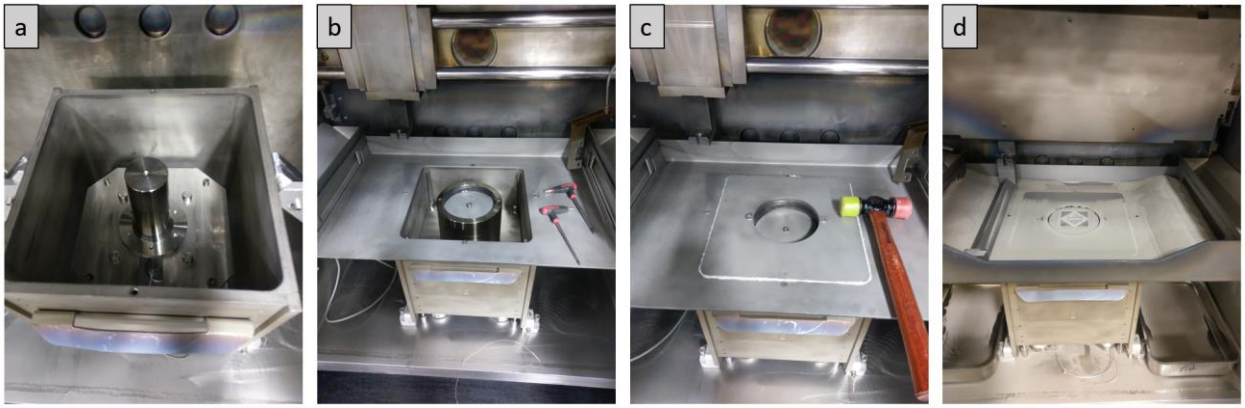

Figure 6. Inserting the Final MiniVat Version into the Arcam build chamber.

The modification of the build chamber requires a smaller build plate. Circular plates 100 mm in diameter were cut from 10 mm thick 316 stainless steel plates with a water jet. Before use, the top surface was machined to ensure a consistent flat surface for raking the first layer.

3.1.2 Process Parameters and Beam Control.

Going from an STL file to a finished part begins with correcting the orientation and organizing the STL geometries in relation to each other. Each individual STL is then loaded into Arcam Build Assembler and saved together as an Arcam Build File (ABF) which can be read by Arcam's "EBM Controller". EBM Controller versions 3.2 and 4.1 were used during this project and behave similar under the conditions and process parameters used. During set up, global build parameter and process themes for each part are selected. The control of the pre- and post-heat parameters are set once for all parts to control the build temperature, sintering powder to be melted, and heating the powder between parts.

During the Arcam process, the electron beam accelerating voltage is maintained at a constant 60 kV while the beam current is varied to change the input power. Primary process variables and parameters to control the beam current include the length of the present line pass being melted, x; the "Power Analyze Current" (set the Minimum and Maximum to the same value), *PA*; the *PropK*, *PK*; and the Scan Length Reference, *SLR*. These four values determine the current used in the process by Equation 1. Figure 7 gives an example plot of the current as a function of line length for 4 different combinations of process parameters. Current can also be locked to a single value by setting the minimum and maximum current values to a single equal value.

$$\text{Current [mA]} = PA * (1 + PK) * \left(\frac{x - SLR}{SLR}\right) \quad (1)$$

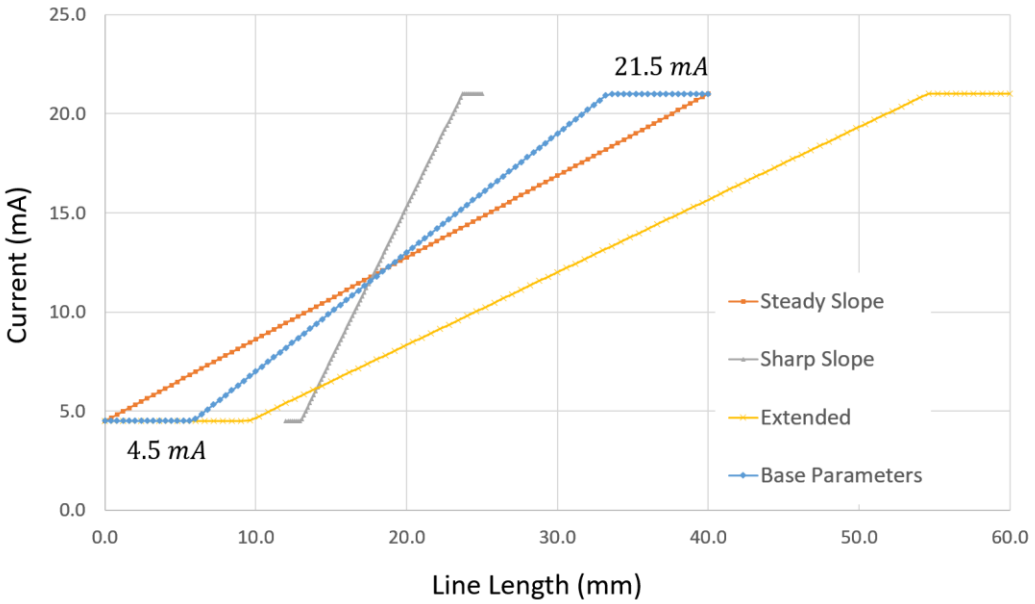

Figure 7. Control of Current/Power during processing.

Once the current is determined by Equation 1, the speed is set depending on a look up table and a "Speed Function" value. Figure 8 shows an example of how the speed is determined for a given scan length of 24 mm and a given set of process parameters. The beam current of 15 mA is set and then a speed is determined based on a given Speed Function value. Figure 9 compares three speed function values for a given current of 21 mA showing that a higher Speed Function leads to a higher speed. The Speed Function acts to limit the fluctuation in energy density. Increases in beam current lead to increases in beam speed and balance the energy density.

In addition, there are other modifiers of speed and current that can be found in the EBM Controller folders named Thickness, Thickness Current, and Turning Point. In most runs, the above modifiers are not applied, except for Turning Point. The tuning point function is controlled by three values: Pre-Exponential Factor, *PEF*; Exponential Factor 1, *EF1*; and Exponential Factor 2, *EF2*. The values modify the base speed, *BS*, (which is determined by the Current and Speed function) by Equation 2 and can be turned off by setting *PEF* to 0. *D* is the distance from the edge after a turn. The idea behind the Turning Point Function is to prevent over melting at edges. Figure 10 shows to variations in turning point function variables and the resulting beam speed.

$$New\ Speed = BS * \left[1 + PEF * e^{-BS*\left(EF1*\left(\frac{D}{.1}\right)-EF2*BS\right)}\right] \quad (2)$$

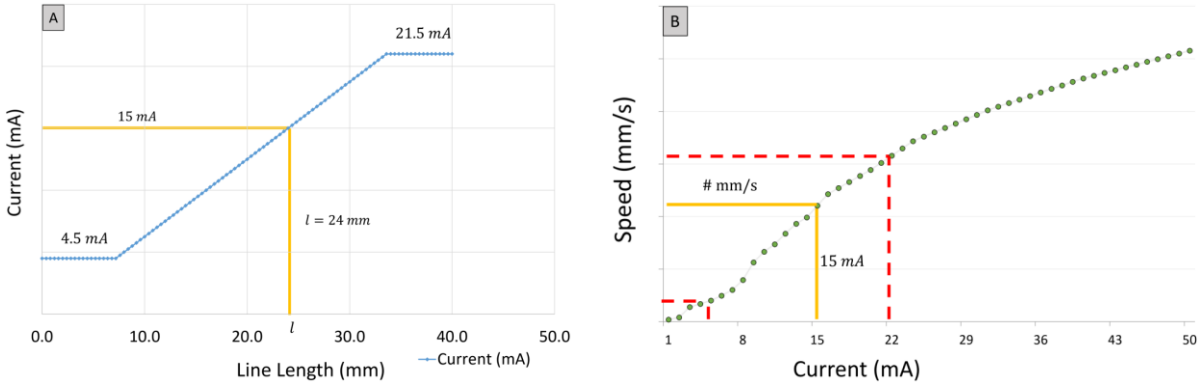

Figure 8. From line length to current to speed in the Arcam.

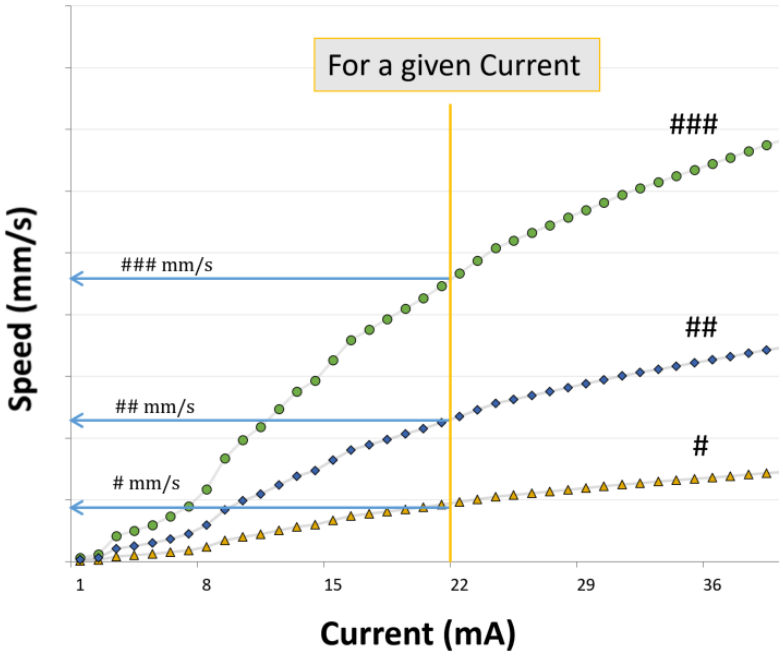

Figure 9. Comparison of Speed Function values.

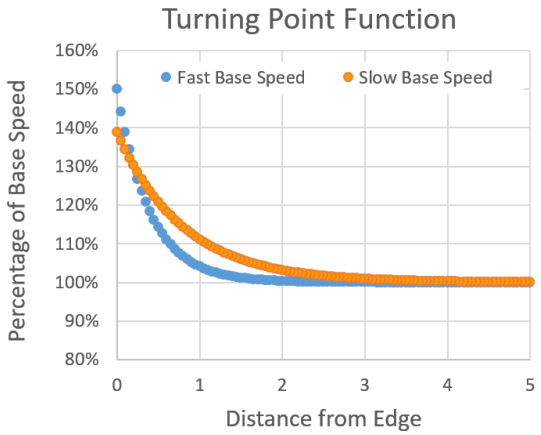

Blue Line	
PEF	0.5
EF1	0.00025
EF2	0
BS	1000

Orange Line	
PEF	0.5
EF1	0.00025
EF2	-0.000001
BS	500

Figure 10. Comparison of 2 base speeds modified by the Turning Point Function.

The actual value of current recorded in the log file during the process may not be the exact value given by the above equations and has uncertainty of ± 3 mA. Furthermore, the expected value can vary ± 1 mA from layer to layer as recorded in the log file. The cause of error could be because the equations given are no longer up to date or other modifiers were not turned off.

3.1.3 Choosing a geometry for S-EBM processing.

A right-angled triangular prism geometry was selected as the part design. This geometry would allow for the selection of a variety of processing conditions at different locations in a single part. In contrast, a cube would experience only a single set of process conditions per part. In specific, the diagonal of the right triangle would experience a gradient of current-speed combinations, see Figure 8. As the process can be set to rotate the raster by 90 degrees, the symmetry of the right triangle allows the diagonal region to experience a repeat of the processing conditions for each layer. Figure 11 shows an example-set of process parameters that creates a wide range of processing conditions across the diagonal. Using this approach, printing a relatively small number of right triangular prisms could give an insight into the behavior of an alloy during the S-EBM process.

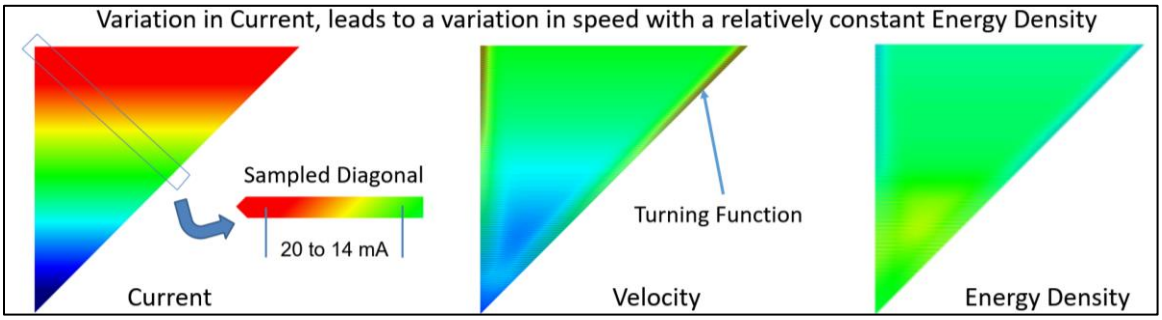

Figure 11. Visualization of generic process parameters for a single layer.

3.1.4 Evolution of Geometries Explored.

The solid triangular geometry was the result of MiniVat size limitations and worked to reduce the amount of parts required. The design started as a “Super Man” shape with separated triangles removed from the corners seen in Figure 12. The sepererated sections were added when further control of the Arcam process algorithm was realized, as described in Section 3.1.2. These geometry ideas are included as they demonstrate the influece of geometry on processing conditions. If all parts of a build are loaded as a single *.stl file, as done in Figure 12, the geometry of each part will influence the scan strategy and process parameters of the neighboring parts. In this particular case, the line length varies while melting a layer. This set up results in different currents and speeds within a single part in a repeatable manner.

Thin walls became a way to observe what happens when the beam moves away and the returns. Sections removed from the right triangular prism increase the complexity of the scan strategy without adding additional parts to the build chamber. For each geometry iteration, overhangs were not part of the design. Eight variations of geometries are given in Figure 13 with each geometry built in the Arcam except for B, C and D. The *.ABF slice images of Figure 13 E and G include spot melts (darker gray). Cubes occasionally were used to isolate the influence of process parameters on the scan strategy.

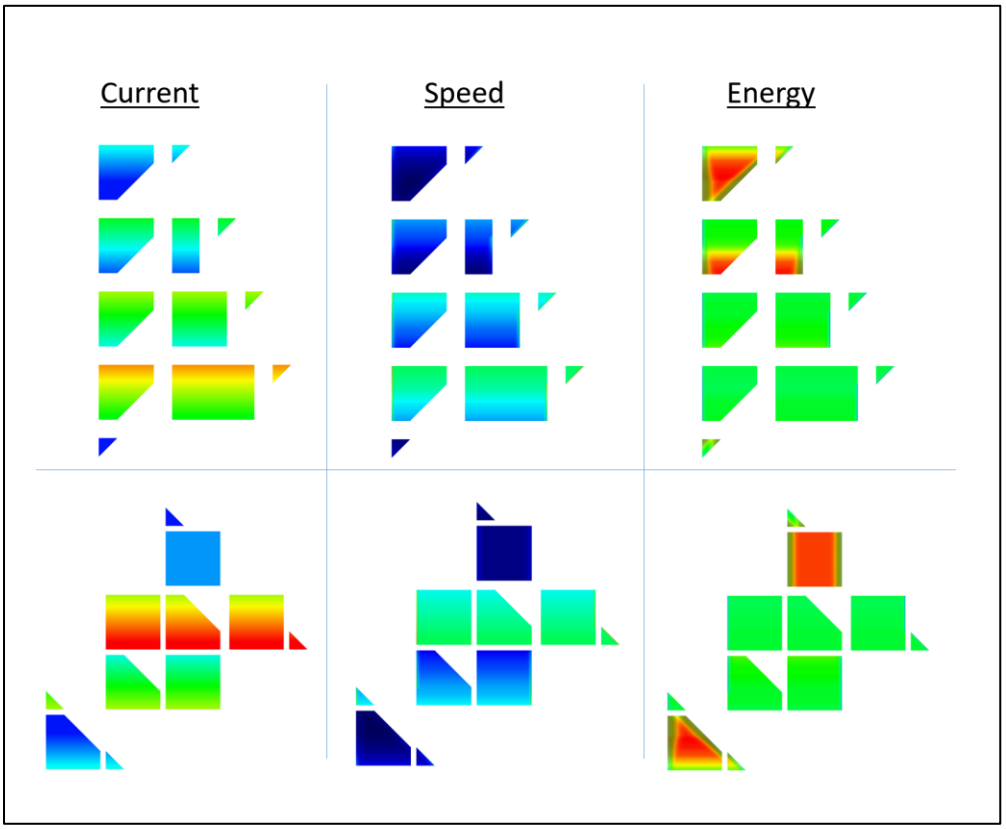

Figure 12. Two “Super Man” geometries viewed in XY plane by Profiler.

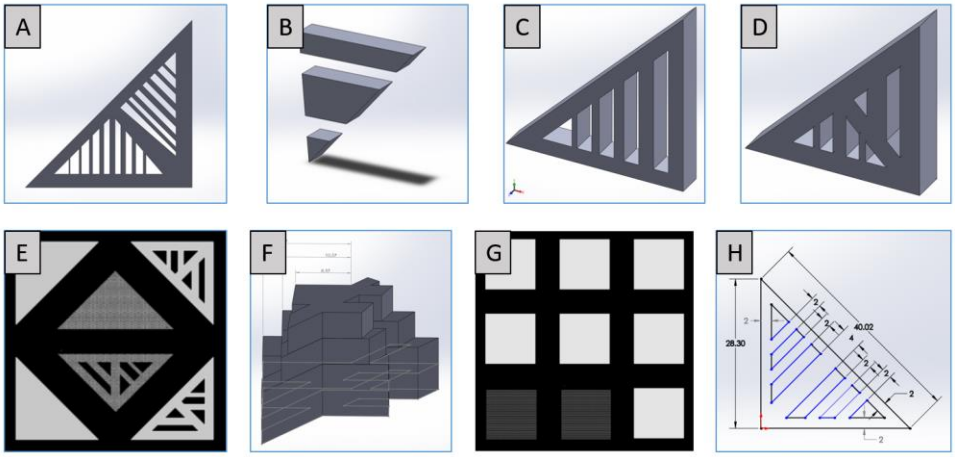

Figure 13. Evolution of Geometries.

3.1.5 From Process Parameters to Process Control.

Once the interaction of the controlling process parameters is understood and the geometry is set, the speed and current can be controlled using a simple excel sheet such as "Process Param _Ni666_F6.xlsx." Modification of the process parameters is possible during the build to minimize porosity or save a failing build. This is done by stopping the build and modifying the constants such as: *PA*, *PropK*, and *SLR*. Figure 14 is a screen clipping from the excel file where control of the process is simplified to 6 values: Min Current, Max Current, Triangle Length, Speed Function, Hatch, PA. Change one of the previous 6 values and new process parameters PropK and SLR are output on the right in the boxed region. Additionally, the resulting velocity, traverse speed, and energy density are calculated for the given parameters and right triangle size. Traverse Velocity and Energy Density are defined in Equation 3 and Equation 4.

$$Traverse\ Velocity\ [\frac{mm}{s}] = \frac{beam\ velocity * hatch\ spacing}{line\ length} \quad (3)$$

$$Energy\ Density\ [\frac{J}{mm^2}] = \frac{Current * 60\ kV}{beam\ velocity * hatch\ spacing} \quad (4)$$

3.2Build Robustness and Best Practices of the Arcam

Throughout the project, many builds ended suddenly during each stage of the build for various reasons. The S-EBM process can seem impossible at times and best practices help to avoid sudden build failure. The recommend practices for each stage of the build will be discussed here. The three primary stages of building include: (1) Setup before building, (2) Preheat and melting, (3) Post build (cool down, build extraction, and cutting samples from each build). The Arcam is not a push button machine.

4 x 28.3x28.3x13 mm Triangles			Temperature: 1180 to 1220 C		
1st and 2nd Tri (Colder - SF)				Solid & Complex	
Min Current =	3	mA	PA	12.5	
Max Current =	9	mA	Prop_K	0.76170213	
Triangle Length =	28.3	mm	Scan_Ref	44.75	
SF =	170		Slope =	0.213	mA/mm
Hatch =	0.125		Y-intercept =	2.98	mA
	Current (mA)	Length (mm)	Velocity (mm/s)	Traverse	Energy
Full =	9	28.3	2843	12.5590769	1.52
3/4 =	7.5	21.225	1528	8.99734982	2.36
1/2 =	6	14.15	1244	10.9893993	2.32
1/4 =	4.5	7.075	857	15.1384717	2.52
Min =	3	1	702	87.7375	2.05
				mm/s	J/mm2

Figure 14. Clipped Example of Controlling the Process Parameters.

3.2.1 Pre-Process Characterization of Powder and Set Up of the Build Chamber.

The first thing to do before attempting to build with any new powder is to characterize the powder. Characterization is required to determine the powder size distribution, shape or morphology, and if there is internal porosity. The characterization is performed in order to predict the processability of the powder. Having a size distribution that fits the recommended size, spherical powder, and no internal porosity is a good starting point. However, it does not guarantee a great build. Oxidation on the powder can lead to Arc Trips. Incorrect process parameters could lead to lack of fusion porosity. Powder that sinters too easily could ‘cake’ in the powder mounds to the side of the process. Or inconsistent raking could occur because the powder packs in such a way that a higher angle of repose is required for it to flow.

When running the MiniVat and a new powder, the setup is even more important. Special care should be made to guarantee each sweep of the rake will produce an even layer of powder. In this project the MiniVat went through many iterations with the final version capable of producing parts at least 20 mm tall. Figure 15 (a) is a picture taken of the final MiniVat set up showing the modified left hopper. There was not enough powder to fill the actual hopper so two blockers were added to the powder-shoot to take up space. The rake then must be set up so that it moves far enough to grab new powder that will cover the entire table as seen in Figure 15 (b). The limits of the rake are powder dependent based on how well it flows. Once the limit is set, the powder that is seen on the right side of Figure 15 (b) should be moved to the left hopper.

Powder size distribution for the Arcam process is typically between 40 and 105 µm [1]. This project showed that larger powder size distribution is viable for the Arcam process with Rene N5 powder being larger than recommend. However, when small powder, referred to as ‘fines’, is included the potential for Arc Tripping is increased. SEM or Laser diffraction techniques are useful in determining the size distribution. However, both techniques should be used with caution as the sample size is very small, 1 to 20 grams, relative to the powder lot, 50 to 200 kg.

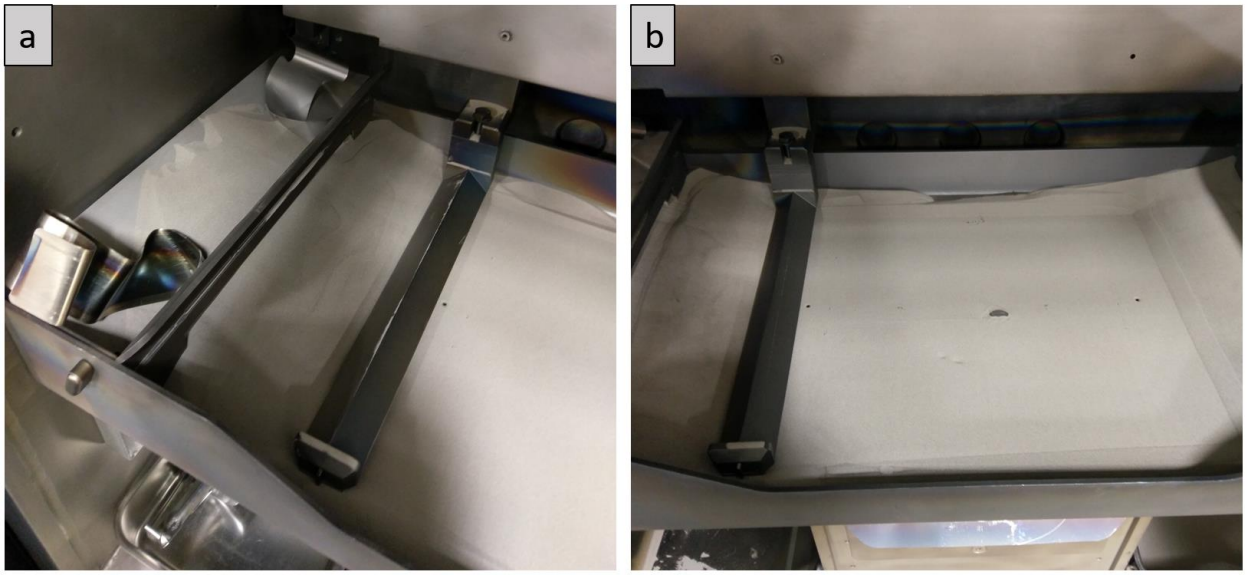

Figure 15. Setting up the build and rake distances.

Taking a sample off the top of powder that has sat for a while may not contain fines or other strangely shaped particles. In this work the containers of powder were only shaken before being poured into the Arcam. The morphology of the powder and presences of internal porosity depends on the process that made it.

Highly spherical powder that contains little to no satellites can be made by the PREP process. PREP powder cost more but it is also less likely to contain internal porosity. Figure 16 compares Hastelloy X, LSHR, Rene N5 (produced by PREP) using SEM and optical microscopy. The first set of images show that Hastelloy X and LSHR are within the standard size distribution but both contain some degree of fines. In the Hastelloy X most of the fines are attached to the surface of the larger particles and the powder is processable. Where the LSHR powder was not processable with the fines appearing to float unattached to the larger particles. In contrast the Rene N5 powder is highly spherical with fewer fines and appears bimodal (or possibly tri modal) when looking at the SEM images. The diameter vs Normalized Frequency plots of Figure 16 confirms that Rene N5 is mostly of the higher size distribution. Rene N5 also contains a significant number of particles below 45 µm and some fines that are seen in the higher magnification SEM images. For Hastelloy X and LSHR, fines appear much more often and dominate the plots given in Figure 16. From just looking at the images and plots both Hastelloy X and LSHR should have failed in the Arcam. The final set of images in Figure 16 is the cross sectioned powder that which reveals presence of internal porosity in both Hastelloy X and LSHR. The size of porosity found in the final part will be compared to that found in the powder to begin with.

Once the powder has been characterized the build chamber must be properly set up. The process starts with taking care of the previous build and each step is crucial in achieving a completed build. For example, forgetting to drop the plate 1.1 mm after leveling the plate causes the rake to

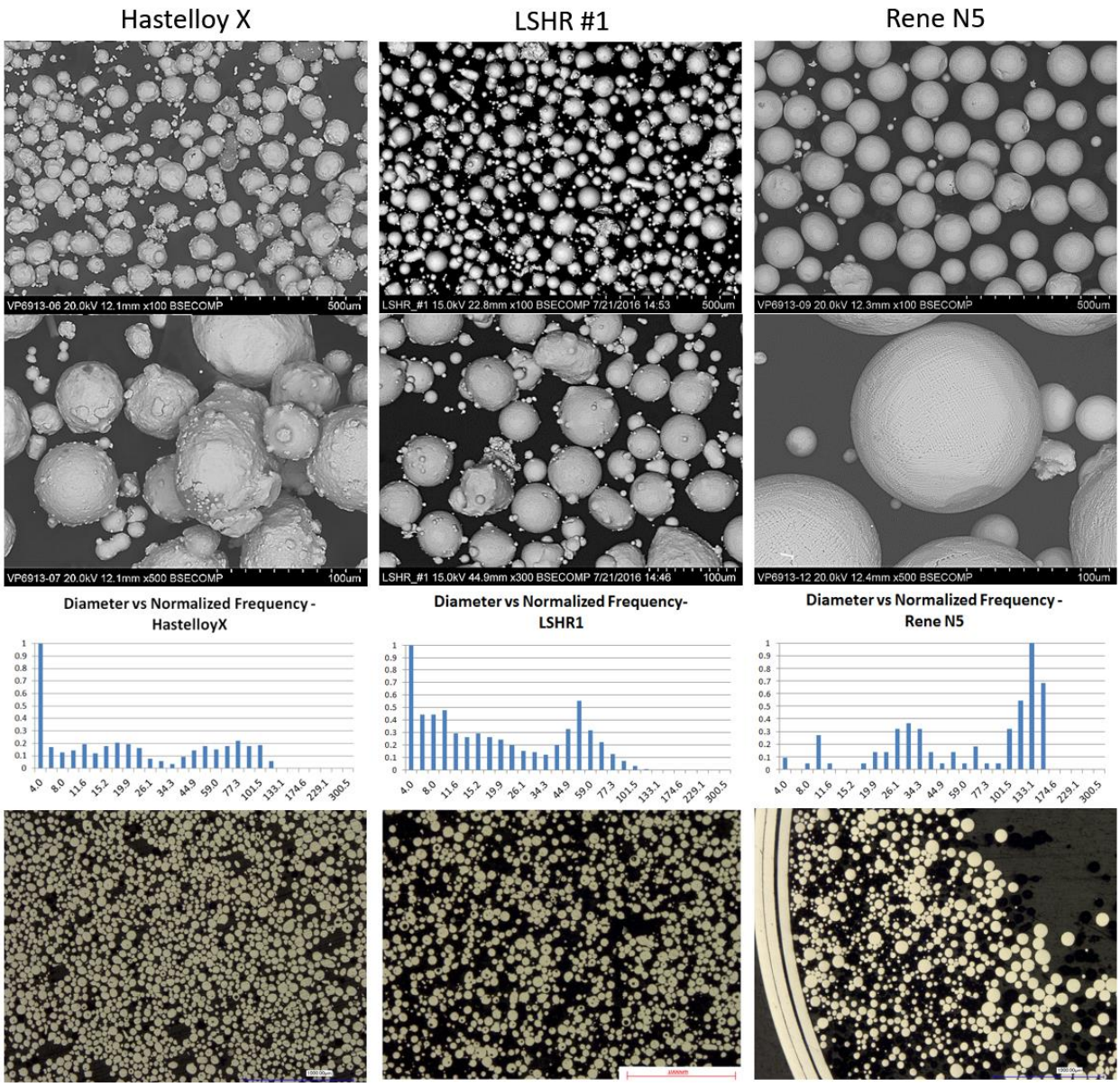

Figure 16. Powder Comparison of Hastelloy X, LSHR, and Rene N5.

crash into the baseplate once it has expanded from heating. The raking method must be correctly selected with the hopper set up. Checking that the thermocouple is grounded ensures that it works properly when the beam is on.

3.2.2 Robustness of Preheat and Melting Steps.

Preheat is a broad term that refers to the entire phenomena of rastering the electron beam over the base plate to heat it during the S-EBM process. For a lack of better vocabulary, the word 'preheat' will be used to describe any one of the following:

(1) the temperature recorded by a thermocouple below the base plate during the **entire cycle** of the build;
(2) **the process** of heating the base plate **at the beginning of the build** to an outgassing temperature and then to the sintering temperature;
(3) the assumed **temperature of the top surface** before the melting step occurs based on the thermocouple below the base plate;
(4) **the process** of heating the new layer of **powder that has just been raked** onto the top of the build;
(5) **the settings** which control the beam in process theme [0] in the EBM Controller software which can be split to Preheat 1 and Preheat 2 (noted by capital 'P');
(6) **the process** of heating the top surface of the build **between melt steps**.

Once the chamber has vacuumed down and the beam turns on, it is time to preheat the base plate to the start temperature. When doing this for the MiniVat the preheat area must be reduced to a 70 mm circle centered on the build plate and the current should be set to < 10 mA. About 20 mA will be required to bring the base plate to 1000 ºC but the smaller plate will increase in temperature rapidly if we start at 20 mA. Losing control of the vacuum and warping the plate can occur if heated too quickly. The operator should watch how quickly the temperature is rising and use this to gauge when to increase the current. Once the temperature has reached the desired starting temperature pay attention to how quickly the base temperature drops and returns during the outgassing and sintering phase before the build starts. At the starting temperature, the current will oscillate to maintain the temperature for set period to sinter the powder surrounding the base plate. The time required is powder dependent and commonly between 10 and 30 minutes.

Figure 17 shows the preheating and starting temperature fluctuations of three unique builds. Build A1 (a) shows a steady increase in temperature with outgassing at 550 ºC and a starting temperature near 1000 ºC. Then once the build starts, the temperature drastically decreases because the long initial layer time, close to three minutes. In this build, there was no preheating between parts and doing so could have drastically reduced porosity and maintained the build temperatures closer to 1000 ºC. Figure 17 (b) is from the first build with Rene N5 which shows a steady increase in temperature to an outgassing temperature. After outgassing the preheat current had to be increased to reach an elevated starting temperature. Once the build started, an appropriate preheat current, determined by the current used in preheating, was used to maintain the elevated temperature. In Figure 17 (c) an out gassing temperature near 950 ºC was used. Upon starting the build, the base temperature began to increase as the preheat current was too high.

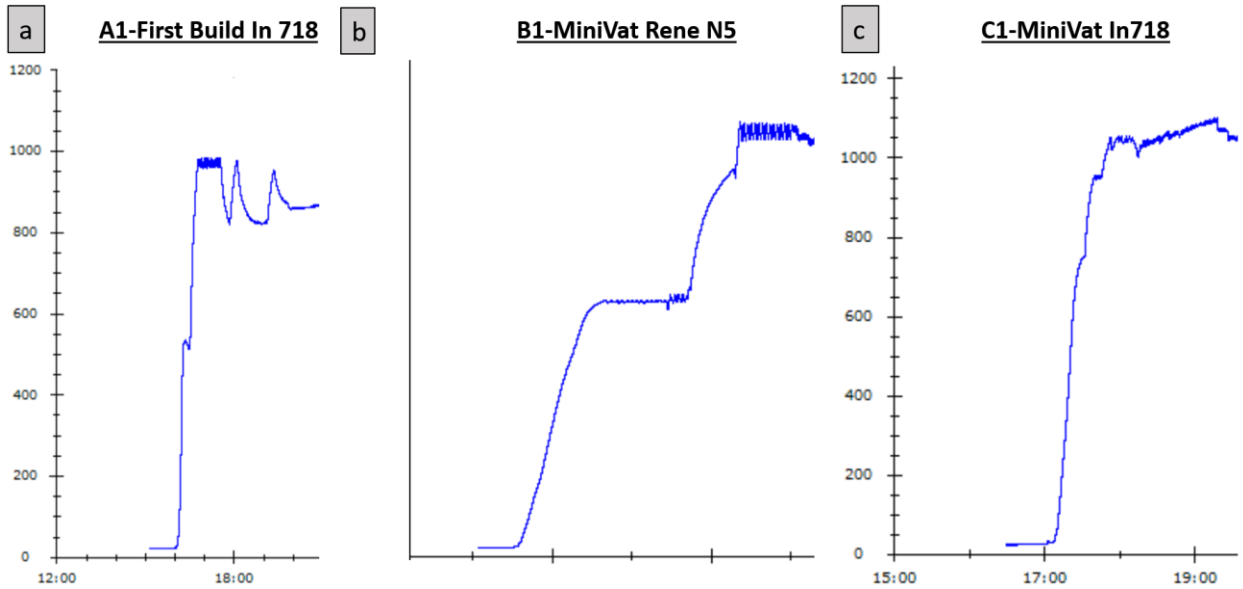

Figure 17. Initial base plate preheating for three unique builds.

The rate at which the base plate is heating and cooling during initial preheat can be used to decide how long to preheat (controlled by Preheat 1 and Preheat 2 repetition settings) and preheat minimum and maximum current settings. For powder with fines that is likely to Arc Trip, the preheat current can be ramped from low to high current.

During this project, preheat parameters used on one day did not necessarily give the same results on the next day. Reusing a thermocouple, a common practice, for high temperature builds leads to build up on the tip and a slower temperature response. Watching the glow of the base plate and checking the bottom temperature is required for each build. Once the melting begins, the leaded glass window is the best option for gaining information on how the build is progressing besides the overview screen.

Common occurrences that can be observed by the operator include:

1. Swelling of the parts, indicated by a variation in surface brightness once new powder is raked onto the part. Dark regions will be low points and bright regions will be raised humps. This phenomenon usually occurs at too high of energy input.
2. Bright spots on the top of the surface can indicate lack of fusion or gas porosity based on the size. High beam speeds or low energy density are common causes.
3. Balling, large defects that occur from unstable melt pools and low energy density.
4. Caking of the powder bed surrounding the parts preheating with too high of a current which will crack and disrupt the powder spreading. Reduce the Preheat current or repetitions.
5. Spatter, occurs most often when the build temperature is low. High beam speeds or low energy density could also be causes.

A ‘good’ build will be uniform height and brightness on the top of each part with little to no spatter. The preheat and post heat during the build stage should have a high enough current and number of repetitions to maintain a constant build temperature. Preheating between parts can be done for long layer times and is the default setting in the Beam Controller V5 software on the Q-series Arcam. Figure 18 (a) shows how the baseplate will glows a solid orange in the center with a border of cooler red where the preheat rasters are not touching. The circular preheat area applied here cannot be applied during melting steps and a square must be used instead. This is due to software limitation. Figure 18 (b) shows a nice uniform array of squares during a good build, where each cube’s top surface is even. This indicates the correct Preheating settings and that the melting process parameters that are within reason. Figure 18 (c) is a picture taken of the IR video software during a build which shows some swelling on the dark parts surrounded by bright powder that is being post heated after melting. Figure 18 (d) is of a build right before it failed due to phase lag between the beam and software controls. A grid is forming from where the pre- and post-heating are incorrectly being applied.

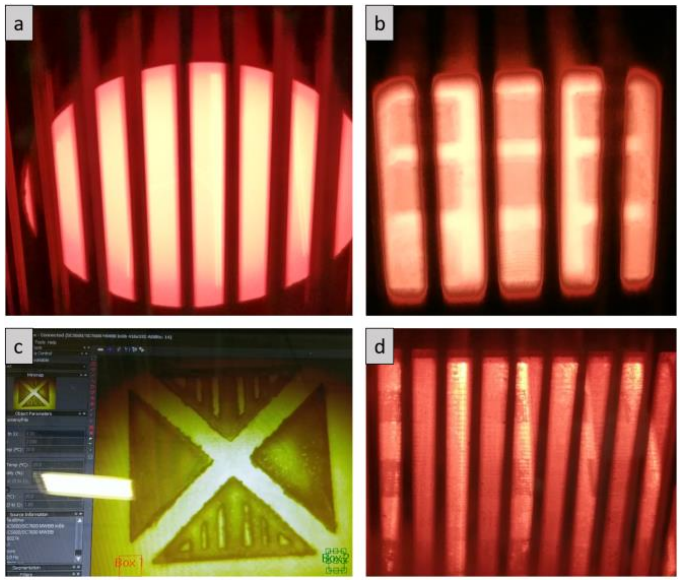

Figure 18. View of various builds at different times in the build.

3.2.3 Best Practices for Post Build.

Once the final layer has been completed, or an error has stopped the build, the Arcam will begin its post build sequence. The post build sequence is dependent on how the build ends. If the user stops the build, then the Arcam will stay idle until the user makes another change and expects the build to be restarted at any time. If an error ends the build or the last layer is reach then the electron beam will be turned off and the turbo vacuum pumps will turn off at an operator specified temperature. After the bottom temperature has reached below 100 ºC the chamber can be vented with air. Below 50 ºC is recommend for handling the powder. It is recommended to

take a picture of the final build overview screen to collect layer height, layer time, etc. As well as taking a picture of the errors that occurred. Figure 19 (a) is of the overview screen with orange boxes indicating the most important data for the post build. Clicking on the red circle with white ‘i’ takes the user to the screen shown in Figure 19 (b) containing the errors and when they occurred.

Once the door is opened, take a picture of the build while it is undisturbed. Note the size of the powder mounds and any discoloration of surrounding powder or parts. Figure 20 shows post build images of (a) the modified hopper that still contains powder; (b) a build that has ended due do an Arc Trip which removed powder from the top surface of the part and surrounding build plate; (c) top surface of the final build F6, which has small humps in the powder surface caused by the vibration in the chain moving the rake; (d) of the right side of the build which has a large mound of powder building up and could disrupt the raking since a single sided rake is used.

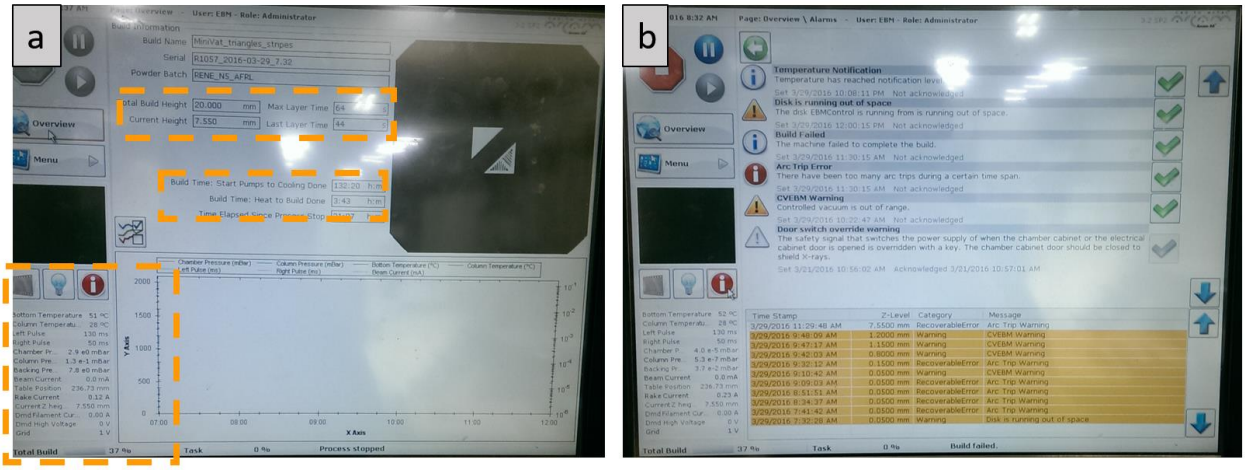

Figure 19. Pictures of the Arcam Computer Screen after Build B1.

Next, remove the entire build by raising the entire build to the original position. Try to remove sintered powder and label the front of the plate before it is lost. Write the name and date on the bottom of the plate with the build name.

Now scan the top surface with a desktop picture scanner to get the best image of the melt pool shape of the final layer or defects. Do this before and sand blasting for powder recover is performed if possible. A Keyence microscope can be used to either create a height map of the top surface or stitch together optical images of the entire surface.

To selectively remove parts from the base plate, use Wire EDM. This method will cut through the build part and base plate for removing samples in the build direction. Or it can be used to cut off all the parts in a horizontal direction if the base plate interface is not of importance. Builds that are known to contain porosity are not recommended for Wire EDM and will be a nightmare

for the operator. The first build of this project with Inconel 718, A1, is an example of this where the operator refused to work with us after that.

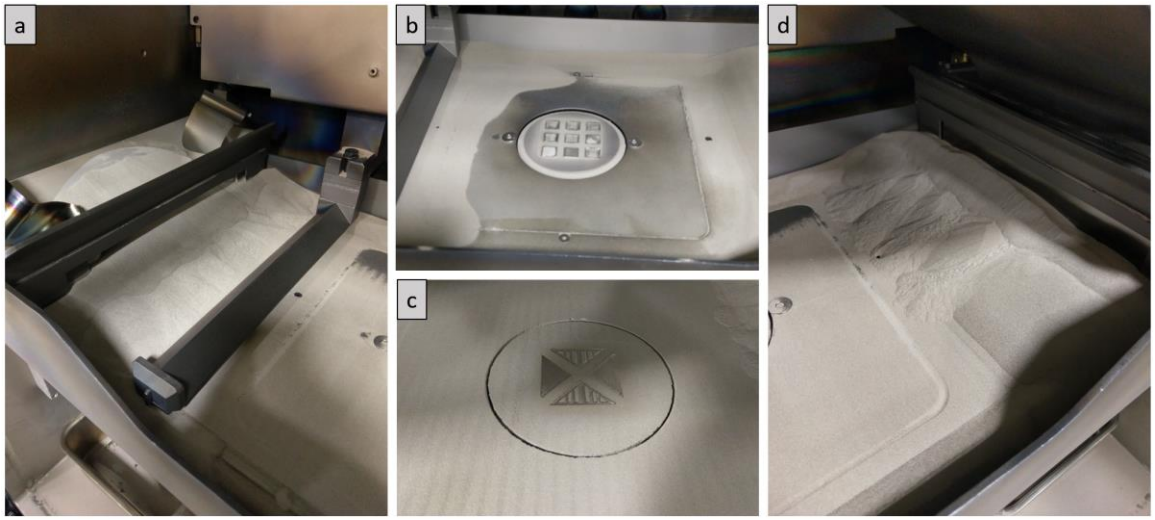

Figure 20. Recommended post build pictures of hoppers, mounds, and build top surface.

3.3Composition Driven CET Maps Developed

To understand how composition played a role in solidification structure a Columnar to Equiaxed Transition (CET) model was developed by Grant Helmreich and Michael Haines (unpublished at this time). The method for solving the CET for any composition is outlined in Suresh's 2002 Acta Materialia paper [32]. The solving method is outlined graphically in Figure 21 with constants listed in Table 1. This routine allows the CET to be estimated for any nickel-based superalloys to be generated for comparison. The method uses the same model parameters for each composition as experimental calibration is impractical to perform.

Figure 22 shows a comparison of the calculated CET line of three alloys used in this project as a baseline using $\phi = 0.5$ and the model parameters from Table 2. The CET line follows a power law in the region of expected solidification conditions and each off the alloys appears parallel. It can also be noted that the last location to solidify, and the most likely to be remelted, is the bottom right of Figure 22. This fits well with most models of the CET that assume remelting and ignore the effects of the powder layer as it is insignificant when a couple of layers are remelted. Also, Narendran recently showed that the most effective way to increase the volume fraction of equiaxed grains is to increase the preheat temperature [19]. The difference between each alloy is limited and the most varied nickel alloy, Hastelloy X is of a different class of nickel superalloys having no gamma prime precipitants. The end of each alloys predicted line indicates where the solidification mode will switch back to columnar regardless of how low the thermal gradient drops.

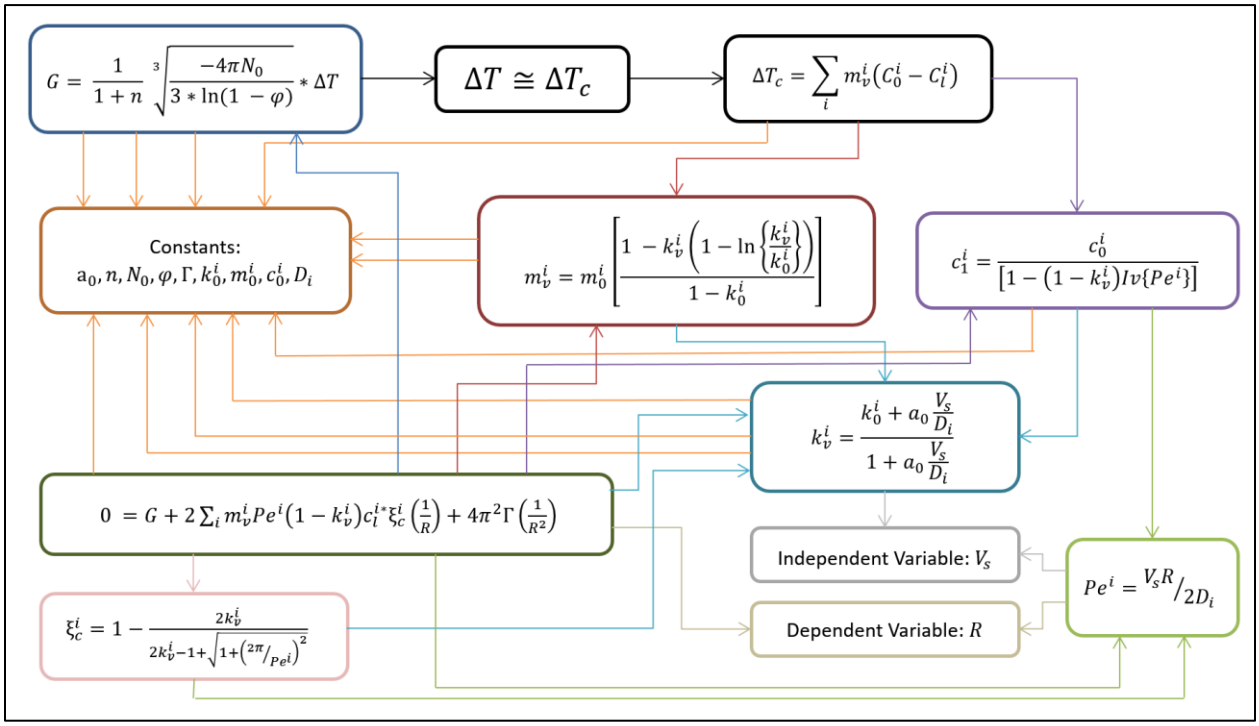

Figure 21. Solver routine expanding composition. With permission from author [33]**.**

Table 1. Constants used in CET calculation with starting values [33]**.**

Input Variable	***Description***	***Value***
n	Material dependent parameter	~3.4
N_0	Nuclei density	~2x10^{15}/m^3
m_0^i	Equilibrium liquidus slope of element *i*	Thermo-Calc
k_0^i	Equilibrium partition coefficient of element *i*	Thermo-Calc
a_0	Characteristic solute diffusion distance	~3 A
D_i	Solute diffusivity of element *i*	~1x10^{-9} m^2/s
C_0^i	Equilibrium concentration of element *i*	Defined by alloy

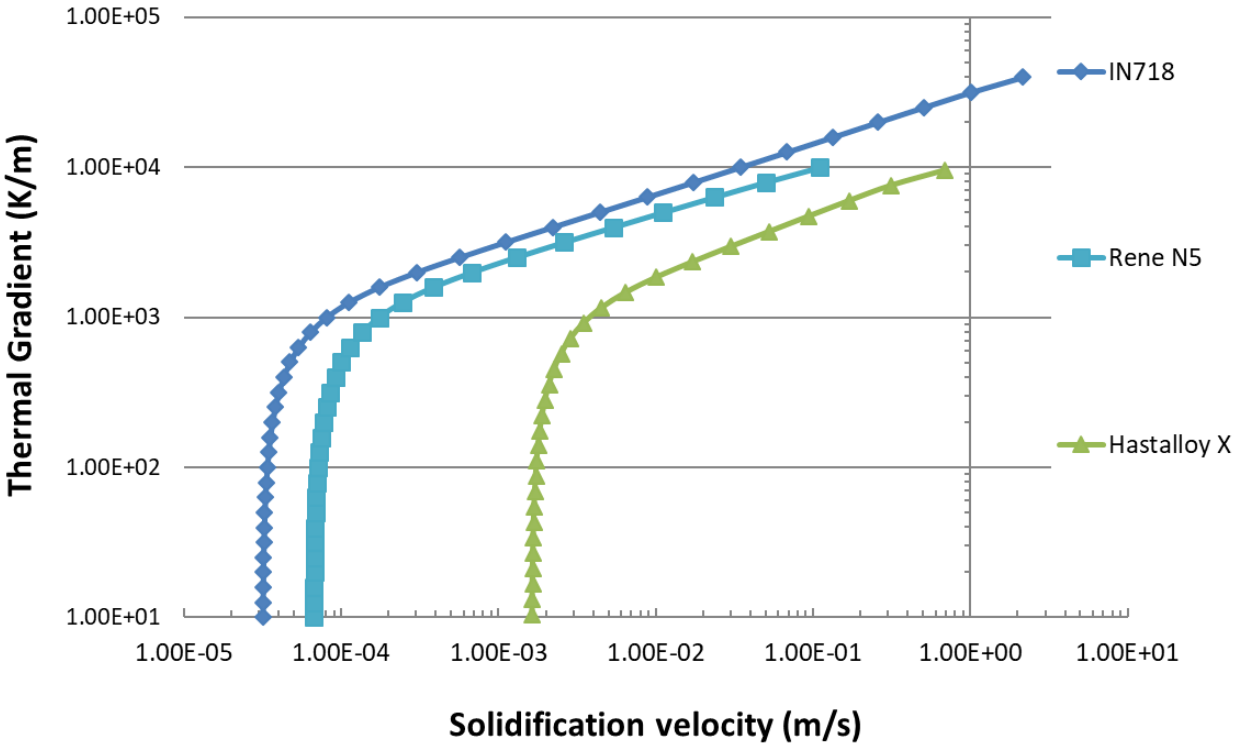

Figure 22. CET Lines Calculated for Traditional Alloy Used in this Work.

3.4Creating Custom High γ' Alloys for Verification

In the creation of the custom alloys, controlling the CET with limited unknowns was the primary goal. Nickel super alloys are predominately composed of gamma, γ, and gamma prime, γ'. To ensure the formation of gamma prime, aluminum is required in the alloy. Therefore, additional goal for the custom alloys was set for ensuring 70% gamma prime at a temperature of 1000 K (727 C). To ensure manufacturability in the Arcam system, the maximum aluminum concentration was set at 6 wt.% as commercial alloys don't typically exceed 6 wt. %. The second alloying element requirement is Chromium. Chromium is added to Nickel superalloys to prevent the hot corrosion or oxidation resistance. In commercial superalloys, chromium addition can usually be up to 15 wt.%. Figure 23 is a ternary phase diagram created in Thermo-Calc to show how the region containing γ and γ' changes with differing amounts of chrome and aluminum. An additional restriction of 0% titanium was set by the powder supplier, Oerlikon, to avoid problems associated with gas atomization.

Other elements, including Iron, Tungsten, Molybdenum, and Tantalum, were also explored to create alloys with high CET and promote the easy formation of equiaxed grains. Of these elements Iron, Tungsten, and Molybdenum serve as solid solution strengtheners and Tantalum influences the formation of gamma prime in conjunction with Aluminum. Each of these elements

were considered with base composition containing Nickel, Aluminum, and Chromium leading to alloys with four elements. The concentration of these elements was incremented through using Thermo-Calc to locate an alloy composition with the highest CET, while maintaining the 70% volume fraction of γ'.

With the above conditions, the first custom alloy composition containing 10 wt.% Chromium, 6 wt.% Aluminum, and balance Nickel (84 wt.%) was designed. The second alloy included the Tantalum to move the CET line further and reduction of Chromium to ensure a two-phase region of only γ' and γ' from solidification to room temperature. Figure 24 shows the equilibrium phase fractions vs temperature for the two custom alloys. Each solidifies over a narrow range at around 1400 °C. The main difference between the two alloy is the solvus temperature and rate at which the γ' phase becomes dominate.

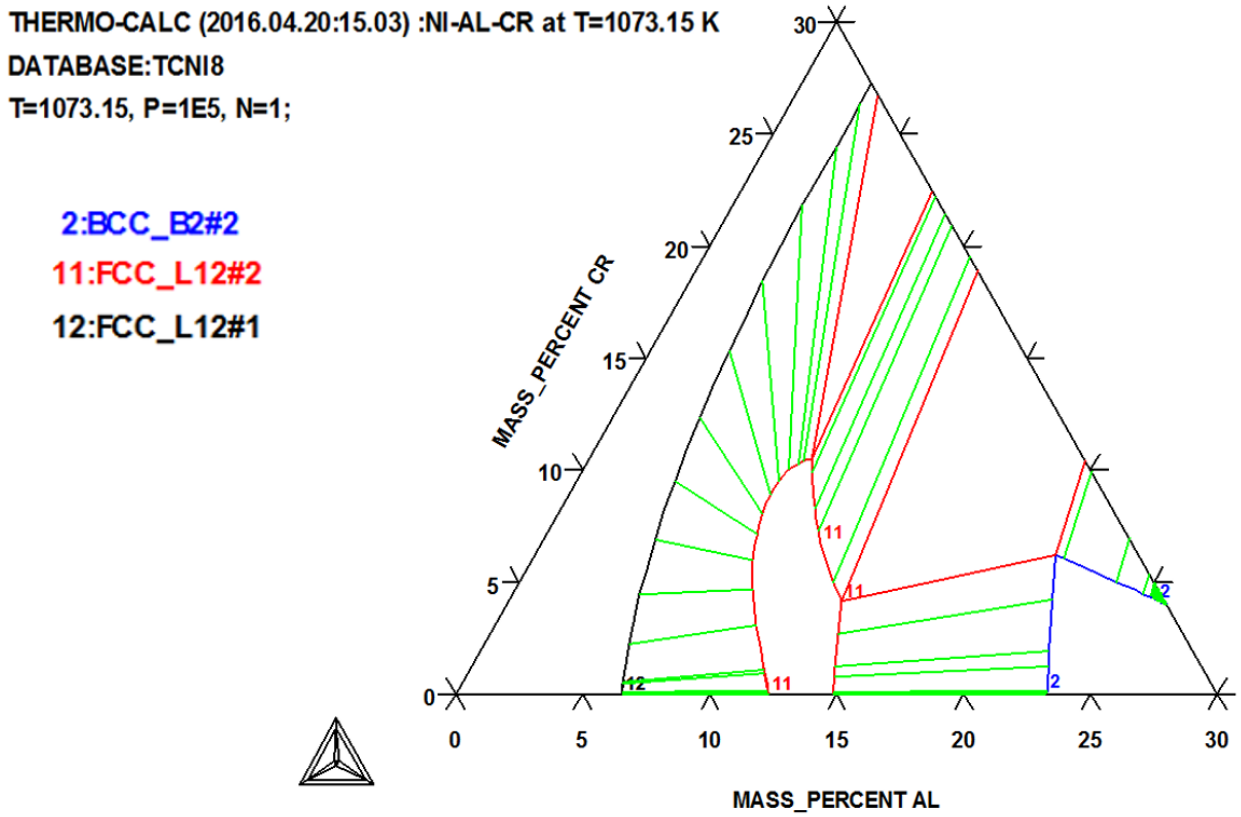

Figure 23. Limited ternary phase diagram of Al, Cr, and Ni.

Figure 25 plots the CET lines for the traditionally processed alloys and the two custom alloys for comparison. The Ni-666 alloy aligns very closely with Rene N5 and Inconel 718, indicating that it could obtain an equiaxed grain structure if processed under similar conditions. The Ni-106 alloy falls in between Rene N5 and Hastelloy X. It appears that the variation in CET due to composition is limited.

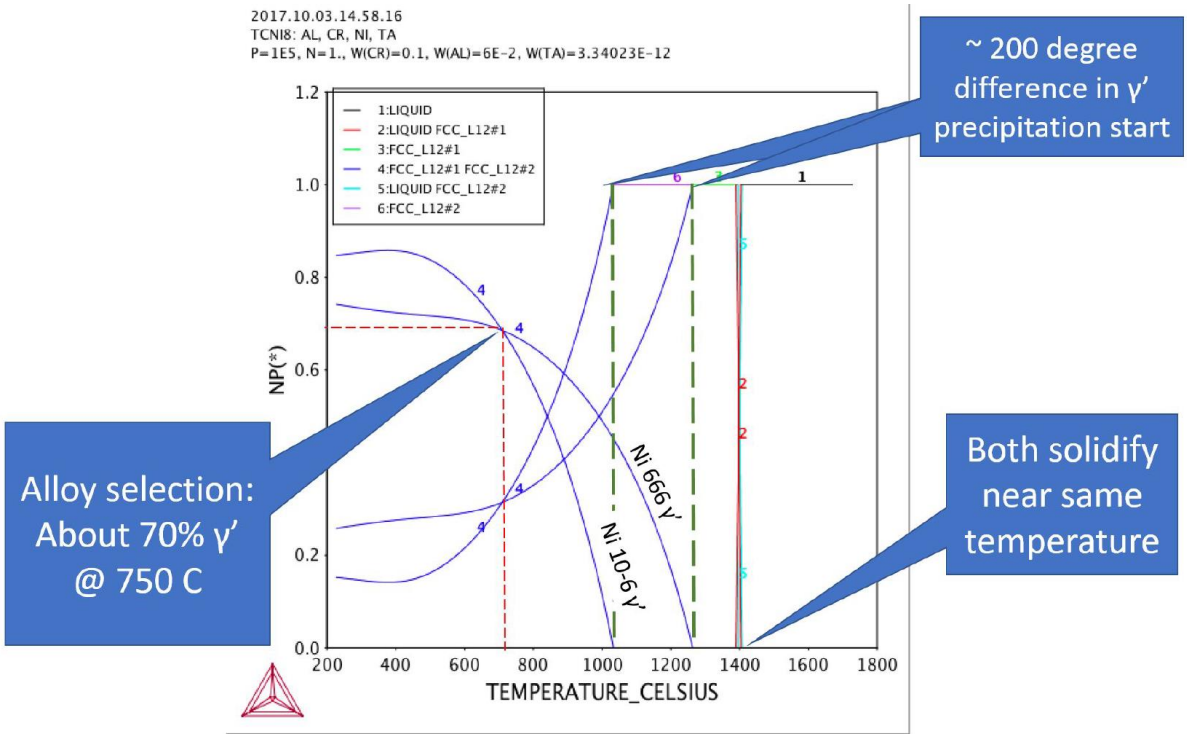

Figure 24. Phases upon cooling from liquid for two custom alloys.

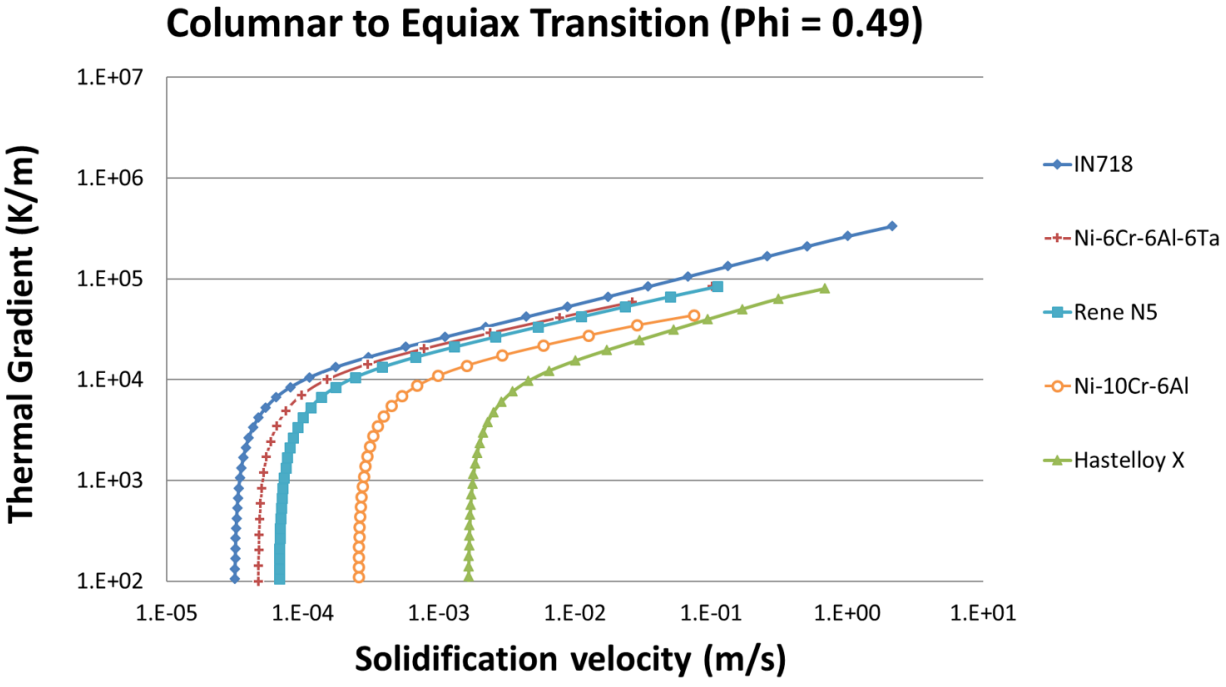

Figure 25. CET lines for processed alloy in this project.

3.5Nickel Alloys Explored with S-EBM

During this project, four traditional alloys and two custom alloys were processed with S-EBM. The compositions of the processed alloys are summarized in Table 2. Inconel 718, Hastelloy X and LSHR powders were available. Rene N5 powder was supplied by AFRL. The two custom alloys, Ni-6Cr-6Al-6Ta (Ni666) and Ni-10Cr-6Al (Ni106) were supplied by Oerlikon.

Table 2. Nickel Alloy Compositions

Alloy	Ni	Cr	Co	Al	Fe	Mo	Nb	Ti	Ta	Other
Inconel 718	53.4	18.6	0.14	0.44	18.5	3	4.96	0.82	0.01	Si .07
Rene N5	62.9	7.16	7.5	6.13	0.09	1	0	0.02	6.6	Hf .16, Re 2.9, W 4.9
Hastelloy X	46.8	22	1.5	0	18	9	0	0	0	Si 1, W .6, Mn 1
LSHR	52.3	13	21	3.5	0	3	1.5	0	1.6	W 4.3
NiCrAlTa	82	6	0	6	0	0	0	0	6	-
NiCrAl	84	10	0	6	0	0	0	0	0	-

3.5.1 Sample Organization and Preparation.

Most samples in this project were selectively extracted by using a Wire EDM process. This approach allows samples to be cut in a systematic fashion from the built parts. Each alloy/process combination is given a capital letter (A-In718 initial builds, B-Rene N5 in the MiniVat, C-In718 processed in MiniVat, etc.) and each build run is given a number based on the order it was processed (1-x builds). Next each part is given a number (1-n cube parts) or letter based on geometry (S-solid or C-complex). These prefixes are then added to the sample orientation/position indicated by a letter (A, B, C, …, i, j, etc.). The labeling follows the order: Build, Run, Part, Location (Example: B1SA = Sample A, cut from the Solid part, produced by the 1st run of Rene N5 (B) in the Minvat). After extraction by wire EDM the parts were mounted in either epoxy or a conductive mount to be polished (120, 320, 500, 800, 1K, 2K, and 4K grit). Etching required additional polishing to 1 um (no colloidal silica) while EBSD or edge lighting in Keyence required over-night final polish of colloidal silica on a Buehler VibroMet™ 2.

3.5.2 Keyence Imaging of Grain Structure Using Edge Lighting.

Using the Keyence with edge lighting allowed for speedy imaging and classification of samples for further grain structure examinations using electron microscopy technique. It is noteworthy that Keyence VHX-2000 is comparatively cheaper than EBSD characterization to run with quick set up. Numerous images can be captured, across large areas of the samples, analyzed and saved within a short duration (e.g. hours compared to days associated with EBSD). Further details on Keyence Imaging can be found in the Appendix, 88A.1.

3.5.3 EBSD to Confirm Grain Structure and to Determine Grain Orientation.

Electron Backscatter Diffraction is performed in a Scanning Electron Microscope and uses the Kikuchi patterns to determine the grain orientation (see Figure 26). When mounting the sample, the Build Direction (Z) is typically aligned with the classic Rolling Direction (RD) and flipped when loaded into the SEM. In addition, samples can be sectioned such that the build direction is perpendicular to the polished surface of the sample and aligned with the normal direction (ND). Regardless of the orientation of the sample all three axis of the Nickel FCC unit cell can be determined in this technique because the Kikuchi pattern is being used. When an Inverse Pole Figure Map is produced from a scanned sample surface, the axis that is plotted can be chosen within the software. From a single sample, the relation of the grain structure to build direction and each grains rotation to neighboring grains can be determined.

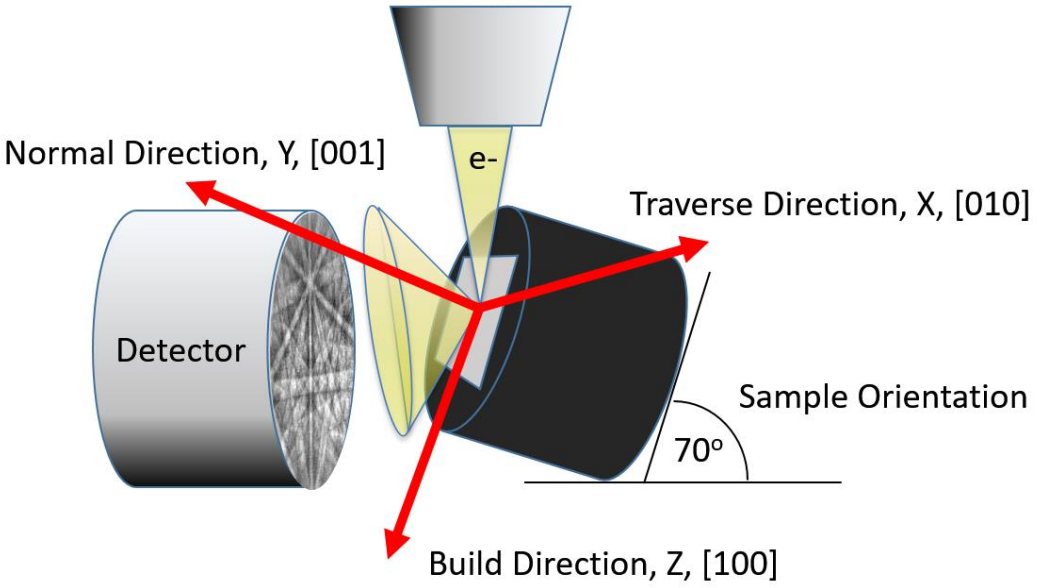

Figure 26. EBSD set up with orientation of sample related to beam. Adapted from [34]**.**

3.5.4 Etching of Polished Samples.

Etching of polished samples was performed in this project to characterize the precipitate structure (γ' in γ matrix). Glycerigia with a swabbing technique was successfully used to observe the γ' precipitants (when observable). This technique required that the samples be polished with 1 hour prior to being etched and then imaged the same day as etched. In alloys that did not have γ' precipitates, the grain boundaries were preferentially etched (In718 and Hastelloy X). SEM was used to capture the precipitant size at various locations of samples.

3.5.5 Micro Hardness Mapping.

Arrays of Vickers hardness indents were made on samples aligned in the build direction to qualitatively determine the gradient in precipitant structure from base plate to the top surface. The hardness maps were performed using a Leco LM with Vickers tip and either 300 or 500 grams. Once the measurements were completed a script in Igor Pro was used to map out the variation in hardness.

3.6 In-situ Infrared Monitoring of the S-EBM Process

In select builds, an IR camera was set up to record the intensity of IR emitted from the top surface of the parts and surrounding sintered powder for an entire layer. In the past, the data gathered in this technique was used to record the spatial location and amount of porosity that appeared during the process[35]. The IR camera was used to track chimney pores in Ti-6-4 [36] and to predict microstructure in Inconel 718 [21]. An early version of the setup is given in Figure 27 which includes a custom viewing port that adds a scrolling Kapton film in front of the lead glass window to prevent metallization on the window. The FLIR 7600, a mid-wave IR camera, was used in this work with a trigger set in the FLIR's ResearchIR software to break each layer into a separate video file. In the current set up it is not possible to record the entire build as the Kapton film must be manually rotated between layers while the beam is off.

In Raplee et. al. [21] to predict Inconel 718 microstructure a code was written in MATLAB to analyze the results and convert from IR intensity to temperature. A fitted calibration curve of both a powder region and melted region are required in order to accurately convert from IR intensity to temperature. In addition, the MATLAB code identifies the melting event for each pixel and switches the calibration curve from powder to solid material. The calibration curves used in Raplee et. al. [21] were used in this work as well and are shown in Figure 28.

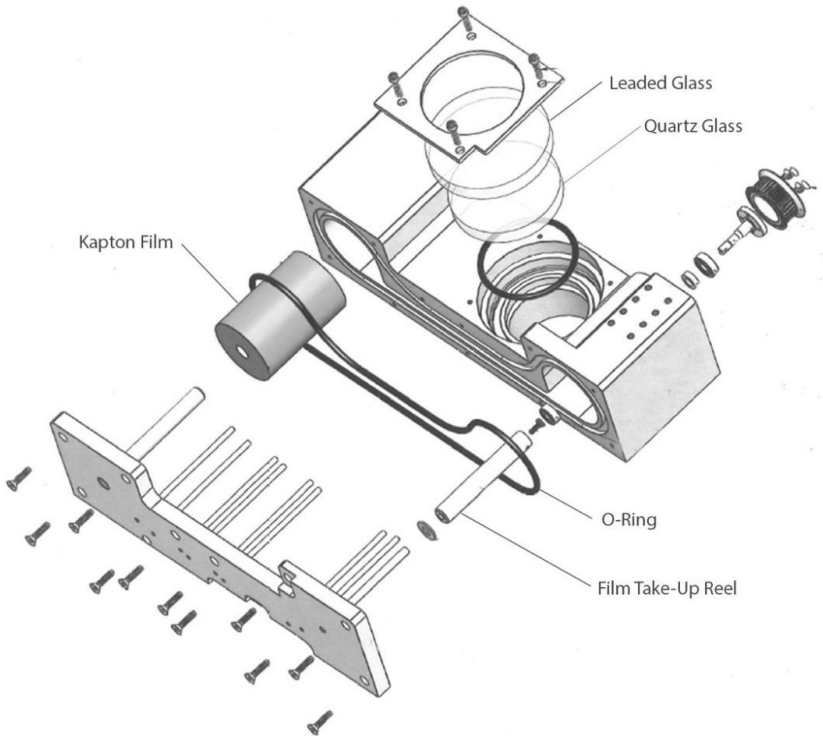

Figure 27. Protected viewing port for IR video. Reproduced with permission [35]**.**

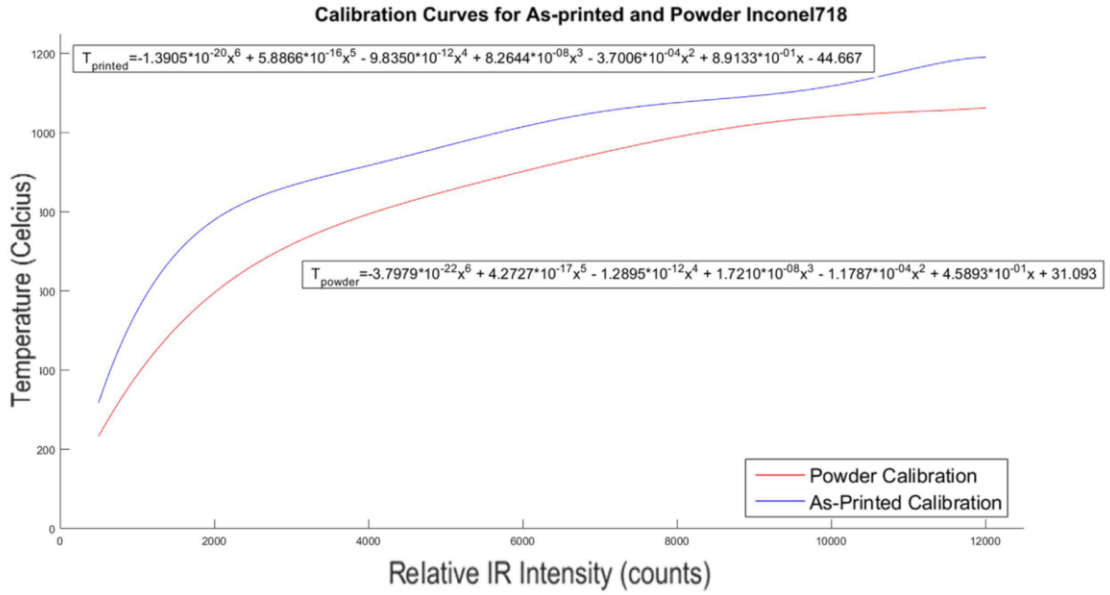

Figure 28. Calibration curves for IN 718. Reproduced with permission [21]**.**

3.6.1 Converting from IR Intensity to G and R values.

The method for converting from IR intensity to spatial G and R values is outlined here. The first step is to screen for good video files. Some of the video was out of focus or the surface too rough to make use of the analyses method. The analysis begins with loading the IR video using a MATLAB code named "AAA_IR_Video_Analysis.m" (primarily for structure and plotting) which uses an additional file named "BBB_IR_Layer_Profile.m" (finding the melt event and applying the calibrations) which contains the function for converting from IR intensity to temperature.

The code starts by taking a user inputs including the location/name of the IR video file. These inputs contain the name of the builds, part, and layer; the x and y coordinates of the window of interest; the frame rate of the video; and the start/stop frame numbers. The current version of the code requires a converter written by FLIR to remove the header sections and read in each frame (*n*) as a matrix of intensity values (*x* and *y*). Each pixel at, at a given *x* & *y* location can then be looked at as a function of time in the *n*th dimension of the 3d matrix. A single frame (*n* = 151*)* of the selected frames, for a selected window is shown in Figure 35 (a-c) for part #3 of three different builds: E4, E2, and F4 respectively. The first build (a), E4, has a smooth top surface rastering from bottom right to top left; the second (b), E2, has a small amount of swelling and rasters from top left to bottom right, and the third, F4, used spot melting which sweeps from top left to bottom right. Frame 151 of Case 3 (c) occurred when the beam was off. Each image also has the same 5 markers (Center, Q1, Q2, Q3, and Q4) used for checking the data. In this case, the center, Q1, and Q4 will be melted while Q2 and Q3 are in the surrounding powder bed. In Figure 29 (a and b) it is possible to see the beam location which appears as the highest intensity in both cases near the center marker.

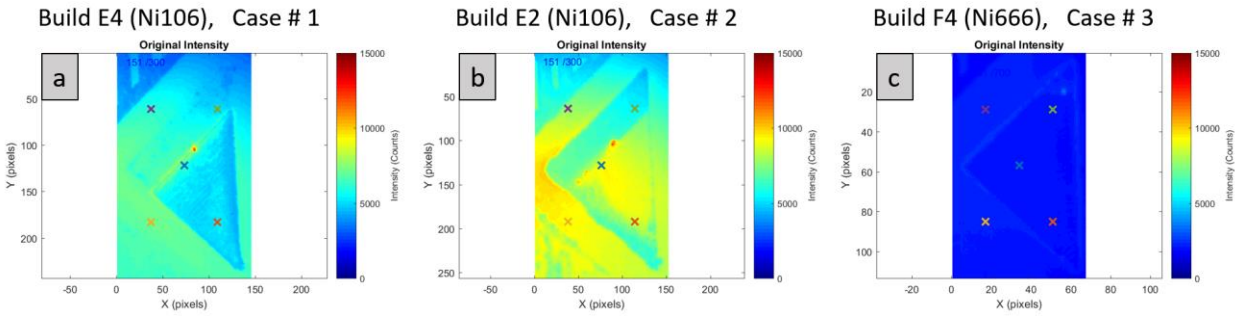

Figure 29. Original intensity at Frame 151.

Now that the area of interest and frames of interest have loaded, the intensity over time is extracted for each pixel individually. There are four specific events of interest during the video: Preheat, melting elsewhere with a drop-in intensity, melting on a pixel giving a spike in intensity, and post heating gradually raising the intensity. To see these events, we can plot the intensity of the 5 marked points over time for the first case, E4, in Figure 30 (a). Q2 and Q3 do not experience melt events which fits well with the positions seen in Figure 29 and they have no intensity spikes in Figure 30(a). In Figure 30 the black markers indicate the frame with the

largest slope which should be attributed to the melt event (if it occurred) and the black lines indicate the trim values given as input. Figure 30(b) shows the data after it has been smoothed and Figure 30(c) shows a piecewise temperature plot using the two Inconel 718 calibration curves. Before the transition, a calibration curve for sintered powder is applied, and after the transition frame a calibration for solid material is used. It is important to note that the transition point is identified on the smoothed curve (b) to improve the accuracy, then taken back to the raw intensity where the local maximum is found and marked as the transition point. All of this takes place in the function "BBB_IR_Layer_Profile.m" and the plotting takes place after the frame was identified.

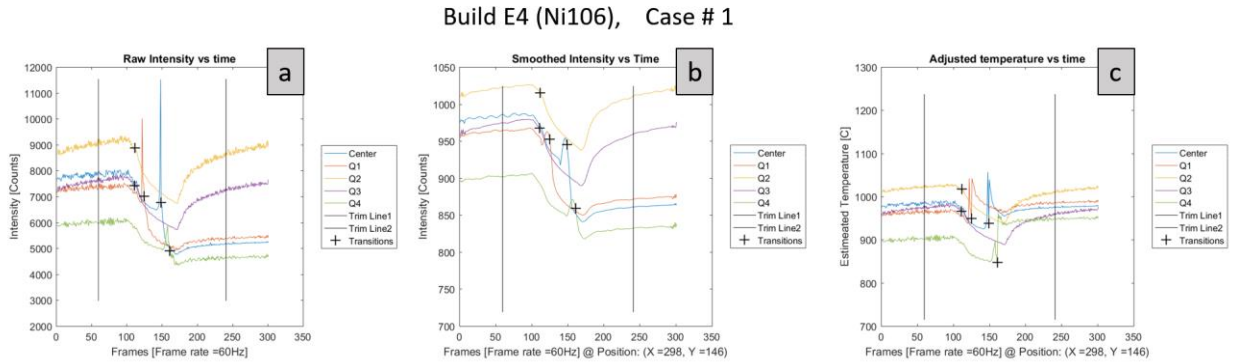

Figure 30. Intensity or Temperature vs Time for Part 3 of Build E4.

Determining the transition point requires that the greatest change in intensity correspond to the melt event, which works well in simple cases such as in Case 1 in Figure 30 and Case 2 in Figure 31(a). For the regions where a melt event does not occur, a possible transition is commonly found when melting begins to occur elsewhere and the powder is no longer being preheated as seen for markers Q2 and Q3 on all plots. The slopes will be compared in a later step to determine which melted and which was powder.

Spot melt presents a challenge to this method as the IR intensity events vary from that of raster melting. The time between preheating and the first melt is often identified as the greatest slope. When the curve is smoothed the melting, region does not contain a specific event which can be identified as the melting step. This is due to each region being remelted by the beam many times before cooling down. This is seen Figure 31 (b) for the Center pixel, Q1, and Q4. In this example, the transition was wrongly identified and will adversely affect the results.

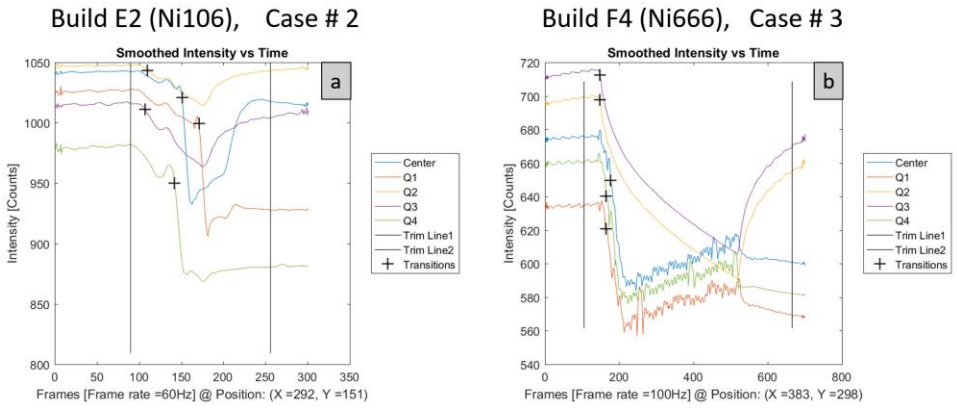

Figure 31. Greatest slope method does not work well for Spot melting.

Next a cutoff (a user input) is applied to the slopes at each pixel. If the slope for a pixel is greater than the cutoff value, it is marked as a melted region. Figure 32 shows the applied cut off with (a-c) mapping the slope values that were calculated and (d-f) giving a black and white image of whether the transition will be applied to that pixel or not (the white region is considered to have melted). Figure 32 (a and d) from case #1 are very clear and work well for this method. Figure 32 (b and e) have a raised region in the middle of the part which cools more slowly and thus is cut off from the having a transition applied to it. And Figure 32 (c and f) of case # 3 used a correct cut off value; however, as we saw in Figure 31 (b) the transition point which was identified is not the final solidification position. At this point, the operator could adjust the trim values to exclude the preheat and initial drop; however, the final melt will still not be identified, and a new method will need to be created for handling spot melting. This new method could look forward multiple points ahead of the identified transition point to check for another local maximum.

Next, a check is put in place to re-map the same frame as before (n = 151) as seen in Figure 33 (a-c) and Figure 33 (d-f) to map frame the transition point. The estimated temperatures on (a-c) are from the Inconel 718 calibration curves discussed previously. In Figure 33 (a) the method appears to have worked well, because the melted material is hotter than the surrounding powder and no transitions have occurred in front of the beam. The beam is a small red dot in Figure 33 (a) and (b). One short coming includes the effect of the IR viewing angle which makes the top of the image appear colder than the bottom. This error is present on Figure 33 (b) as well which has two additional problems: (1) the transitioning frame occurs on sweeps prior to the beam passing over a pixel (ahead of the raster line) (2) the swollen region left of the center point appears much lower in temperature than the surrounding melted material. The difference in temperature does match with Figure 32 (e) which identified the transition correctly during the raster.

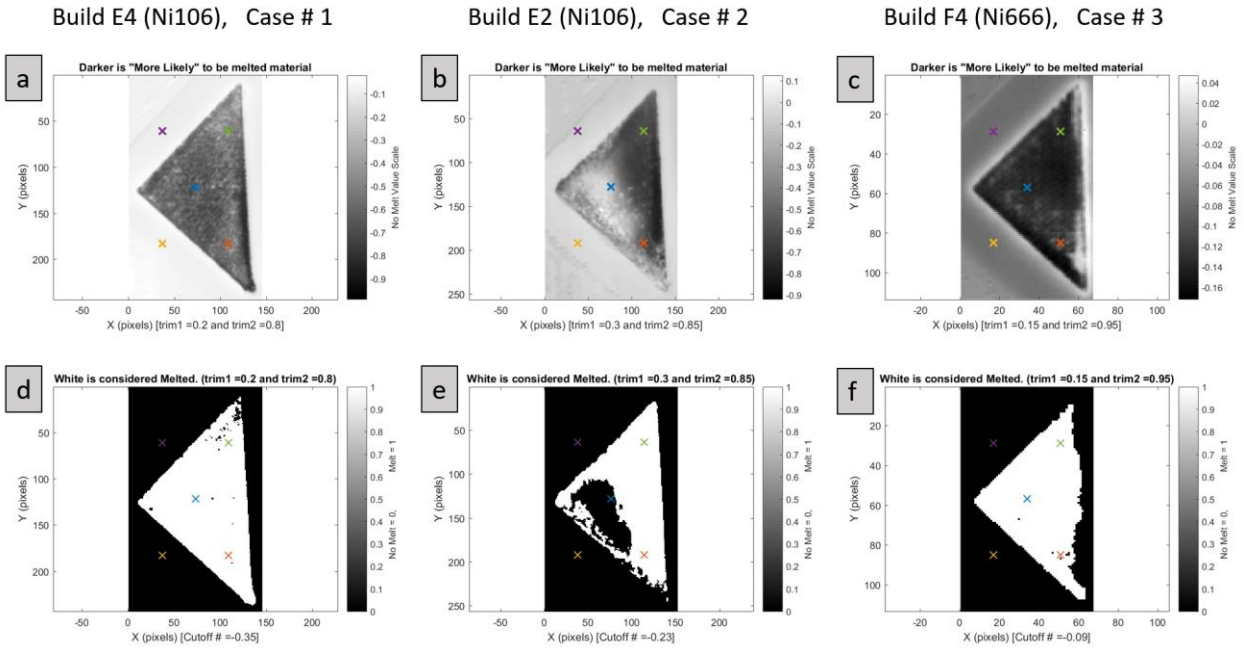

Figure 32. Mapping the slope and applying a cut off term.

From Figure 33 (c) it is possible to see the a passage of spots during frame 151, which was not clear in Figure 29 (c). In addition, the transition has been applied to the entire part, giving it a higher temperature than the surrounding powder. However; the temperature is much less than Figure 33 (a) and (b), which indicates that the integration time of the video used for case # 3 is less than that of the calibration curve and the other two cases. During the time frame of this project the preferred settings on the IR camera where changed depending on the results of other projects. The earlier videos (such as case # 3) had higher frame rates and shorter integration times to catch the beam; later videos had slower frame rates and longer integration times to average out the effect of the fast-moving beam.

From Figure 33 (d) the method is found to be accurate, because the transition occurs first for the powder bed, then for the bottom right corner and moves in a smooth fashion toward the top left edge. Figure 33 (e) has a few problem areas, because some regions of surrounding powder transition at the same time as that of melting at the top left edge. A clean sweep is observed across the part from top left edge to bottom right corner, which does not match the with Figure 33 (b)'s low temperature region left of the center point. This indicates that the transition frame was correctly identified but the calculated slope did not meet the cutoff value. There may be some merit in adding the time the transition was identified to the method for setting trim and cutoff values and preventing powder being considered a false positive. Figure 33 (f) again shows that spot melting will require a new method as the entire melt transition occurred near the same point, very early in the video.

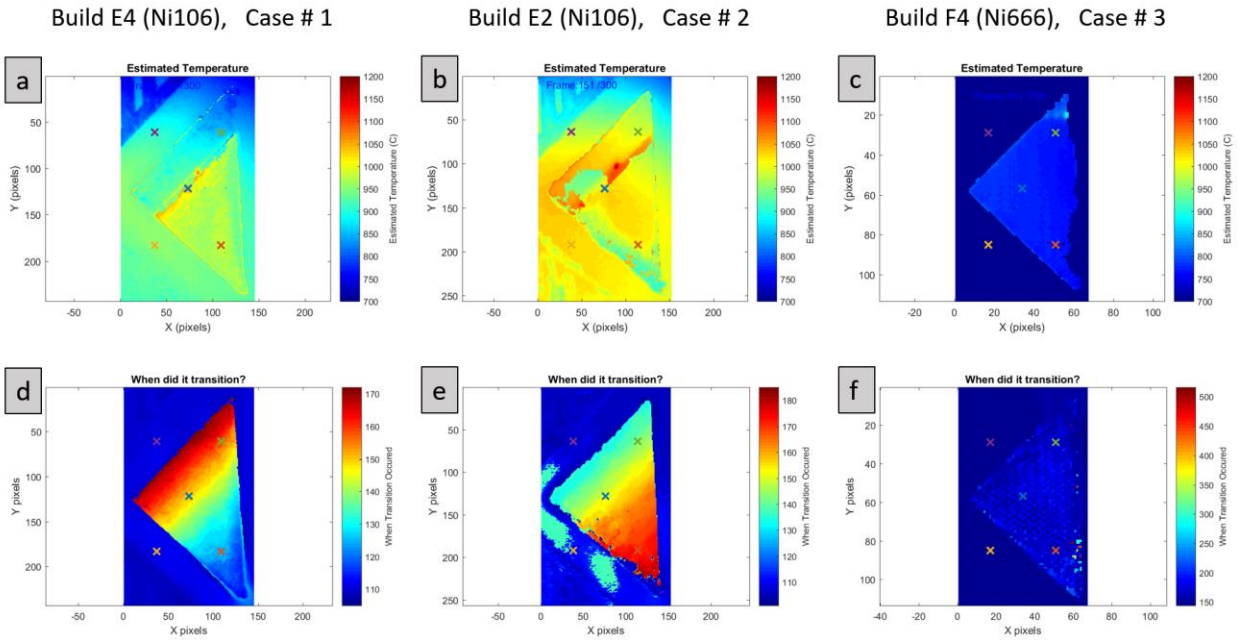

Figure 33. Estimated temperature of frame 151 and transition frame maps.

Once the transition frames, cutoff, and trim values have been selected; the code estimates thermal gradient and solidification velocity values from the top surfaces. The method for calculating thermal gradient relies on the temperature differences between the left and right pixels versus the top and bottom pixels of every melted point. From this, the thermal gradient magnitude and direction is calculated. For solidification velocity estimation, the local maximum near the transition points is identified and then looks for the same at a user defined distance ahead. By identifying the times for both conditions, the time difference (given by frame rate and user defined frames) can be estimated. Then, the estimations of G and R for the top surface can be plotted and compared.

3.7Semi-Analytical Heat Transfer Model

A rapid transient heat transfer model to predict the thermal gradient and solidification velocity at the solid liquid interface was used in this project. The SAHTM was developed by Alex Plotkowski [37] and modified to mimic the S-EBM process. The transient model uses Komanduri and Hou's approach for multi-pass arc and laser welding [38] which is developed based on standard equations developed by Carslaw and Jaegar [39]. Other heat transfer models were also considered (e.g. Truchas), however, lack of scale lead to discontinuing the methods.

3.7.1 SAHTM Basics.

The SAHTM takes in a grid of points and beam path that will take place in the same coordinate system. As the model progresses the temperature, T, is calculated for each point on the grid using Equation 5.

$$T(x,y,z) = T_0 + \frac{q}{c_p \rho (4\pi\alpha)^{\frac{3}{2}}} \int_{\tau=0}^{\tau_i=t} \frac{1}{\tau^{\frac{3}{2}}} \exp\left(-\frac{r_0^2+x^2+y^2+z^2}{4\alpha\tau}\right) \cdot I_0\left(\frac{r_0}{2\alpha\tau}\sqrt{x^2+y^2}\right) d\tau_i \quad (5)$$

Where the parameters for Equation 5 are defined in Table 3.

Table 3. Transient heat transfer model parameters

Parameter	Description
T_0 [K]	Initial Temperature
q [W]	Absorbed power, $e \cdot I \cdot V$
e	Efficiency
I [mA]	Beam Current
V [kV]	Voltage
c_p [J/kg-K]	Specific Heat
ρ [kg/m^3]	Density
α [m^2/s]	Thermal Diffusivity, $k/\rho c_p$
k [W/m-K]	Thermal Conductivity

In our research, we could not measure the melt pool width under in-situ conditions, even with the IR camera. Interestingly, the final melt pool shape can be observed and analyzed on the top surface of each part. This method was used to calibrate the SAHTM model and using the beam efficiency value until the top surface melt-widths matched. The model was used primarily to calculate the spatial variation of G and R for a single slice in the XY plane. Even though this region is remelted at the subsequent layer, the calculations provide valuable insights that cannot be observed by any other modeling tool.

The thermal properties such as conductivity, density, and specific heat were extracted from JmatPro. The incorporation of beam path in SAHTM is more difficult because it is related to the geometry of the layer being printed and a variety of S-EBM process parameters mentioned in the previous sections. Acquiring the path is one part of Arcam Loop 3 which is described in the next section.

3.7.2 From Arcam Logfile to G and R Maps.

A combination of codes written in multiple languages is currently required to solve the SAHTM for an entire layer. The Arcam Loop 3 is a collection of these codes and their accompanying files all in one folder tree beginning with ArcamLoop_3 (AL3) at the base containing 4 branches which are used in order: A-LogFile, B-Path_File_Generation, C-SAHTM, and D-PythonAnalysis (which will be referred to by their prefix letter). Figure 34 gives a map of the folder that make up the Arcam Loop with two levels of folders illustrated. From each of the 4 branches are a set of folders which contain either input files, output files, or python files to move through the Arcam Loop. The detailed steps of moving through AL3 is given in the Appendix, A.2.

3.7.3 Mapping the Results of the SAHTM.

The files output into the Data/ folder are named by the Sim.txt file and will be output at the requested frequency and tacked onto the end of the output file. This allows for a stack of output files to be read into ParaView and played as a video. The file structure includes 11 columns: (x, y, z, T, G, V, Gmag, V_theta, Gx, Gy, Gz) where x, y, and z are the coordinates; T, G, and V are Temperature, Thermal Gradient, and Solidification Velocity. The additional output columns are not used at this time. In the current version of the code, the temperature is only calculated for coordinates that are connected to a melt pool. Once the temperature drops below the given solvus, the temperature is no longer calculated. This means that a large portion of the rows will show either the initial preheat (un-melted) or the solidus temperature. In this version of the code it is more meaningful to map G or V.

The output data files can also be plotted using python code found in AL3/D-PythonAnalysis/2-PythonAnalysis/AAA-MultiPlot_SAHTM.py to compare multiple runs. Figure 35 shows three methods for plotting the last output data file using three different options. Option 1 maps thermal gradient of 8 different runs side by side. In this case very little was changed between the 8 runs. Options 2 maps solidification velocity in the same order as the previous options. Option 4 creates scatter plot of individual runs with histograms shown above and to the right in order to give an idea of point density.

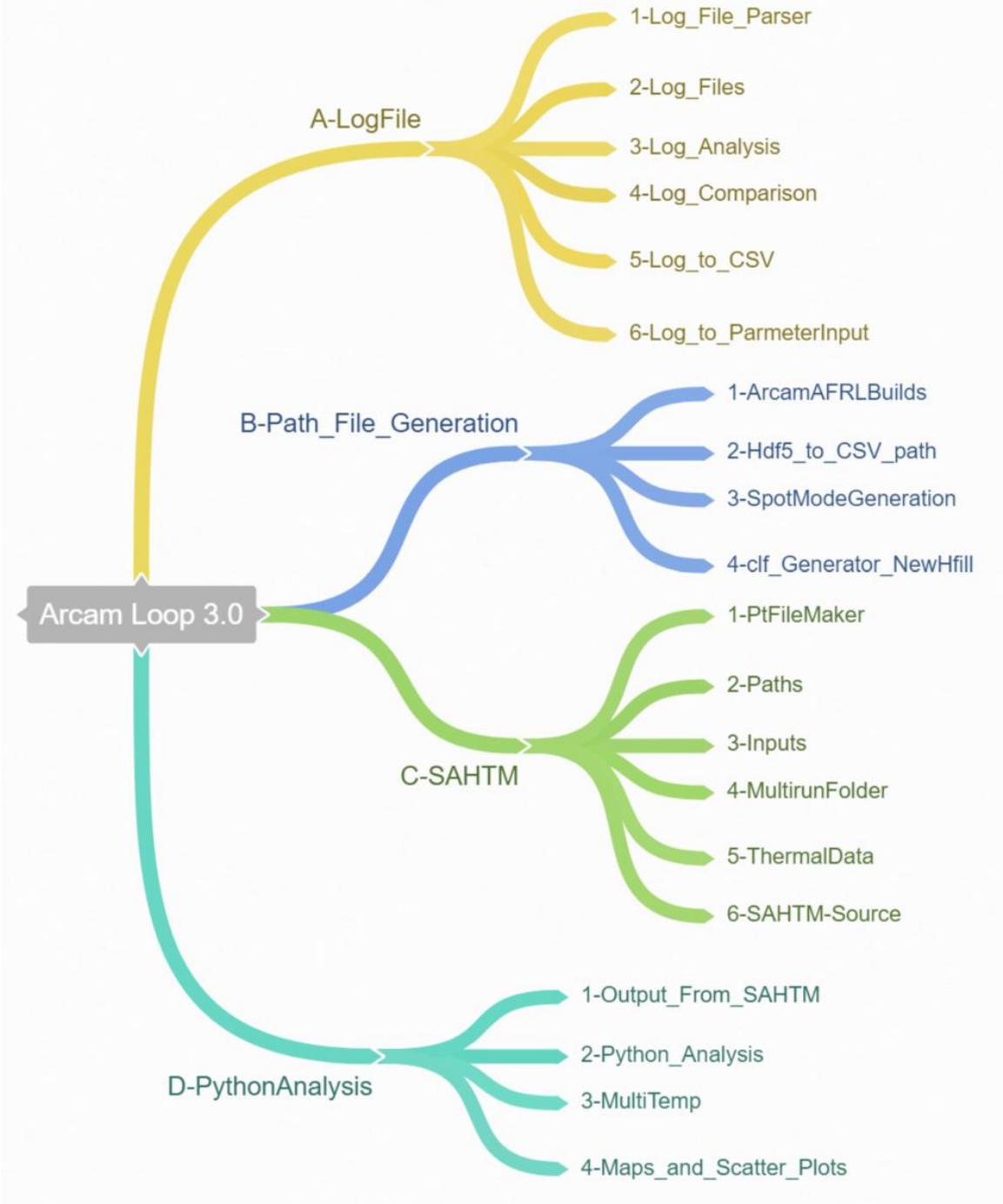

Figure 34. Folder Map of Arcam Loop 3.

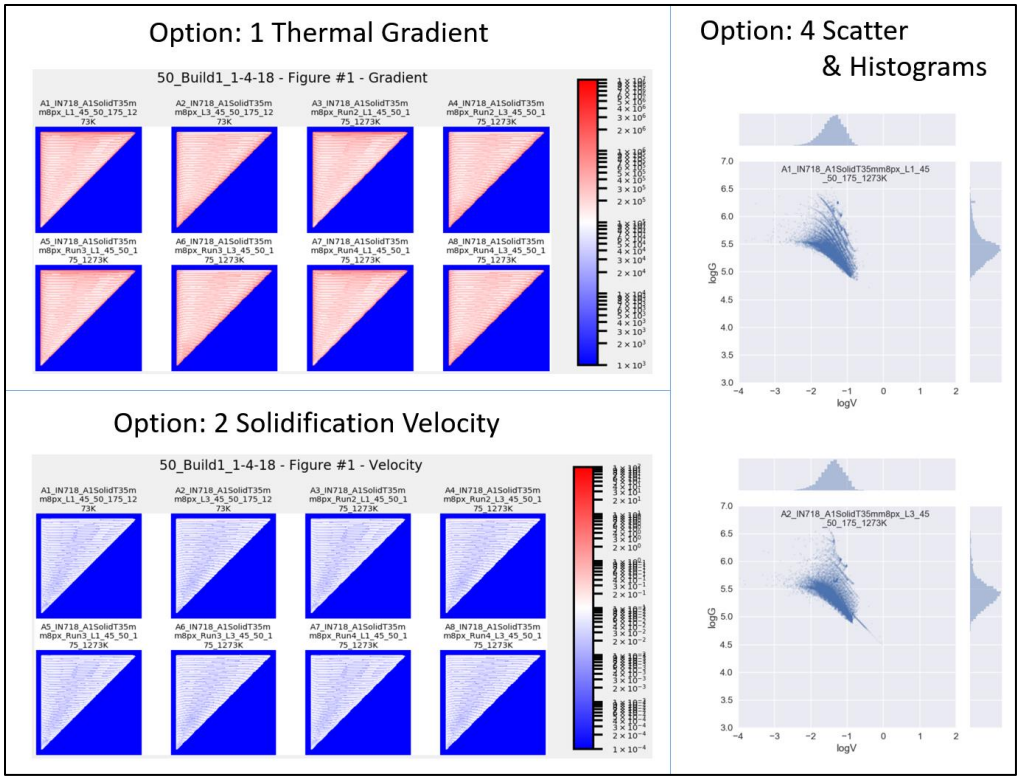

Figure 35. Three plotting options for comparing multiple runs side by side.

3.8Cracking and Processability of Nickel Based Superalloys

The weldability of nickel based superalloys is related to the amount of γ' precipitation [40–42] and occurs by multiple mechanisms. The causes include solidification cracking [15,29], liquation cracking [43,44], or strain age cracking [45]. In solidification cracking, solute partitioning in the interdendritic liquid region depresses the local solidification temperature and cracking occurs when strains applied in this widened freezing range cannot be accommodated by the interdendritic liquid. Solidification cracking tends to occur at weld centerlines, high angle grain boundaries, or constrained regions and can be avoided by reducing heat input and modifying the melt pool shape in reference to the thermal stress directions. Liquation cracking is related to the formation of liquid at the interdendritic regions of the (n-1)th pass during the deposition of the nth bead. The dwell time of these regions within the liquid-solid phase field region and imposed thermal stresses promotes the tendency for this type of cracking. Stain age cracking occurs during post-weld heat treatment due to simultaneous precipitation of strengthening precipitates and local strain accumulation at the grain boundaries caused by the volume change associated with the precipitation from the supersaturated solid solution [46]. The S-EBM process complicates the mechanism for causing cracking of high γ' alloys due to the multi-pass and multi-layer nature. The driving force for cracking during the S-EBM process may come from a combination of the above-mentioned mechanisms.

4. RESULTS AND DISCUSSION

The results and discussion section will be broken into sections based on results of each build and subsequent discussion section will explore key findings. The results section is arranged to focus on summarizing the builds, followed by spatial G and R results. The discussion sections will focus on build robustness, spatial G and R, Porosity defects, solidification grain structure, and microstructure evolved through solid state transformation.

4.1 Build Results and Processing Summary: Success/Failure

A total of 35 builds were attempted in this project spanning 6 different alloy compositions, performed on 2 different Arcam machines, and 8 different part geometries. Each part within each build experienced unique processing conditions controlled by more than a dozen process parameters. The following sub section 4.1.1 will organize this information chronologically and give an overview of all builds attempted with different alloy chemistry. The details include top surface finish, log files, parameters used, and powder characterization. Result images that build the story will be included in the discussion sections to follow.

4.1.1 Arcam builds overview for all builds completed during this project.

The builds are organized by build "Set" in Table 4 which is broken by alloy and build time frame. This ordering is used because modifications that changed all following builds were introduced in this order. Next the alloy processed and assigned prefix, for sample identification, are given. The Arcam S12 and A2 were used in this project with upgrades and software that make them run nearly the same and both can be run with the MiniVat. "Build Pass" simply means that there are samples or information to gain from the build and does not indicate that the build went to full height. All the geometries processed were simple in the Z direction were with no overhangs. "Tri" refers to right triangular prisms and "SC" refers to Solid and Complex geometry. "Complex" in this project typically refers to thin walls. Further detail for each build Set will be given in the Appendix, A.3.

Once the Arcam build chamber is opened, the top surface of the build and surrounding powder mounds give great insight into the history of a build that will not show up in the log file. The images below in Figure 36 and Figure 37 document this first glimpse at builds (when available) that are listed in Table 4.

Table 4. Completed Build Summary

Set #	Alloy	Prefix	System	Build Pass	Geometry	# of Parts	Dates
1	IN 718	A	S12-Full	1/1	Triangular	16/16	4/21/2015
2	IN 718	A	S12-Full	1/1	Tri & Cubes	13/22	8/31/2015
3	IN 718	A-	S12-MV	0/4	Triangular	0/8	9/25-29/15
3	IN 718	A	S12-MV	1/1	40 mm Cube	1/1	9/30/2015
4	LSHR	T	A2-MV	0/5	Tri-40-SC	0/10	3/18-23/16
5	ReneN5	B	A2-MV	2/2	Tri-40-SC	4/4	3/29-30/16
6	Haste-X	H	A2-MV	2/5	Tri-40-SC	4/10	4/1-8/16/16
7	IN 718	C	A2-MV	3/5	Cubes & Tri	24/42	12/27-1/02/17
8	Ni-6-6-6	F	S12-MV	4/5	Cubes & Tri	16/20	1/13-19/17
9	Ni-10-6	E	S12-MV	4/5	Tri-28-SC	14/20	9/26-10/2/17
10	Ni-6-6-6	F	S12-MV	1/1	Tri-28-SC	4/4	10/4/2017

The initial builds began on the full build chamber of the Arcam S12 with many parts on the build plate (16 & 22) for (Set # 1 and # 2). Build A1 (Set # 1) went to completion but used process parameters with a low energy density leading to lack of fusion to various degrees. A2 from Set # 2 required contours and a third of the parts to be turned off at the beginning of the build in order to reduce the layer time, keep the temperature above 800 °C and save the build. A2 eventually ended in build errors regardless of the changes made.

Moving to the early versions of the MiniVat system 2 triangular parts were attempted but the uneven dual rake system lead to Arc Trips. Each Arc Trip would clear the plate of powder and require that the build be stopped soon after. The first four builds in the are represented by Figure 36 (A-). Each of the A- builds were terminated early when no more powder was being deposited on the surface. A3 made it the farthest of Set #3 with only 1 large cube (40 mm x 40 mm) in the center of the build plate.

Due to machine scheduling, the MiniVat was moved to the S12 system after a few changes to the MiniVat to allow for the difference in rake height. The first set of builds with this setup used alloy LSHR (Set # 4) and did not make it past 10 layers due to arc trips. It was later found that the size distribution of the LSHR powder was bimodal and contained fines which caused the Arc Trips. Figure 36 T1 is representative of the LSHR runs (Set # 4).

When the Rene N5 builds began in Set # 5, the build was set to start at an elevated temperature to prevent and Arc Tripping (higher heat → more sintering → less likely to Arc Trip). B1 fixed some of the Arc Tripping errors but Set # 5 was plagued by early termination of builds. The two builds in this set made it to ~7 and ~4.5 mm and this rough start prevented further build attempts for Rene N5. The following build Set # 6 finally had 2 builds go to the full 20 mm that was planned. The short rake used after the dual rake system can be seen in B1 and H6.

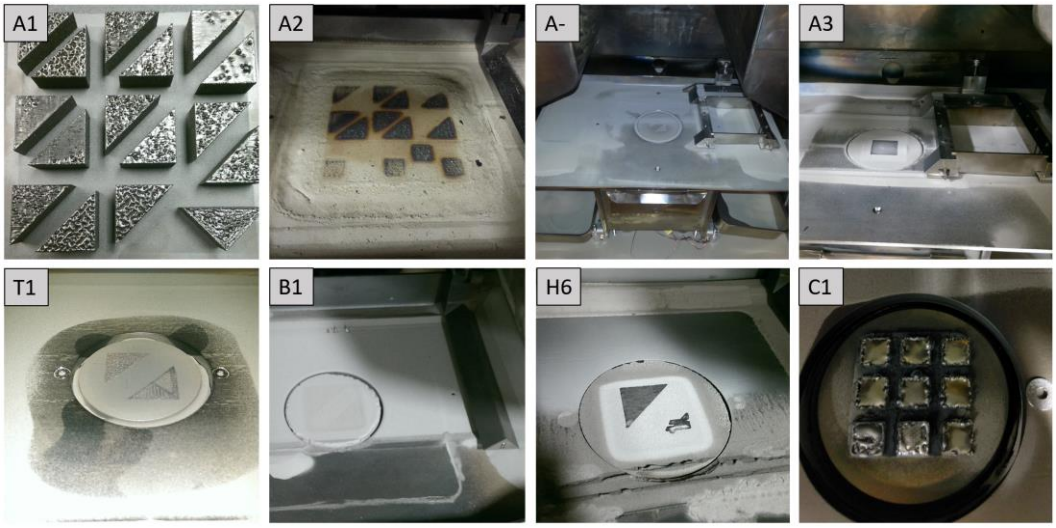

Figure 36. Initial Pictures of Various Builds.

After a long wait due to scheduling of other projects, build Set # 7 began with recycled Inconel 718 that was used to test a new understanding of process controls including preheat settings. This powder was contaminated, leading to Arc trips unless processed at high temperatures and cracking was found throughout the builds. The short rake was discontinued with C1. C2 in Figure 37 is representative of this as the 9 cubes vary the heating between parts. The part 6 has no rotation per layer which lead to the early termination of this build as the part lifted up on the ending side. C4 kept in line with C2 during the process parameters experimentation, as the strategy moved towards controlling the current along the varying line lengths of the right triangles.

The first round of custom alloys moved the MiniVat to the S12 (Set # 8) began with an array of cubes and moved to triangular parts of the same surface area as the 20mm x 20 mm cubes. F2 corresponds to the parameter development stage, because the parameters were changed on the fly while watching the results through the front Arcam window. F4 used the parameters that lead to best surface finish of the early cube runs for Ni666 in Set # 8 and which also included spot melting.

The second custom alloy was built in the fall of 2017 (Set # 9) using the Solid and Complex 28 mm triangles developed during Set # 8. E1 part was successfully built to final height by terminating two of the four parts. E2 adopted increased preheat near that of B1, but the center region began to swell and the final part was locked into hard sintered powder. E5 was the last of Set # 9 and included a new experimental density point net with the addition of a sweeping raster taking place at the end of the layer.

Following the end of 5 builds, Set # 10 placed Ni-6-6-6 back into the S12 for one final build at higher temperatures to remove cracking. F6 was the final build of the project with parameters similar to E2 without swelling of the center corners.

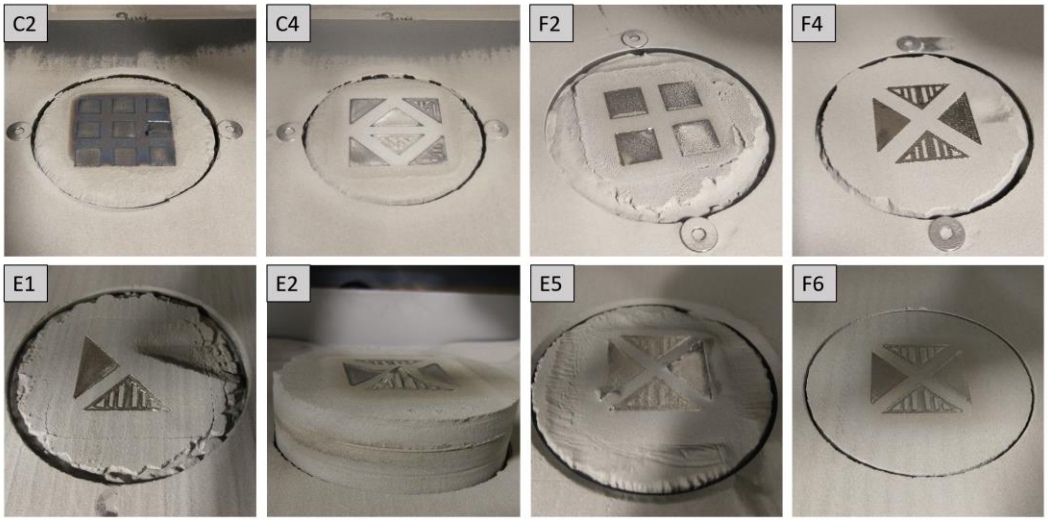

Figure 37. Initial Pictures of Various Builds Continued.

4.2G and R Variations During Processing

During the beginning of the project, the melt pool used to add material in the S-EBM process was assumed to be an elongated elliptical source. Based on this assumption, the hatch spacing could be chosen such that the single pass beads over lapped to prevent lack of fusion. Each bead was assumed to be mostly unaffected by the previous pass. The triangular right prism, explained in 3.1.3, hinged on this idea because it created a scenario where the line length was always changing. If the line length changes, then the current/power can be made to change with it (using the Arcam algorithms in Beam Viewer described in 3.1.5). Each value of current is then given a different beam speed based on the Speed Function. This leads to the line of thought that each pass of the beam would see a different current and speed and thus a different *G* and *R* combination. From this it was assumed that a gradient in solidification conditions could be created across the right triangular prisms..

In most cases the shape of the melt pool extended the full length of the part. This is clear in the surface height measurements shown in Figure 38 (a), where the final melt pool is observable along the bottom of the cube. Although, the surface height is not quantitatively accurate, it does capture the trends of the top surface. Figure 38 (d) shows the height of the trace across the middle of part 1 which has a large variation in height as seen in (b) and (c) as well. Previous hatches with 90º rotations have left a mark on the build surface. The hatch spacing for this build was 0.125 mm and the final melt pool is about 2 mm across (16 x the hatch spacing). Because of this, previous methods for predicting *G* and *R* such as Rosenthal and Truchas were discontinued and will not be presented here. The SAHTM can model the thermal history of the entire layer to calculate a thermal gradient and solidification velocity at the melt pool interface as described in section 3.7. In addition, some builds have IR video which can also estimate the solidification conditions from viewing the top surface, section 3.6.

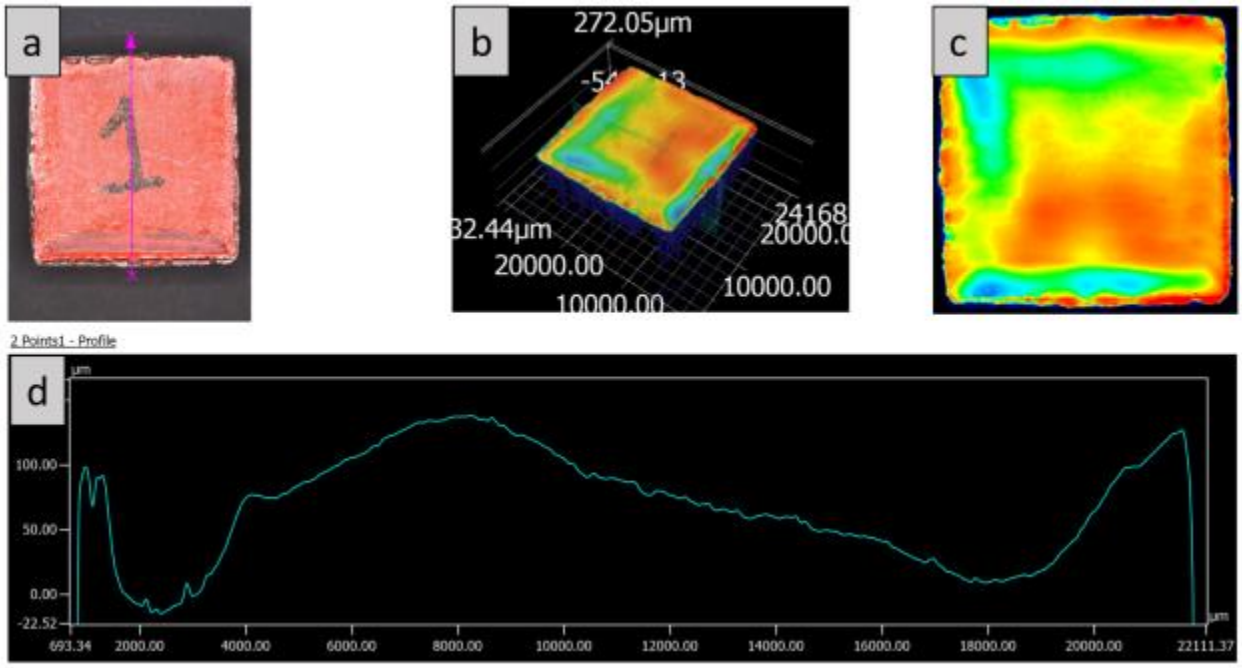

Figure 38. 3D Keyence of top surface of Part 1 from build F2 with Ni-6Cr-6Al-6Ta.

4.2.1 Results of SAHTM Analysis.

Using the Arcam Loop 3, the SAHTM can be run for every part of every build and output the *G* and *R* at each coordinate on a slice of the top surface. Figure 39 plots as a comparison the thermal gradient for 8 parts that were built during this project with the same scale. For each of the models the raster direction is going east and west while the traverse direction is either north or south. The chosen images for this document were picked based on their variation from each other and not related to the energy density or preheat temperatures. The stripe pattern that is observed in the top surface strongly linked to the hatch spacing used to melt the part regardless of energy density equivalents.

The model predicts that there is a variation in G and R of many orders of magnitude; however, the trends show no gradients across the parts in thermal gradient. For example, it was expected that lower currents would lead to smaller thermal gradients and larger currents would lead to higher thermal gradients. This was expected to create a gradient from long edge to corner as the current increases while the line length increases. Instead, the variations appear to occur as jumps in the melt pool. Large melt pools that are rapidly jumping across the part show larger variations in the thermal gradient (see E2 part 3 and F5 part 1). When the melt pool length is closer to the hatch spacing the variations occur rapidly as small jumps in the melt pool occur. Overall the thermal gradient appears evenly mixed. The exception is the corners having a greater variation than the bulk. This is where an area melt could occur depending on the raster direction going into the corner or leaving the corner.

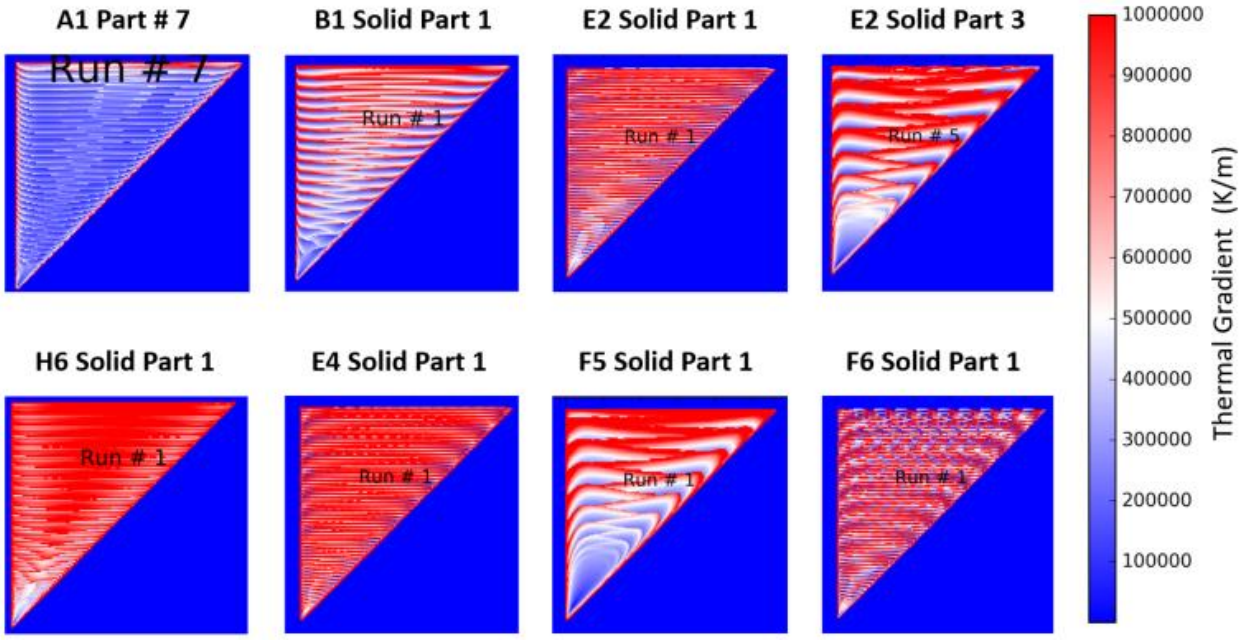

Figure 39. Spatial variation of thermal gradient for various parts.

4.2.2 Results of IR Video Analysis.

Once the velocity and gradient are calculated for each pixel of the part, as explained in 3.6.1, the *G* and *R* values can be plotted to give spatial information about the solidification conditions on the top of the part. Figure 40, Figure 41, and Figure 42 plot the spatial variation of thermal gradient, velocity, and G/R. The G/R is plotted because the CET curve moves diagonally on a gradient vs velocity map (from low gradient and low velocity to high gradient and high velocity). High values of G/R are more likely to be columnar while extremely low values of G/R are more likely to be equiaxed. The layers and parts selected for the following plots came from the same three parts that were shown in the earlier methods section. Complete process parameters and temperature for each of these builds can be found in the Appendix, subsections: A.3.9 for E4 & E2, and A.3.8 for F4.

Figure 40 is from the smoothest top surface of the three parts presented in this section. This made it possible to correctly select the top of the part as a melted region. This analysis ignored the surrounding powder (white space). The gradient plot is made up of thermal gradients which fall between Log(3.5) and Log(5.5) or cyan to orange. There is a slight variation from the top left edge to the bottom right corner in overall gradient as there is more cyan in the bottom right corner.

The velocity plot of Figure 40 similarly has a slight variation from the top left edge to the bottom right corner where the bottom right corner has more area fraction of high velocity. The *G/R* plot of Figure 40 shows that most regions are estimated to contain lower gradients and higher estimated velocities. These trends can also be seen in the Velocity vs Gradient plots of Figure 43

(a) where most of the data points lie on a diagonal (high *G* & low *R* to low *G* & high *R*). Figure 43 (d) shows a similar trend to (a) and is from the same build, but from a few layers later when the raster occurs in a different direction.

When comparing part 3 of Build E4 Figure 40 to part 3 of Build E2 in Figure 41, the major difference is the preheat temperature. For build E4 the base temperature throughout the build was near 1050 ºC, while E2 was near 1200 ºC. This elevation in preheat temperature leads to an overall decrease in thermal gradient. Part 3 from build E2 has a large white region that was identified as un-melted due to surface swelling.

The video used to generate Figure 42 is from a part that was melted with Dehoff fill spot pattern, part 3 of F6. The calculated transition point has a large uncertainty as explained in the earlier subsection, 3.6.1, but the pattern that is emerging in Figure 42 fits with the top surface roughness of the part, Appendix Figure 121. Of interest from this part are the exaggerated division of values obtained which give the images their texture. The velocity plot is relatively low and consistent. However, the gradient plot is either high or low with a clear gap between the values. The separation in gradient values occurs all the IR data that was recorded.

The trends observed in Figure 43 are observed across all IR video that was analyzed. The hard diagonal cut off is a function of the frame rate and will be limited by the camera. The dual grouping of high and low thermal gradients is due to the method that is employed and the frame rate compared to the beam speed. High gradients indicate that the pixel observed the beam while it's neighboring pixels did not observe the beam. In the velocity a similar phenomenon occurs and pixels that observed the beam will have more drastic cooling rates than pixels that did not observe the beam. Despite the systematic errors, the trends of the G and R data calculated from IR intensity indicate that the part sees relatively uniform cooling conditions.

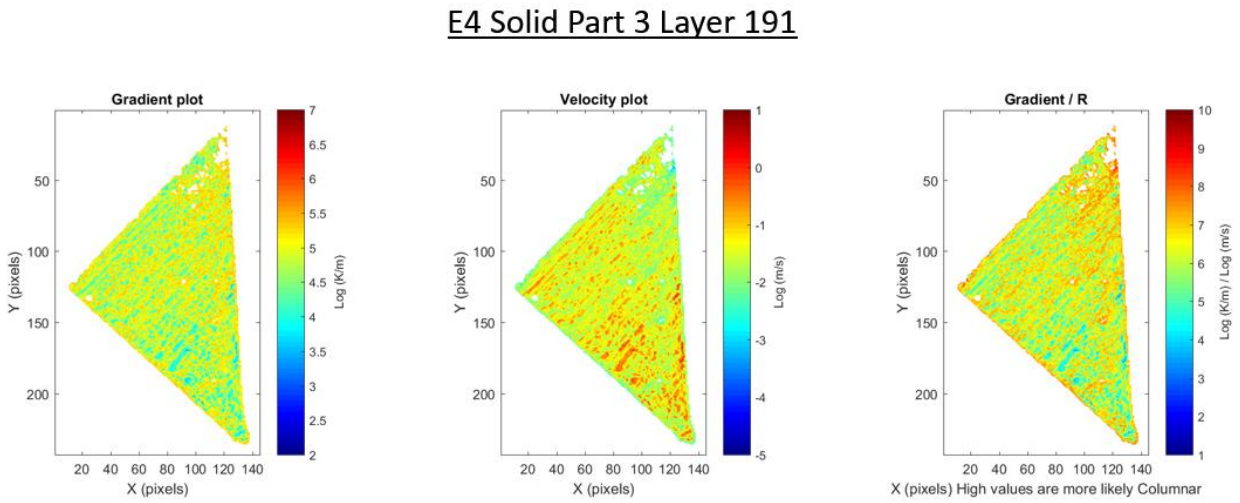

Figure 40. Spatial variation of *G*, *R*, and *G/R* from IR Video of E4

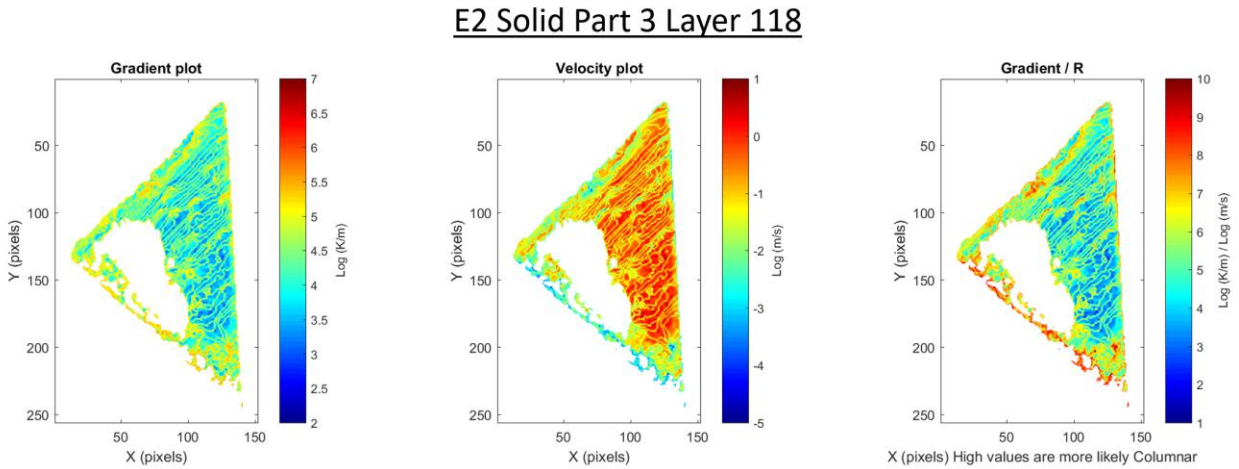

Figure 41. Spatial variation of *G*, *R*, and *G/R* from IR Video of E2.

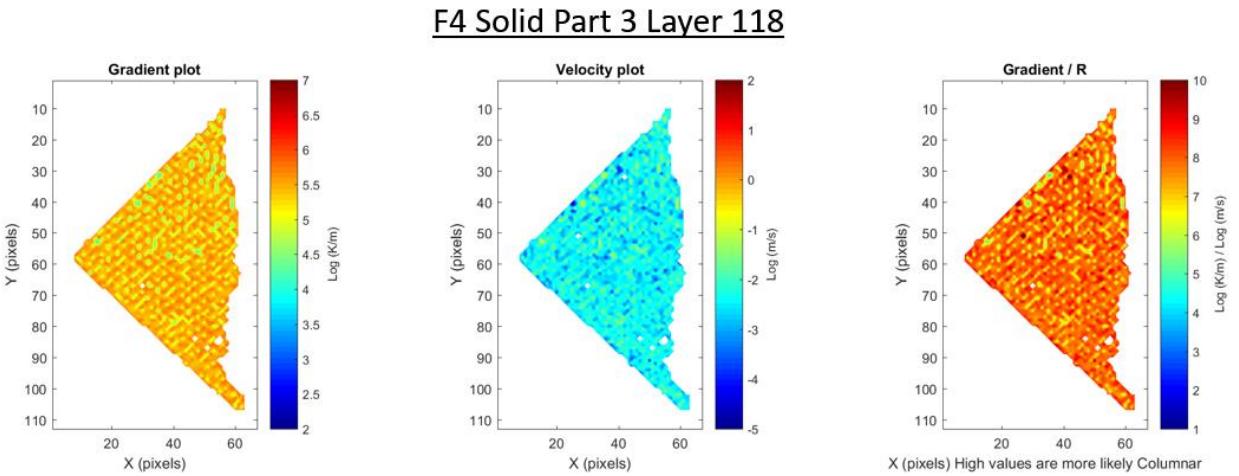

Figure 42. Spatial variation of *G*, *R*, and *G/R* from IR Video of F4.

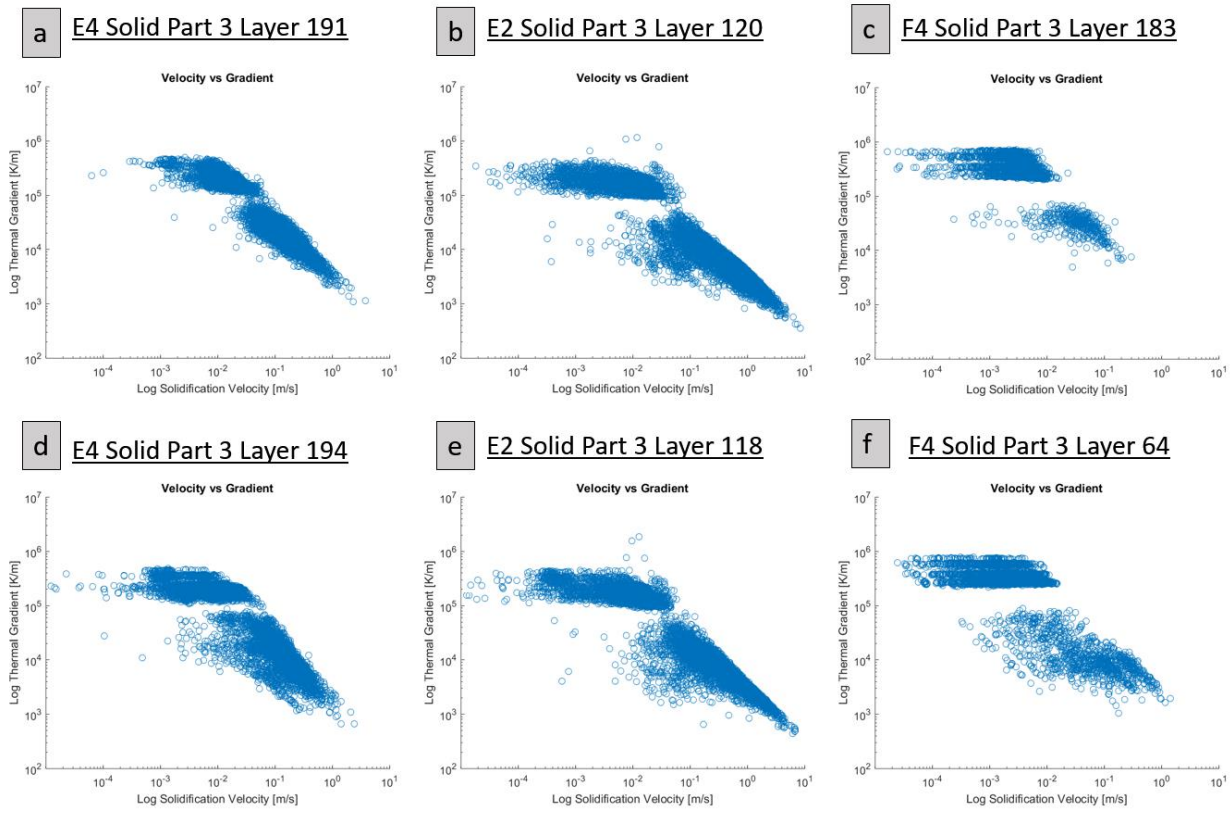

Figure 43. Log scale plots of Gradient and Velocity.

4.2.3 Experimental Results for Spatial Variation of G and R.

To get an idea of the spatial variation of G and R that occurs during experiments, samples were removed from the diagonals of the parts. The grain structure is the clear indicator of solidification conditions that might have occurred during processing. Build B1 shows the greatest variation of grain structure in three distinct regions resulting from standard raster melting. Further detail on B1 can be found in Appendix A.3.5. Samples Solid-A (SA) and Complex-A (CA), taken from the diagonal, were imaged using edge-lighting to highlight differences in grain orientation Figure 44. The grain structure transitions from an equiaxed morphology (inset i) to columnar morphology (inset ii) as one traverses from left to the right. Interestingly, the optical microscopy also indicated a large grain directly above the base plate. The right edge of sample SA, which borders the powder bed, contains interrupted grains due to lack of fusion defects observed in the outer 1 to 2 mm. The matching diagonal cut of the Complex part CA (Figure 44), also exhibits a variation in grain orientation across the sample with a mixed grain structure, left of center, and columnar grain structure oriented with the build direction, right of center. The “Z” direction corresponds to the build direction. The surface relief in the optical micrographs suggests large variations in crystal orientation as a function of locations. In both SA and CA sections the base plate is at the bottom of the image. Dark line observed by the edge light technique highlights the grains with dark lines and the transition from base plate to Rene N5 has an even darker boundary.

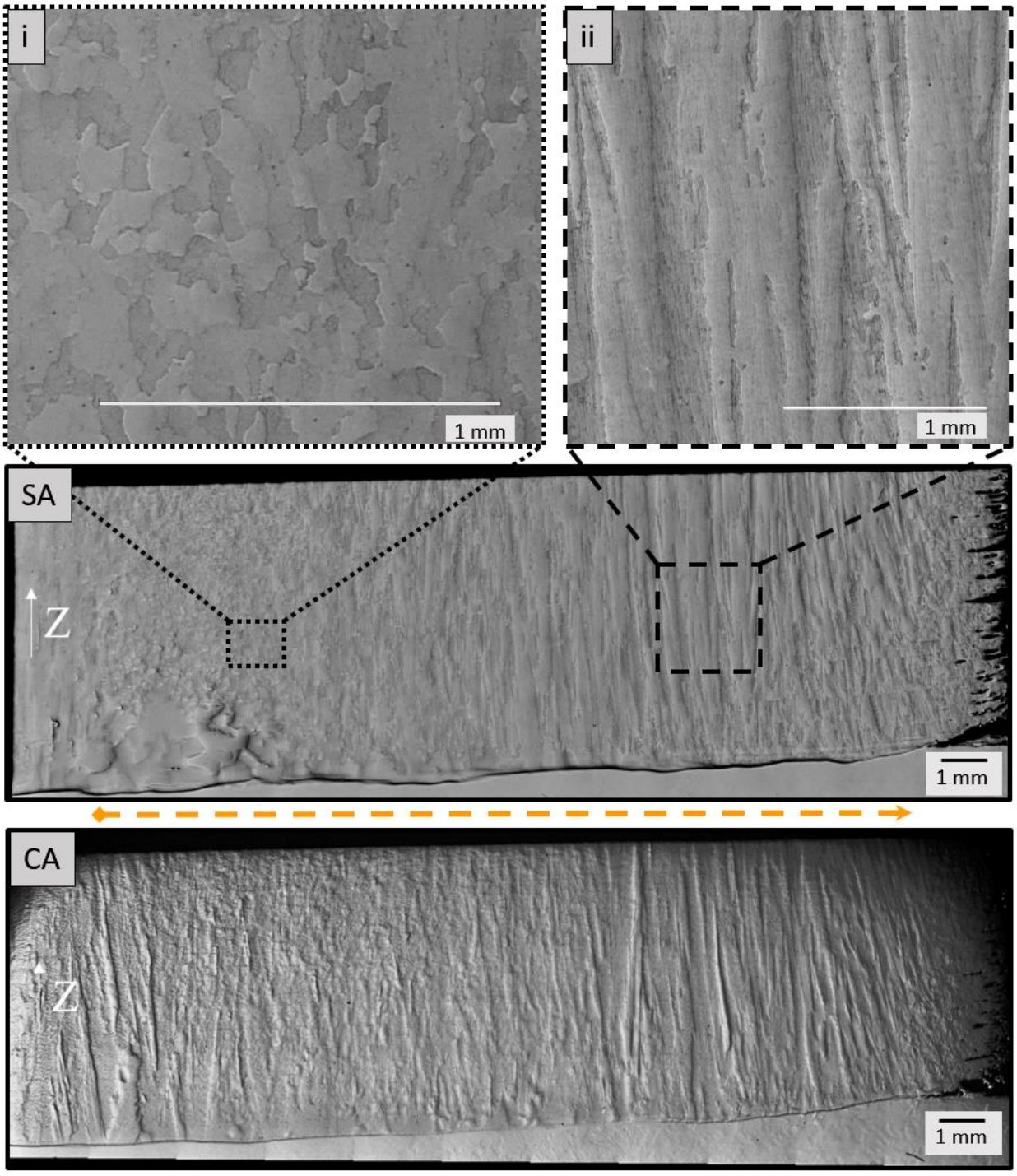

Figure 44. Stitched optical micrographs of sample A from build B1. Adapted from [47]**.**

Large area EBSD scans were taken for each of the diagonal samples of the Solid and Complex parts. Overlays of the inverse pole figure (IPF) maps, scaled to the edge lit image, are given for samples SA and CA in Figure 45. Each IPF map was generated after rotating the data set along the A1 direction or along the [100] crystallographic direction parallel to the build direction (Z). This rotation is performed to highlight grains epitaxially grown in the build direction in red. Dashed boxes indicate partitioned regions of each map which were plotted in the pole figures surrounding the EBSD image. Regions a-f go across the center of the sample while regions i-iii give additional PFs for regions of interest on SA. The Pole Figures (PF) give a better understanding of the texture observed while the IPF maps give spatial information. The PF intensity scale was limited from 0 - 5 to compare each PF regardless of maximum frequency. This was done to highlight the difference between columnar and equiaxed and keep all the PF scales equal. EBSD (see region iii) confirmed the presence of large grains with a random texture close to the substrate.

All other builds with raster patterns produced columnar grains and some with spot melt regions did not achieve equiaxed grains. Variation in process parameters were attempted to produce a variety of solidification conditions which resulted in a variety of grain structures. Builds with custom alloy Ni-6Cr-6Al-6Ta show this best with focus given to samples F23, F33, and F24. Each of the parts were 20mm x 20mm cubes. F23 and F33 were raster filled that started at a 45º and traversed diagonally across the cubes and F24 used spot melting. For more details on the processing conditions experienced by each part see the Appendix A.3.8. Figure 46 shows the edge lit images taken from the Z orientation and XY with Inverse Pole Figure (IPF) maps overlaid. The EBSD data has been rotated in the same way as Figure 45 to show the growth direction of the grains in red. Pole figures on the sides are 001 and of the regions superimposed. Each of the builds contained cracks, which appear along the grains boundaries and will be discussed in a later subsection.

4.3Discussion of Spatial Variation of *G* & *R* and Melt pool shape

From the various methods of describing the variation in *G* and *R*, a pattern has repeated for the solidification conditions. There is local variation of many orders of magnitude, but that variation repeats across the layer of the part for all parts sampled and is related to the melt pool shape. The following subsections will break this down based on the alloy, preheat & geometry, processing parameters, and melt pool shape.

4.3.1 Influence of Alloy Composition.

An initial assumption during this project was that process parameters could be easily transferred across the different alloys. This would lead to little variation in solidification conditions from alloy to alloy. All the nickel-based alloys considered in this research are expected to have similar density, thermal conductivity, and specific heat. However, the solidification temperature and solidification range does vary greatly among the alloys. Figure 47 plots the solidus, liquidus, and difference in a comparison that aligns with observations on the CET. Alloys Inconel 718 and Rene N5 have large solidification ranges while the two custom alloys and Hastelloy-X have much smaller solidification ranges. The solidification range is important in the CET phenomenon

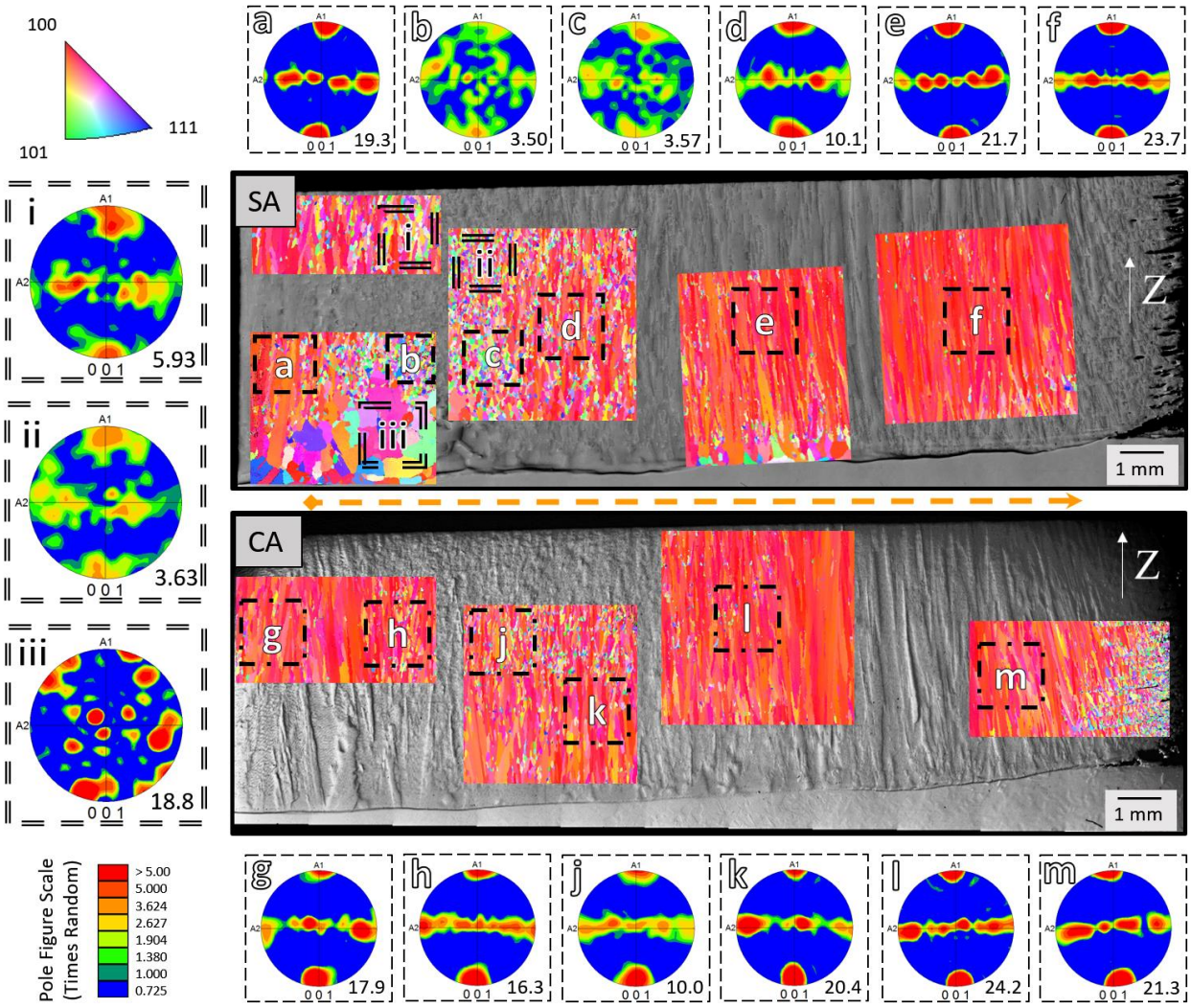

Figure 45. EBSD overlaid on optical images of the diagonal samples from B1 S & C. [47].

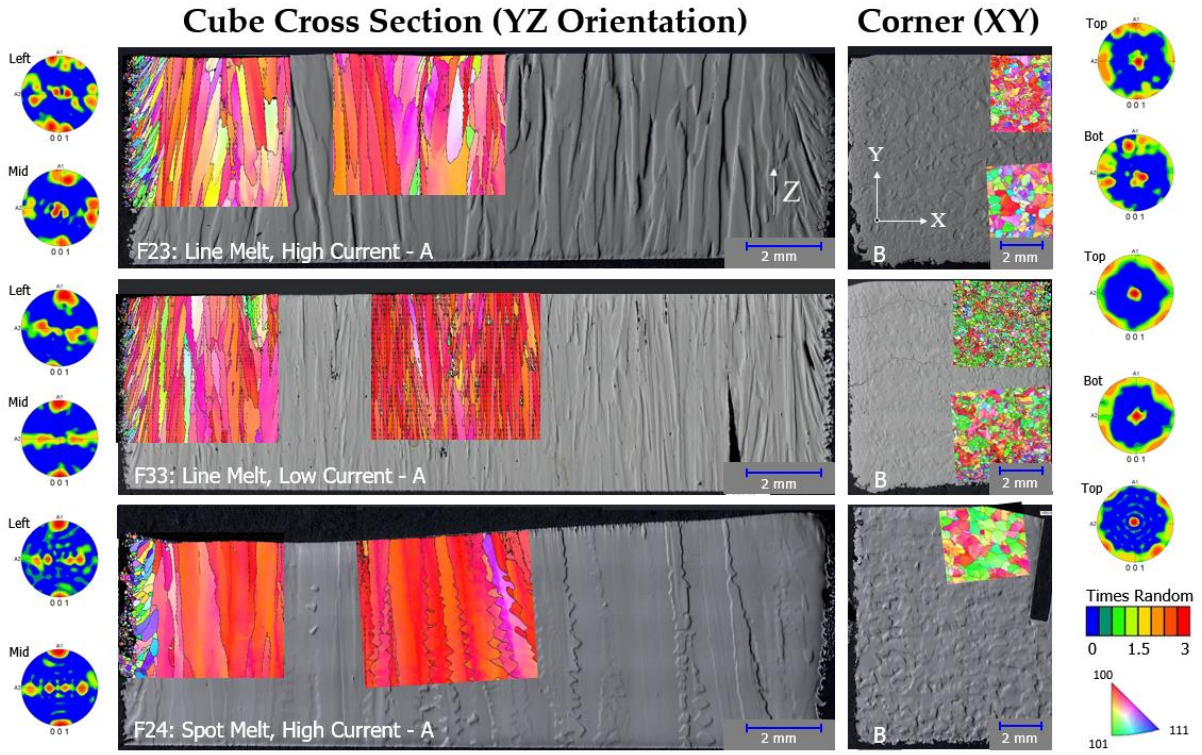

Figure 46. Keyence edge lighting with EBSD IPF maps overlaid on F23, F33, and F24.

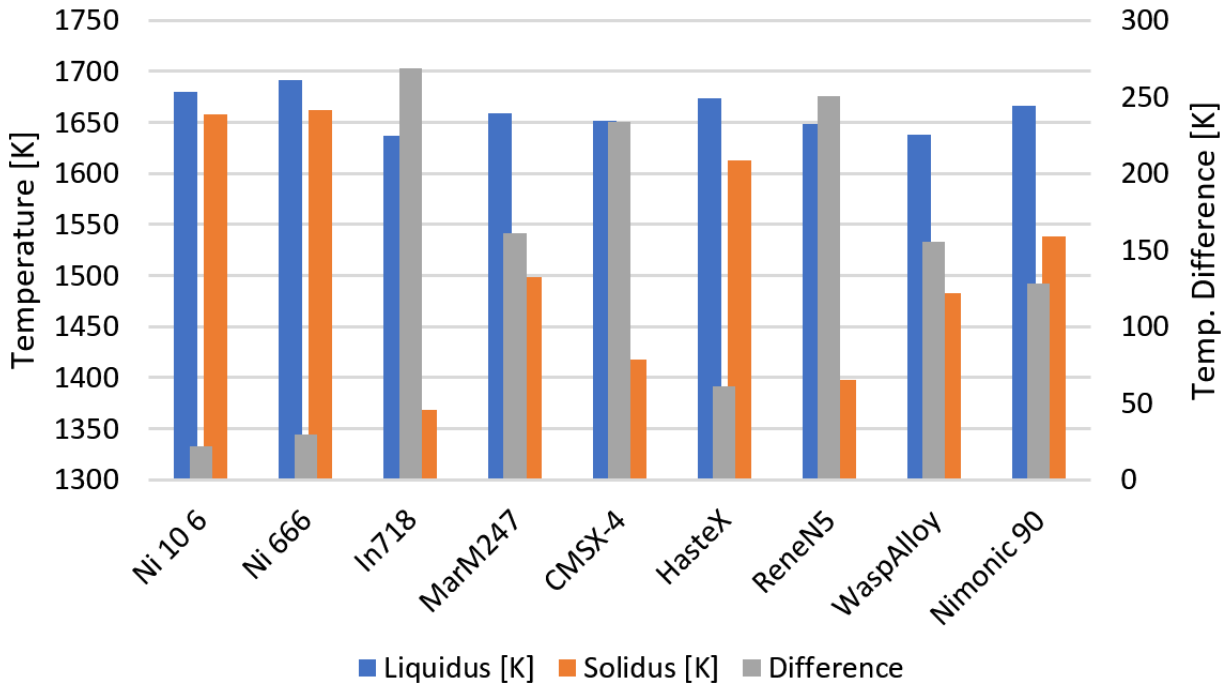

Figure 47. Solidification range of traditional and custom alloys from JmatPro.

as it controls the amount of undercooling. A large solidification range is more likely to have a CET which matches our observations with the sensitivity analysis. In addition, the closer the preheating temperature is to the solidus, the lower the thermal gradient at the interface.

4.3.2 Influence of Preheat.

Preheat has a large effect on the melt pool and how well the process is performing. At lower preheats the melt pool is more likely to become an elongated elliptical shape and produce spatter during processing. Such a melt pool would have higher thermal gradients and solidification velocities. Where the solidification velocities would be on the same order of magnitude as that of the beam deflection speed. During elevated preheats, the melt pool is more likely to resemble a line that reaches to each side of the part. With an extremely wide melt pool the thermal gradients and the solidification velocity are reduced. In the case of a line source the solidification velocity will have a magnitude and direction on the same order of magnitude as the traverse velocity.

4.3.3 Process Parameters and Geometry.

Similar to the preheat, the process parameters and geometry first influence the melt pool shape which in turn determines the *G* and *R*. It is not possible to discuss one and to ignore the others. The best example of this come from the top surface of B1 which was scanned after the samples were removed by wire EDM. Figure 48 (a) and (b) show the full top surface of the Solid and Complex parts with arrows indicating the final raster traverse direction. Figure 48 (c) outlines the final melt pool which stretches the entire 40 mm of the solid parts top edge. Outlines of the shape traversing the entire part can be seen in (a) and (c). The traverse velocity during this build ranged from 5 mm/s for the long edge to 10 mm/s moving into the corner. For the complex geometry, the final raster traverse left a large melt pool in the bottom left corner with no ripples observed in Figure 48 (d) as it appears to be an area melt. The rest of the Complex part has ripples that are constrained by the thin walls, best seen in Figure 48 (e), (f), & (g). In addition, Figure 48 (g) shows that a large melt pool initial formed on the complex part but was terminated as the beam began to skip along the thin walls.

Another clear example of the link between process parameters, geometry, melt pool shape and G & R can be found in the scanned top surfaces of build F2 and F3. Figure 49 compares the top surface of 4 related raster melted parts which rotate 90 degrees on each layer. Parts F21 and F31 have a starting raster of 0 degrees while F23 and F33 have a starting raster angle of 45 degrees. All the other process parameters used in F21 are repeated for F23, and same goes for F31 parameters repeated for F33. The major difference between the F2 build and F3 build is the resulting size of the melt pool. For F2, the melt pool is large as the process used a current of 18 mA while melting this part. F31 uses a higher energy density than F21 but a lower current to produce a much smaller melt pool which terminates along the bottom edge. When looking at the two builds, F2 looks much brighter and mirror like, while F3 parts do not reflect light back to the scanner due to the rough top surface. When moving to parts F23 and F33, we see that the general trends in brightness continue. The final melt pools are more similar in shape because they both terminate in the top right corner. It is important to note that these two builds are comparable because the preheat temperature was nearly the same.

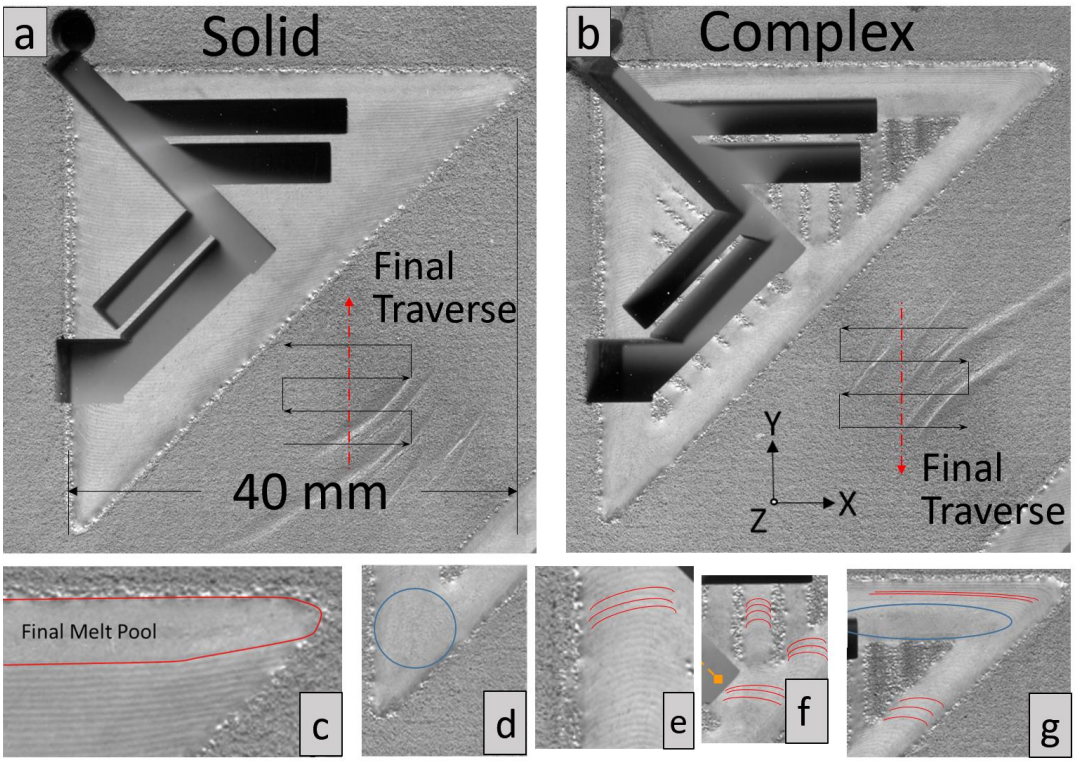

Figure 48. Top surface scan of build B1 with melt pools identified. Adapted from [47].

Current =	18	mA
SF =	63	-
Velocity =	2518	mm/s
Power =	1080	W or J/s
Hatch =	0.125	mm
Length =	20	mm
transverse =	15.7	mm/s
Focus off =	20	mA
Rotate =	1800	Deg/mm
Energy =	3.4312947	J/mm2

Current =	4	mA
SF =	150	-
Velocity =	756.92083	mm/s
Power =	240	W or J/s
Hatch =	0.056	mm
Length =	20	mm
Transverse =	2.12	mm/s
Focus off =	20	mA
Rotate =	1800	Deg/mm
Energy =	5.6620377	J/mm2

Figure 49. Scanned top surface of parts F21, F31, F23, & F33 with edge lengths of 20 mm.

4.4Discussion of Defects: Porosity

Porosity can come from a variety of sources: Lack of fusion, key hole, or gas porosity from powder production. Build 1 with IN 718, A1, contained the worst chimney porosity or lack of fusion porosity. This kind of porosity is best observed in cross-sections that are parallel to the build direction. Figure 50 shows the diagonal cut of three parts produced in this build which all contain chimney porosity using dark field optical microscopy. In the case of part 7, when the sample was cut off the plate it revealed no porosity on the XY plane. However, the Z plane reveals these layer defects which are not completely removed when melting the next layer. Part 1 shows the most extreme case where some of the porosity extends the entire height of the sample. After this build, no other builds were performed at a preheat temperature below 900 ºC and the energy densities used prevented porosity to this degree.

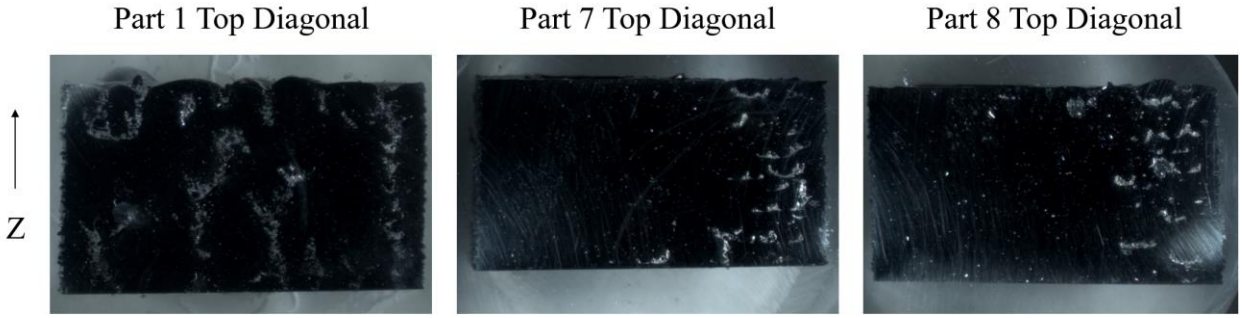

Figure 50. Dark field optical microscopy taken of build 1.

A more common form of porosity, that is observed in almost all powder bed AM builds, is gas porosity. Parts 5 and 6 of build 1, A1, showed the least amount of chimney porosity but gas porosity was not eliminated. The spherical gas porosity ranges from a few microns to 100 μm as seen in Figure 51. Gas porosity was observed in all builds with the least amount of porosity observed in the Rene N5 builds. This difference is due to the PREP powder that was used for build B1 and B2.

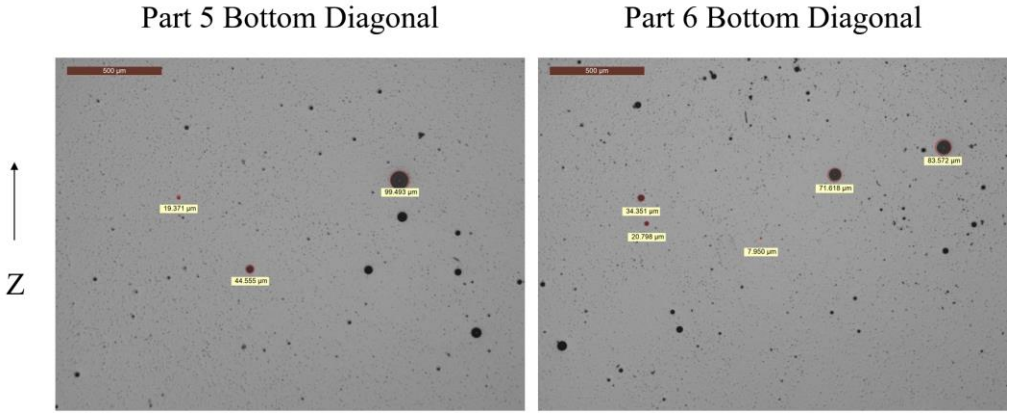

Figure 51. Spherical gas porosity in build A1 with Inconel 718.

4.5Solid-State Transformation Microstructures

The evolution of the precipitant structure is of importance as the creep resistance is depended on the volume fraction and size of precipitants in γ' alloys. In this work, alloys Rene N5, Ni-6Cr-6Al-6Ta, and Ni-10Cr-6Al have a high volume fraction of γ' in a γ matrix. A combination of etching and harness maps were used to characterize the precipitant structure, size, and distribution across samples taken from these alloys. The thermal history of the parts will also be used to explain the variations.

From the first build with Rene N5, the diagonal cut of the solid part (B1SA) and the thin walls of the complex part were characterized by a micro hardness indenter. Figure 52 gives the positions that were mapped which include regions of columnar and equiaxed microstructure and thin wall regions. Note that the indents include the base plate region and try to avoid edge regions with lack of fusion. Figure 53 maps the hardness values with a red grid overlaid to indicate the position of each indent. The map shows that there is little difference across the diagonal but there is a gradient from top to bottom. The top region which is last to solidify and has been aged the least is the hardest. There is then a decline in hardness moving toward the base plate and a drastic decrease in hardness at the base plate. The trends observed for B1SA indicate that there is little diffusion from the steel plate to the part due to the drastic change at the border. The same trend is observed in the thin walls of the complex part. Figure 54 shows the change in hardness as a function of height. The plot starts from the base plate and increases in height along the x-axis. The values from B1SA and each of the vectors from B1CB are aligned based on the jump in hardness that occurs at the transition from baseplate to part. Even though there is a large distribution of values at each height there is a systematic increase in hardness as a function of height. Figure 55 shows the spread of hardness values of the from left to right and shows no variation along the diagonal. There is also no difference between each of the thin walls.

Due to the trends that were observed in the hardness it was clear that there must be a microstructural change from the base of the part to the top of the part. The diagonal sample B1SA was lost in subsequent polishing after the hardness mapping so etching was performed on the diagonal part of B1CA. This is a fair comparison due to the similarity of hardness in the thin walls and solid part seen in Figure 54 and Figure 55. Figure 56 shows how the precipitation structure varies as a function of height for the center diagonal of B1CA after etching. At the top of the sample (a) the dendrites are visible with secondary arms and a fine γ' precipitant size within the dendrite arms. Between the dendrite arms, the interdendritic region, there is a larger γ' precipitant size as well as carbides that are identified. Moving down the sample (b), toward the base plate, the secondary dendrite arms become less clear and the interdendritic region has coarsened. At the bottom of the sample (c), close to the base plate, the dendrite arms are no longer visible and the interdendritic region has coarsened further and no longer outlines the dendrite arms. The region which was the primary dendrite has not coarsened a significant amount.

In contrast, the two custom alloys do not have a strong presence of dendrite arms near the top surface and have a variation in γ' size from top to bottom. Figure 57 compares the two custom alloys, Ni-666 and Ni-106, with images taken near the top of the part and close to the base plate for samples F61A and E43A respectively.

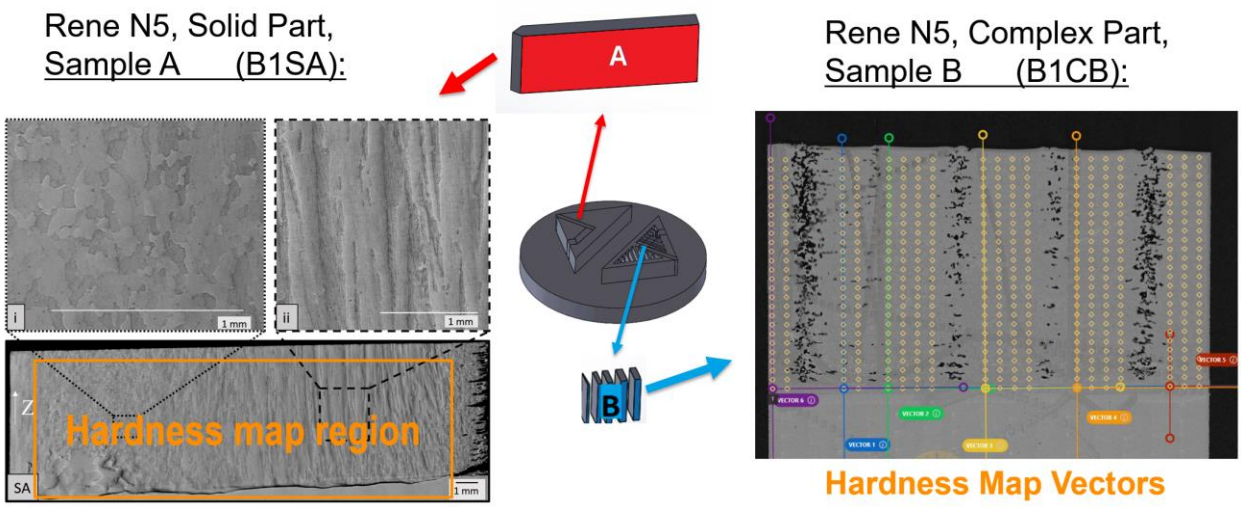

Figure 52. Regions of interest for sample B1SA and B1CB. Adapted from [47]**.**

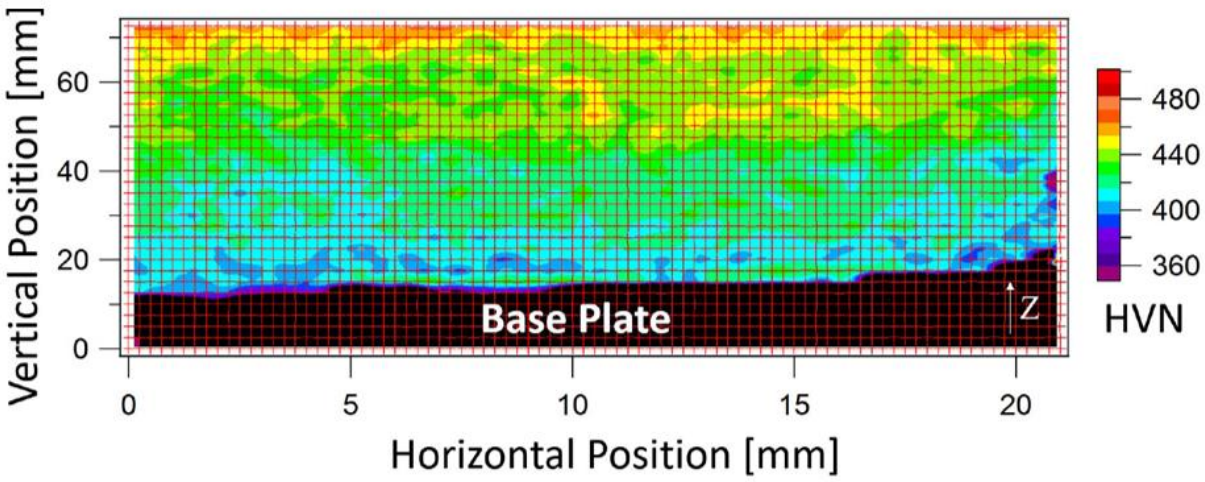

Figure 53. Hardness Map of B1SA. [47]**.**

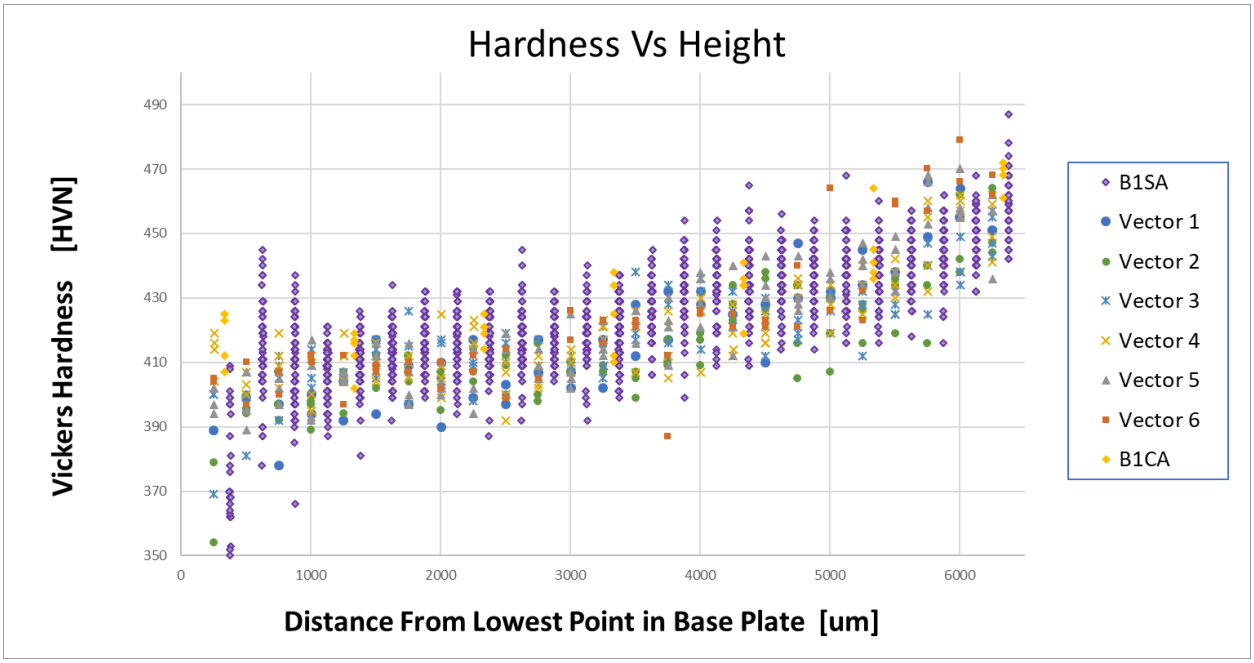

Figure 54. Vickers Hardness as a function of height for B1SA and B1CB.

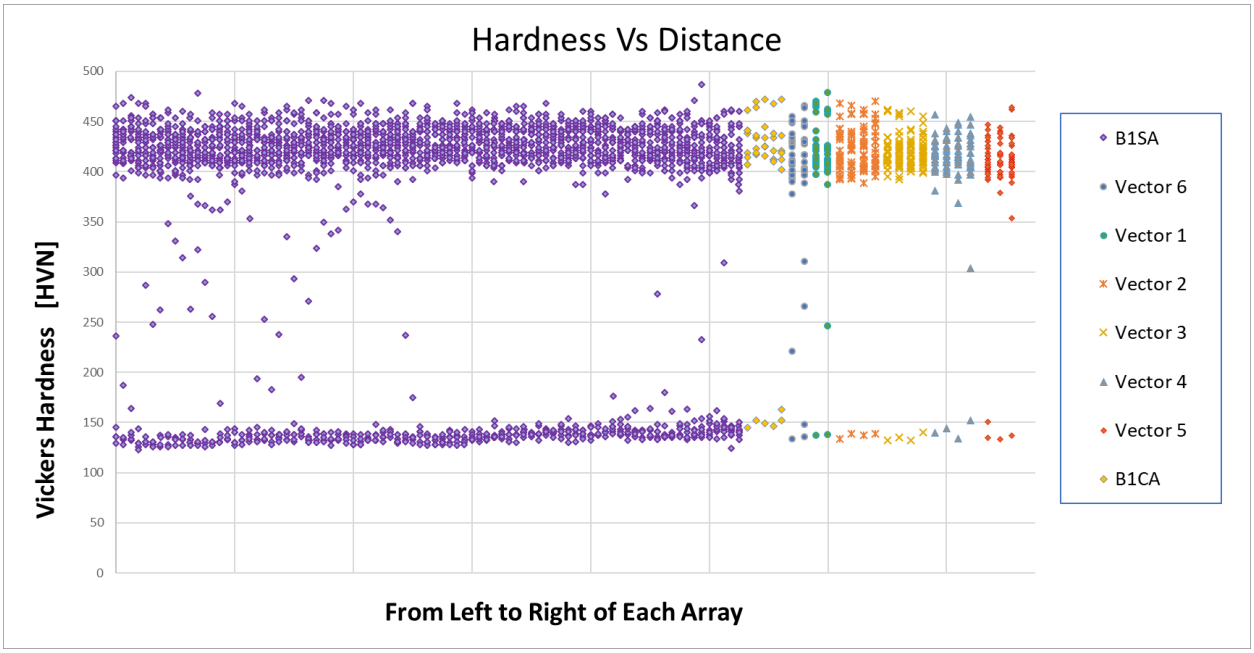

Figure 55. Vickers Hardness from left to right for B1SA and B1CB.

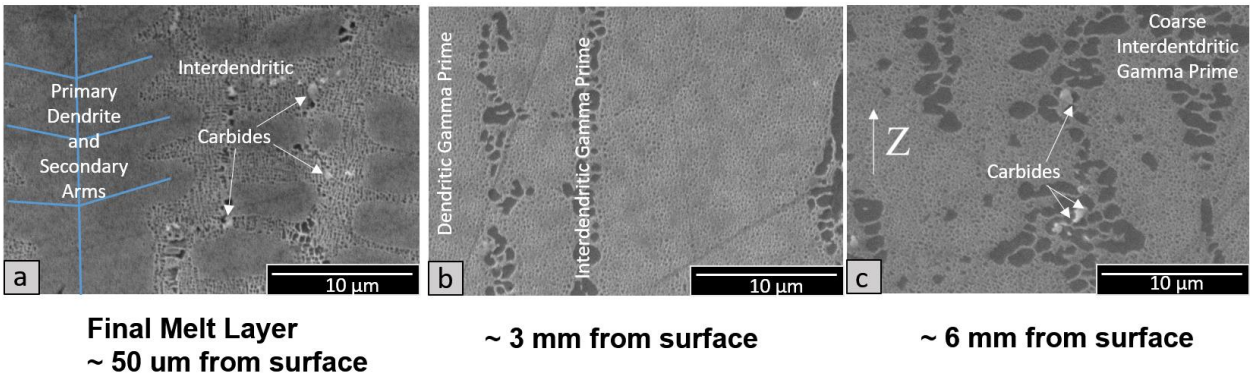

Figure 56. Variation in precipitation structure with height from B1CA. Adapted from [47]**.**

The top of the Ni-666 sample, F61A has large cuboidal γ' precipitants that are greater in size than any observed at the top or bottom of E43A which are both cuboidal as well. Moving from the bottom of Ni-666 sample, the γ' structure changes and becomes bimodal. Further characterization given in Figure 58 shows that the structure is more complicated as the γ' appears to be spherical (or rounded cubes) closest to the base plate before it becomes bimodal at close to 3mm. When acquiring the SEM images for this sample it was extremely difficult to focus the electron beam. For each of the images in Figure 58 the SEM had to be aligned. Once the SEM was aligned at a Z height, it was possible to move in the XY plane without losing focus but moving either up or down in the Z direction would lead to loss of focus. At the very top of sample F61A in Figure 58 a grain boundary can be observed running directly through the middle of the image but no dendrites are observable as seen in Figure 56 (a). Moving down sample F61A steady growth is observed at 11 and 9 mm before the bimodal distribution is observed spanning 7 mm to 3mm. The gradient in size and change in structure from top to bottom of the part indicates that the build took place at a temperature below the gamma prime solvus leading to growth if the γ' phase. It is not possible to get an accurate estimate of the temperature at varying heights during the experiment as the only temperature reading comes from a thermal couple placed at the bottom of the base plate. To make matters more difficult, the thermocouple was not properly grounded during this build and would show a different temperature when beam was on vs when the beam was off.

Figure 59 places the Anomaly Plots for builds B1, F6, and E4 side by side with an estimated γ' solvus drawn over the temperature profile. The plot of the temperature, in red, in relation to the γ' solvus explains the differences in the precipitant structure between the three builds. For builds B1 and E4 the estimated γ' solvus is below the thermocouple temperature and little gradient is observed from top to bottom of the samples. In comparison the temperature of build F6 was not maintained above the gamma prime solvus and thus the γ' precipitants began to coarsen over the length of the build.

If the alloy was processed above the γ' solvus also becomes evident in the hardness maps and precipitant structure of the two custom alloys. Similar to the region sampled of B1SA in Figure 52, a micro hardness map of sample F61A was performed and given in Figure 60. A strong gradient is observed from the top to the bottom of the sample with no gradient in hardness from left to right of the sample.

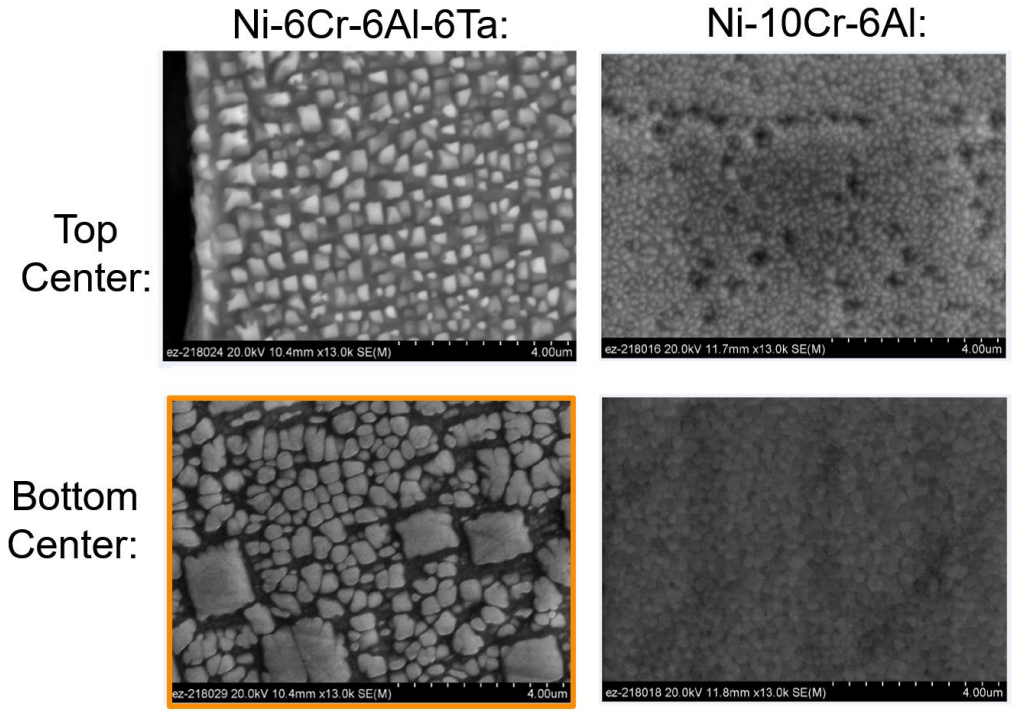

Figure 57. Comparison of custom alloy γ' structure at top and bottom, F61A and E43A.

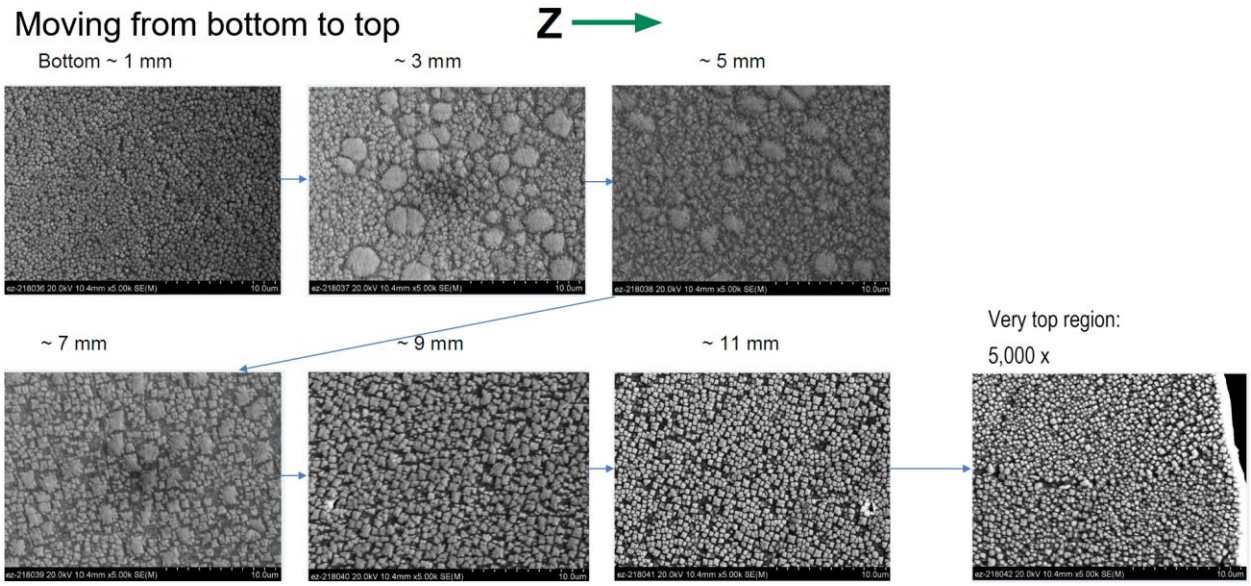

Figure 58. Additional SEM images of the γ' structure in sample F61A, Ni666.

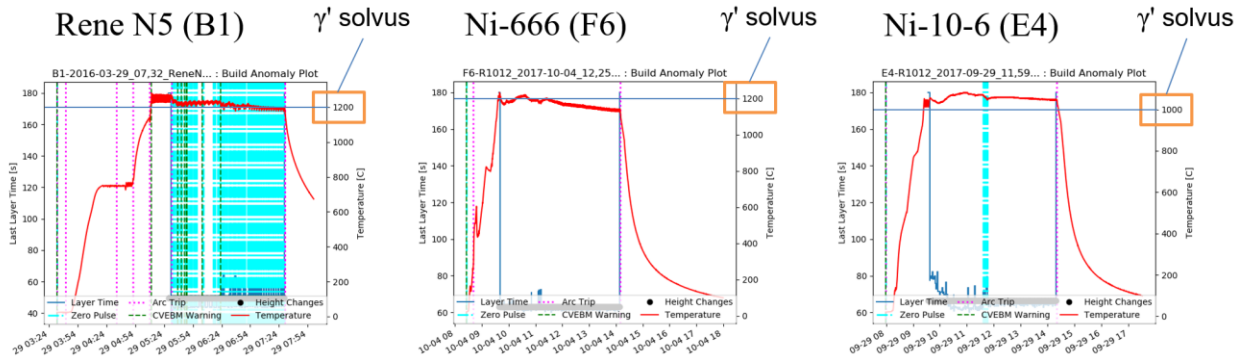

Figure 59. Anomaly plots for builds B1, F6 and E4 with estimated γ' solvus drawn.

The gradient is similar to B1SA, where the top has a higher hardness than the bottom of the sample, close to the base plate. This gradient from top to bottom is best observed in Figure 61 by mapping the hardness in the Z direction, from the base plate toward the top of the sample. The consistency from left to right of the sample is best seen in Figure 62 which plots the hardness along the XY plane.

In contrast to both B1SA and F61A, the hardness map of E43A shows no gradient from top to bottom of the sample. The hardness map is given in Figure 63 in which the hardness only varies by about 20 HVN, with some outliers, while F61A and B1SA both vary by about 50 HVN. Figure 64 and Figure 65 confirm the lack of gradients along the height and across the sample of E43A by plotting hardness as a function of height and distance respectively.

In summary, none of the mapped samples show a gradient from left to right. Samples B1SA and F61A both show and increase in hardness moving from the bottom of the sample to the top of the sample. In sample, B1SA this gradient can be explained by the coarsened γ' precipitants in the interdendritic region. Due to the heavy segregation upon solidification, the composition of the interdendritic region will be more solute rich and could precipitate at a higher temperature than the cores of the dendrites which would be more Ni rich. No EDS was used in the work to confirm this. Due to a difference in composition the precipitated γ' could then coarsen as the build continues to create a gradient in hardness from top to bottom. The dendritic γ' then forms upon cooling and thus has little difference from top to bottom. In the case of E43A, the solidification range of the custom alloy Ni-10Cr-6Al has a much smaller solidification range compared to Rene N5.

Due to the smaller solidification window there is less segregation upon solidification and the build took place above the gamma prime solvus. Then upon cooling the γ' precipitants form with no observable gradient in hardness in any direction. Alloy Ni666 also has a short solidification window but begins to precipitate γ' at a higher temperature than Ni106. Build F6 was processed at a higher temperature than build E4 to avoid the coarsening of the γ' during the process. The variation in hardness and γ' size as a function of height show that the build did not take place above the γ' solvus.

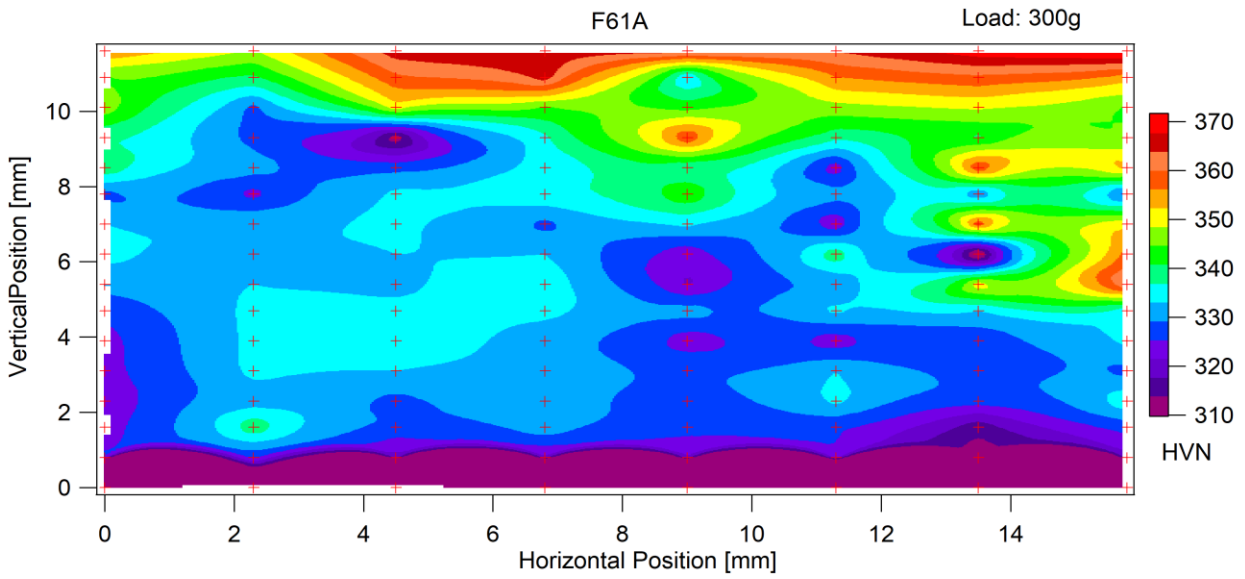

Figure 60. Hardness Map of F61A, Ni666.

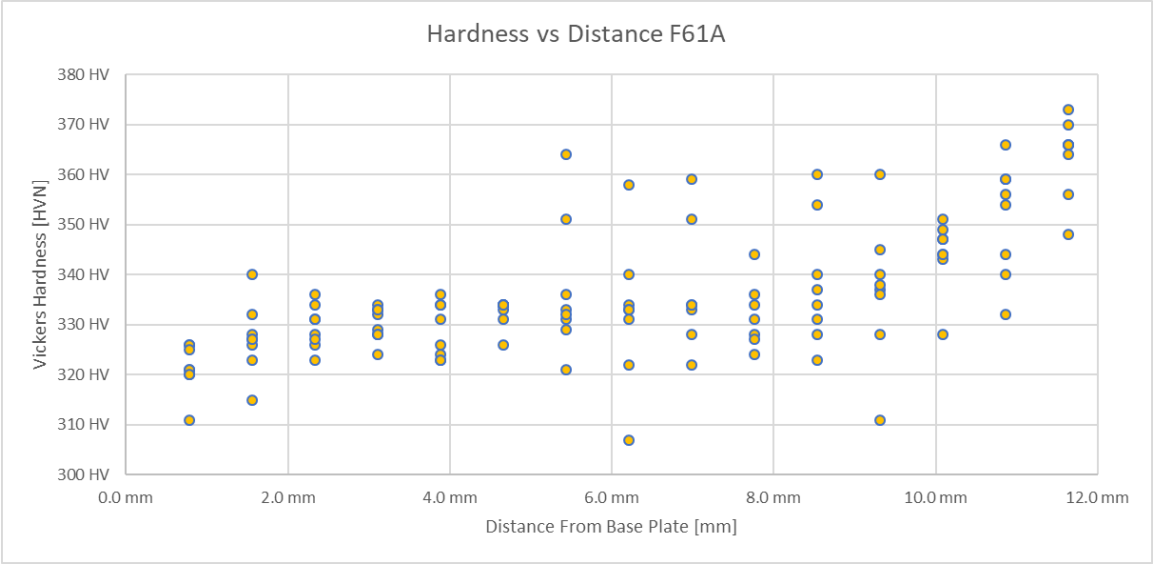

Figure 61. Hardness as a function of height for sample F61A, Ni666.

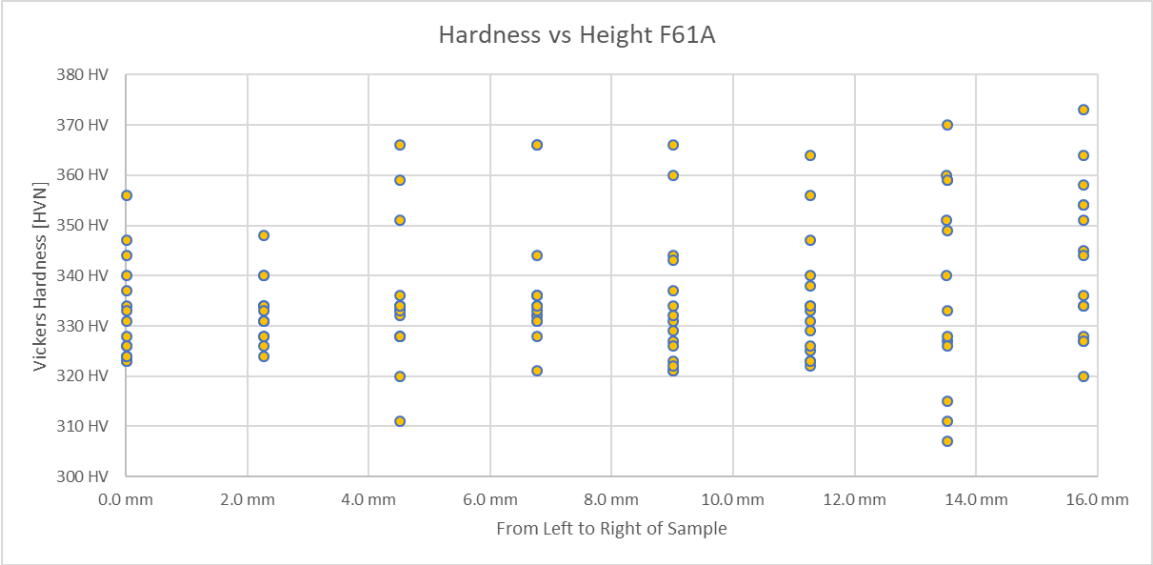

Figure 62. Hardness across sample F61A, Ni666.

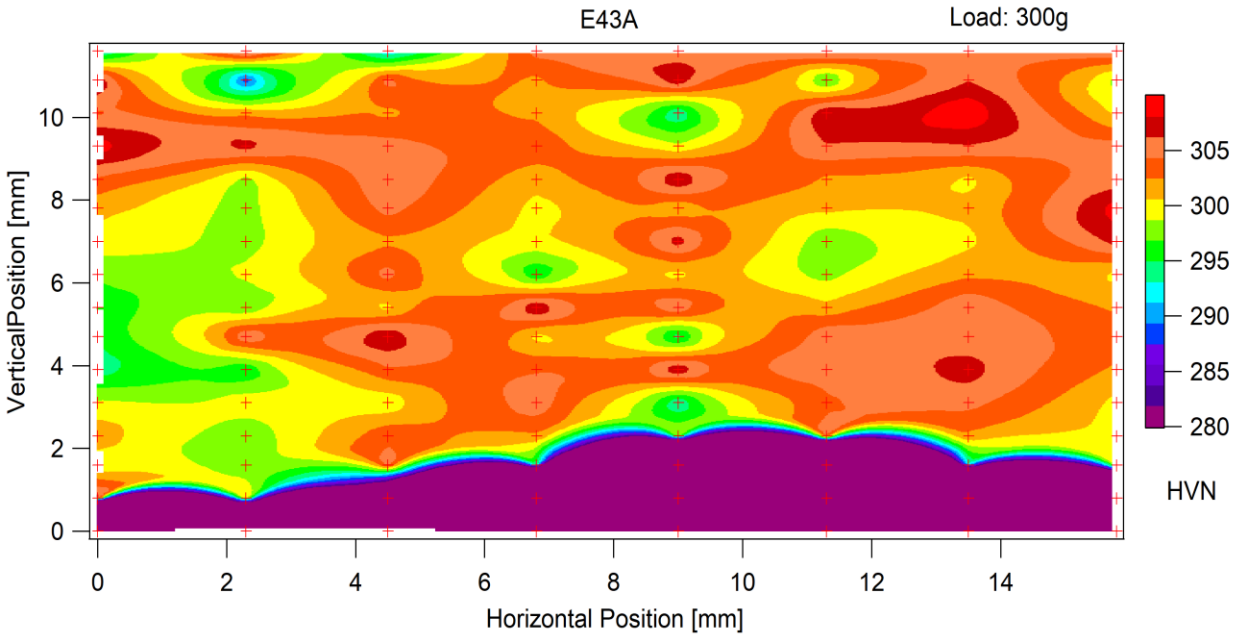

Figure 63. Hardness Map of E43A, Ni106.

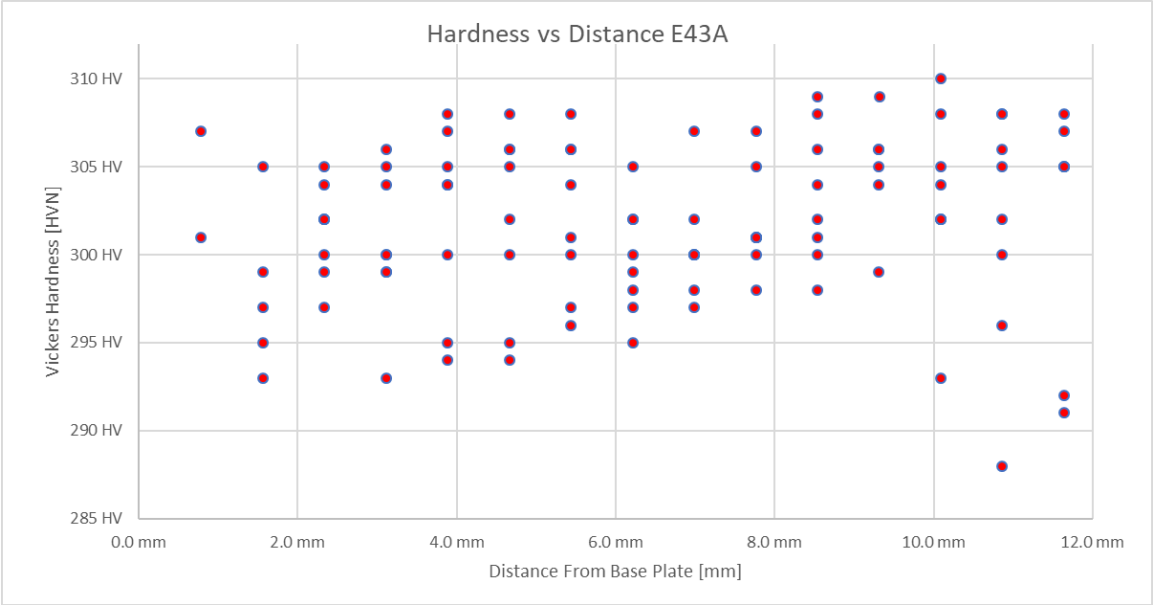

Figure 64. Hardness as a function of height for sample E43A, Ni106.

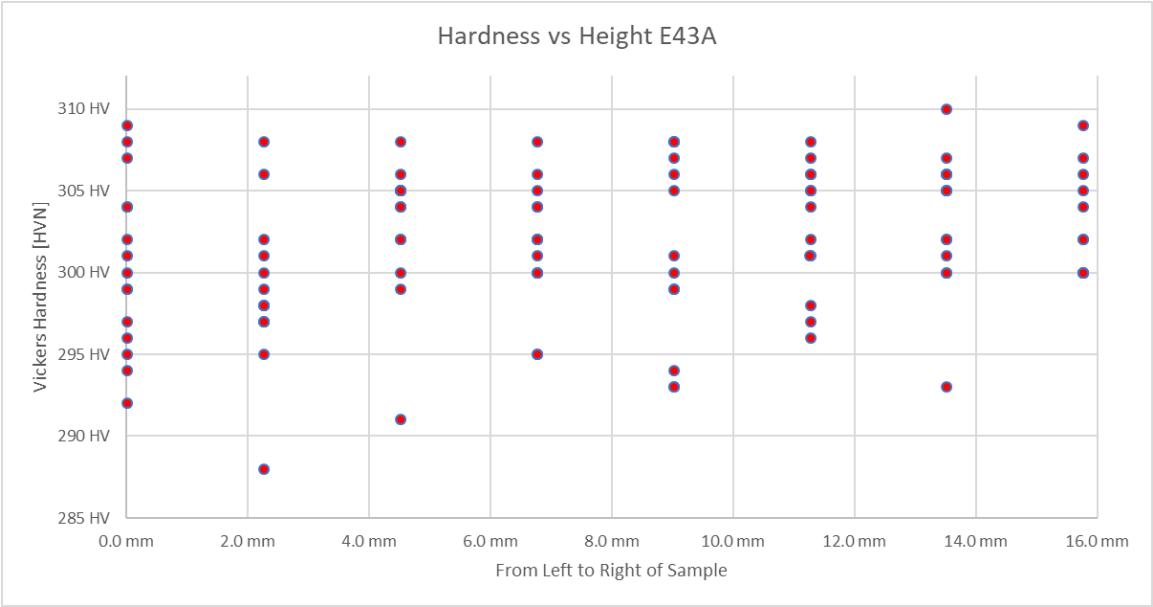

Figure 65. Hardness across sample E43A, Ni106.

4.6Cracking of High γ' Nickel Alloys During Processing

Cracking was observed in the high γ' nickel alloys that were processed including: Custom alloy Ni-6Cr-6Al-6Ta (F1-5), Ni-10Cr-6Al (E4 & E5), and Rene N5 (B1). The location and type of cracking observed is different in each case and the subsections will be broken up by alloy.

4.6.1 Cracking in Custom Alloy Ni-6Cr-6Al-6Ta.

Cracking on the initial Ni666 builds was evident during processing. The IR video of the top surface during the processing reveals cracks early in the initial builds (F1-F5). When the builds are removed from the build chamber the cracks can be emphasized by using a Sharpie marker. By coloring the top surface with a Sharpie marker, the cracks become evident as cracks absorb the ink. Un-cracked regions keep the color of the Sharpie marker. Figure 66 compares the surface of build F5 (a) as seen by the IR camera during processing, (b) with Sharpie marker to highlight the locations of the cracks after processing, and build F4 (c) using a red Sharpie to highlight cracks.

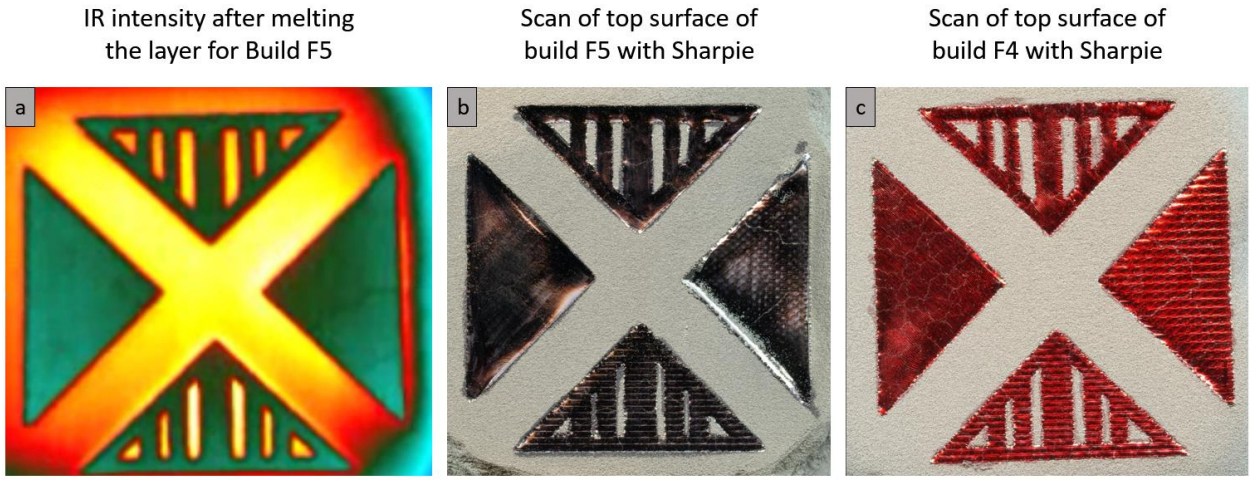

Figure 66. Cracking observed on top surfaces of build F4 and F5 with IR and Sharpie.

The cracks that are observed on the top surface of builds F4 and F5 extend deep in to the part and occur in both the Solid and Complex parts. The cracks appeared regardless of the melting strategy (spot or raster) and regardless of the melt pool size and energy density used (F4 had a smaller melt pool, smaller hatch, and higher velocity than F5). Parts from build F5 and F4 were removed from the base plate using a wire EDM that cut in the XY plane at about 5 mm from the top surface of the part. The samples were then cut into half along the diagonal and then both remaining parts were mounted as samples A and B. Figure 67 has stitched edge lit Keyence images of the diagonal sample (F54A) and the XY plane (F54B) with cracks indicated by red arrows. In sample A, cracks can be observed extending from the bottom of the sample to the top of the sample along the grain boundaries of the columnar structure. Sample B contains cracks that extend across the thin walls of the part.

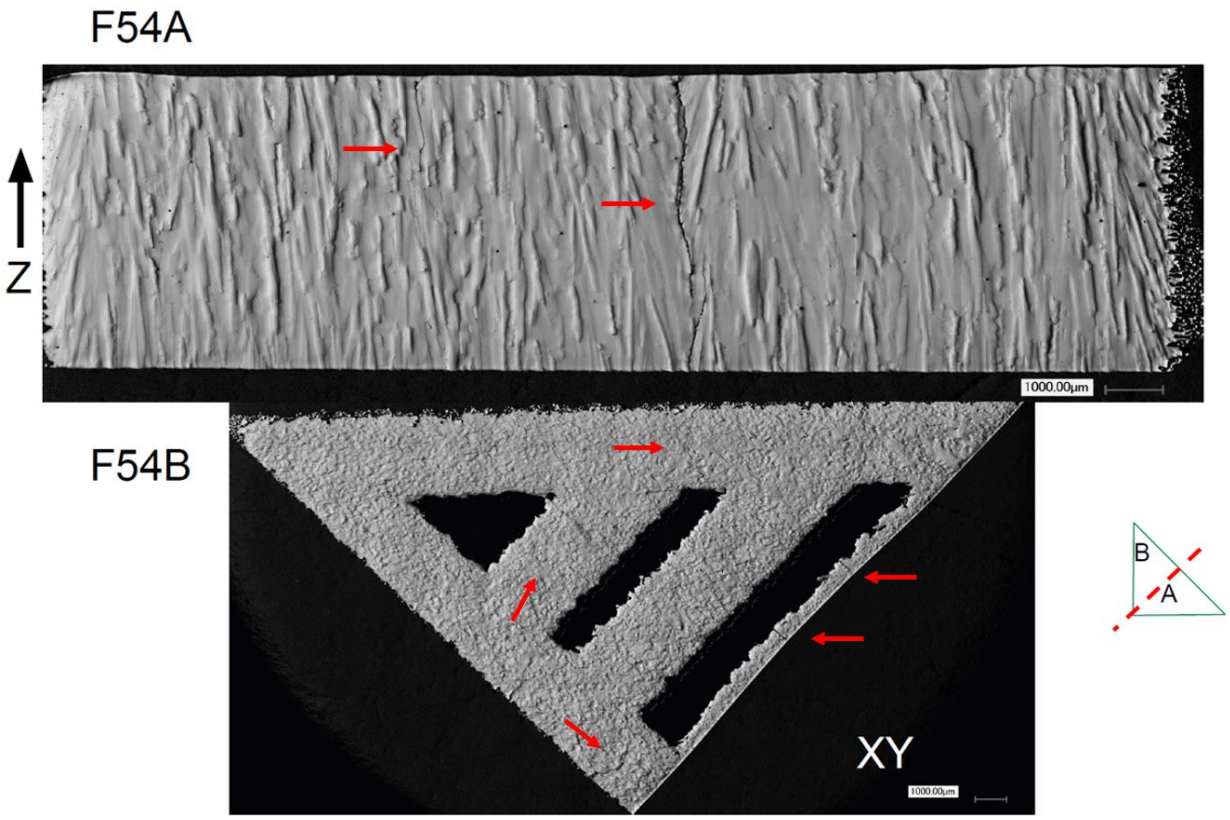

Figure 67. Stitched Keyence edge lighting of samples F54A and F54B.

Figure 68 contains representative data of the grain structures and trends observed during the F-series builds (Ni666). Each of the subfigures (a-f) contains stitched edge lit Keyence images of the resulting grains structure. EBSD was performed near the top left edge and top center of each sample. The data was then used to create Kernel Average Misorientation maps (KAM) that are overlaid on the regions the EBSD was performed on. Note that the grain boundaries are identified as black lines in the KAM maps. Pole Figures displayed on the left and right are created from the entire EBSD. Pole figures shows that a columnar structure aligned with the build direction resulted from each scan strategy. Each of the samples in Figure 68 comes from 20x20x15 mm^3 cuboidal part sectioned across the part (YZ) and perpendicular to the build direction (XY). Subfigures (a) and (b) contain a coarse columnar structure with cracks aligned with the build direction and going along the grain boundaries. The KAM maps were used understand the cracking mechanism as they show regions of strain within grain boundaries. The KAM maps indicate that there is a variation of strain between grains but that high areas of strain do not necessarily lead to cracks. In the S-EBM process each grain boundary is a high angle grain boundary and thus the part with more grain boundaries is more likely to contain cracks. This is seen in subfigures (c) and (d) which contain a fine columnar grain structure and a much higher number of cracks. The high angle grain boundaries can be identified by creating IPF maps which show similar results to the edge lit Keyence images. Grain boundaries that have large misorientation show up as thicker lines in the edge lit images. Sub figures (e) and (f) show a

columnar structure that resulted from a spot melting strategy. Again, the high levels of strain within the KAM maps do not necessarily lead to cracks.

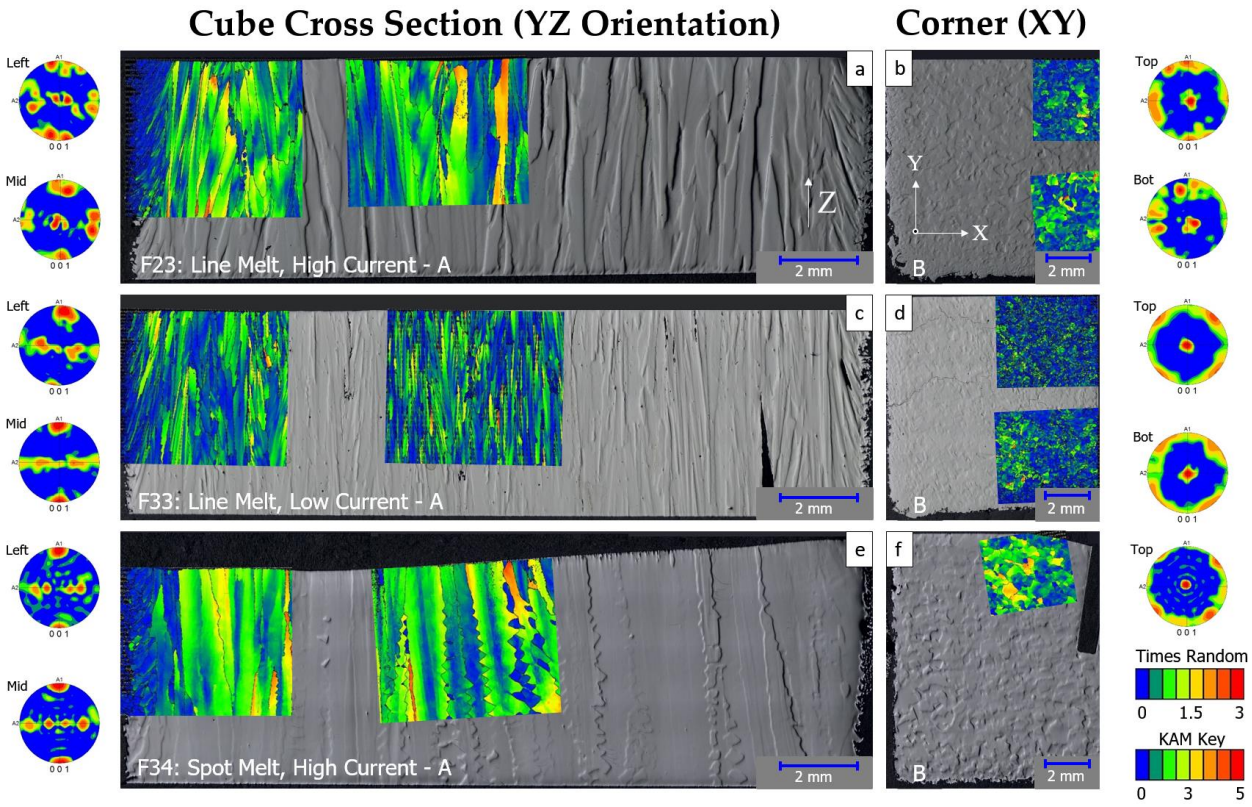

Figure 68. Stitched Edge lit Keyence images with EBSD kernel average misorientation.

When Ni-6Cr-6Al-6Ta was repeated for the final time in build F6, the baseplate temperature was increased to near 1200 °C as shown previously in Figure 59. This was done to prevent formation of γ' prior to the end of the build and prevent cracking. Section 4.5, showed that the build took place below the gamma prime solvus as there was a gradient in hardness and γ' size in the build direction. Despite the formation of γ' during the build, cracking was avoided on build F6. This can be best seen in Figure 69 of sample F61A which was removed along the diagonal of a solid right triangular prism. The images in Figure 69 were taken after etching the surface with (a) containing a stitched image of the entire sample, (b) is from the top region, and (c) looks at the part/baseplate interface. The etching reveals many features at different length scales. First each grain reflects light differently dependent on its orientation to the polished plane. There is a mix of high and low angle grain boundaries but no cracks were observed along any of the grains in (a). Figure 69 (b) zooms into the top surface to reveal two more features that can be revealed by etching: (1) the dendrite arms can be seen along the top surface of the build growing epitaxially from the previous layer; (2) there are stripes from left to right that pass through the grain boundaries that signify the depth of the melt pool upon each layer. At the interface between the

baseplate and the part, Figure 69 (c), there is a transition from equiaxed stainless steel to columnar nickel without any cracking. In addition, there appears to be a level of dissolution across the boundary which is revealed by the difference in etching rates. The rates of etching create a wave pattern above the interface in the nickel alloy. Each of these layers has experienced high temperatures during processing and the lines that were highlighting the layer heights at the top of the sample are no longer present at the bottom.

4.6.2 Evidence of Cracking in Custom Alloy Ni-10Cr-6Al.

In builds E1-E5 no cracks were observed on the top surface nor upon polishing the cross sections for grain structure characterization. However, upon etching to characterize the precipitation structure a few cracks were revealed due to water droplets and continued etching taking place in the cracks along grain boundaries. The main difference between builds completed with Ni-10Cr-6Al is the temperature at which they were built and the scan strategies. The Build Anomaly Plots are given for builds E2, E4, and E5 in Figure 70.

The geometry for each of the builds is the same: 4 right triangular prisms, 2 are solid, 2 are complex. Build E2 and E4 use similar build parameters, raster scan strategy, and different pre/post heating to change the build temperature. Build E5 was an experimental build which used spot melting followed by a raster melt to smooth the top surface. A scan of the top surface for each build is given in Figure 71 to show that each part obtained relatively smooth top surfaces regardless of process approach. Build E2 experienced swelling in the center and build E5 experienced swelling on each of the parts.

The diagonals were sampled from multiple parts of each build. Samples E21A, E43A, and E53A were found to be characteristic each build and were chosen for etching. The etchant did not behave the same as for Ni-6Cr-6Al-6Ta but the grain boundaries and precipitants were still revealed. Figure 72 gives representative images after etching of the diagonal cuts E21A, E43A, and E53A. Red arrows indicate cracks and labels are included on areas of interest which have inset images. Figure 72 (A) from build E2, which was processed at near 1200 °C, has a raised top left corner due to swelling which tilt the growth direction of grains in that region. In the rest of the sample only columnar grains are observed which span from the base plate to the top layer. Regardless of the swelling, E21A and all other samples taken from build E2 showed no signs of cracking.

Figure 72 (B) contains multiple regions marked by red arrows which appear to be cracks upon further investigation. B-1 and B-2 zoom in on two such locations where the grain boundaries are much more defined than the rest of the grains. In addition, there are signs of water marks which could have formed after the sample was etched, cleaned, and dried. Upon cleaning the samples and setting them to the side, the remaining water and etchant slowly seeps out of the cracks. Figure 72 (C) contains cracks not only along the grain boundaries as indicated by C-1 and C-2 but cracks also appear at the part/build plate interface. The energy density of spot melting is much higher than that of raster melting and the base plate often swells and distorts. The base plate is at a clear angle compared to the top surface of E53A in Figure 72 and upon cooling the part cracks at the interface.

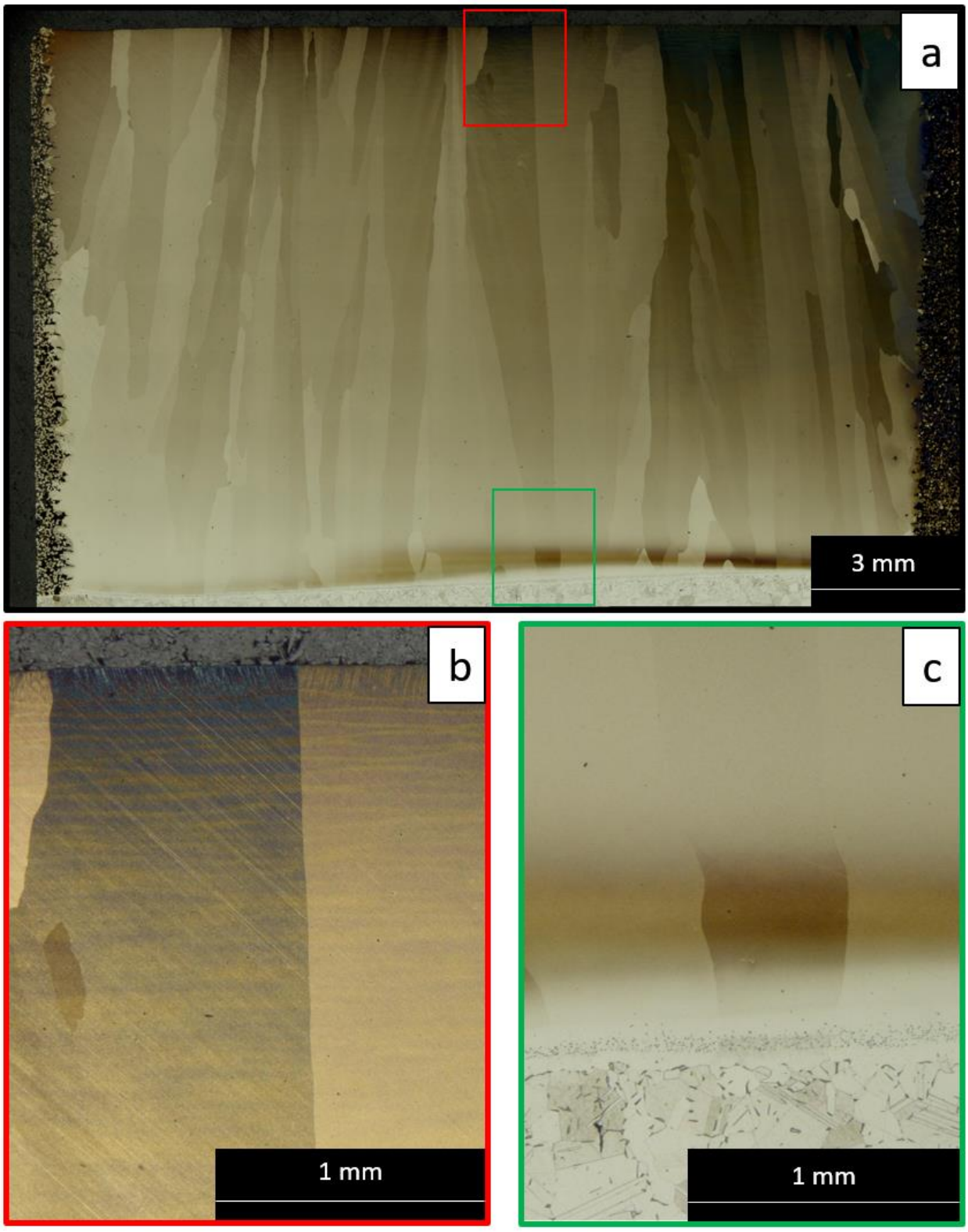

Figure 69. Keyence Images of F61A after etching with Glycerigia.

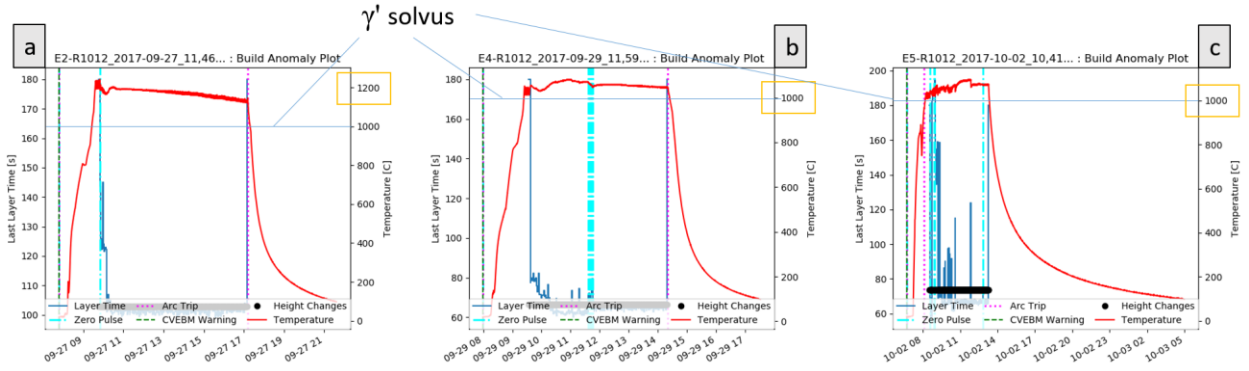

Figure 70. Build Anomaly Plots for three characteristic builds with Ni-10Cr-6Al.

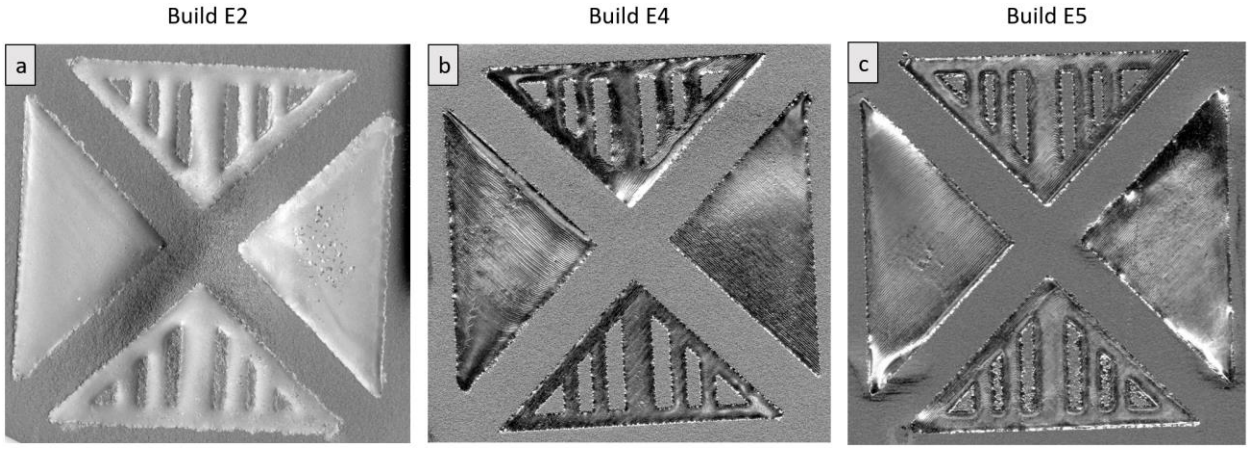

Figure 71. Top Surfaces of Builds E2, E4, and E5.

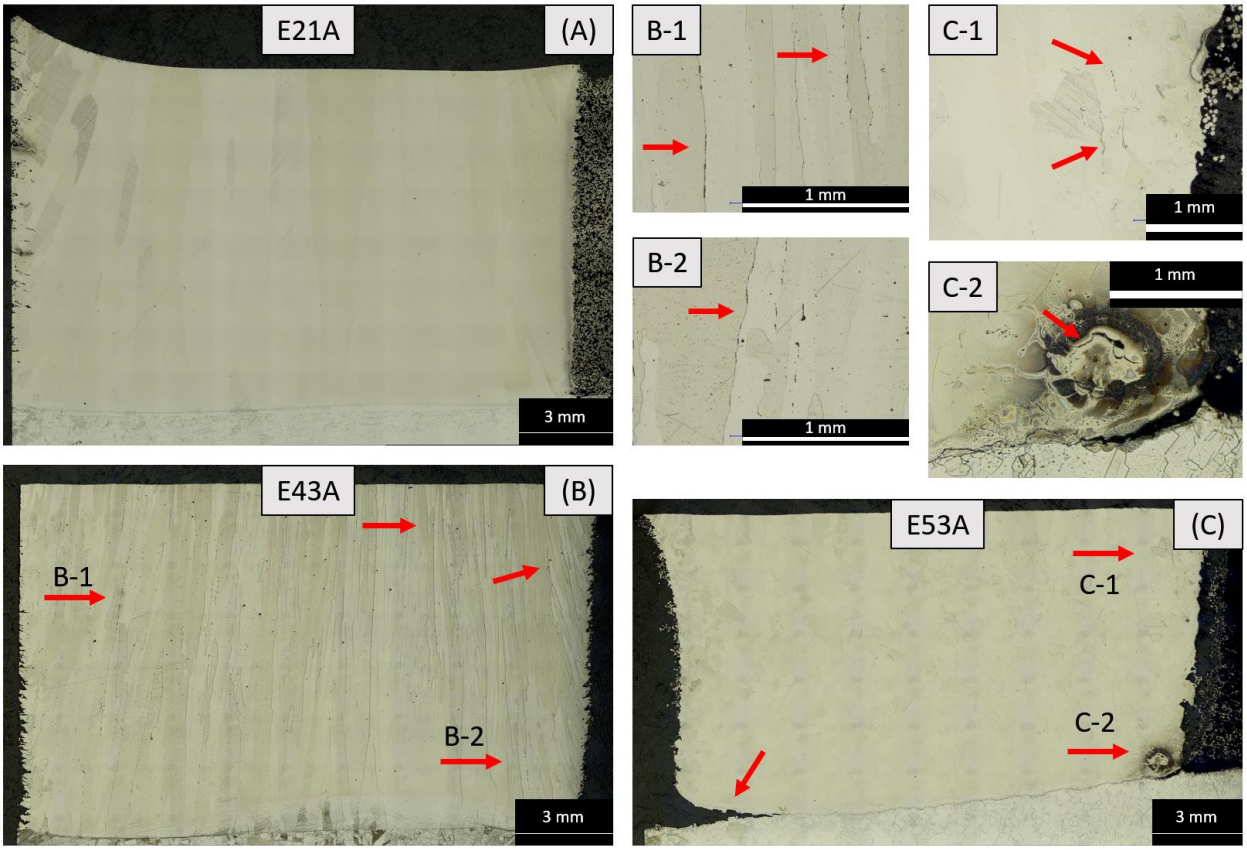

Figure 72. Representative Keyence edge lit images of builds E2, E4, & E5 after etching.

4.6.3 Cracking in Rene N5 Build B1.

It was initially believed that the Rene N5 builds did not crack as no cracks were observed in the wire EDM removed samples in the build direction. This included 6 samples from the Solid part and 6 samples from the Complex part. The cracks were not observed until additional samples were cut in the XY plane perpendicular to the build direction (Z). In addition, the cracks were not observed on the top surface, as seen in Ni-6Cr-6Al-6Ta. Figure 73 (A) is a scan of the top surface of build B1 for the complex part. The last raster began along the top leg of the right triangular prism and then moved to the bottom left corner of the part. Figure 73 (B) and (C) are cropped regions of (A) with weld pool ripples outlined in red. The large melt pool that extended form the left to the right side of the complex part in (A) was forced into the thin walls. As the raster moves into the thin walls the traverse speed of the raster fill speeds up and the large melt pool is left to solidify. A region of the large melt pool is circled in (D) on the top surface and in subfigure (E). After the samples were removed from the part in line with the build direction, the top part of the build was cut off the build plate 2 mm from the top surface. The remaining XY pieces were then mounted with the top surface down, ground flat, and polished. Figure 73 (E) is a reconstruction of the full part after each region was imaged and stitched with the Keyence edge lighting. The Keyence stitching was performed to correlate the microstructure estimated by the

SAHTM to the experimental results. The cracks in the circled region that are shown in subfigure (F) were not expected.

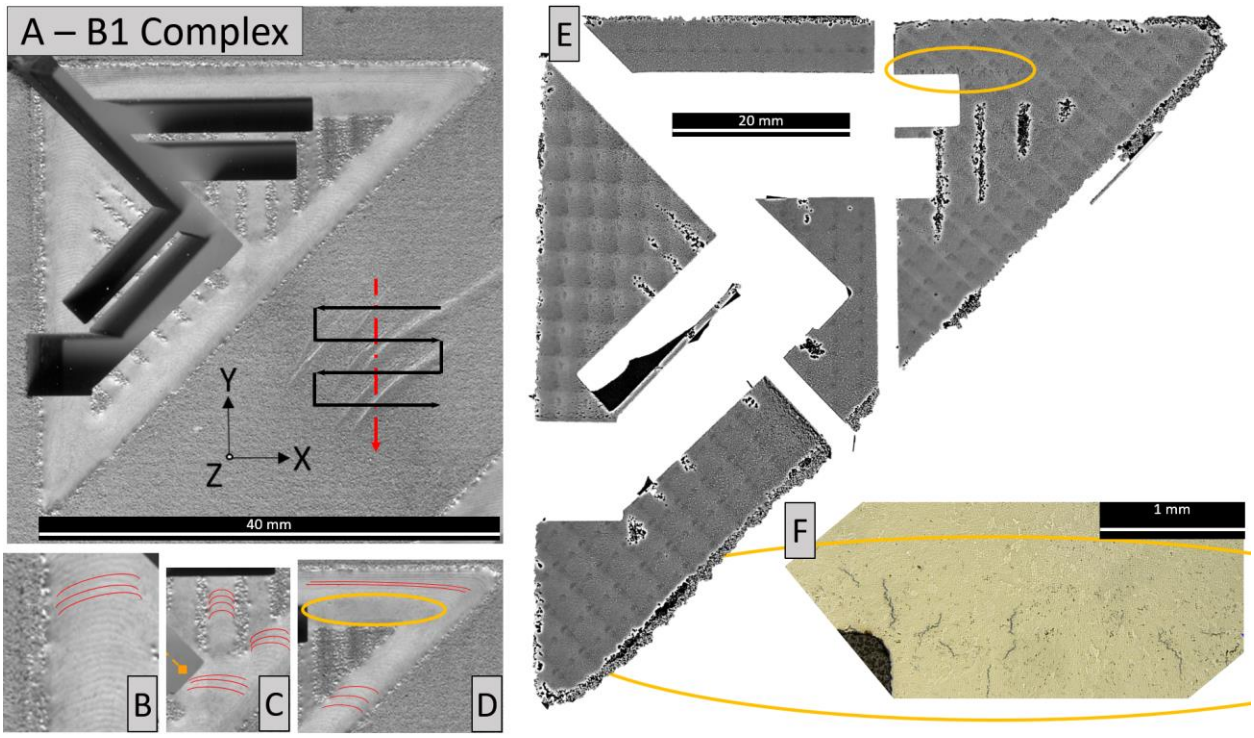

Figure 73. Location of cracks in B1 complex part. Adapted from [47]**.**

EBSD was performed on the cracked regions and a characteristic crack of the region is displayed in Figure 74. The sample surface is the XY plane of the part and thus Figure 74 (a) graphically displays the amount of twist between the grains by showing the (001) orientation in an IPF map. Figure 74 (b) plots the image quality of the EBSD scan to highlight the crack in black and contains color-coded grain boundaries. Red and green lines outline low angle grain boundaries while blue lines outline high angle grain boundaries. Figure 74 (c) is an IPF map which gives information on the growth direction and finds that the orientation is with the build direction (100). The 5 lines marked on (c) mark the position that misorientation plots are taken from in subplots 1-5 of Figure 74. Lines 1-4 cross the crack and contain misorientations that range from 4 to 54 degrees while line 5 crosses a range of grains that do not have cracks. The 5th misorientation scan and subfigure (b) show that the misorientations between un-cracked grains are just as great as those in the cracked region.

Similar EBSD was performed on the B1 Solid part in the XY orientation and the results were found to match line 5. In both cases, the presence of highly misoriented grains can occur if there is no stress concentration. In the case of the Complex geometry the thin walls became a location of stress concentration.

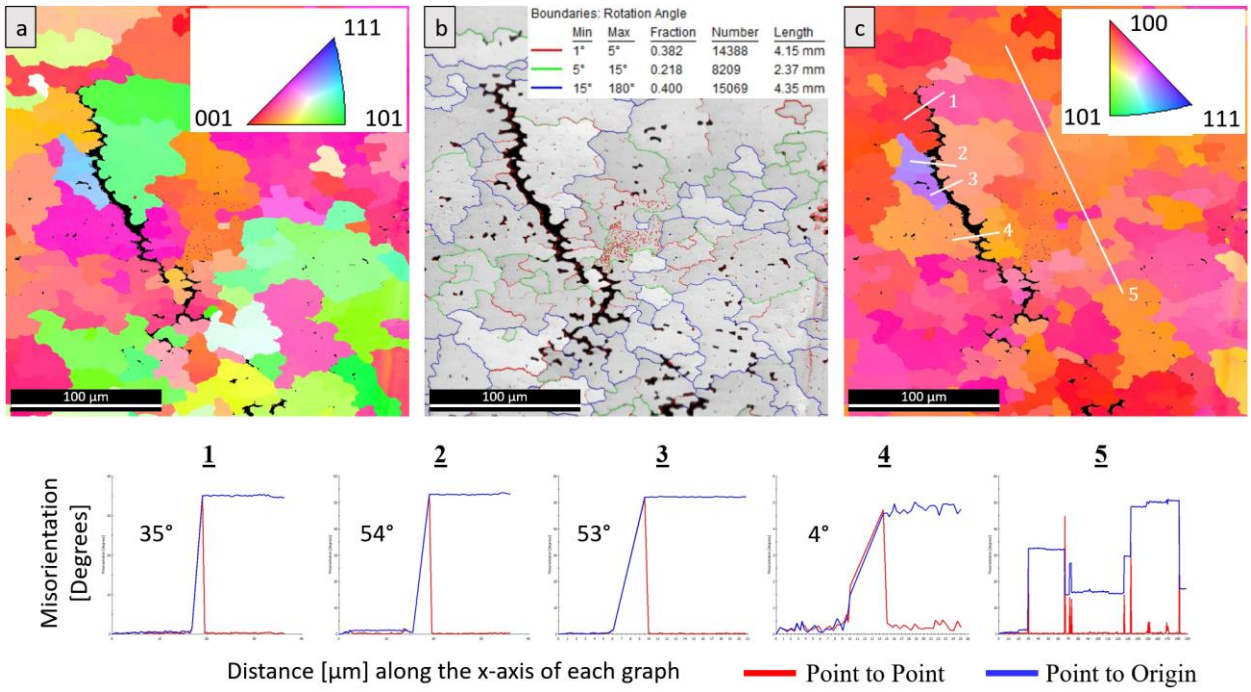

Figure 74. EBSD of cracked region in XY orientation of B1 Complex.

4.6.4 Discussion of Cracking in S-EBM.

Each of the high γ' alloys that were processed for this project ended up containing cracks. In each case the location and size of the cracks varied greatly. In the Ni-6Cr-6Al-6Ta builds at low temperature (F1-5) the cracks were extensive and observable on the top surface and between the grain boundaries in sectioned samples. When the processing temperature was raised to near the gamma prime solvus during processing of build F6, the cracks were no longer present in the regions sampled. Presence of cracks could still exist in build F6 as builds with Rene N5 and Ni-10Cr-6Al did not initially show cracks. In each of those cases the cracks were observed when attempting to characterize the grain or precipitant structure. Similar to Ni666, when Ni106 was processed at a higher temperature the cracks that were observed at low temperature processing were no longer observed. Rene N5 was only processed at high temperatures but it would be expected to crack due to the high γ' content and high Aluminum content similar to Ni666 and Ni106. Further characterization of the crack surfaces will be required to understand the underlying mechanism of the cracks formed during processing of high γ' nickel alloys.

5. CONCLUSIONS

5.1 Overview

The effect of alloying element concentrations on the CET boundaries during S-EBM processing of high gamma prime nickel base superalloys appears to be less than originally believed. The process parameters have the largest effect on the resulting solidification grain structure by changing the spatial and temporal variations of G and R by many orders of magnitudes, followed by alloy and geometry. To reap benefits of alloying for AM, the geometry, application and environment must be known a-priori. This conclusion stems from the two primary factors of our CET model: (1) the amount of aluminum; (2) the N_0 value for the specific alloy. Aluminum has the largest effect on the CET but changing the aluminum concentration also leads to variations in the volume fraction of γ'. The N_0 value is not known a-priori, as a result, it needs to be extracted from experimental measurements for each alloy being processed. This leads to a fundamental question: Does PREP produced Rene N5 powder have the same N_0 values as a custom alloy with only Nickel, Aluminum, and Chromium? Current results show it is not possible to answer this question until both alloys have be processed under identical processing conditions. However, process parameters used for one alloy may lead to cracking or porosity when processing the next alloy. Due to uncertainties of energy absorption on powder bed of each alloy, one to one comparisons or extensions cannot be made for different material feedstocks.

In addition to the CET, changing the Nickel alloy composition must consider other weldability limits such as cracking. This is most clearly observed in relation to aluminum addition and the resulting γ' volume fraction. Higher aluminum additions increase the solidification temperature range of the alloy and make it more likely to produce equiaxed grains, and may also decreases the resistance to solidification cracking. Cracking during AM of nickel alloys is caused by a material weakness and an evolving directionality and magnitude of thermal stresses. Cracking is mostly observed along the highly-misoriented grain boundaries (a weak point) and the extent of precipitation in the previously processed layers. Elevated preheat temperatures above the gamma prime solvus temperature were shown to avoid cracking in the custom alloys. However, over-sintering becomes a new limitation with preheat temperatures above the gamma prime solvus temperature and closer to the solidus temperature.

The spatial and temporal variations of melt pool shape as a function of geometry, preheat and processing conditions needs to be a key point of future research. In this work, the melt pool was

most often observed to be a line source that traverses the part perpendicular to the beam deflection. This allows for a strong thermal gradient in the build direction and epitaxial growth of grains that continue over many layers regardless of hatch rotation. The interaction of beam scanning and geometry will influence by allowing or preventing a line source. Short line lengths can lead to area melts while long line lengths could lead to elliptical melt pools. The preheat will directly influence the size of the melt pool and changes in process parameters or part layer geometry could change the temperature of the build indirectly.

5.2 Describing the Spatial Variation of Thermal Gradient and Solidification Velocity

During this work, the SAHTM and the in-situ IR video predicted large local variations in the solidification conditions (G and R) consistently across the part. The scale of variation was related to the melt pool size. Spot melting created large area melts and created relatively consistent thermal gradients. Raster processing conditions which produced thin melt pools produced short length scales of variation. As the melt pools increased in width (in the hatch direction) the variations increased in length scale.

Original plan to produce a variation in solidifications along the diagonal of the right triangular prism was not possible during this work on a single part. This was stifled by the Arcam's speed function which alters the speed to maintain similar energy density during changes in beam power.

5.3 Control of CET for Traditional Alloys produced by S-EBM

The variation in the modeled CET line for traditional alloys is highly sensitive to the amount of elemental additions, with aluminum being the strongest contributor. During this work, and previous work, it was shown that the CET can be controlled for IN 718 by the process parameters. Raster melting is unable to produce equiaxed grains (in most cases) but spot melting can introduce equiaxed grains.

Hastelloy X showed columnar grains in the samples that were taken from 1 build at a standard preheat temperature. However, Hastelloy X was not processed with spot melting.

Rene N5 was shown to produce equiaxed grains during raster melting when the preheat is an elevated temperature. Increasing the preheat had a twofold effect: (1) lowered the thermal gradient and allowed for a CET to take place; and (2) was above the γ' solvus and prevented cracking. However, the drawback of over-sintered powder surrounding the part was identified.

5.4 Control of CET for Custom Alloys produced by S-EBM

The two custom alloys produced for this project were chosen to have a high gamma prime volume fraction upon solidification and a limit of 6 wt.% Aluminum. Standard raster melting of the two custom alloys showed that only columnar microstructure was possible. Spot melting

produced equiaxed grains. Cracking adds an upper limit of CET manipulation. Additional Aluminum content could increase the chance of equiaxed grains but would further increase the amount of cracking during processing.

5.5Alloy Design Rules for CET of Nickel Alloys produced by S-EBM

All the traditional alloys and the custom alloys produced during this project are predicted to have CET lines that move only one order of magnitude in the temperature gradient intercepts, in comparison to many orders of variations in G and R induced by processing strategies. Spot melting and raster melting have been shown to have drastic differences in G and R leading to changes in microstructure. Both conclusions have a clear consequence for alloying for additive manufacturing: process parameters have more control over the solidification conditions than changing the alloy has over the CET line. This indicates that traditional alloys are great starting points for AM by electron beam powder melting and changes to them to control the CET may not be a fruitful exercise. Inadvertent changes made for shifting the CET could have detrimental effects on the properties of the alloy. An example from this work, the large effect that aluminum has on the CET and on the γ' volume fractions after processing.

6. RECOMMENDATIONS

6.1 S-EBM Lessons Learned

Many builds failed for various reasons during this project as the S-EBM process is dependent on many different input parameters. When starting a new alloy, modifying the build chamber, or changing the melt strategy, the flow of the process can become chaotic. Machine maintenance is key to improve the chance of build success. When it comes to the MiniVat, simple design is better. The final version of the MiniVat uses as much of the standard infrastructure of Arcam equipment as possible. Each change to the machine requires further tuning in settings and chances for the build to fail increases. Whenever possible, it is recommended to use the hoppers and the standard rakes. Modifications should be made to reduce the amount of powder that is inaccessible. For example, in the hopper corners, in front of the build plate, lost through the powder sensor holes. A square build column would also help removed preheating limitations due to the current software limitations.

Avoiding cracking by choosing an alloy or process parameter set adjusted for the part geometry should take priority over controlling the CET or solidification grain structure. Small tweaks to the process parameters can have large effects on the resulting grain structure. Small changes to the alloy requires expensive retesting of the process. Simplifying the changes to alloy chemistry is better in this case as well. For example, a large portion of elements commonly used in Nickel-based superalloys were removed for the custom alloy during this research. These drastic changes to the alloys might have removed some of the phenomenon that is relevant to final application (e.g.: reduced segregation during solidification and a smaller solidification temperature range). It is our recommendation that existing alloys must be fine-tuned instead of recreating an alloy from scratch due to uncertainty in pre-processing (e.g. powder making) of these alloys. It is also recommended that the existing alloy by chosen based on their casting or welding, before attempting to process it with S-EBM.

The N_0 value was shown to have a significant control on the CET model and is largely unknown in welding. Due to the increased number of variables in AM it is recommended to calibrate this value for each new alloy and process. It may be possible to tune this value by changing the method of which the powder is produced.

In-situ IR video used in this work could predict trends in the solidification conditions during this project. However, measurement of absolute solidification conditions are not possible for the

following reasons: (1) the top surface viewed by the IR camera is remelted upon the next layer; (2) key stoning effects, spatial and temporal resolutions add scatter to the data; (3) current methods of analyzing the data does not work for spot melting again due to limited spatial and time-resolution; (4) Top layer surface roughness can be drastically changed the predicted solidification conditions; (5) IR imaging and analyses requires a calibration for intensity to temperature of powder and melted material. A black body source calibration experiment is required to create a calibration for the material.

Set up is also complex when performing in-situ IR video of the Arcam process. Each piece requires fine tuning, from the Kapton film window, to the positioning, angle, zoom, focus, frame rate, integration time, and calibration curve. Each variable could drastically alter the results of the predicted temperature or solidification conditions. Our recommendations are to use the IR video as a quality assurance to record defects during parameter development. Then, in the future improvements in IR imaging and analyses, it can be transitioned to near IR at the end of a layer for quality assurance during production.

Continuing research on the Arcam S-EBM process will require a better understanding of process parameter control, than currently possible. There are thousands of linked settings and endless combinations between them for setting up the builds. It is not possible to optimize each of them when changing the internal set up and the alloy as regularly as was done in this project. Each alloy will require changes to the process parameters and further repetition than was possible in this work. Each modification reduces the standard comparison of data that is possible between research groups, machines, alloys, and geometries.

Powder size distribution in this project was important when fines were present in the distribution. Mean distributions above and below the standard 70 μm mean did not cause significant issues. However, the flowability and internal porosity between powders was noticeable. Powders that had a high angle of repose before flowing were difficult to work with and spread easily across the baseplate. Internal porosity was carried into the final part.

Powder contamination is a strong concern when working with multiple alloys. It is recommended to replace all the consumables (O-rings, shields, thermocouples, etc.) when switching between powders. Always assume the surface is dirty and the powder is not the same when outside the work space. Label sieves and throw away unlabeled sieves. All the metal powder is gray and looks the same.

6.2Future Work

To move powder bed S-EBM AM further we must start with a geometry and end application as the starting point. The process, material, and geometry are closely related to extend lesson learned from one application to another. To advance the benefits of the AM, the application must fit the limits of the process. S-EBM will require post processing to the surface and heat treatments to homogenize the solid-state microstructure. To optimize the process parameters, one must take into consideration the build layout, alloy, and each layer slice geometry. Processing

maps of power and velocity based on single line beads are not adequate. In-situ IR video will be useful during development then move to near infrared imaging for qualification.

REFERENCES

[1] C. Körner, Additive manufacturing of metallic components by selective electron beam melting — a review, Int. Mater. Rev. 6608 (2016) 1–17. doi:10.1080/09506608.2016.1176289.

[2] J.R. Davis, A.S.M.I.H. Committee, ASM Specialty Handbook: Heat-Resistant Materials, in: ASM Spec. Handb. Heat-Resistant Mater., 1997: p. 36.

[3] C.T. Sims, N.S. Stoloff, W.C. Hagel, Superalloys II, in: Superalloys II, 1987. doi:10.1080/10426919208947432.

[4] R.C. Reed, The Superalloys, Cabridge, 2007. doi:10.1016/S1369-7021(07)70022-6.

[5] M.M. Kirka, Y. Lee, D.A. Greeley, A. Okello, M.J. Goin, M.T. Pearce, R.R. Dehoff, Strategy for Texture Management in Metals Additive Manufacturing, Jom. 69 (2017) 948. doi:10.1007/s11837-017-2297-7.

[6] S.C. Flood, J.D. Hunt, Columnar and equiaxed growth, J. Cryst. Growth. 82 (1987) 552–560. doi:10.1016/0022-0248(87)90347-2.

[7] J. Hunt, Chapter 10 Pattern formation during solidification, (2014).

[8] C. Bezençon, M. Gäumann, Single-Crystal Laser Deposition of Superalloys : Processing – Microstructure Maps, Acta Mater. 49 (2001) 1051–1062.

[9] J.D. Hunt, Steady state columnar and equiaxed growth of dendrites and eutectic, Mater. Sci. Eng. 65 (1984) 75–83. doi:10.1016/0025-5416(84)90201-5.

[10] W. Kurz, B. Giovanola, R. Trivedi, Theory of microstructural development during rapid solidification, Acta Metall. 34 (1986) 823–830. doi:10.1016/0001-6160(86)90056-8.

[11] S.S. Babu, J.W. Elmer, J.M. Vitek, S. a. David, Time-resolved X-ray diffraction investigation of primary weld solidification in Fe-C-Al-Mn steel welds, Acta Mater. 50 (2002) 4763–4781. doi:10.1016/S1359-6454(02)00317-8.

[12] J.D. Hunt, P. Road, Steady State Columnar and Equiaxed Growth of Dendrites and Eutectic, Mater. Sci. Eng. 65 (1984) 75–83. doi:10.1016/0025-5416(84)90201-5.

[13] C. Körner, H. Helmer, A. Bauereiß, R.F. Singer, Tailoring the grain structure of IN718 during selective electron beam melting, MATEC Web Conf. 14 (2014) 8001. doi:10.1051/matecconf/20141408001.

[14] H.E. Helmer, C. Körner, R.F. Singer, Additive manufacturing of nickel-based superalloy Inconel 718 by selective electron beam melting: Processing window and microstructure, J. Mater. Res. 29 (2014) 1987–1996. doi:10.1557/jmr.2014.192.

[15] a. Bauereiß, T. Scharowsky, C. Körner, Defect generation and propagation mechanism during additive manufacturing by selective beam melting, J. Mater. Process. Technol. 214 (2014) 2497–2504. doi:10.1016/j.jmatprotec.2014.05.002.

[16] A. Rai, H. Helmer, C. Körner, Simulation of grain structure evolution during powder bed based additive manufacturing, Addit. Manuf. (2016). doi:10.1016/j.addma.2016.10.007.

[17] R.R. Dehoff, M.M. Kirka, W.J. Sames, H. Bilheux, a. S. Tremsin, L.E. Lowe, S.S. Babu,

Site specific control of crystallographic grain orientation through electron beam additive manufacturing, Mater. Sci. Technol. 31 (2014) 1743284714Y.000. doi:10.1179/1743284714Y.0000000734.

[18] R.R. Dehoff, M.M. Kirka, F. a. List III, K. a. Unocic, W.J. Sames, Crystallographic texture engineering through novel melt strategies via electron beam melting: Inconel 718, Mater. Sci. Technol. 0 (2014) 1743284714Y.000. doi:10.1179/1743284714Y.0000000697.

[19] N. Raghavan, R. Dehoff, S. Pannala, S. Simunovic, M. Kirka, J. Turner, N. Carlson, S.S. Babu, Numerical modeling of heat-transfer and the influence of process parameters on tailoring the grain morphology of IN718 in electron beam additive manufacturing, Acta Mater. 112 (2016) 303–314. doi:10.1016/j.actamat.2016.03.063.

[20] M.M. Kirka, Y.S. Lee, D.A. Greeley, A. Okello, M.J. Goin, M.T. Pearce, R.R. Dehoff, Strategy for Texture Management in Metals Additive Manufacturing, Jom. In Review (2017) 523–531. doi:10.1007/s11837-017-2264-3.

[21] J. Raplee, A. Plotkowski, M. Kirka, R. Dinwiddie, A. Okello, R.R. Dehoff, S.S. Babu, Thermographic Microstructure Monitoring in Electron Beam Additive Manufacturing, Nat. Sci. Reports. (2017) 1–16. doi:10.1038/srep27398.

[22] D. Dye, O. Hunziker, R.C. Reed, Numerical analysis of the weldability of superalloys, Acta Mater. 49 (2001) 683–697. doi:10.1016/S1359-6454(00)00361-X.

[23] J. Gockel, J. Beuth, Understanding Ti-6Al-4V Microstructure Control in Additive Manufacturing via Process Maps Joy Gockel and Jack Beuth Department of Mechanical Engineering, Carnegie Mellon University, Pittsburgh, PA 15213, Solid Free. Fabr. Proc. (2013) 666–674.

[24] M. Thomas, G.J. Baxter, I. Todd, Normalised model-based processing diagrams for additive layer manufacture of engineering alloys, Acta Mater. 108 (2016) 26–35. doi:10.1016/j.actamat.2016.02.025.

[25] Y. Kok, X. Tan, S.B. Tor, C.K. Chua, Fabrication and microstructural characterisation of additive manufactured Ti-6Al-4V parts by electron beam melting, Virtual Phys. Prototyp. 10 (2015) 13–21. doi:10.1080/17452759.2015.1008643.

[26] Y.H. Kok, X.P. Tan, N.H. Loh, S.B. Tor, C.K. Chua, Geometry dependence of microstructure and microhardness for selective electron beam-melted Ti–6Al–4V parts, Virtual Phys. Prototyp. 2759 (2016) 1–9. doi:10.1080/17452759.2016.1210483.

[27] A.A. Antonysamy, J. Meyer, P.B. Prangnell, Effect of build geometry on the ??-grain structure and texture in additive manufacture of Ti6Al4V by selective electron beam melting, Mater. Charact. 84 (2013) 153–168. doi:10.1016/j.matchar.2013.07.012.

[28] M. Ramsperger, R.F. Singer, C. Körner, Microstructure of the Nickel-Base Superalloy CMSX-4 Fabricated by Selective Electron Beam Melting, Metall. Mater. Trans. A. (2016). doi:10.1007/s11661-015-3300-y.

[29] J.W. Park, J.M. Vitek, S.S. Babu, S.A. David, Stray grain formation, thermomechanical stress and solidification cracking in single crystal nickel base superalloy welds, Sci.

Technol. Weld. Join. 9 (2004) 472–482. doi:Doi 10.1179/136217104225021841.

[30] W.J. Sames, K.A. Unocic, G.W. Helmreich, M.M. Kirka, F. Medina, R.R. Dehoff, S.S. Babu, Feasibility of in situ controlled heat treatment (ISHT) of Inconel 718 during electron beam melting additive manufacturing, Addit. Manuf. 13 (2016) 1–10. doi:10.1016/j.addma.2016.09.001.

[31] M. Ramsperger, L. Mújica Roncery, I. Lopez-Galilea, R.F. Singer, W. Theisen, C. Körner, Solution Heat Treatment of the Single Crystal Nickel-Base Superalloy CMSX-4 Fabricated by Selective Electron Beam Melting, Adv. Eng. Mater. 17 (2015) 1486–1493. doi:10.1002/adem.201500037.

[32] S.S. Babu, J.W. Elmer, J.M. Vitek, S.A. David, Time-resolved X-ray diffraction investigation of primary weld solidification in Fe-C-Al-Mn steel welds, Acta Mater. 50 (2002) 4763–4781. doi:10.1016/S1359-6454(02)00317-8.

[33] M. Haines, Cet Calculator explanation, (2015).

[34] M.A. Division, Welcome to oim analysis 5.3, Analysis. (n.d.).

[35] R.B. Dinwiddie, R.R. Dehoff, P.D. Lloyd, L.E. Lowe, J.B. Ulrich, Thermographic in-situ process monitoring of the electron-beam melting technology used in additive manufacturing, 8705 (2013) 87050K. doi:10.1117/12.2018412.

[36] Z.C. Cordero, R.B. Dinwiddie, D. Immel, R.R. Dehoff, Nucleation and growth of chimney pores during electron-beam additive manufacturing, J. Mater. Sci. 52 (2017) 3429–3435. doi:10.1007/s10853-016-0631-z.

[37] A. Plotkowski, M.M. Kirka, S.S. Babu, Verification and validation of a rapid heat transfer calculation methodology for transient melt pool solidification conditions in powder bed metal additive manufacturing, Addit. Manuf. 18 (2017) 256–268. doi:10.1016/j.addma.2017.10.017.

[38] R. Komanduri, Z.B. Hou, Thermal analysis of the arc welding process: Part I. General solutions, Metall. Mater. Trans. B. 31 (2000) 1353–1370. doi:10.1007/s11663-000-0022-2.

[39] H.S. Carslow, J.C. Jaeger, J.E. Morral, Conduction of Heat in Solids, Second Edition, 1986. doi:10.1115/1.3225900.

[40] S.D. DuPont, J. N., Lippold, J. C., Kiser, Welding Metallurgy and Weldability of Nickel-base Alloys, Wiley, 2009.

[41] S.S. Babu, Thermodynamic and kinetic models for describing microstructure evolution during joining of metals and alloys, 2009. doi:10.1179/095066009X12506720908654.

[42] S. a David, S.S. Babu, J.M. Vitek, Welding : Solidication and Microstructure, (2003).

[43] M. Montazeri, F.M. Ghaini, O.A. Ojo, Heat Input and the Liquation Cracking of Laser Welded IN738LC Superalloy, Weld. J. 92 (2013) 258–264.

[44] O.A. Ojo, N.L. Richards, M.C. Chaturvedi, Contribution of constitutional liquation of gamma prime precipitate to weld HAZ cracking of cast Inconel 738 superalloy, Scr.

Mater. 50 (2004) 641–646. doi:10.1016/j.scriptamat.2003.11.025.

[45] M.B. Henderson, D. Arrell, R. Larsson, M. Heobel, G. Marchant, Nickel based superalloy welding practices for industrial gas turbine applications, Sci. Technol. Weld. Join. 9 (2004) 13–21. doi:10.1179/136217104225017099.

[46] J.E. Franklin, W.F. Savage, Stress Relaxation and Strain-Age Cracking in Rene 41 Weldments, Weld. J. 53 (1974) 380s–387s. http://aws.perusion.com/wj/supplement/WJ_1974_09_s380.pdf.

[47] C. Frederick, A. Plotkowski, M. Kirka, M. Haines, A. Staub, E.J. Schwalbach, D.A. Cullen, S.S. Babu, Geometry Induced Spatial Variation of Microstructure Evolution during Selective Electron Beam Melting of Rene-N5, Manuscript Submitted for Publication. (2018).

APPENDICES

A.1 Further detail on Keyence Edge Imaging

For optical images the Keyence VHX-2000 with a Z50L zoom lens was used. The sample is placed on the stage with the build plate oriented transversely (left and right) and the focus set such that the features in the middle of the sample are in focus. If the focus is acquired at the edge of the part, the brightness and contrast settings will not yield a clear image of the center regions. Images are taken at 100x with a user determined area for image stitching. The image stitching is done with the autofocus turned off, this produces clear images in a timely fashion (2-4 minutes). If the sample is not flat, or a lower magnification is used, then a checkerboard will be seen on the image, where the light will reflect into the lens for one side leading to bright images and miss other sides leading to dark images.

One of key features of the Z50L is the ability to adjust the angle of the illumination. Figure 75 (a) and (b) show stitched images with the same focus, white balance, contrast and brightness to demonstrate the difference between planar lighting and an ideal edge lighting. The edge lighting feature tilts the light source such that it glances the sample at a non-perpendicular angle. If the sample has a well-polished and textured surface (e.g. Rene N5 builds), the glancing light will illuminate the surface facing the light source while creating a shadow on the surfaces facing away from it. Having an angle such that the light is not reflected towards the lens allows for better characterization. With these setup, brightness can be reduced such that the surface can be well illuminated and avoid an excessive amount of glare or overexposure. If the edge lighting angle is high then the image, will show three dark spots in a triangular arrangement. This can be ignored for a single image to achieve a highly edge lit image, however, in a stitched image with ~21 individual shots this can produce a polka-dot or checker-board effect.

Figure 75 (c) shows the effect of image processing to improve the visibility of the grain structure. In this image the brightness was reduced by 15% and the contrast increased by 65%. The image will turn yellow with Keyence's default white balance settings and therefore, the saturation is reduced to 0% to produce a greyscale image. When the microscope's brightness is set to a low level with minimal glare, image will exaggerate and reveal any contours on the surface. Sharpness may be increased; however, this will produce noise in the image that appears like static in monochromatic areas. If the contrast is too high on a grayscale images, then the gradient between light and shadow will be too steep and cause the contours to appear as seen in Figure 75 (d).

Some deficiencies in image processing are unavoidable at this point but are barely noticeable when the image is expanded or zoomed in. When Figure 75 (d) is compressed or zoomed out (thumbnail) it can be easily seen that there is a checkerboard of bright spots. Along the bottom edge below the build plate interface there is a series of triangular dark spots. The features and texture of the build masked this effect but since the build plate was flat and smooth this effect is clear.

Drawbacks of optical imaging and analyses limit our efforts to quantify grain size or porosity. The shadows lead to issues in thresholding in image processing software (such as the one in ImageJ) to produce binary images.

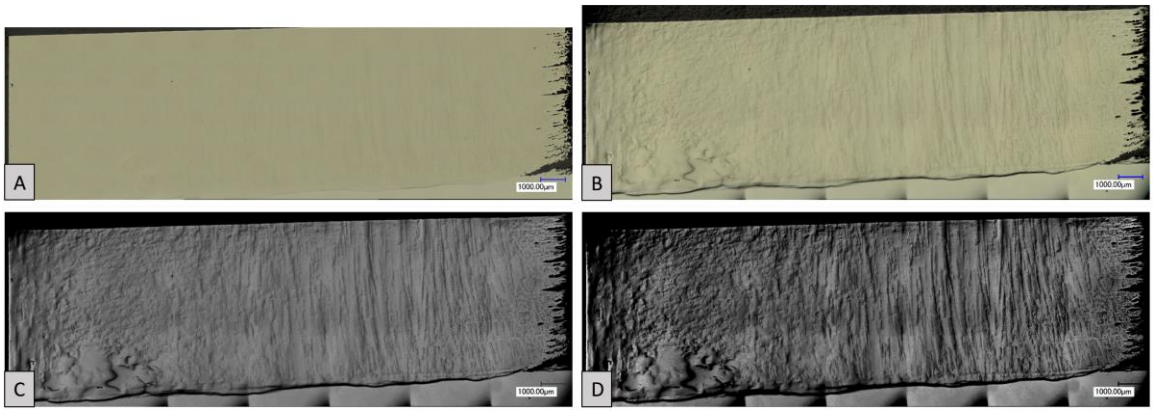

Figure 75. Comparison of OM stitching and post processing of Keyence Images.

As a result, the software will recognize some surfaces but not the entire surface of individual grains. Edge lighting will exaggerate the size of pores unlike planar lighting that would illuminate straight into the pore while the edge light will cause the pore to cast a shadow up to 2-3 times its own area. Therefore, the precision of grain boundary analyses by optical microscopy, is many orders of magnitude lower than that of electron backscattered diffraction (EBSD) imaging.

A.2 Further Detail on Using Arcam Loop 3

If the part has been built in the Arcam using EBM Controller version 3 or 4, then begin with the logfile containing all the process parameters. From AL3/A/1/1-Parser.py (written originally by Edwin Schwalbach) can be used to extract specified lines from either the zipped log folder or the *.plg file. In its current version, 1-Parser.py will parse every file in the AL3/A/2-Log_Files folder and output *.hdf5 files in AL3/A/2/Z-hdf5_Files.

The *.hdf5 files can be quickly analyzed using AL3/A/3/1-build_analysis.py to generate an array of plots and text files that summarize the build placed in ./A-BuildAnalysisFolder/. Alternatively, multiple log files can be compared using AL3/A/4/1-LogFile_Comparitor.py or AL3/A/5/ 1-Log_File_to_csv.py. These side loops are illustrated in Figure 76 and are optional for the main AL3 but inspired the code used. The rest of the AL3 is illustrated in below and explained in text below.

The important python file in this branch is AL3/A/6/AAA-Log_to_ParameterInput.py which takes the original logfile.plg from AL3/A/2-Log_Files/ and outputs to AL3/A/2/A/logfile/ two files: (1) ParameterInput.txt and (2) AdditionalFile.txt. The first contains the process parameters responsible for controlling the beam during the melting step of the Arcam and a few ranges for plotting in the next step in a specified order, naming, and included line returns. The second gives useful build information that is left off the ParameterInput.txt file, primarily the hatch spacing for each melt theme. An example output from using the logfile produced by the first Inconel 718 build is given in Figure 78.

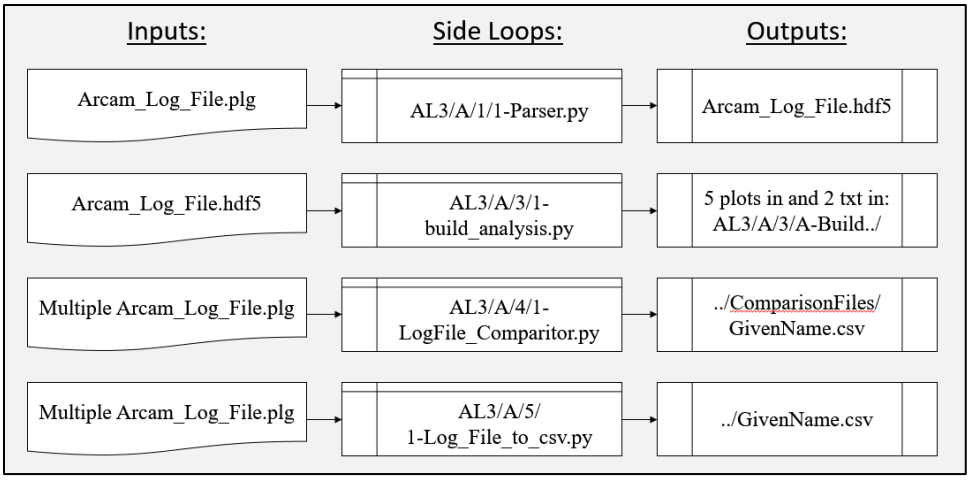

Figure 76. Arcam Loop Side Loops for Analysis and Comparison.

Once the process parameters are extracted or entered in the format that matches the ParameterInput.txt file, the executable jar program named "Profiler_w_TXT_Integer.jar" [unpublished] is used to estimate the beam path and combination of current & speed for each layer. The latest version of the program can be found at AL3/B/Profiler_w_TXT_Integer.jar and upon running it will open a graphical user interface.

Before running the program, additional *.png files are required that must be generated using the Arcam Build Assembler program (requiring an Arcam key because it is proprietary software). During this step, load each part.stl file (for standard raster) or the part.clf file (for spot melt) and then select the Tools/GenerateLayerImages option. This will bring up box asking for pixels per mm. The number given sets the hatch spacing and upon entering it, layers will be generated in the chosen folder. Once four layer images of interest have been created, stop the layer generation. Then rename the files in the following format "A1SolidT35mm 8px_(1).png" because this name will be carried forward and cut from (A1 is the Alloy and Build Number, SolidT35mm describes the part, 8 px is the pixel density, and "_(1)" is the first layer). Finally, save the remaining 3 images as the same with the layer number iterated upon.

Now place the four image_layer_(#).png files into the same folder as the ParameterInput.txt file and give the folder a useful name (in this case "1-A1-35mmTri-H125-S12"), and place that folder in AL3/B/1-ArcamAFRLBuilds/. Now run Profiler_w_TXT_Integer.jar and browse for AL3/B/1/1-A1-35mmTri-H125-S12 and select the first layer slice image "A1-SolidT35mm8px_(1).png" in the first tab. The rest of the parameters could be set by clicking the check boxes or typing in values under each tab, but it is best to use the ParameterInput.txt file for keeping track of which options were selected. Next, select the "Other Setup" tab and click "Generate Text Files?", and on the "Finish" tab check "Run a stack of images?" and "Use Text File Input for parameters?". Output will placed be in the same folder as the image selected and include: a *.hdf5 for each run (a run is a set of parameters), and 3 folders (Current, Energy, Speed) filled with scaled color maps and corresponding scale bars as seen in Figure 79.

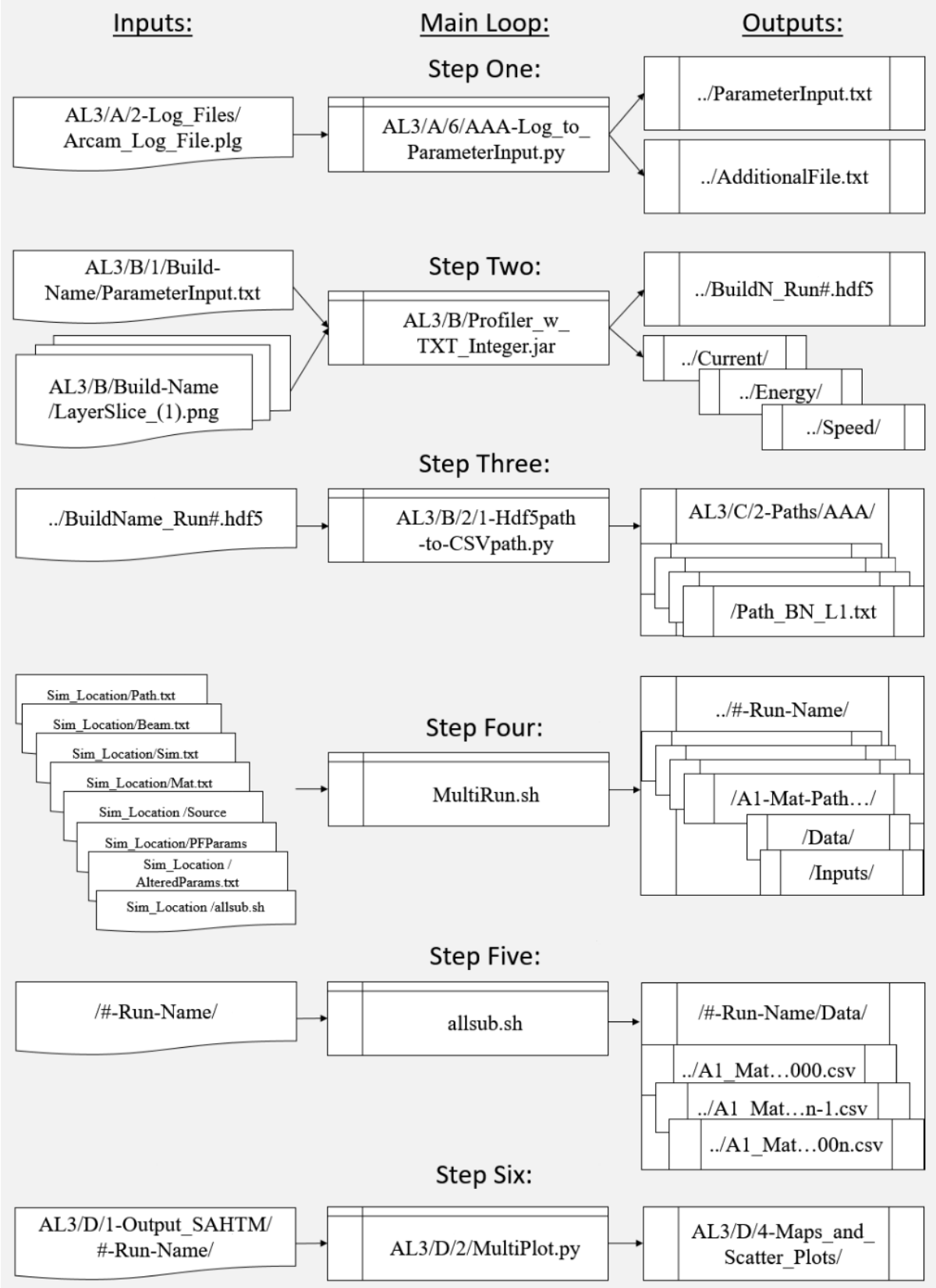

Figure 77. Main AL3 described in a flow chart.

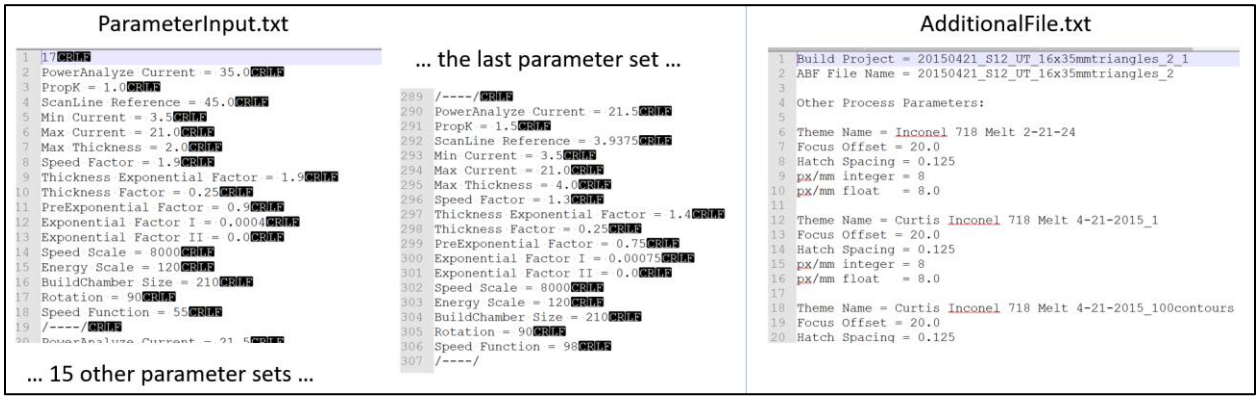

Figure 78. Example ParameterInput.txt file and Additional File.txt.

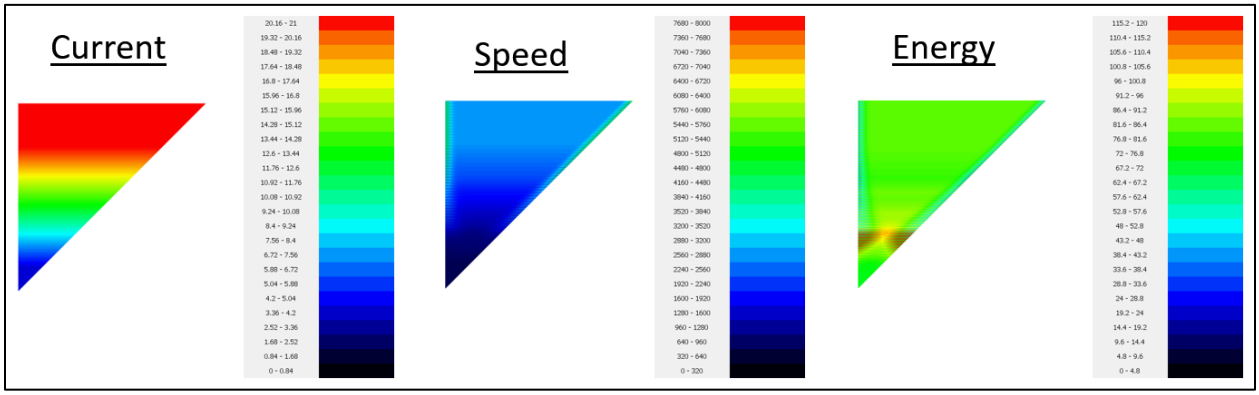

Figure 79. Visualized Output from Profiler.

Each pixel of the image indicates the current (bound by the process parameter and min/max values) or speed with speed function visible on every other layer of an edge and the calculated energy based on current and speed. The *.hdf5 file contains the values stored as X & Y coordinates, current, and speed columns for each layer (4 images = 4 layers), each rotated 90 degrees.

Next the *.hdf5 files are converted to Path_files_L#.csv/txt files representing each layer with L# and keeping the original name from the *.hdf5 file. This is done using AL3/B/2/1-Hdf5path-to-CSVpath.py which can be set to run every *.hdf5 file in every subfolder of AL3/B/1/ and places them all together in AL3/C/2-Paths/AAA.

Now, it is time to set up additional files and the folder trees for the SAHTM which can be run locally or sent to a server. AL3/C/1-PtFileMaker has become outdated and Ptfiles are no longer used by the SAHTM. AL3/C/3-Inputs/ contains subfolders for input files that fall into the categories Beam/, Mat/, or Sim/. Beam files set the beam radius, efficiency, and penetration depth. Mat files contain the material constants obtained by averaging values from JmatPro. Sim files control the simulation settings such as number of cores used and time steps. In the current version, the Sim file also takes over the role of defining the coordinate grid, which the Ptfile did in the past. AL3/C/4-MultirunFolder/ contains various versions of bash scripts for organizing the Input files (Path, Beam, Mat, and Sim) for each running on Newton or ACF. The SAHTM code is written in C++ and the latest version of the code is stored in AL3/C/6-SAHTM-Source/. It first takes in ParameterInput.txt which contains the location of the Input Files and outputs into the Data/ folder located with the compiled source code.

A.3 Detailed Build Summaries by Build Set

A copy of the build summary table from 4.1.1 is given as Table 5 to organize the following subsections which are broken by build Set #. Each subsection contains a summary of the build layout and process plans for each part. When available, the log file was used to create a Build Anomaly Plot showing common defects and the temperature during the build. In addition, the top surface of the builds or picture taken while the build is still in the Arcam are given.

A.3.1 Build Set # 1: Inconel 718 First Build, A1.

The first build consisted of 16 triangular right prisms built using a raster fill (1-15) and the 16th triangular prism using contour fill only seen in Figure 80 (a). When the build was designed each triangle was set to have a range of currents used starting with low currents at part 1 and high currents at part 15. However, the naming of a variable was incorrectly passed down. In the profiler, it was named Power Analyze but in the Arcam EBM Controller V3 settings this is under a different folder and set as a range with Maximum, Minimum. In addition, the settings passed on were for Titanium and the speed function was too large (SF = 98) leading to a low energy density and lack of fusion. The color coding of the triangles groups the build by similarity of processing conditions which match the degree of porosity/surface roughness observed. Figure 80 (b) is an image of the top surface of all parts showing varying degrees of lack of fusion and

balling. Figure 80 (c) was taken after wire EDM was used to remove the top of each part from the baseplate. The outcome of this build was a set of parts with the lowest allowable energy input in the center of parts 7 and 8.

Table 5. Copy of Completed Build Summary from Results Section

Set #	Alloy	Prefix	System	Build Pass	Geometry	# of Parts	Dates
1	IN 718	A	S12-Full	1/1	Triangular	16/16	4/21/2015
2	IN 718	A	S12-Full	1/1	Tri & Cubes	13/22	8/31/2015
3	IN 718	A-	S12-MV	0/4	Triangular	0/8	9/25-29/15
3	IN 718	A	S12-MV	1/1	40 mm Cube	1/1	9/30/2015
4	LSHR	T	A2-MV	0/5	Tri-40-SC	0/10	3/18-23/16
5	ReneN5	B	A2-MV	2/2	Tri-40-SC	4/4	3/29-30/16
6	Haste-X	H	A2-MV	2/5	Tri-40-SC	4/10	4/1-8/16/16
7	IN 718	C	A2-MV	3/5	Cubes & Tri	24/42	12/27-1/02/17
8	Ni-6-6-6	F	S12-MV	4/5	Cubes & Tri	16/20	1/13-19/17
9	Ni-10-6	E	S12-MV	4/5	Tri-28-SC	14/20	9/26-10/2/17
10	Ni-6-6-6	F	S12-MV	1/1	Tri-28-SC	4/4	10/4/2017

The flow of the build is best seen in the Build Anomaly Plot, Figure 81, which shows the build starting at 1000 ºC after being held for a time. The temperature drops nearly 200 degrees in the first layers and must be stopped multiple times and forced to preheat back to 1000 ºC. After a few stop/starts the build was allowed to continue near 875 ºC. Looking back at this build the preheat current or the number of preheat repetitions should have been increased to bring the temperature back up to 1000 ºC. These changes could have removed the lack of fusion defects that were experienced. The energy density equation used to describe good processing conditions leaves out the preheat temperature which plays a large role in this build. Also in Figure 81, take note of the occasional Arc Trip warning and Zero pulse messages. These are common indicators that the build is not going smoothly. In this case, the lack of fusion defects and low process temperature are the most likely the cause.

The following diagram, Figure 82, gives a quick overview of the way that each part was processed (current and speed function) with the resulting porosity. Porosity was calculated from Figure 80 and normalized to the most porous part, Part 1. The main take away from this is the reduction in Speed Function lead to higher energy density process parameters and less porosity over all.

Figure 83 plots the current for 1 layer of the build excluding the rakes and attempts to pick out each park. The figure attempts to identify which peak corresponds to which part but because the incorrect process parameters were changed in the software it is difficult to tell which is the part melting and which is the contour. In this build a preheat current near 40 mA was used but over sintering did not occur due to the overall lower temperature of the build.

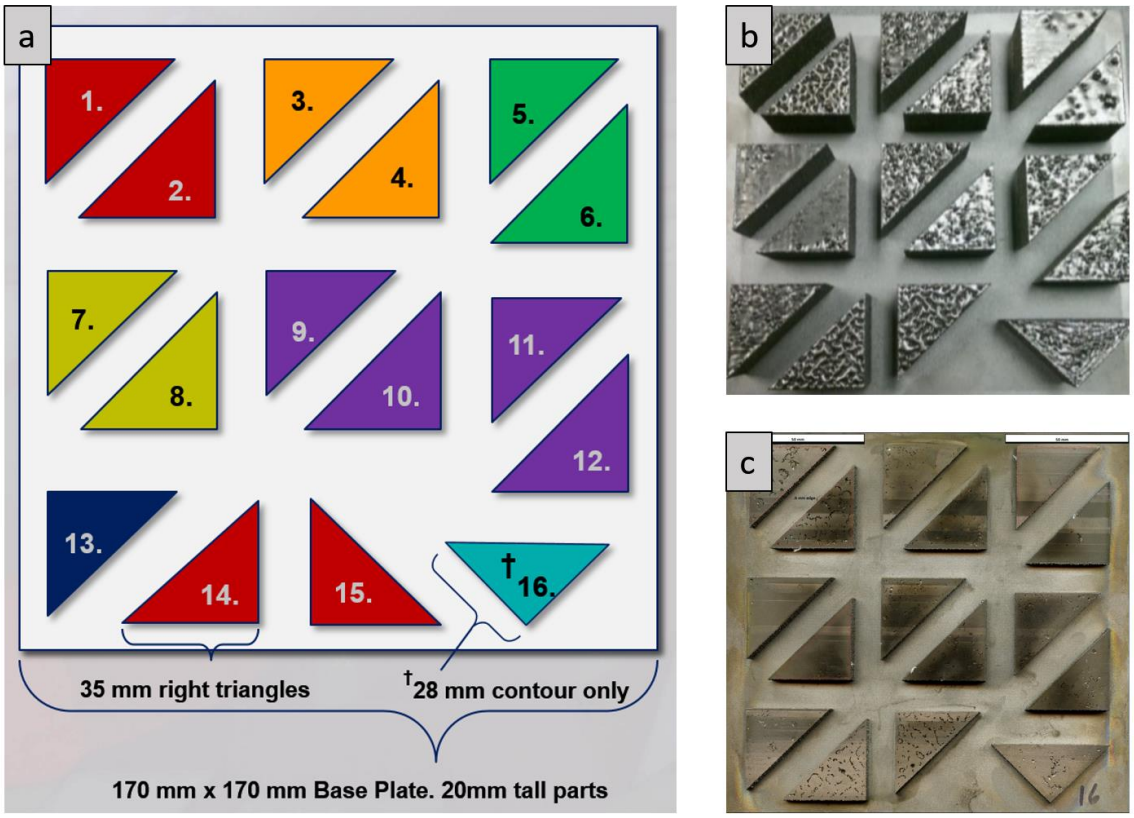

Figure 80. (a) Build A1 Layout (b) Image of top surface (c) After wire EDM removed top.

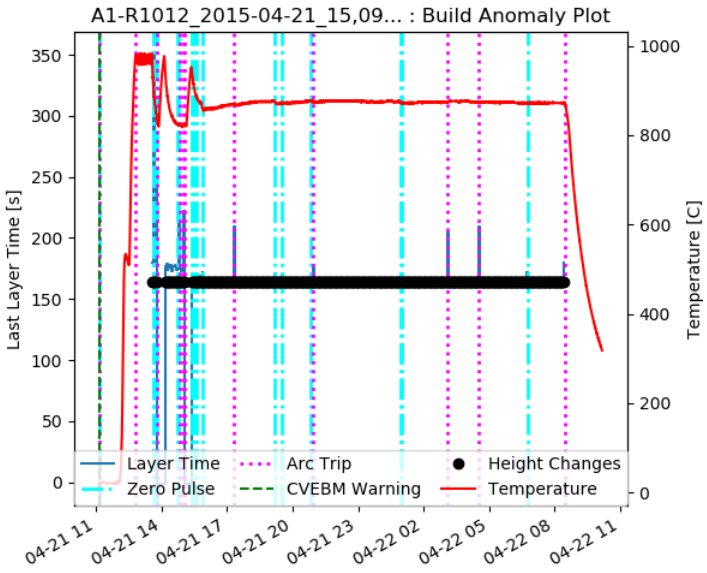

Figure 81. Build Anomaly Plot for build set # 1, A1.

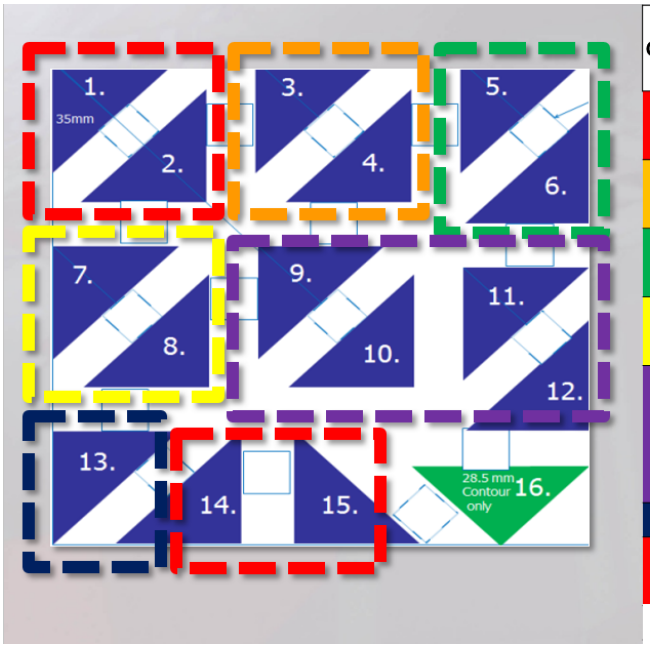

Grouping	Part #	Normalized Average Porosity	Average Current [mA]	Speed Function
A	1	*100%	15	98
A	2	79%	15	98
B	3	30%	4.5	98
B	4	43%	4.5	98
C	5	**4%**	15	**70**
C	6	**7%**	15	**70**
D	7	37%	4.5	**70**
D	8	NA	4.5	**70**
E	9	42%	4.5	98
E	10	34%	4.5	98
E	11	38%	4.5	98
E	12	23%	4.5	98
F	13	30%	4.5	98
A	14	85%	15	98
A	15	87%	15	98

*Maximum porosity was 10.8% area fraction

Figure 82. Grouping of process parameters and resulting normalized porosity.

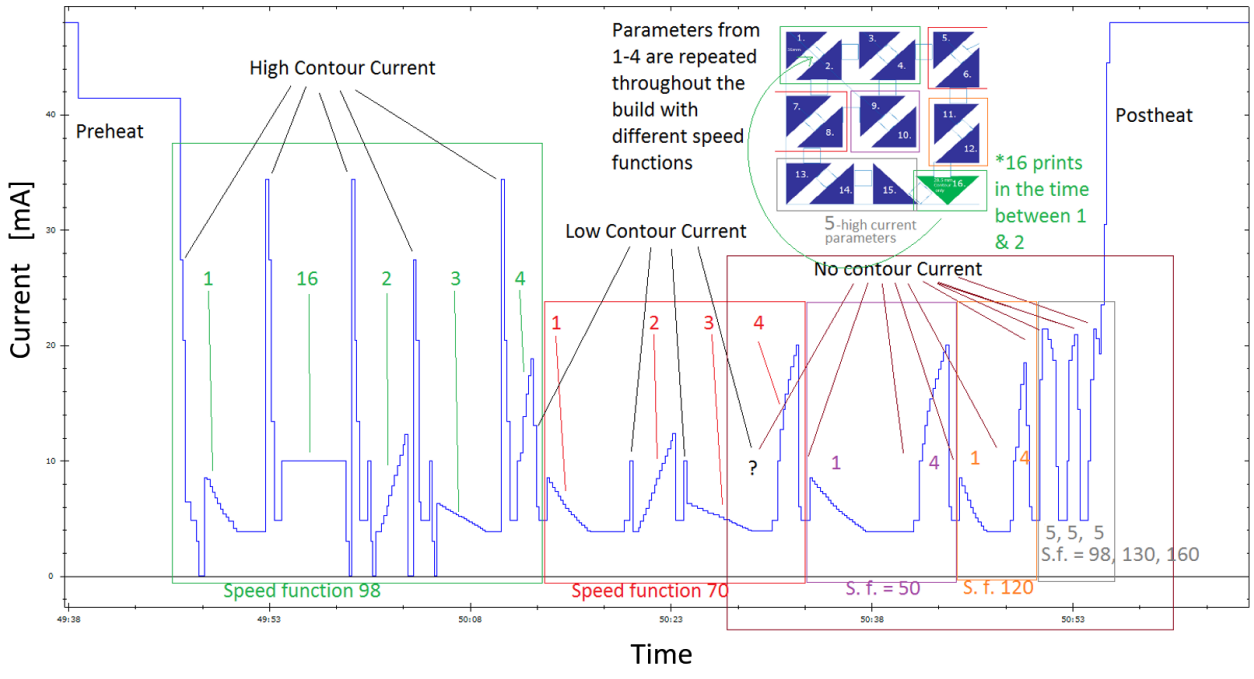

Figure 83. Current vs Time Plot for a single layer of build A1.

Only parts 7 and 8 were heavily characterized due to the large amount of porosity in the other parts. After all the parts were cut off the plate by Wire EDM, as seen in Figure 80 (c), parts 7 and 8 were cut diagonally and mounted to characterize the growth direction. Figure 84 shows that primarily columnar grains were observed in both parts with a high aspect ratio. The interesting feature of these images is that whenever a defect occurs, the following layers take a little while to reset the grain structure before column grains take over again. This phenomenon is present in all builds of this project that contained columnar grain structures.

The resetting in microstructure at a defect is very similar to the initial transition from base plate to columnar grain structure. The initial grain structure of part 7 can be seen in Figure 85 where the original grains form epitaxially from the base plate. Competition takes place in the following layers and the grains best oriented with the build direction begin to win out. If a pole figure is made of the higher section, it is common to find the Z direction have a strong probability while the X and Y direction are random.

In addition, the corner of part 7 was characterized to reveal some deviation from the primarily columnar structure observed. Figure 86 shows three cross sections of the corner that were performed. This indicates that the geometry can influence the resulting grain structure in multiple ways. When an edge is near, it introduces new random orientations from which epitaxial growth can occur from. The grains in Figure 86 also have a gray scaling for the aspect ratio of the grains. Highly columnar grains are dark while circular grains are full color. This make it possible to easily identify the region of randomly oriented grains on the left side of the 5 mm cross section shown.

A.3.2 Build Set # 2: Inconel 718 Second Build, A2.

The second build with Inconel 718 (Build A2) used the full Arcam S12 build chamber. The process parameters were changed and the base Energy Density was increased. The geometries build included an array of triangular right prisms, cubes, and rectangles. The build was set up to have 3 processing conditions applied to each part at various heights as seen in Figure 87 (a) as three different colors. The first 8 mm would be a raster fill for all parts as dictated by the scheme laid out in Figure 87 (c) which used ramped as a function of line length in the triangle and constant current variations.

Due to a rotation on each layer of 90 degrees the average current could be thought of as moving from high to low across the diagonal as seen in Figure 87 (d) for part 1, 3, 4, and 6. The next set of layers, would use a spot melt (Dehoff Fill) before the final set of layers would switch back to the original parameters.

Triangular part # 7 was the exception to this rule. As the rest of the parts switched to spot melt, part 7, which used the same parameters as part # 7 on build A1, continued to use raster melting. The build failed in the middle of the spot melt region (12.05 mm) after an Arc Trip that terminated the build. Figure 87 (b) shows a sketch of characterization plans that would allow for characterization of the raster region and spot melt region in one sample.

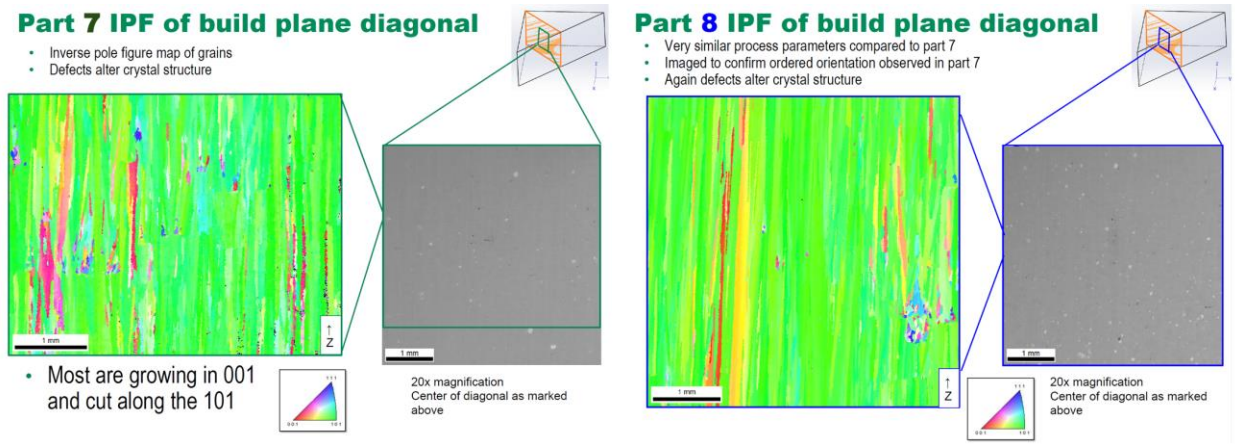

Figure 84. EBSD of the center of the diagonal of parts 7 and 8.

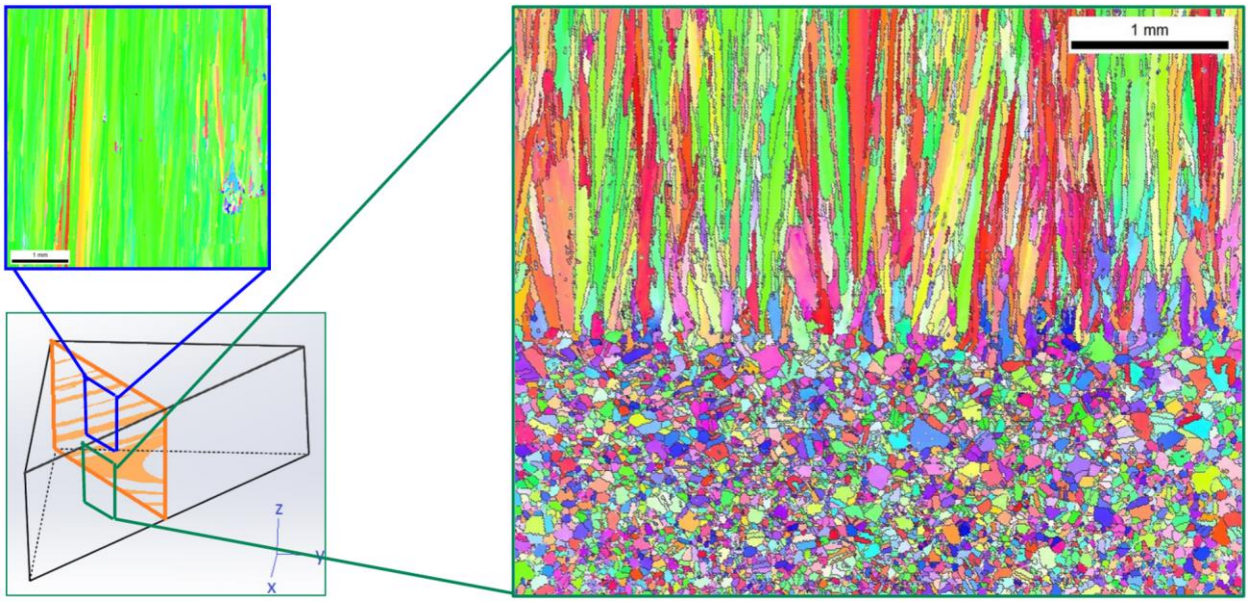

Figure 85. Transition from baseplate to bottom of part 7, of Build A1.

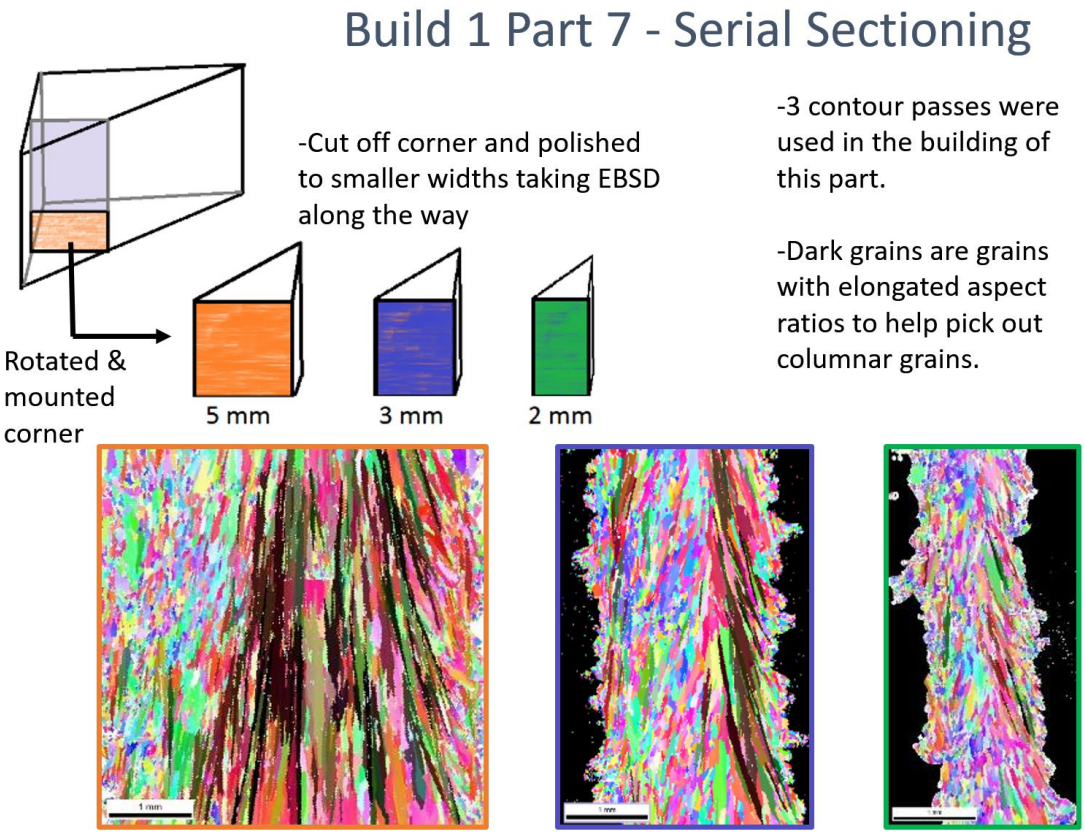

Figure 86. EBSD serial section of part 7 corner, of build A1, and gray scale for aspect ratio.

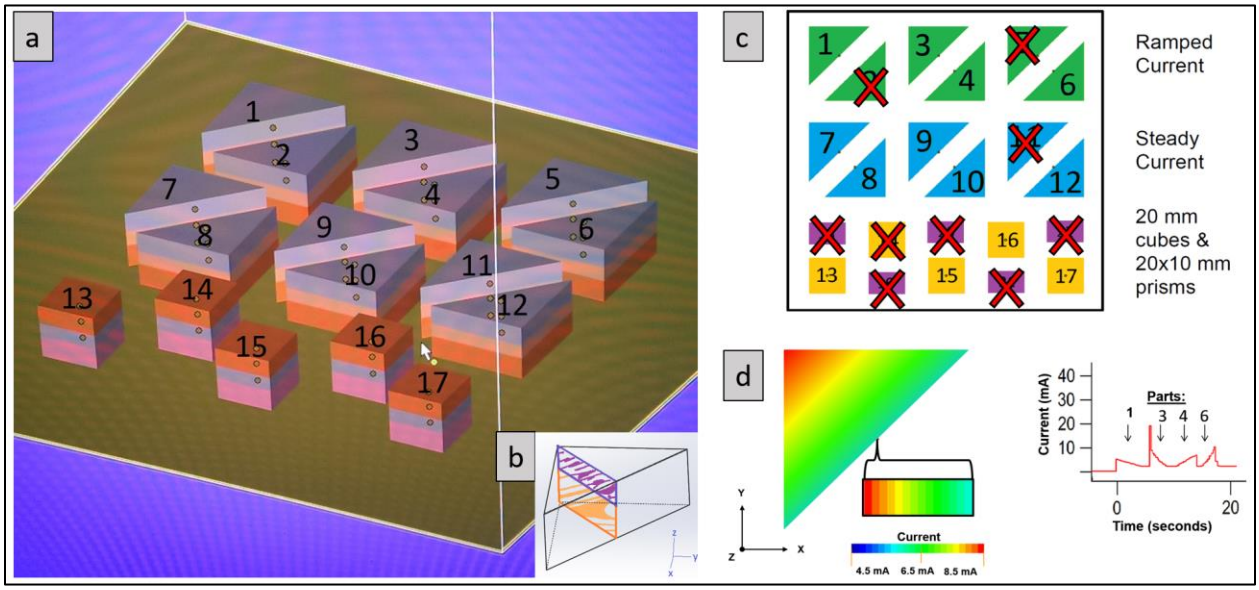

Figure 87. Build Layout and Processing Description.

Build A2 was initially processing at a low temperature due to the long layer times, inadequate preheat current and preheat time settings. There is a clear difference in wall on the side of the parts which is visible in Figure 88 which includes a zoom in on part 7 in (a) and (b) from a different angle. The cubes also see this transition which is visible in Figure 88 (c). Figure 88 (d) is from a desktop photo scanner giving a clear view of the top surfaces of continued and canceled parts. The spot melted top surfaces are much rougher than the raster fill leading to a higher likely hood of lack of fusion defects.

Similar to A1, build A2 got off to a bad start that required a few restarts of the process early on before the base temperature began to steady out in the middle of the build at around 910 ºC. During the steady temperature there were no Arc Trips or Zero pulses which indicates a smooth build. Then note the jump in temperature at around 2 AM where the process changed drastically and the base temperature stabilized at 1000 ºC. This is the point where the second set of process parameters kicked in and spot melt began occurring on all parts except for part 7. Then an arc trip occurred that the Arcam did not recover from and the build ended near 4 AM.

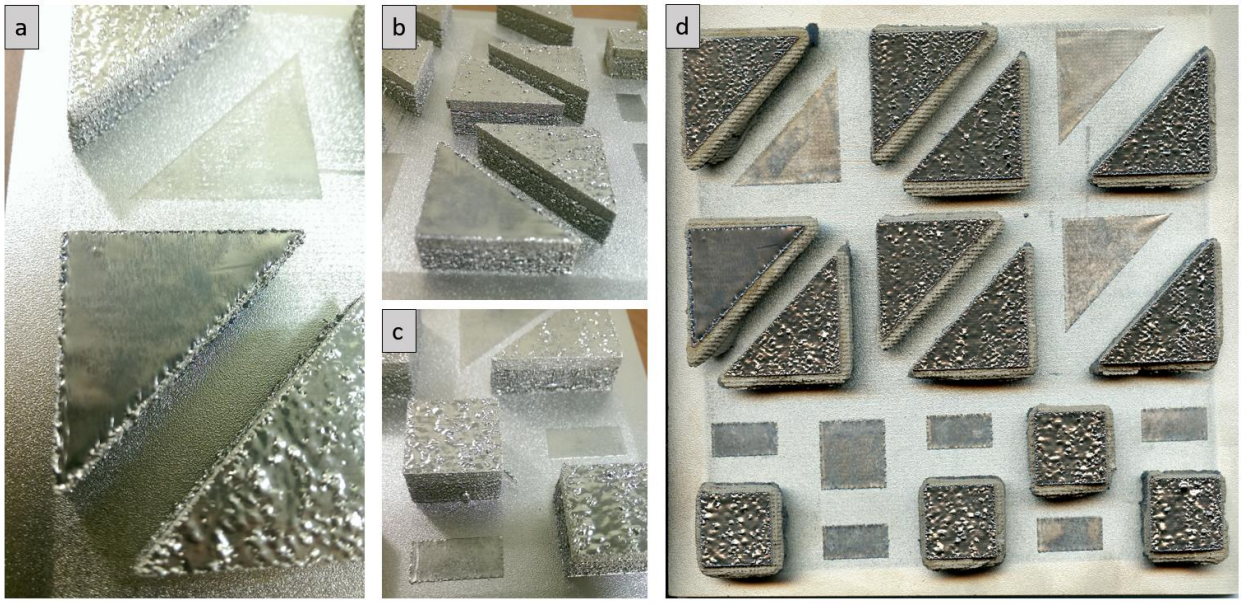

Figure 88. Additional images from various angles to observe the difference in height.

The current used during 2 different layers is given in Figure 90; (a) shows the current vs time for the first layer which contained all the planned parts and contours. This makes it easy to distinguish between which part is being melted when. Figure 90 (b) is from the 4rth layer of the build when some parts have been canceled and the contours were removed from all the parts. These changes were made to shorten the layer time and save the build.

Characterization of build 2 was primarily carried out for part 1 and part 7. Part 1 was chosen because the parameters produced a dense during the raster section and it switched to a spot melt

on the top surface. Part 7 is an interesting part because it repeats the process parameters used in build A1 and does not switch to spot melting after 8 mm. Figure 91 give a quick comparison of the diagonal cross sections samples from build A2 and A1. Figure 91 (a) shows how part 7 is initially full of chimney porosity. However, near the top of the part, the porosity disappears. Two things change to make this happen. (1) Part 7 becomes the first part to melt after the preheat is applied (2) the temperature of the build increases because more energy is being input into the melting steps. These changes in the process can be seen in Figure 92. Figure 91 (b) is given as comparison to (a) and as a lesson in repetition of experiments. Even though the process parameters were supposed to be the same, the outcome and level of porosity is quite different. Figure 91 (c) shows the cross section of part 1 where the center of the part is porosity free for the first 8 mm before becoming full of porosity during the spot melt region. Part 13 is given in (d) and contains about the same level of porosity as (a) in the first 8 mm but then transitions to spot melt and contains the same level of porosity as (c). Keyence images are available in the characterization folder.

EBSD was performed in the center of part 1 of build A2 and stitched together to reveal the grain structure from the base plate until the top of the part, Figure 93. In this sample the transition is immediate once the process parameters change. The process parameters used on the top portion of the build are the same as those used on a cube geometry which gives equiaxed grain structure. In this build, the transition is not perfect as the spot melt region is full of layer defects, a rough top surface. The broken grains (and lack of columnar grains) in this section could be caused by defects rather than by a Columnar to Equiaxed transition. Competition of growth and introduction of random thermal gradients could be the cause of low aspect ratio grains.

In addition to stitching from bottom to top of the image, a large EBSD map was made of the grain structure in the spot mode region and near the interface of the raster and spot. Figure 94 shows the interface of the raster and spot. It also shows how the grain width does not change drastically as a function of the process parameters that were used on part 1. The current and velocity may have changed but they did not have a significant impact on the shape of the melt.

A.3.3 Build Set # 3: Inconel 718 Using MiniVat, A3.

When moving to the MiniVat the triangular right prism part geometry used in A2 was transferred to the smaller base plates fitting only 2 parts of that size in the center of the circular plate seen in Figure 95 (a) and (c). Figure 95 (b) zooms in on the top surface of a failed attempt during build Set # 3 (A-) showing an un even surface and a lack of powder surrounding the base plate due to inadequate preheating and sintering. The largest problem during these initial MiniVat builds was controlling the settings for the preheat. Figure 95 (d) shows the first build to make it ~3 mm before the build was stopped. In this case the powder surrounding the part was over-sintered and could not be removed with the PRS system. During this time, control of the preheat settings was improved. The Build Anomaly Plot for build A3 is given in Figure 96 showing the initial temperature beginning at 1000 ºC similar to build A1 and A2. However, in this case the temperature rapidly increases once the build begins before falling after an Arc Trip. Changes in preheat current are made with more restarts and the temperature reaches a maximum above 1200 ºC during this build.

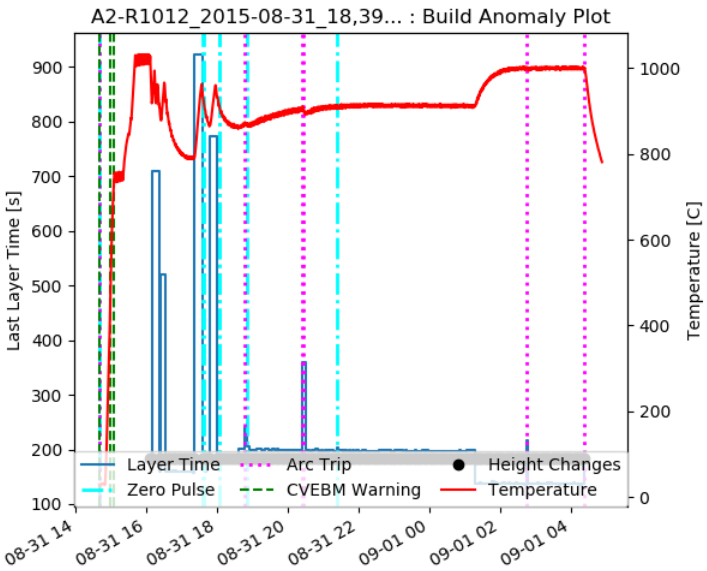

Figure 89. Build Anomaly Plot for build set # 2, A2.

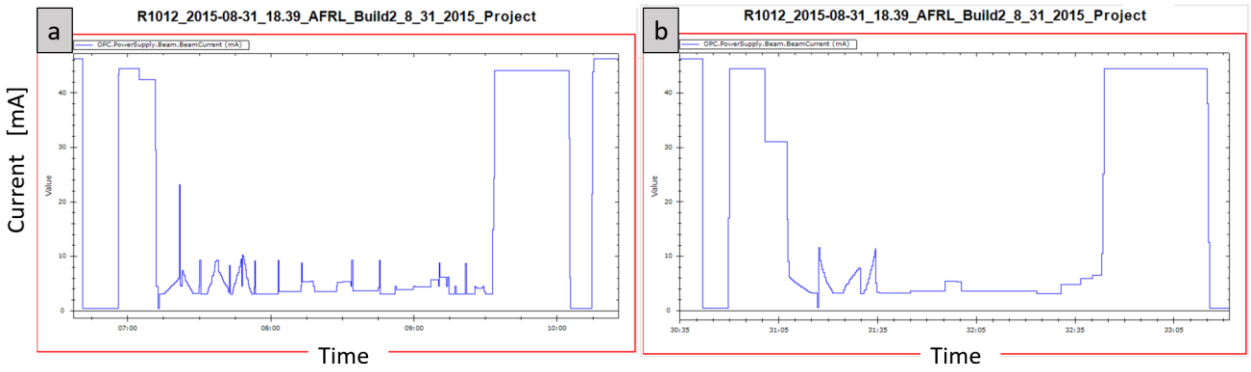

Figure 90. Current vs time for Layer 1 and Layer 4 of build A1.

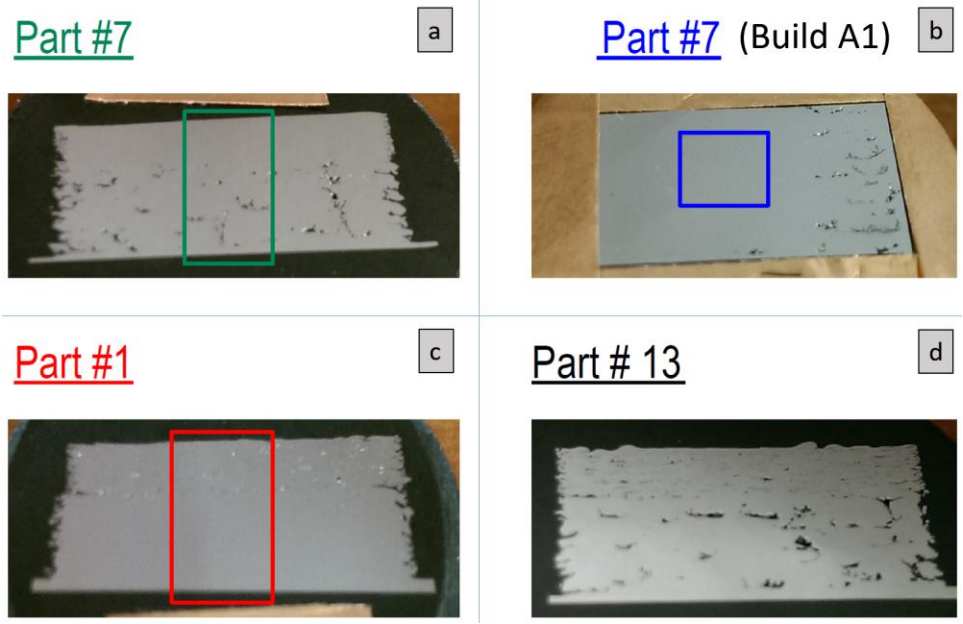

Figure 91. Mounted diagonal cross section of select parts from build A2 and A1.

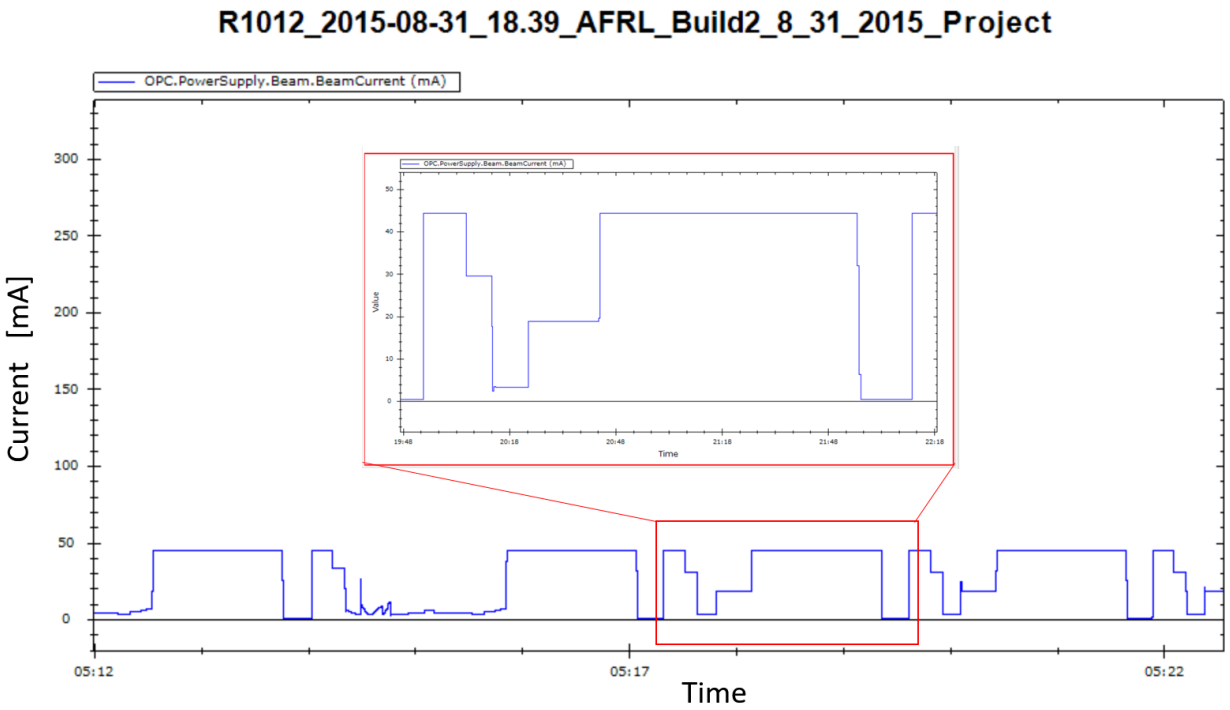

Figure 92. Current vs Time for second region of A2 where spot melt is used.

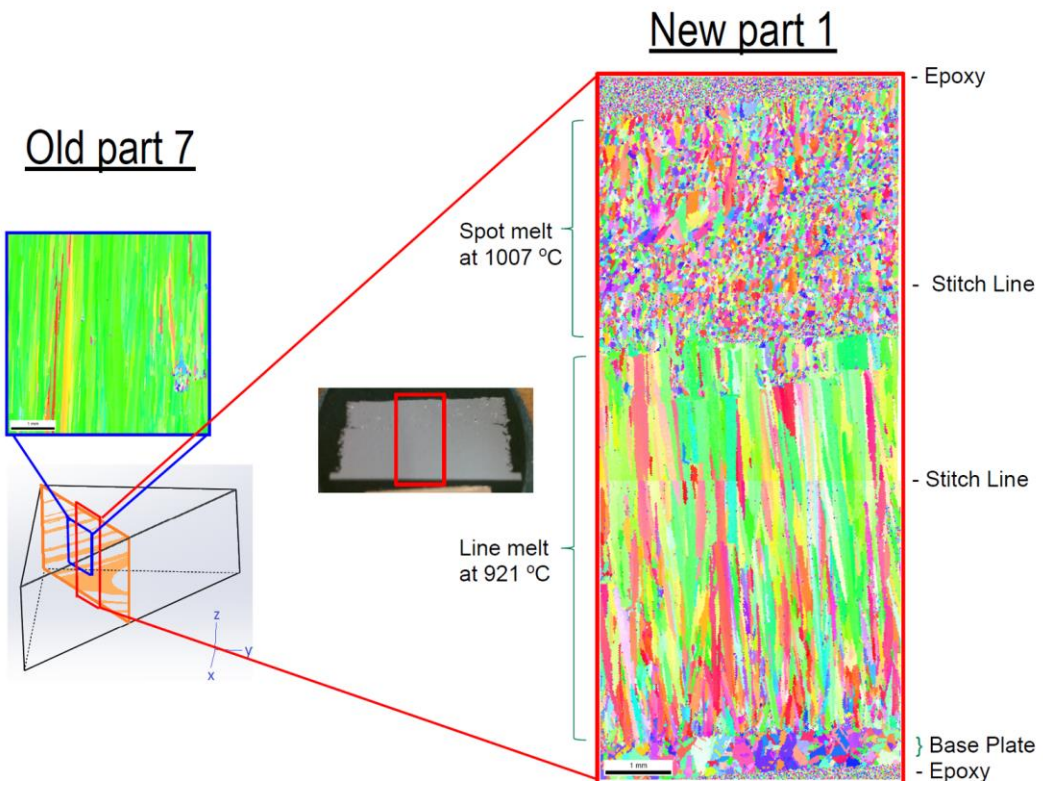

Figure 93. EBSD comparison of part 1 from A2 and part 7 from A1.

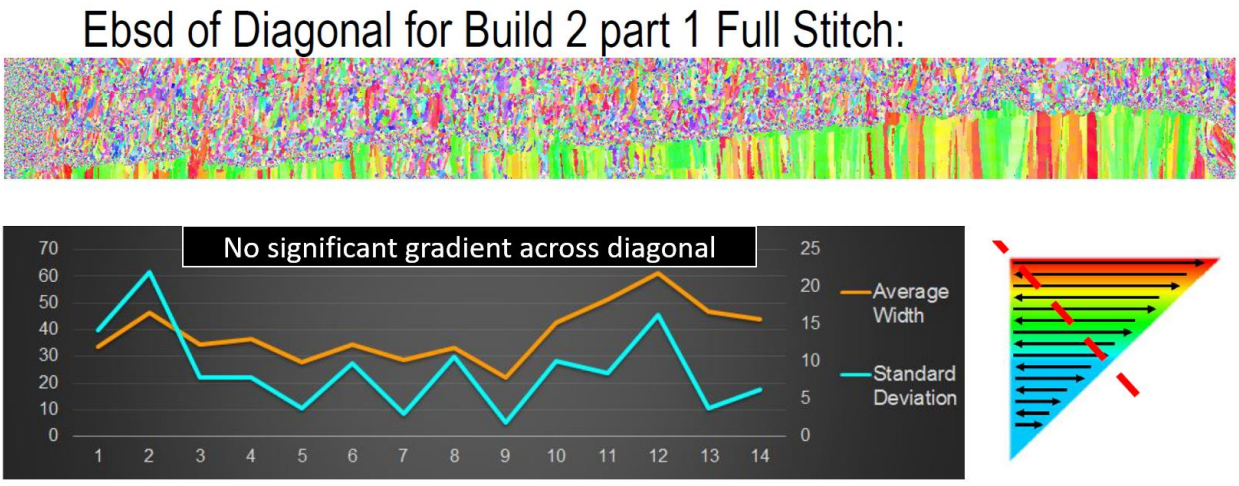

Figure 94. Large EBSD map of spot mode region and top of raster region for part 1.

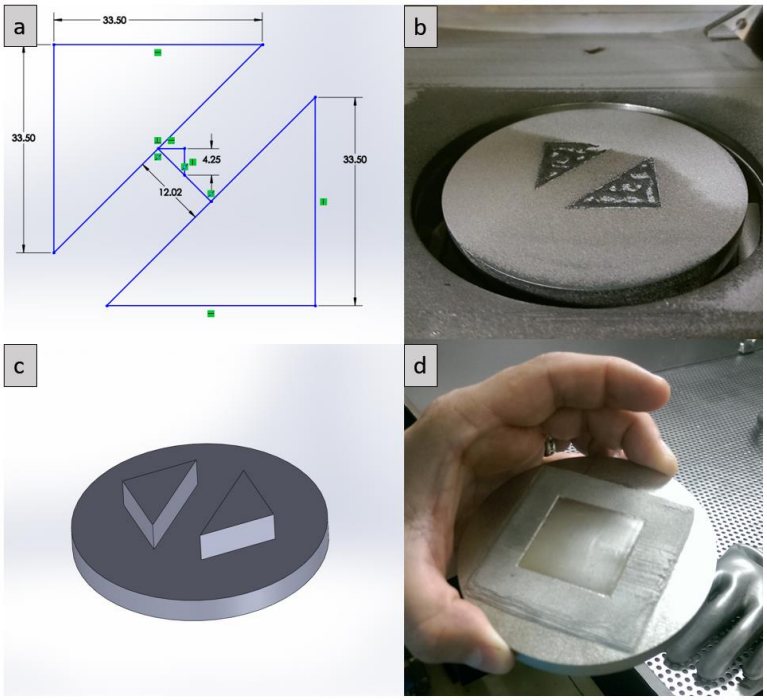

Figure 95. Images of Geometry attempted in A- and A3 final part.

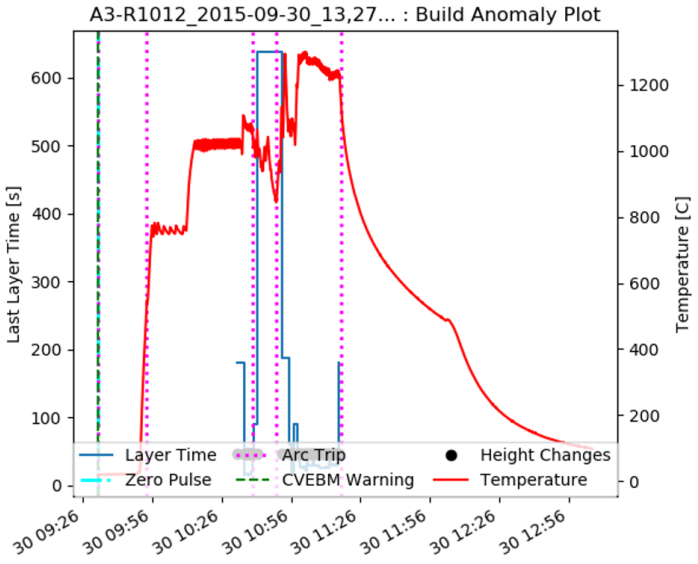

Figure 96. Build Anomaly Plot for build set # 3, A3.

A.3.4 Build Set # 4: LSRH Build Attempts, T1-5.

Build Set # 4 with alloy LSHR never made it off the base plate due to continuous Arc Trips from the point that the base plate was lowered. Figure 97 depicts the failures from when the chamber was opened (d) showing no powder around the base plate and build column. When the build would finally make it to the melt step, lack of fusion was common as seen in the crumbling parts of (a) and (c). Also of note in (c) is the hard sintered powder surrounding the base plate which indicates the initial preheat temperature was adequate, however once powder was swept on to the plate the errors began as seen in Figure 97 (b) from a build that never made it past the first layer. It was later determined that the powder contained a large percentage of fine particles which repeal each other and lead to Arc Trips.

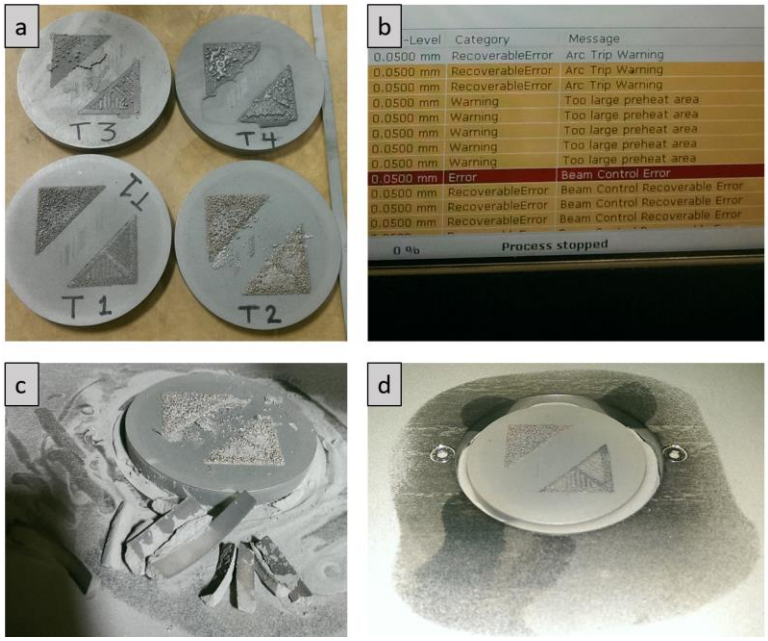

Figure 97. LSHR Builds gave nothing but Arc Trips and Problems.

A.3.5 Build Set # 5: Rene N5 Using MiniVat, B1-2.

Rene N5 builds B1 and B2 used elevated preheats to decrease the chance of Arc Tripping which lead to scorching of powder surrounding the base plate in Figure 98 (a) which is not turned over by the shortened rake. The elevated preheats also lead to over-sintering the powder seen in Figure 98 (b) which required the thermocouple, set below the base plate, to be cut off to remove the build. Build B2 repeated the process melt parameters of B1 with a reduced preheat allowing the sintered material to be broken free with the tap of a hammer. Pelling of the powder bed is visible in Figure 98 (c) which only made it 4.2 mm of the planned 20 mm. The geometry was the same as that attempted in the LSHR builds (T1-T5) and the layout is seen in Figure 98 (d). The leg length of each triangle is 40 mm and the thin walls of the complex part are less than 1 mm. The part was originally drawn to have a leg length of 33 mm but was rescaled later to be 40 mm.

Single passes were arrayed in the center of the part but due to over sintering they were never characterized. Figure 98 (e) is from a desktop scanner of the top surface after samples were removed from Solid and Complex parts. The samples were given the names A-F and further details will be given in a later section which covers the metallography. Table 6 summarizes the builds attempted with Rene N5 with a representative Temperature for each build from the log file.

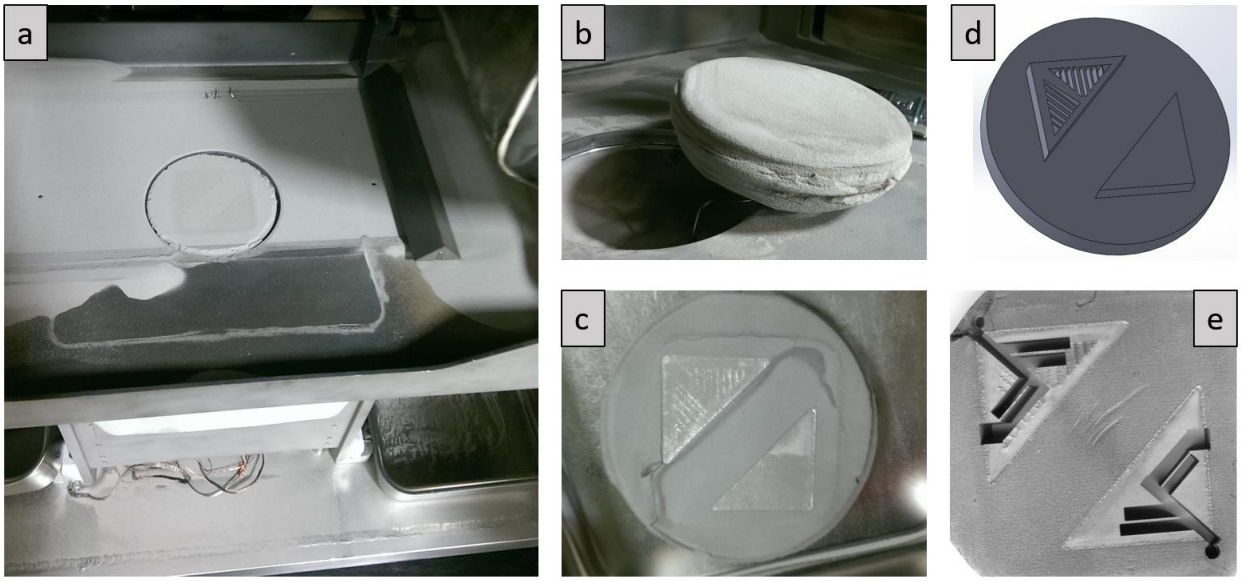

Figure 98. Post build images of B1 (a and b) and B2 (c).

Table 6. Summary of Rene N5 Builds

Build	**Geometry**	**Height**	**Parts Characterized**	**Samples**	**Date**	**~ Temp.**
B1	Tri-40-SC	7.55 mm	Solid & Complex	Z & XY	3/29/16	Elevated
B2	Tri-40-SC	4.2 mm	Solid & Complex	Z-plane	3/30/16	Elevated

The Build Anomaly Plots for both B1 and B2 are given in Figure 99 showing the elevated temperatures and problems with the pulse sensors. From the end of the build, raking appeared to have gone well but the censors were either clogged or at the wrong heights. Arc Trips ended both B1 and B2 at points that appeared to have stabilized in build temperature.

Figure 100 shows the processing conditions of build B1 and B2 which have a variation in beam current, line length, beam velocity, energy density, traverse velocity, and time of return. These variations are repeated along the diagonal mirror line due to the symmetry of the part and 90º rotation of the hatch fill on each layer.

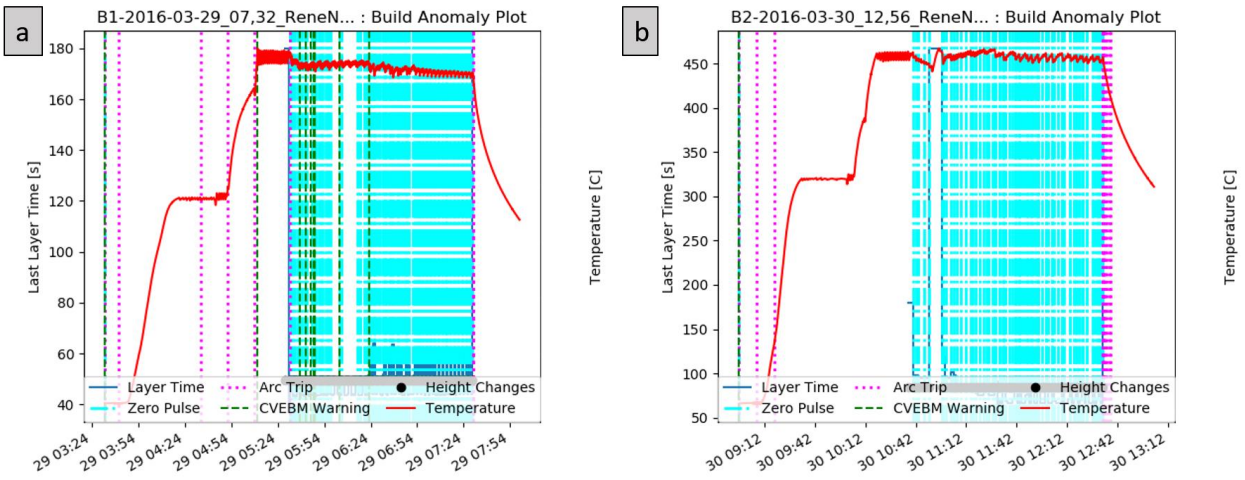

Figure 99. Build Anomaly Plot for build set # 5, B1 & B2.

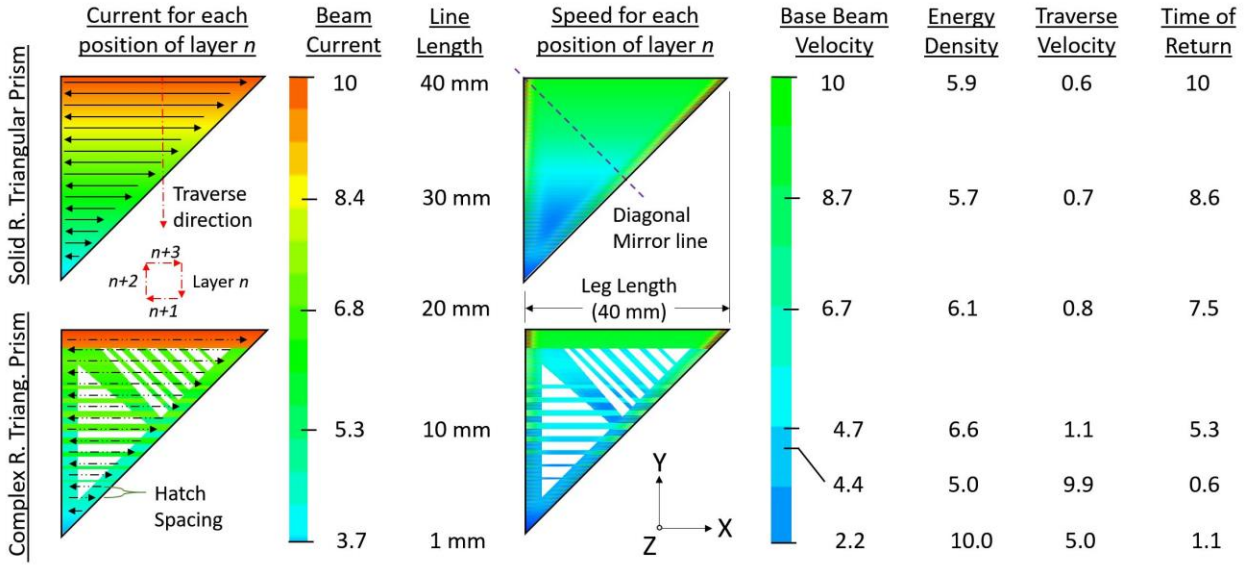

Figure 100. Normalized Processing of Solid and Complex Geometries. Adapted from [47]**.**

A.3.6 Build Set # 6: Hastelloy X Using MiniVat, H1-6.

After the two short builds with Rene N5, the build chamber was again stripped clean and each piece of the MiniVat was sand blasted and wiped with alcohol. Hastelloy-X was the next powder to enter the Arcam and began with the same geometry used in the Rene N5 builds. The first build, H1, was a test run to control the preheating and eventually failed due to Arc Tripping and will not be analyzed further. At this point, a second error was plaguing the system: "Disk is running out of space warning". After cleaning out the build chamber, the log files and material files were removed from the Arcam computer to free up space. This error has not been seen since. Clearing unused process themes from the computer is essential for the Arcam Beam Controller software to function correctly.

The second Hastelloy X build, H2, went to completion (20 mm) and was the first build to do so without error in this project seen in Figure 101 (a). This build theme was attempted a third time, H3, but failed after a bad rake and a series of Arc Trips that the Arcam did not recover from. H3 will not be characterized further as the final height is much less than H2. Build H4 through H6 used a new geometry and the first two of this series ended in errors (H4 and H5). H4 had a problem with the thermocouple and never started even though two attempts were tried. Build H5 was started on the same day as H4 and the result is seen in Figure 101 (b) which had the error "Focus out of range," at 2.3 mm. H6 went to completion, seen in Figure 101 (c), and the geometry used is seen in Figure 101 (d) as a complex 'X' shape with decreasing cross section as the height increased. After this set of builds the Arcam underwent maintenance and the software was updated.

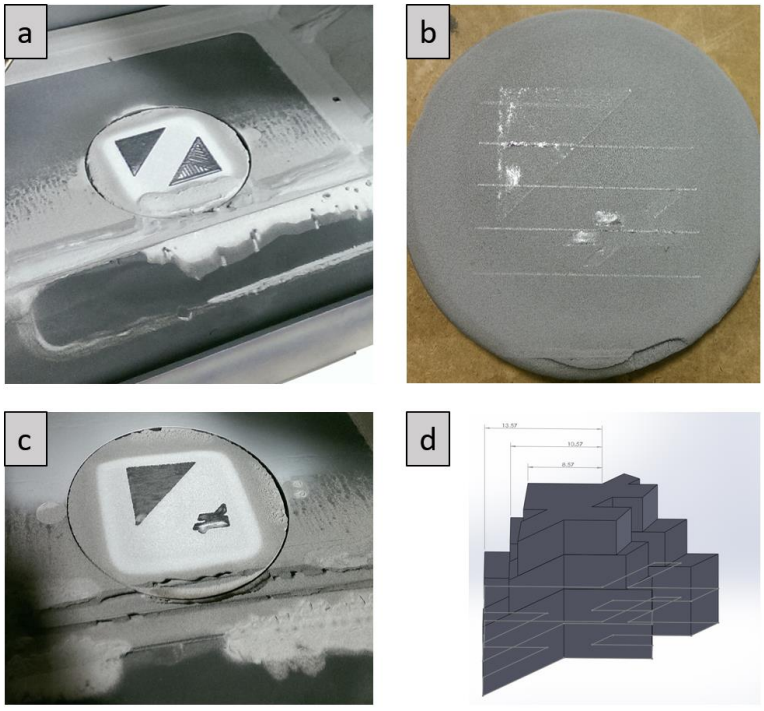

Figure 101. Hastelloy X initial build images for H2, H5, and H6.

Table 7 summarizes the builds attempted and completed for Hastelloy X. The parts characterized are listed and the sampled locations and orientations will be discussed in greater detail in a later section. Temperature listed in Table 7 are a single value representative of the build.

Table 7. Summary of Hastelloy X Builds

Build	**Geometry**	**Height**	**Parts Characterized**	**Samples**	**Date**	**~ Temp.**
H1	Tri-40-SC	4.1 mm	None	None	4/1/16	1150 C
H2	Tri-40-SC	20 mm	Solid & Complex	Z-plane	4/2/16	1180
H3	Tri-40-SC	1.6 mm	None	None	4/4/16	1150 C
H4	Tri-40S & X	0 mm	None	None	4/5/16	< 160 C
H5	Tri-40S & X	2.3 mm	None	None	4/5/16	1130 C
H6	Tri-40S & X	20 mm	Solid Only	Z-plane	4/6/16	1120 C

The Build Anomaly Plot for builds H2 and H6 are given in Figure 102 (a) and (b) indicating a large number of Zero Pulse layers and Arc Trips. These kinds of errors can be linked to lack of fusion defects which stretch across the entire part occasionally and reset the microstructure.

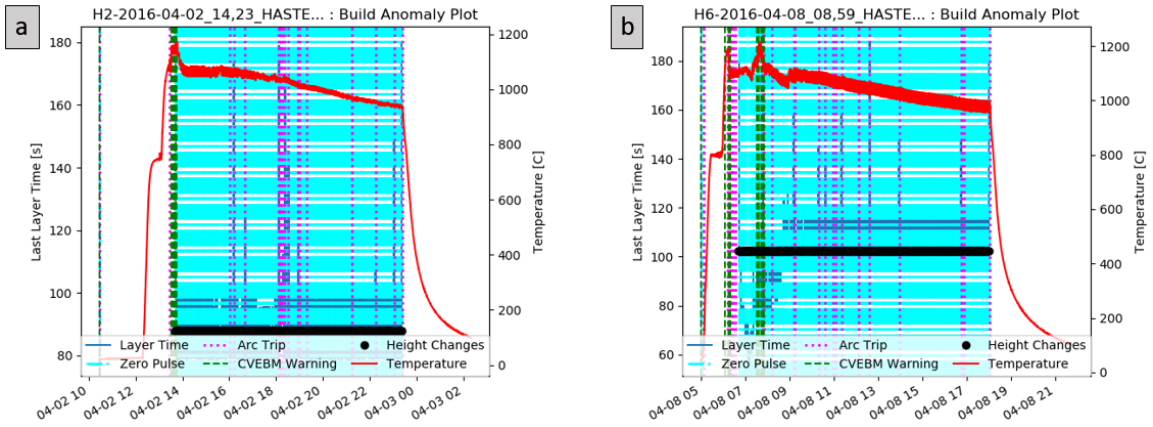

Figure 102. Build Anomaly Plot for build set # 6, H2 & H6.

A.3.7 Build Set # 7: Inconel 718 Using MiniVat, C1-5.

Post H6 machine time on the Arcam was booked until the end of 2016 when the next major round of builds began which included Inconel 718 and Ni-6Cr-6Al-6Ta. During this time recycled Inconel 718 was placed in the MiniVat to gain a better understanding of the process parameters for the new software. In addition, the IR camera was set up for the first time in this project. This would insure that IR video would be recorded for the Ni666 builds. In setting up the

first series of builds, 9 cubes 15 x 15 x 15 mm^3 were arranged with a variety of process parameters. Due to previous work with the IR camera, a pause for preheating between parts was introduced to maintain temperature while processing. An overview of the IN 718 MiniVat builds is given in Table 8. Build C1 has two temperatures listed as a change in processing lead to a shorter layer time and a drop-in temperature. Due to build C4 having no Log File, there is no temperature recorded to represent the build.

The first build, C1 was setup well and appeared to be off to a good start but an Arc Trip removed the surrounding powder after I left for the night and ruined the raking. A new way of loading powder from only 1 side was employed unsuccessfully for this set of builds. The build continued to 10 mm but stopped getting powder on each layer. The same parts were melted repeatedly as the build plate dropped in the chamber.

Figure 103 (a) shows the top surface of failed build C1 and (b) shows the fix to the reduced powder setup. These alterations were made here because limited powder would be available for the upcoming custom alloy builds. C1 will not be analyzed further.

Table 8. Summary of later MiniVat Builds with IN 718.

Build	**Geometry**	**Height**	**Parts Characterized**	**Samples**	**Date**	**~ Temp.**
C1	9 Cubes (15)	10 mm	None	None	12/27/16	1096/900
C2	9 Cubes (15)	10 mm	None	None	12/28/16	1090 C
C3	9 Cubes (15)	2.5 mm	None	None	12/29/16	1060
C4	6 Tri-S&C	10 mm	1-6	Z & XY	12/30/16	NA
C5	9 Cubes (15)	10 mm	1-9	Z & XY	1/2/2016	1100

C2 repeated most of the parameters from C1 and Figure 104 gives the reasoning behind the chosen process parameters. During this build, the Energy Density was maintained across the parts based on previous Inconel 718 parameters. The speed, current, and hatch combinations were varied to achieve varied Energy Density. The build was eventually canceled due to the swelling which occurred on part 6 which was beginning to break the rake blades. Figure 105 (a) is a scan of the top surface of build C2 showing how the ending raster melt pools are observable on cubes 1, 2, 3, 4, 5, and 9. The point net melts are observably different. Cube 7 is close to an area melt and cube 8 has a golf ball like surface with individual melt pools visible. The swelling that occurred on cube 6, which did not rotate raster direction on each layer is visible in Figure 105 (b) and (c).

Figure 106 summarizes the starting process parameters and resulting Energy Density calculated using Equation 4. This was the first set of builds where such a table was setup to allow for on the fly changes to process parameters. This way the current, speed, and hatch could be changed with relation to the Energy Density if a part appeared to have a rough surface, swelling, or lack of fusion. Tweaks to the process parameters are no longer gut feelings and blind changes. Red boxes indicate the major difference between builds.

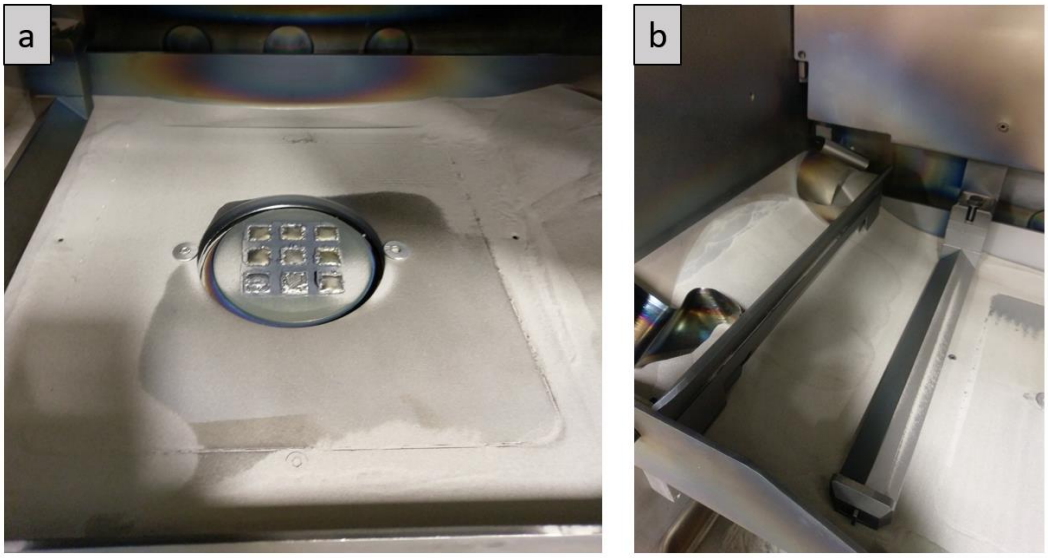

Figure 103. Failed build C1 and reduce powder setup raking from one side.

The Build Anomaly Plot for Build C2 is given in Figure 107 which shows a mostly steady with few Arc Trips and Zero Pulse warnings that were common on the previous builds. There is a section of longer layer times early on where process parameters were being altered but most of the build from there out was consistent.

Build C3 was plagued with problems from the start and only made it to 2.5 mm before being canceled. No further characterization will be discussed. Due to these problems the preheat temperature was maintained at a high temperature for builds C4 and C5 to mimic the Rene N5 and Hastelloy X builds.

The Log File for C4 was lost or overwritten. The C4 build switched to new geometry of solid and complex triangles. The complex triangles have fewer and thicker thin walls than the geometry used for Rene N5 and Hastelloy X. The top surface of build C4 can be seen in Figure 108 (a) with all 4 parts showing relatively smooth top surfaces. Parts 3 and 4 had spot melts and the rest were raster. Figure 108 (b) is included because cracks were noticed on the top surface of the parts. Marking the top surface with a sharpie is a quick test to highlight the cracks, large and small. Each of the parts has some degree of cracking micro cracking seen as gray regions depleted of red sharpie. The history of the recycled powder used for this set of builds is not known and it is a mix of various projects. The main intent of these builds is to exert process control and to set up the IR camera which was achieved.

An overview of the process parameters used can be seen in Figure 109. The parameters for parts 1, 2, 5, & 6 used the same base Energy Density as build C2. Parts 5 and 6 achieved it with a much smaller hatch spacing and increased speed function to maintain the same traverse velocity and energy density. The spot pattern applied to parts 3 and 4 were Dehoff fill method skipping 11 pixels by 5 pixels. 6 and 4 px/mm spacing was applied respectively to the solid and complex parts.

Part 1	Base Parameters for Inconel 718 from Michael Kirka
Part 2	Slow & Hot: Current, Speed, Hatch, and Traverse speed. Energy = Base
Part 3	Fast & Cool: Current, Speed, Hatch, and Traverse speed. Energy = Base
Part 4	Line Order 10: Speed reduced and Energy increased
Part 5	Small Hatch: Speed increased and hatch reduced to match Energy to Base.
Part 6	No rotation: Base parameters otherwise
Part 7	Spot1: Equiaxed? Energy needs to be close to swelling
Part 8	Spot 2: Columnar? Energy = Base +
Part 9	Repeat Base Parameters as control

Figure 104. Build C2 summary of part processing.

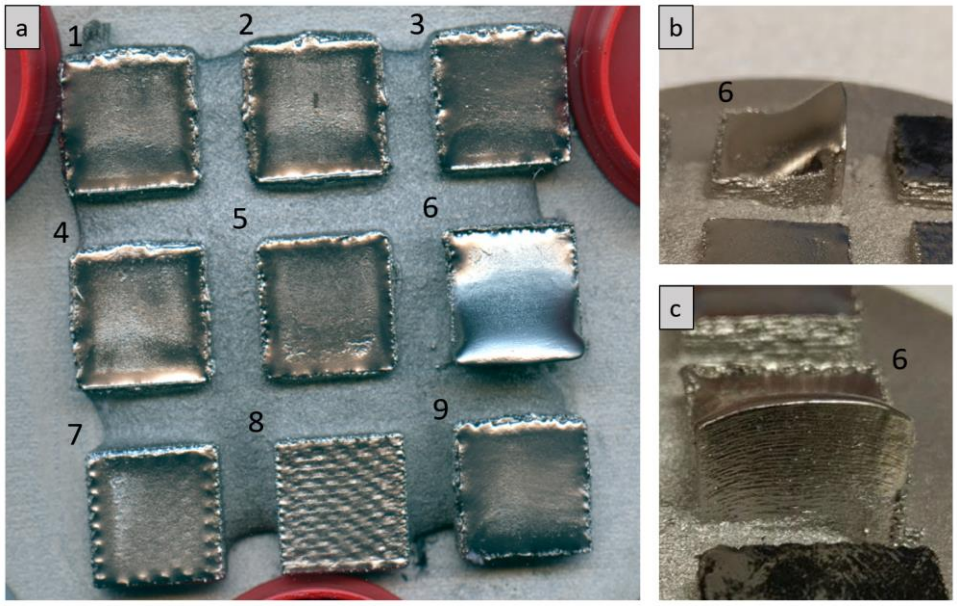

Figure 105. Scan of top surface of build C2 and images of part 6 from an angle.

9 x 15 mm cubes

1st Part 15 mm Box		Base	2nd Part 15 mm Box		Slow Hot	3rd Part 15 mm Box		Fast Cool
Current =	18	mA	Current =	20	mA	Current =	16	mA
SF =	63	-	SF =	52	-	SF =	77	-
Velocity =	2518	mm/s	Velocity =	2275.667	mm/s	Velocity =	2794	mm/s
Power =	1080	W or J/s	Power =	1200	W or J/s	Power =	960	W or J/s
Hatch =	0.125	mm	Hatch =	0.154	mm	Hatch =	0.1	mm
Length =	15	mm	Length =	15	mm	Length =	15	mm
Transvese =	21.0	mm/s	Transvese =	23.4	mm/s	Transvese =	18.6	mm/s
Focus off =	20	mA	Focus off =	20	mA	Focus off =	20	mA
Rotate =	1800	Deg/mm	Rotate =	1800	Deg/mm	Rotate =	1800	Deg/mm
Energy =	3.4312947	J/mm2	Energy =	3.424143	J/mm2	Energy =	3.435934	J/mm2

4th Part 15 mm Box		L.Ord. 10	5th Part 15 mm Box		Small h.	6th Part 15 mm Box		No Rot.
Current =	18	mA	Current =	18	mA	Current =	18	mA
SF =	53	-	SF =	214	-	SF =	63	-
Velocity =	2128	mm/s	Velocity =	8407	mm/s	Velocity =	2518	mm/s
Power =	1080	W or J/s	Power =	1080	W or J/s	Power =	1080	W or J/s
Hatch =	0.125	mm	Hatch =	0.0375	mm	Hatch =	0.125	mm
Length =	15	mm	Length =	15	mm	Length =	15	mm
Transvese =	0.148	mm/s	Transvese =	21.0	mm/s	Transvese =	21.0	mm/s
Focus off =	20	mA	Focus off =	20	mA	Focus off =	20	mA
Rotate =	1800	Deg/mm	Rotate =	1800	Deg/mm	Rotate =	7200	Deg/mm
Line Order =	10							
Energy =	4.0601504	J/mm2	Energy =	3.425717	J/mm2	Energy =	3.431295	J/mm2

7th Part 15 mm Box		Spot # 1	7th Part 15 mm Box		Spot # 2	9th Part 15 mm Box		Base
Current =	21	mA	Current =	15	mA	Current =	18	mA
px/mm =	4	#	px/mm =	4	#	SF =	63	-
on time =	0.25	ms	on time =	0.25	ms	Velocity =	2518	mm/s
Power =	1260	W or J/s	Power =	900	W or J/s	Power =	1080	W or J/s
Length =	15	mm	Length =	15	mm	Hatch =	0.125	mm
Area =	225	mm^2	Area =	225	mm^2	Length =	15	mm
# of Spots =	3600	#	# of Spots =	3600	#	Transvese =	21.0	mm/s
Part time =	0.90	s	Part time =	0.9	s			
						Focus off =	20	mA
Focus off =	2	mA	Focus off =	2	mA	Rotate =	1800	Deg/mm
Energy =	5.04	J/mm2	Energy =	3.6	J/mm2	Energy =	3.431295	J/mm2

Figure 106. Process Parameters of Build C2.

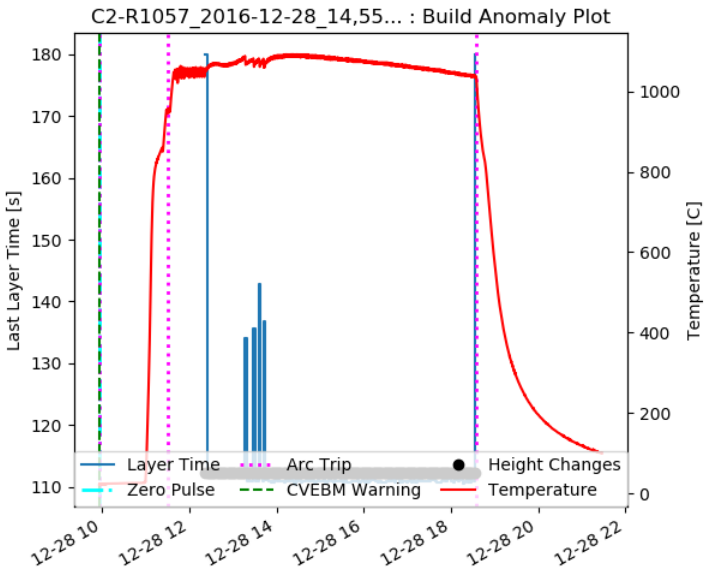

Figure 107. Build Anomaly Plot for build set # 7, C2.

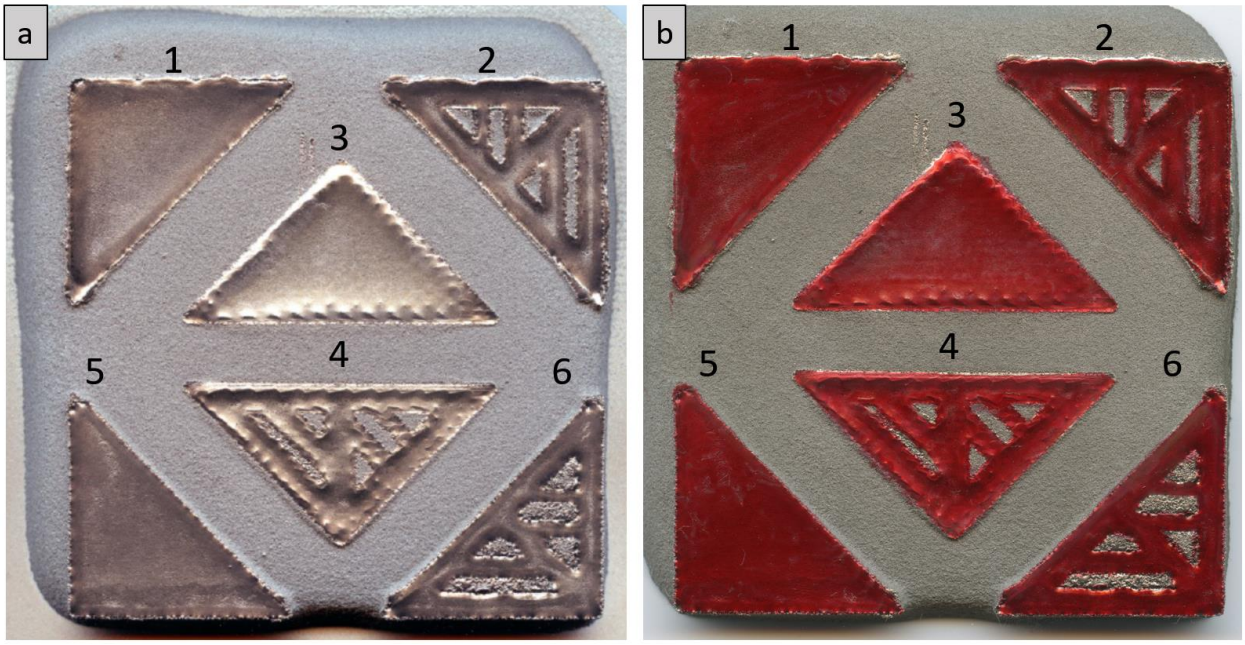

Figure 108. Top surface scan of build C4 with and without sharpie marker.

6 Triangles

Part 1 and 2		Base
Current =	18	mA
SF =	63	-
Velocity =	2518	mm/s
Power =	1080	W or J/s
Hatch =	0.13	mm
Length =	15	mm
Transvese =	21.0	mm/s
Focus off =	20	mA
Rotate =	1800	Deg/mm
Energy =	3.43	J/mm2

2nd Part Complex T		Base
Current =	18	mA
SF =	63	-
Velocity =	2518	mm/s
Power =	1080	W or J/s
Hatch =	0.125	mm
Length =	15	mm
Transvese =	21.0	mm/s
Focus off =	20	mA
Rotate =	1800	Deg/mm
Energy =	3.431	J/mm2

3rd/4th Spot Tri		Spot#1x2
Current =	19	mA
px/mm =	4	#
on time =	0.25	ms
Power =	1140	W or J/s
Length =	15	mm
Area =	225	mm^2
# of Spots =	3600	#
Part time =	0.90	s
Focus off =	2	mA
Energy =	4.56	J/mm2

5th and 6th		Small h.
Current =	18	mA
SF =	214	-
Velocity =	8407	mm/s
Power =	1080	W or J/s
Hatch =	0.04	mm
Length =	15	mm
Transvese =	21.0	mm/s
Focus off =	20	mA
Rotate =	1800	Deg/mm
Energy =	3.43	J/mm2

6th Part Complex T		Small h.
Current =	18	mA
SF =	214	-
Velocity =	8407	mm/s
Power =	1080	W or J/s
Hatch =	0.038	mm
Length =	15	mm
Transvese =	21.0	mm/s
Focus off =	20	mA
Rotate =	1800	Deg/mm
Energy =	3.426	J/mm2

Figure 109. Process Parameter Summary of Build C4.

Build C5 was the last build of this series with recycled Inconel 718 powder. It repeated most of the parameters used in C2 except for part 6 which changed to a starting rotation of 45 degrees. Build C5 went to completion of 10 mm with a relatively smooth top surface as seen in Figure 110 (a). Due to each part having a smooth surface, further characterization will focus on C5 rather than C2. The sharpie test is also applied to build C5, Figure 110 with large cracks observed on parts 4, 5, 6, 7, 8, and 9. Smaller micro cracks absorbed the sharpie ink on 1, 2, and 3. The top surface of each part also showed the possibility of gas porosity as small gray dots. Metallography will clarify the matter in a later section. Note the over sintered powder between each of the parts in both Figure 108, C4, and Figure 110 C5.

The summary of starting process parameters is give in Figure 111. This was the last build used to modify and control process parameters before moving to the new custom powder. Most of the process parameters are hidden within subfolders while setting up the build and it takes builds like this one to flush them out. Not all the parameters behave as intended and some are unintentionally overwritten by other parameters. One example of this is the parameter named Line Order which is supposed to skip lines while melting, which works in the preheating setting. However, this parameter never modified the melting in any build it was attempted in during this series of builds.

The Build Anomaly Plot given in Figure 112 appears similar to C2 in temperature except for the region of Zero Pulse warnings that took place between 10:30 AM and 12:30 PM. Because of this similarity in temperature and process parameters C2 was not cross sectioned where C5 was.

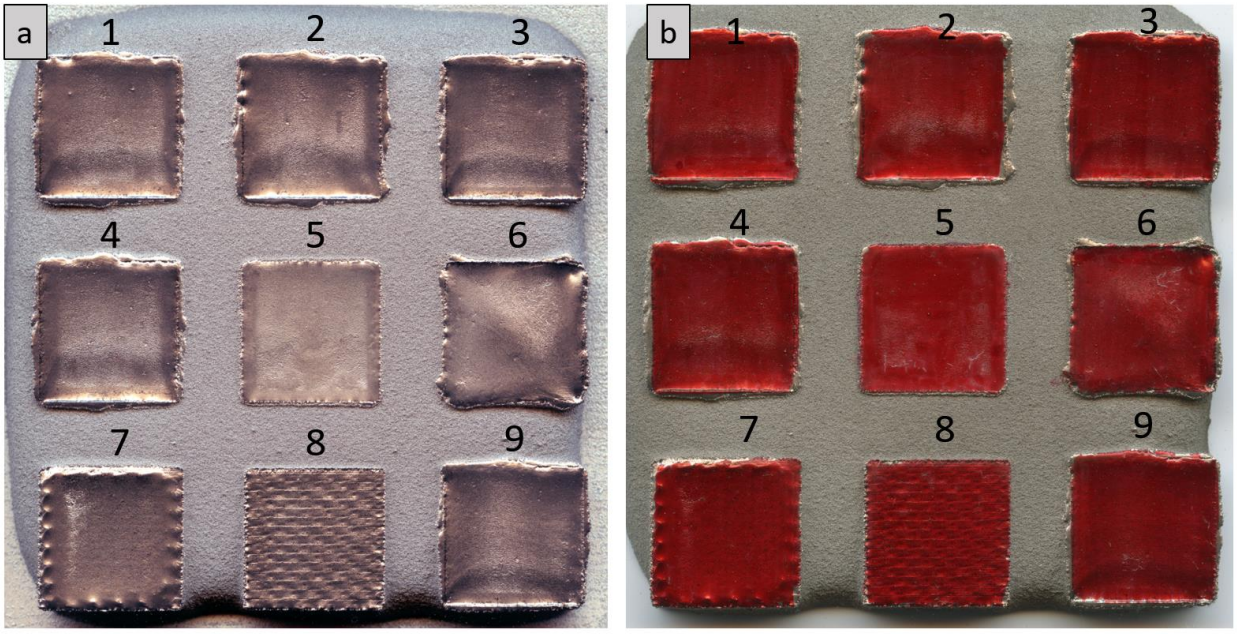

Figure 110. Top surface scan of build C4 with and without sharpie marker.

9 x 15 mm cubes

1st Part 15 mm Box		Base	2nd Part 15 mm Box		Slow Hot	3rd Part 15 mm Box		Fast Cool
Current =	18	mA	Current =	20	mA	Current =	16	mA
SF =	63	-	SF =	52	-	SF =	77	-
Velocity =	2518	mm/s	Velocity =	2275.667	mm/s	Velocity =	2794	mm/s
Power =	1080	W or J/s	Power =	1200	W or J/s	Power =	960	W or J/s
Hatch =	0.125	mm	Hatch =	0.154	mm	Hatch =	0.1	mm
Length =	15	mm	Length =	15	mm	Length =	15	mm
Transvese =	21.0	mm/s	Transvese =	23.4	mm/s	Transvese =	18.6	mm/s
Focus off =	20	mA	Focus off =	20	mA	Focus off =	20	mA
Rotate =	1800	Deg/mm	Rotate =	1800	Deg/mm	Rotate =	1800	Deg/mm
Energy =	3.4312947	J/mm2	Energy =	3.424143	J/mm2	Energy =	3.435934	J/mm2

4th Part 15 mm Box		Turning	5th Part 15 mm Box		Small h.	6th Part 15 mm Box		**45 S.Rot**
Current =	18	mA	Current =	18	mA	Current =	18	mA
SF =	63	-	SF =	214	-	SF =	63	-
Velocity =	2518	mm/s	Velocity =	8407	mm/s	Velocity =	2518	mm/s
Power =	1080	W or J/s	Power =	1080	W or J/s	Power =	1080	W or J/s
Hatch =	0.125	mm	Hatch =	0.0375	mm	Hatch =	0.125	mm
Length =	15	mm	Length =	15	mm	Length =	15	mm
Transvese =	21.0	mm/s	Transvese =	21.0	mm/s	Transvese =	21.0	mm/s
Focus off =	20	mA	Focus off =	20	mA	Focus off =	20	mA
Rotate =	1800	Deg/mm	Rotate =	1800	Deg/mm	Rotate =	1800	Deg/mm
Contour =	0					Start Angle =	45	Deg
Energy =	3.4312947	J/mm2	Energy =	3.425717	J/mm2	Energy =	3.431295	J/mm2

7th Part 15 mm Box		Spot # 1	7th Part 15 mm Box		Spot # 2	9th Part 15 mm Box		**Base**
Current =	19	mA	Current =	14.3	mA	Current =	18	mA
px/mm =	4	#	px/mm =	4	#	SF =	63	-
on time =	0.25	ms	on time =	0.25	ms	Velocity =	2518	mm/s
Power =	1140	W or J/s	Power =	858	W or J/s	Power =	1080	W or J/s
Length =	15	mm	Length =	15	mm	Hatch =	0.125	mm
Area =	225	mm^2	Area =	225	mm^2	Length =	15	mm
# of Spots =	3600	#	# of Spots =	3600	#	Transvese =	21.0	mm/s
Part time =	0.90	s	Part time =	0.9	s			
						Focus off =	20	mA
Focus off =	2	mA	Focus off =	2	mA	Rotate =	1800	Deg/mm
Energy =	4.56	J/mm2	Energy =	3.432	J/mm2	Energy =	3.431295	J/mm2

Figure 111. Process Parameter Summary of Build C5.

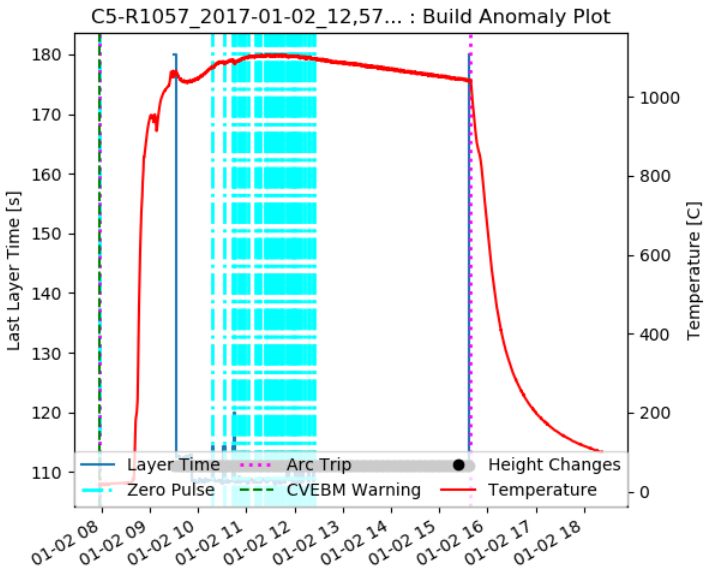

Figure 112. Build Anomaly Plot for build set # 7, C5.

A.3.8 Build Set # 8: Ni-6Cr-6Al-6Ta Using MiniVat, F1-5.

The next set of builds was moved from the A2 to the S12 due to scheduling conflicts. However, the latest version of the Beam Controller V4 was updated from V3 on the S12 so that process parameters could be transferred directly. Also, the IR camera housing worked the same for both S12 and A2 making that transition straight forward. The geometry changed once more moving to the new powder which had never been processed before. 20 mm x 20 mm cubes were chosen because that is the size which most consistently produces equiaxed grains when using spot melting. An overview of the Ni-6Cr-6Al-6Ta builds is given in. The first build of this series, F1, failed early on due to an Arc Trip and no further characterization was performed. The Log File of build F4 stopped recording at 1.8 mm even though the build went to completion.

Build F2 began after the chamber was cleaned out and the filament replaced following build F1. The Build Anomaly Plot is given in Figure 113 and indicates a mostly consistent build with only a slight dip in temperature near the beginning. Other warnings of note are the Zero Pulse warnings at the beginning which go away and come back at the end. Also, the one outlier layer in the center of the build where an Arc Trip occurred but the process was able to restart. The process parameters used in Build F2 are given in Figure 114 showing three raster patterns and 1 spot melting. For the first three cubes the Energy Density is maintained with parts 1 and 2 change drastically the hatch spacing and beam speed. Part 3 repeats parameters from part 1 but rotates the initial raster by 45 degrees causing the line length to change across the part and not correctly calculated in Figure 114.

Table 9. Overview of Ni-6Cr-6Al-6Ta builds

Build	Geometry	Height	Parts Characterized	Samples	Date	~ Temp.
F1	4 Cubes (20)	1.4 mm	None	None	1/13/17	1050 C
F2	4 Cubes (20)	15 mm	All 4	Z and XY	1/16/17	1050 C
F3	4 Cubes (20)	15 mm	All 4	Z and XY	1/17/17	1050 C
F4	4 Tri (28.3)	15 mm	All 4	Z and XY	1/18/17	1020 C
F5	4 Tri (28.3)	12.25	All 4	Z and XY	1/19/17	1150/950

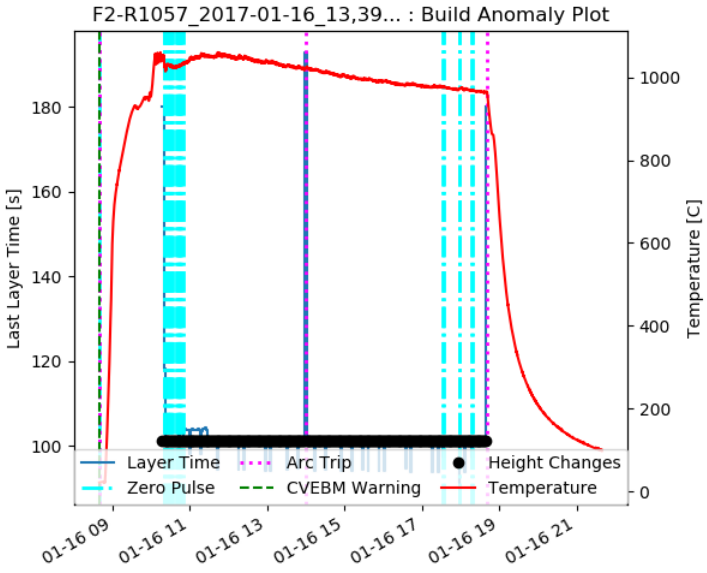

Figure 113. Build Anomaly Plot for build F2.

The final cube uses the Dehoff spot fill with 11 pixels by 5 pixel jumps (standard) and a 6 px/mm grid. The parameters chosen here are most likely to give an equiaxed microstructure when producing an Inconel 718 part with the same dimensions. Note the drastic difference in Energy Density between raster and point melting. Scans of the top surface of build F2 are given in Figure 115 to show the differences in processing conditions.

Part 1 shows a steady line source melting from top to bottom of the part on the last layer with a large final melt pool along the bottom. Part 2 created a similar sized melt pool but has a rougher surface and produced more spatter during processing, visually observed, during processing. Part 3 has swollen bottom left and top right corners and the final raster appears to have ended in the top right corner. Part 4 also has some swelling going on in the center along with a golf ball pattern surrounding it. This indicates individual melt pools surrounding an area melt in the center of the part. This kind of swelling often indicates a greater possibility of equiaxed grains when using the parameters on Inconel 718.

Different from Inconel 718 is the cracking that is observed on the top surface of each of these parts in Figure 115 (b). For parts 1-3 the cracking appears as fine white lines across the top of each part and in the craters of parts 1 and 2. On parts 3 and 4 the sharpie marker, used to highlight the cracks, is absorbed into the swollen regions and appears pink. The cracking was initially invisible to the naked eye and the Sharpie test was not performed until after build F4 took place. Build F3 began similar to F2 and has a similar temperature profile as seen in the Build Anomaly Plot Figure 116. The parts are similarly organized in that parts 1 and 3 have the same process parameters with an initial raster rotation of 45 degrees. Initially there was trouble with the rake and first layer times were lower than the final layer times. No long layer times kept the temperature consistent and process parameters were tweaked slowly while watching through the window to see the effects of the changes after a few layers. The final process parameters landed on can be seen in Figure 117 which parts 1 and 2 contain beam speeds much less than parts 1 and 2 of build F2. In addition, the energy density is greater than that used in build F2 but the current is much lower. This unique parameter set was obtained by looking through the build window and watching for an increase or decrease in surface roughness. There is also a drastic difference in surface finish when it comes to comparing F3 to F2. Build F3 top surface scan in Figure 118 (a) is dark because it is very wavy and does not reflect light directly back to the scanner (exception is the spot melt). Build F2 is the opposite, bright and shiny with a smooth top surface. Regardless, all parts have cracks that are similar in appearance across build F2 and F3 as seen in Figure 115 (b) and Figure 118 (b).

Build F4 picked up where build F3 left off as the cracks had not yet been spotted and moved to triangular geometries. The Build Anomaly Plot is given in Figure 119 which consistently had Zero Pulse warnings to start the build. Unfortunately, the Log File stopped recording early in the build so the process parameters and build temperature history are not certain. Only the process parameters marked in the excel file are left to document the build which indicate the build took place between 960 and 980 ºC. The estimated parameters can be seen in Figure 120. The parameters were chosen to vary the current across the part from 8 mA on the long end to 4 mA on the short end. This way the parts stays in a similar regime to the parts built in F3.

4 x 20x20x15 mm cubes					
1st Part 15 mm Box		Base	2nd Part 15 mm Box		Small h.
Current =	18	mA	Current =	18	mA
SF =	63	-	SF =	214	-
Velocity =	2518	mm/s	Velocity =	8407	mm/s
Power =	1080	W or J/s	Power =	1080	W or J/s
Hatch =	0.125	mm	Hatch =	0.0375	mm
Length =	20	mm	Length =	20	mm
transverse =	15.7	mm/s	transverse =	15.8	mm/s
Focus off =	20	mA	Focus off =	20	mA
Rotate =	1800	Deg/mm	Rotate =	1800	Deg/mm
Energy =	3.4312947	J/mm2	Energy =	3.425717	J/mm2
3rd Part 20 mm Box		45 deg 1	4th Part 20 mm Box		Spot # 1
Current =	18	mA	Current =	20	mA
SF =	63	-	px/mm =	6	#
Velocity =	2518	mm/s	on time =	0.25	ms
Power =	1080	W or J/s	Power =	1200	W or J/s
Hatch =	0.125	mm	Length =	20	mm
Length =	20	mm	Area =	400	mm^2
transverse =	15.7	mm/s	# of Spots =	14400	#
			Part time =	3.60	s
Focus off =	20	mA			
Rotate =	1800	Deg/mm	Focus off =	2	mA
Energy =	3.4312947	J/mm2	Energy =	10.8	J/mm2

Figure 114. Process Parameters for Build F2.

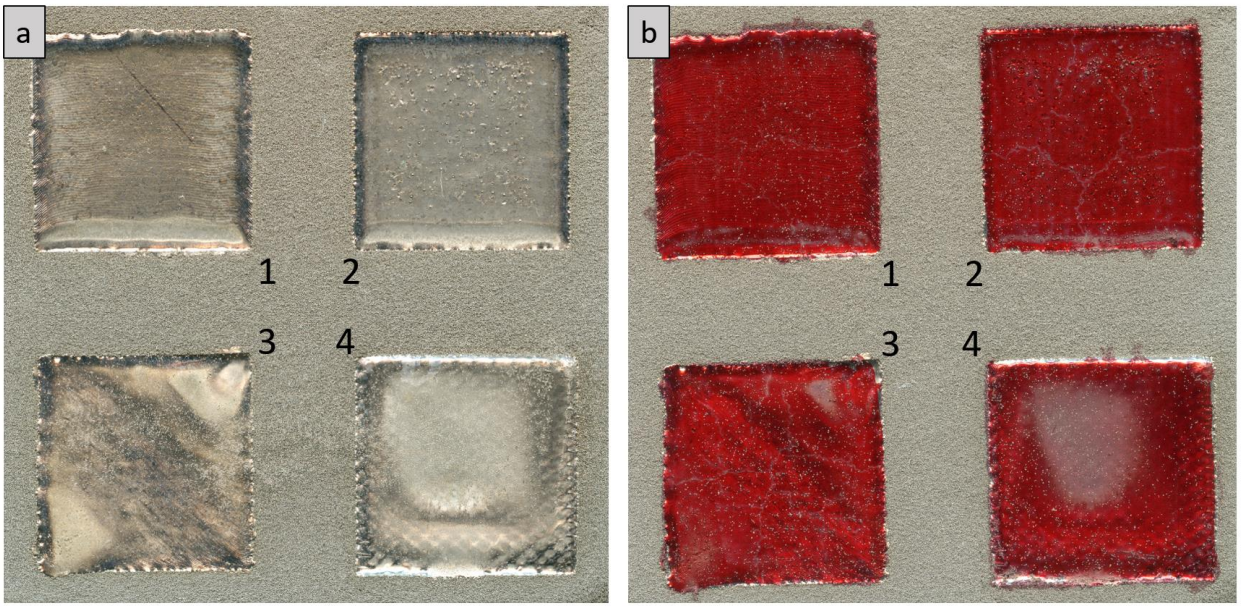

Figure 115. Top surface scan of build F2 with and without sharpie marker.

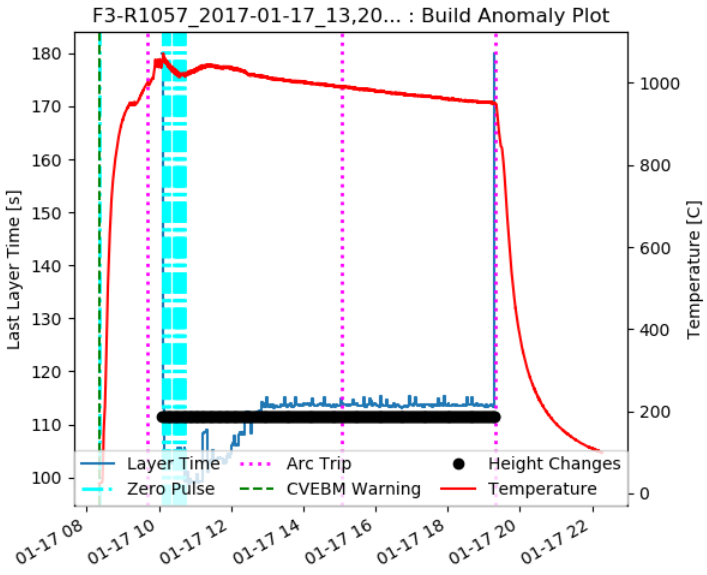

Figure 116. Build Anomaly Plot for build F3.

4 x 20x20x15 mm cubes					
1st Part 15 mm Box		Small	2nd Part 15 mm Box		Large
Current =	4	mA	Current =	4	mA
SF =	150	-	SF =	140	-
Velocity =	756.92083	mm/s	Velocity =	706.9625	mm/s
Power =	240	W or J/s	Power =	240	W or J/s
Hatch =	0.056	mm	Hatch =	0.08	mm
Length =	20	mm	Length =	20	mm
Transverse =	2.12	mm/s	Transverse =	2.83	mm/s
Focus off =	20	mA	Focus off =	20	mA
Rotate =	1800	Deg/mm	Rotate =	1800	Deg/mm
Energy =	5.6620377	J/mm2	Energy =	4.243507	J/mm2

3rd Part 20 mm Box		2 45Deg	4th Part 20 mm Box		Spot # 2
Current =	4	mA	Current =	23	mA
SF =	140	-	px/mm =	6	#
Velocity =	706.9625	mm/s	on time =	0.22	ms
Power =	240	W or J/s	Power =	1380	W or J/s
Hatch =	0.08	mm	Length =	20	mm
Length =	20	mm	Area =	400	mm^2
Transverse =	2.83	mm/s	# of Spots =	14400	#
			Part time =	3.17	s
Focus off =	20	mA			
Rotate =	1800	Deg/mm	Focus off =	2	mA
Energy =	4.2435066	J/mm2	Energy =	10.9296	J/mm2

Figure 117. Ending Process parameters for build F3.

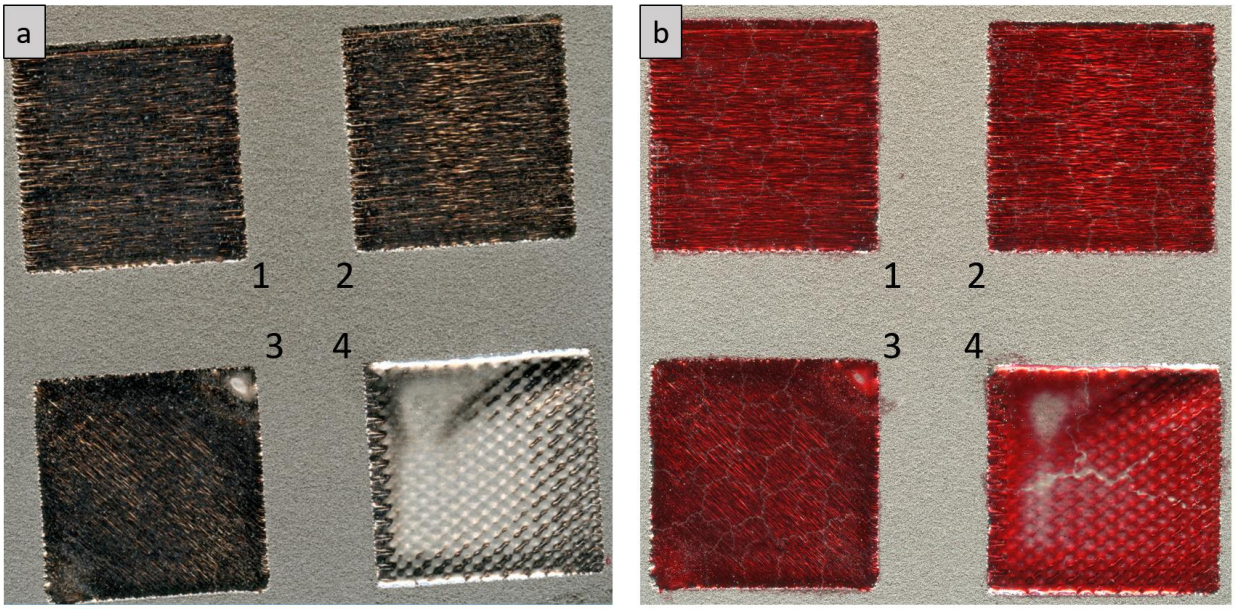

Figure 118. Top surface scan of build F3 with and without sharpie marker.

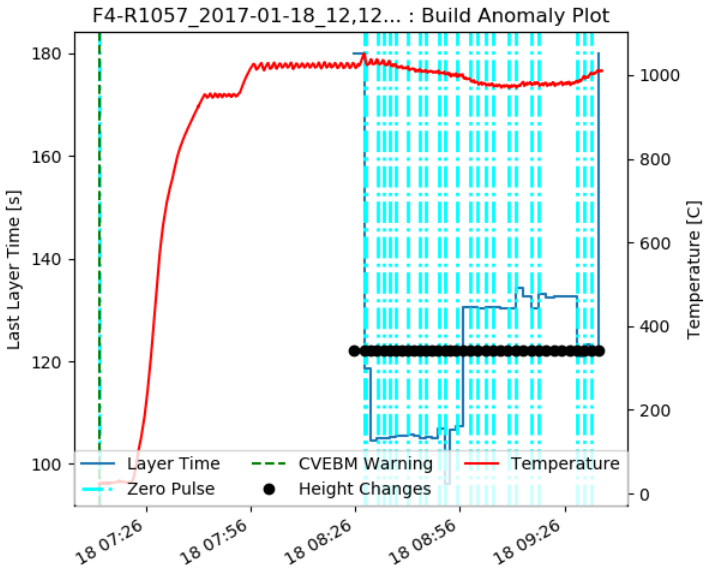

Figure 119. Build Anomaly Plot for beginning of build F4.

4 x 28.3x28.3x15 mm Triangles			Temperature: 980 to 960 C		
1st and 2nd Tri (Line)				Solid & Complex	
Min Current =	4	mA	PA	10	
Max Current =	8	mA	Prop_K	0.6014184	
Triangle Length =	28.3	mm	Scan_Ref	42.4	
SF =	100		Slope =	0.142	mA/mm
Hatch =	0.125		Y-intercept =	3.99	mA
	Current (mA)	Length (mm)	Velocity (mm/s)	Transverse	Energy
Full =	8	28.3	1180	5.2120141	3.254
3/4 =	7	21.225	904	5.3214566	3.719
1/2 =	6	14.15	737	6.5061837	3.910
1/4 =	5	7.075	599	10.58937	4.004
Min =	4	1	507	63.391146	3.786
				mm/s	J/mm2
3rd Tri (Spot)		Solid	4th Tri (Spot)		Complex
Current =	18	mA	Current =	19	mA
px/mm =	6	#	px/mm =	6	#
on time =	0.22	ms	on time =	0.22	ms
Power =	1080	W or J/s	Power =	1140	W or J/s
Length =	20	mm	Length =	20	mm
Area =	400	mm^2	Area =	400	mm^2
# of Spots =	14400	#	# of Spots =	14400	#
Part time =	3.17	s	Part time =	3.17	s
Focus off =	2	mA	Focus off =	2	mA
Energy =	8.554	J/mm2	Energy =	9.029	J/mm2

Figure 120. Estimated process parameters for build F4.

When the parts were removed from the machine, cracks were noticed on the top surface of the parts. Figure 121 shows the top surface which looks similar to the top of F3 with cracks clearly visible on part 1 of build F4. After coloring the top surface with a red Sharpie marker, the cracks became clear on each of the part. The cracks in this build are thick and follow grain boundaries for the entire length of the samples removed.

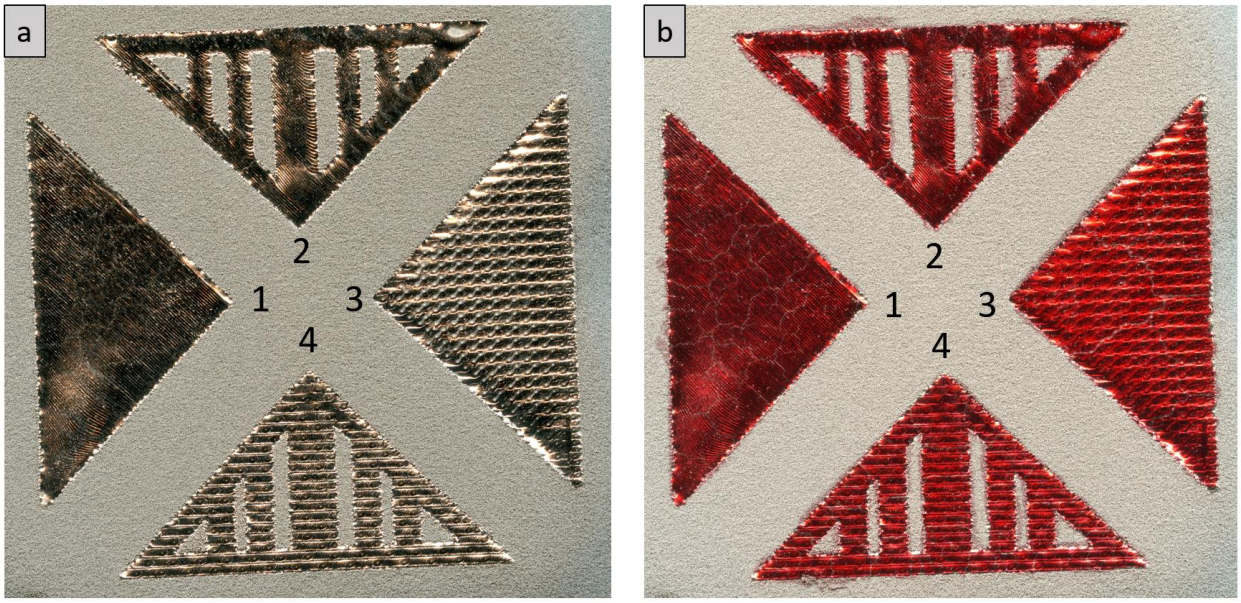

Figure 121. Top surface scan of build F4 with and without sharpie marker.

Build F5 repeated the geometry used in F4 and moved back to higher current parameters as build F2 appeared to have less cracking than build F3 or F4. The preheat was initially high (close to 1200 ºC) and the build was watched and parameters adjusted. Cracks on the top surface were noted and later the build was changed to have a much lower preheat and continued to change the process parameters. The top surface of the build still in the Arcam and after being marked with a Sharpie marker is shown in Figure 123. The final set of process parameters is seen in Figure 124 showing a higher energy density than any of the previous builds. The current was again altered along the length of the triangle, this time from 19 mA to 16 mA. The high energy density lead to a little bit of swelling on each of the raster parts (1 & 2). The build was stopped early after a long layer time and Arc Trip as indicated in Figure 122.

A.3.9 Build Set # 9: Ni-10Cr-6Al Using MiniVat, E1-5.

Build Set # 9 took place 9 months after Ni666 builds with the primary goal of repeating the same solid and complex right triangular prism geometry as build Set 8. A quick summary of build Set # 9 in Table 10 which contained 5 builds.

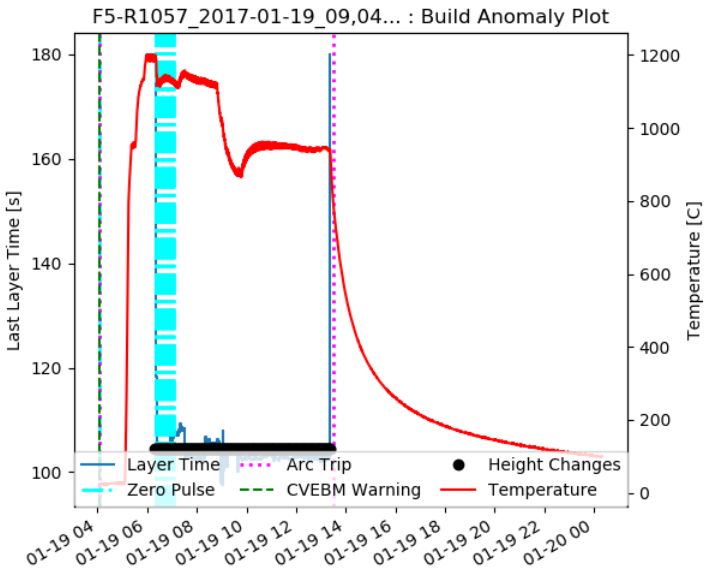

Figure 122. Build Anomaly Plot for build F5.

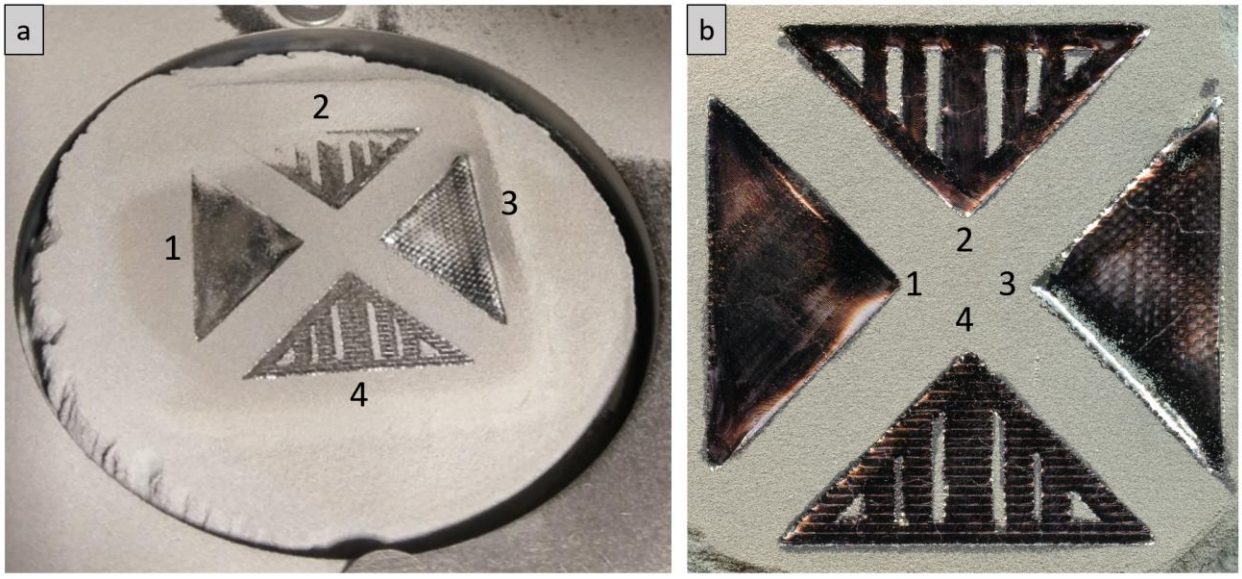

Figure 123. Image of build F5 in the MiniVat and a scan with sharpie marker.

4 x 28.3x28.3x15 mm Triangles			Temperature	1130 to 960 C	
1st and 2nd Tri (Line)				**Solid & Complex**	
Min Current =	16	mA	PA	10	
Max Current =	19	mA	Prop_K	-0.59893617	
Tri Length =	28.3	mm	Scan_Ref	-56.3	
SF =	60		Slope =	0.106	mA/mm
Hatch =	0.075		Y-intercept =	15.99	mA
	Current (mA)	Length (mm)	Velocity	Traverse	Energy
Full =	19	28.3	2508	757.9356042	6.061
3/4 =	18.25	21.225	2401	967.5945159	6.081
1/2 =	17.5	14.15	2294	1386.912339	6.102
1/4 =	16.75	7.075	2188	2644.865809	6.125
Min =	16	1	2188	18712.4256	5.851
				mm/s	J/mm2
3rd Tri (Spot)		**Solid**	4th Tri (Spot)		**Complex**
Current =	18	mA	Current =	19	mA
px/mm =	6	#	px/mm =	6	#
on time =	0.22	ms	on time =	0.22	ms
Power =	1080	W or J/s	Power =	1140	W or J/s
Length =	20	mm	Length =	20	mm
Area =	400	mm^2	Area =	400	mm^2
# of Spots =	14400	#	# of Spots =	14400	#
Part time =	3.17	s	Part time =	3.17	s
Focus off =	2	mA	Focus off =	2	mA
Energy =	**8.554**	J/mm2	Energy =	**9.029**	J/mm2

Figure 124. Final process parameters for build F5.

Table 10. Overview of Ni-10Cr-6Al builds

Build	Geometry	Height	Parts Characterized	Samples	Date	~ Temp.
E1	2/4 Tri (28.3)	13 mm	None	None	9/26/17	1030 C
E2	4 Tri (28.3)	13 mm	1 & 2	Z-diag.	9/27/17	1200 C
E3	4 Tri (28.3)	3.95 mm	None	None	9/28/17	900/1000
E4	4 Tri (28.3)	13 mm	3 & 4	Z-diag.	9/29/17	1050
E5	4 Tri (28.3)	11.7 mm	1 – 4	Z-diag.	10/2/17	1070

The first build began with two classes of process parameters named ‘Cold’ and ‘Hot’. Each set was altered once the build started to create a smooth top surface. The goal was to produce two sets of process parameters which a low and high range of currents. The final process parameters that were settled on for build E1 are given in Figure 125. Parts 1 & 2 used the Cold settings and parts 3 & 4 used the Hot settings.

However, during the build it was noticed that the rake was not properly distributing powder on the entire build plate and parts 2 & 3 were canceled to save the build. The lack of powder can be seen in the scans of the top surface after the build was completed in Figure 126. The Sharpie marker test was applied to the surface to look for cracks and none were observed for this alloy. A large difference in melt pool can be observed between parts 1 and 4 of Figure 126 (a). Part 1 has a small melt pool that ended on the top right edge while part 4 has a large deep melt pool crater on the top right of the part. The build appears to have been steady with few Arc Trips and only a few Zero Pulse warnings at the beginning of the build, Figure 127.

Build E2 began the next day with the plans to elevate the build temperature close to that of Rene N5 by using a higher preheat than build E1. The Build Anomaly Plot, Figure 128 shows that the build was steadily decreasing in temperature as the build increased in height but overall was a successful build. The top surface of the build was not scanned before an attempt was made to sand blast the surrounding sintered powder. Thus, the melt pool shape and surface roughness is not clearly visible in Figure 129 (a). The speckled pattern on the top of parts 1 and 2 cannot be explained.

In addition, the build “cake” was imaged when the build completed and was being removed from the Arcam in Figure 129 (b). From this image the swelling which occurred is visible in the center of the build. Process parameters that closely resemble build E1 are seen in Figure 130. The main changes to E2 are to the Speed Function which reduced the energy input and gave smoother top surfaces of the part.

Build E3 brought the processing temperature back down and the build was started at around 900 ºC as seen in the Build Anomaly Plot, Figure 131.

4 x 28.3x28.3x13 mm Triangles			Temperature: 1010 to 1040 C		
1st and 2nd Tri (Cold)				Solid & Complex	
Min Current =	5	mA	PA	12.5	
Max Current =	13.5	mA	Prop_K	0.602411	
Triangle Length =	28.3	mm	Scan_Ref	24.98235	
SF =	60		Slope =	0.301	mA/mm
Hatch =	0.125		Y-intercept =	4.97	mA
	Current (mA)	Length (mm)	Velocity (mm/s)	Traverse	Energy
Full =	13.5	28.3	1677	7.407489	3.86391
3/4 =	11.375	21.225	1326	7.80657	4.11903
1/2 =	9.25	14.15	1015	8.963118	4.376
1/4 =	7.125	7.075	547	9.662839	6.25324
Min =	5	1	364	45.46146	6.599
				mm/s	J/mm2
4 x 28.3x28.3x13 mm Triangles			Temperature: 1025 to 1000 C		
3rd and 4thnd Tri (Hot)				Solid & Complex	
Min Current =	16	mA	PA	25	
Max Current =	19	mA	Prop_K	0.360426	
Triangle Length =	28.3	mm	Scan_Ref	84.7	
SF =	100		Slope =	0.106	mA/mm
Hatch =	0.075		Y-intercept =	15.99	mA
	Current (mA)	Length (mm)	Velocity (mm/s)	Traverse	Energy
Full =	19	28.3	4134	10.95671	3.67653
3/4 =	18.25	21.225	3961	13.99647	3.68594
1/2 =	17.5	14.15	3788	20.07597	3.69621
1/4 =	16.75	7.075	3614	38.31449	3.70746
Min =	16	1	3614	271.075	3.54146
				mm/s	J/mm2

Figure 125. Final process parameters for build E1.

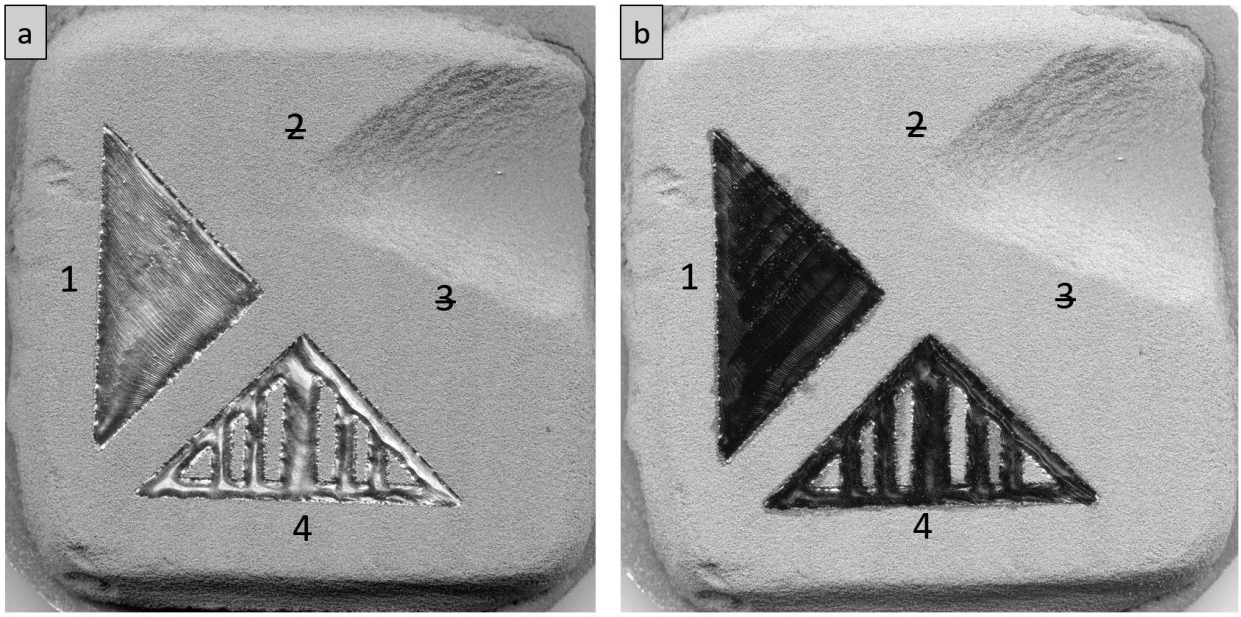

Figure 126. Top surface scan of build E1 with and without sharpie marker.

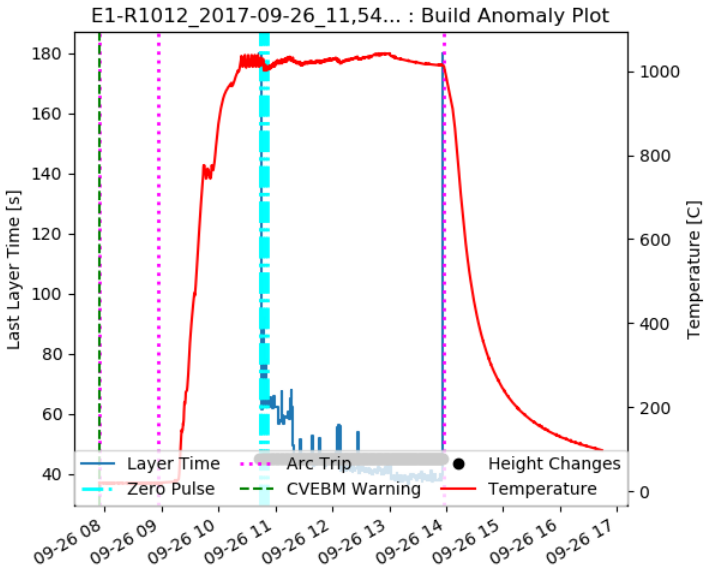

Figure 127. Build Anomaly Plot for build E1.

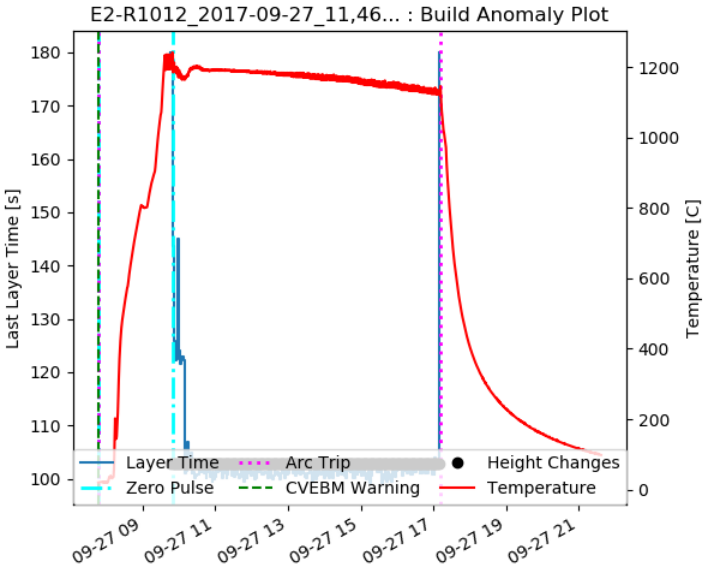

Figure 128. Build Anomaly Plot for build E2.

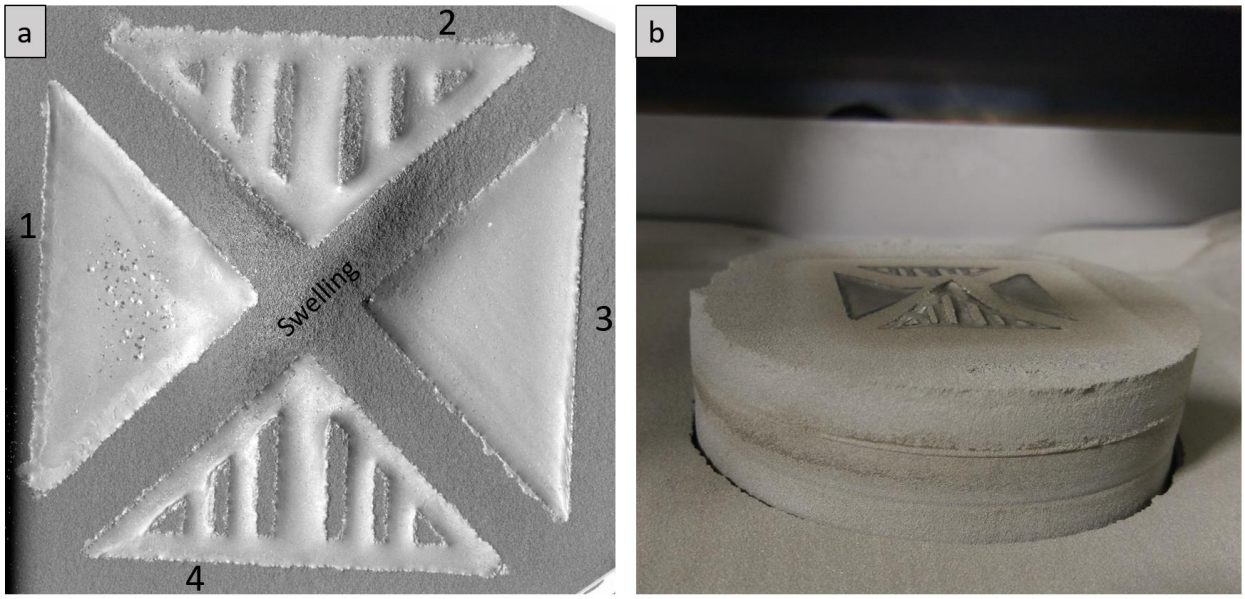

Figure 129. (a) Top surface scan of E2 and (b) picture of the build in the Arcam.

4 x 28.3x28.3x13 mm Triangles					
1st and 2nd Tri (Cold)				Solid & Complex	
Min Current =	5	mA	PA	12.5	
Max Current =	13.5	mA	Prop_K	0.60241135	
Triangle Length =	28.3	mm	Scan_Ref	24.9823529	
SF =	80		Slope =	0.301	mA/mm
Hatch =	0.125		Y-intercept =	4.97	mA
	Current (mA)	Length (mm)	Velocity (mm/s)	Traverse	Energy
Full =	13.5	28.3	2225	9.82700236	2.91257772
3/4 =	11.375	21.225	1759	10.3585918	3.10423247
1/2 =	9.25	14.15	1347	11.9003975	3.29590795
1/4 =	7.125	7.075	725	12.8136042	4.71561531
Min =	5	1	482	60.190625	4.98416489
				mm/s	J/mm2
4 x 28.3x28.3x13 mm Triangles					
3rd and 4thnd Tri (Hot)				Solid & Complex	
Min Current =	16	mA	PA	25	
Max Current =	19	mA	Prop_K	0.36042553	
Triangle Length =	28.3	mm	Scan_Ref	84.7	
SF =	120		Slope =	0.106	mA/mm
Hatch =	0.075		Y-intercept =	15.99	mA
	Current (mA)	Length (mm)	Velocity (mm/s)	Traverse	Energy
Full =	19	28.3	4948	13.1121908	3.07215522
3/4 =	18.25	21.225	4741	16.7526502	3.07951909
1/2 =	17.5	14.15	4534	24.0335689	3.08755422
1/4 =	16.75	7.075	4328	45.8763251	3.09635677
Min =	16	1	4328	324.575	2.95771393
				mm/s	J/mm2

Figure 130. Screen shot of process parameters for build E2.

To compensate, the energy density was increased by changing the speed function. Spatter was heavy during the beginning of the build and the preheating was adjusted to fix this. As the preheat increased the spatter decreased. There is a minimum temperature that the S-EBM process can cleanly process nickel-based alloys. The top surface looks similar to E1 and all parts were kept this time as seen in Figure 132 (a). The build chamber looked great after the build ended and was removed, Figure 132 (b). The final process parameters used are given in Figure 133. Due to the early termination of the build there will be no further characterization of the produced parts.

Build E4 was a retry of build E3 with an increased starting temperature and went to completion. The Build Anomaly Plot shows that the build was consistent except for the region of Zero Pulse warnings that dropped the temperature slightly in the middle of the build. The temperature was maintained above 1000 ºC and the top surface of the build looks smooth for all the parts in Figure 135 (a). Also, the build chamber looks smooth in Figure 135 (b) with the powder mound on the right beginning to build up. The single sided sweep is not intended for taller builds and will eventually cause problems as powder builds up on the no racked side. This could be fixed by setting smaller limits on the pass that the rake is able to use. In this build and with the MiniVat setup there seems to be a consistent problem with the powder sensors. The readings that the powder sensors get change the position that the rake will move to. Each zero pulse changes the position that the rake moves to. It may be that too long of a signal is also read as a zero pulse and would cause further problems. The final process parameters can be found in Figure 136 which are very similar to E3 and E1 with small changes in the Speed function to change the energy density.

Build E5 was an experimental build that had a unique processing structure of spot and raster. The first 0.5 mm, 10 layers, all parts were produced with the final process parameters of parts 3 and 4 of build E2 to stabilize the build. These parameters can be seen on the top of Figure 137. The next 0.5 mm switched to two different kinds of spot melting. The first was the classic Dehoff fill, top of Figure 138, for parts 1 & 2. The second is a new density function fill, bottom of Figure 138, for parts 3 & 4. After the height of 1 mm was reached, equal to 20 layers, and for the rest of the build, the Sweeping surface melt parameters were applied after each layer was melted with the spot pattern. The parameter steps followed the order: rake, preheat, spot melt 1, 2, 3, & 4, sweep all parts at once regardless of order, post-heat, and repeat.

Figure 139 shows that the build steadily increased in temperature with a few long layer times occasionally occurring. The sweeping was done to remove the pitted ‘golf ball’ like surface of the part so that the final part would be smooth and even. Unfortunately, the combination of parameters caused the corners of the parts to swell up, which can be seen in Figure 140 (a). The build was eventually stopped at 11.7 mm due to the swelling interfering with the rake and excess powder build up as seen on the left of Figure 140 (b). The swelling that was observed in these parts was non-uniform. The Dehoff fill pattern caused swelling in the center of the part while the new fill caused the corners to swell. This highlights the difference between the two spot methods and how a new method will have to be created to deal with changes in geometry as changes in geometry will lead to varied time of return.

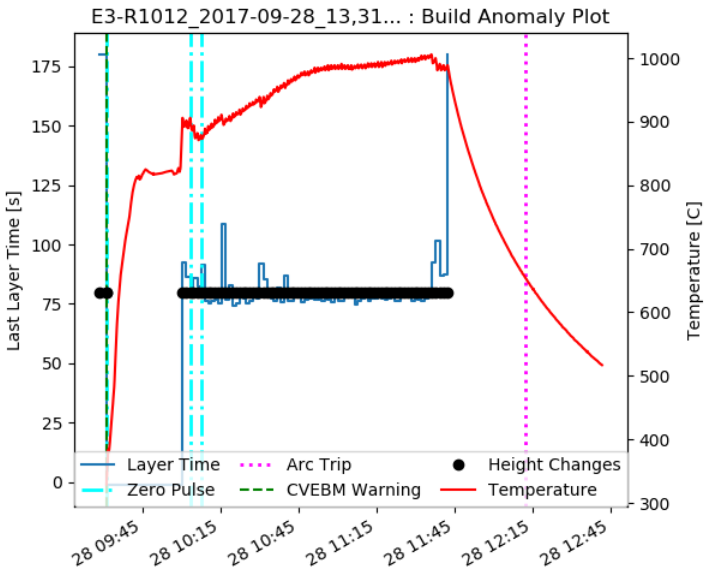

Figure 131. Build Anomaly Plot for build E2.

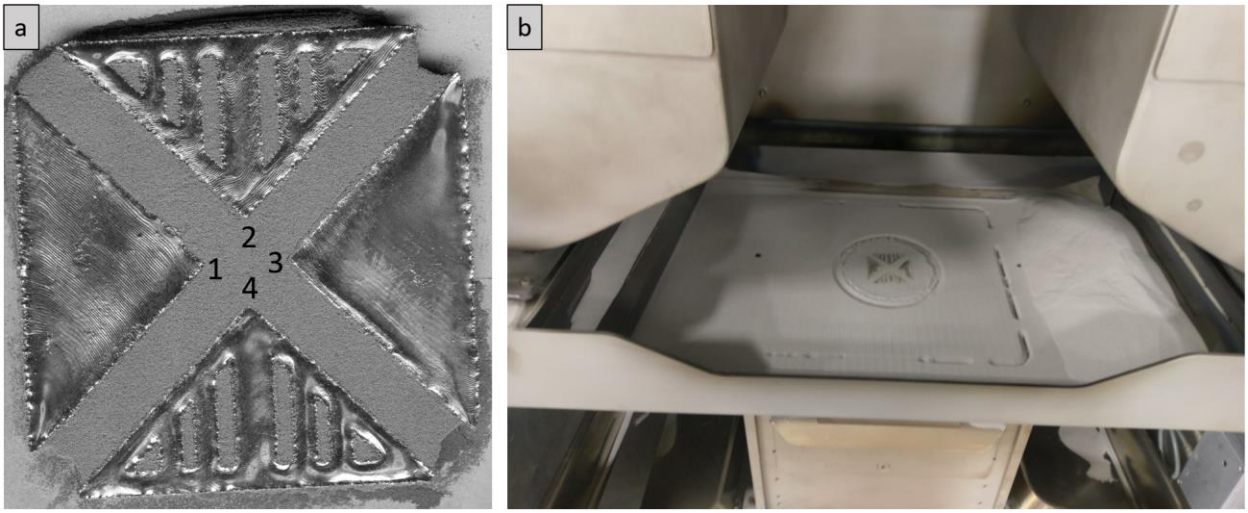

Figure 132. (a) Top surface scan of E3 and (b) image of the build and mound in the Arcam.

4 x 28.3x28.3x13 mm Triangles			Temperature: 825 to 960 C		
1st and 2nd Tri (Cold)				Solid & Complex	
Min Current =	5	mA	PA	12.5	
Max Current =	13.5	mA	Prop_K	0.60241135	
Triangle Length =	28.3	mm	Scan_Ref	24.9823529	
SF =	50		Slope =	0.301	mA/mm
Hatch =	0.125		Y-intercept =	4.97	mA
	Current (mA)	Length (mm)	Velocity (mm/s)	Traverse	Energy
Full =	13.5	28.3	1403	6.19773263	4.61812567
3/4 =	11.375	21.225	1109	6.53055883	4.9238477
1/2 =	9.25	14.15	848	7.4944788	5.2335347
1/4 =	7.125	7.075	458	8.08745583	7.47132714
Min =	5	1	305	38.096875	7.87466164
				mm/s	J/mm2
4 x 28.3x28.3x13 mm Triangles					
3rd and 4thnd Tri (Hot)				Solid & Complex	
Min Current =	16	mA	PA	25	
Max Current =	19	mA	Prop_K	0.36042553	
Triangle Length =	28.3	mm	Scan_Ref	84.7	
SF =	90		Slope =	0.106	mA/mm
Hatch =	0.075		Y-intercept =	15.99	mA
	Current (mA)	Length (mm)	Velocity (mm/s)	Traverse	Energy
Full =	19	28.3	3728	9.87897527	4.07761781
3/4 =	18.25	21.225	3571	12.6183746	4.08849062
1/2 =	17.5	14.15	3414	18.0971731	4.10036122
1/4 =	16.75	7.075	3258	34.5335689	4.11337358
Min =	16	1	3258	244.325	3.92919267
				mm/s	J/mm2

Figure 133. Screen capture of final process parameters for build E3.

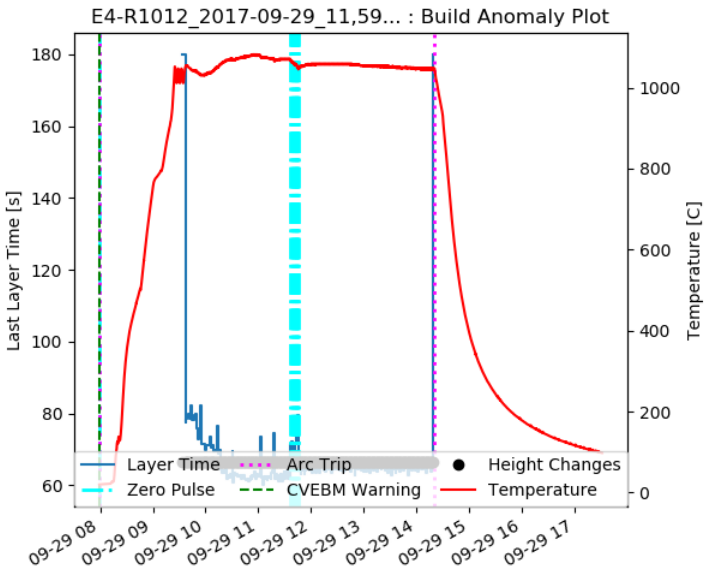

Figure 134. Build Anomaly Plot for build E4.

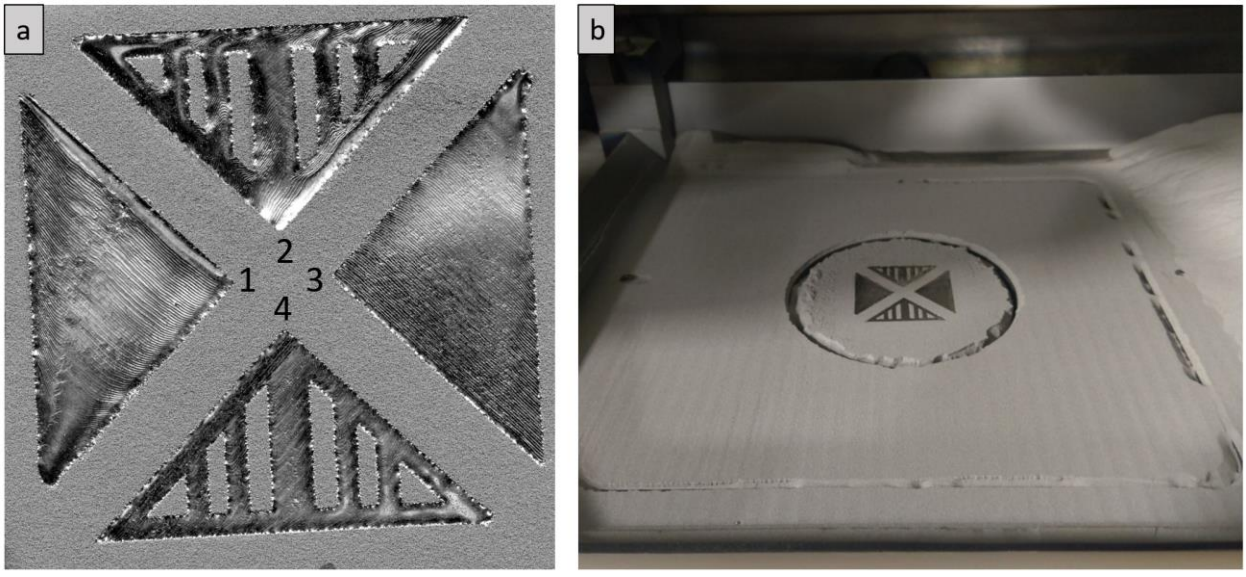

Figure 135. (a) Top surface scan of E4 and (b) image of the build and mound in the Arcam.

4 x 28.3x28.3x13 mm Triangles			Temperature: 1025 to 1090 C		
1st and 2nd Tri (Cold)				Solid & Complex	
Min Current =	5	mA	PA	12.5	
Max Current =	13.5	mA	Prop_K	0.60241135	
Triangle Length =	28.3	mm	Scan_Ref	24.9823529	
SF =	60		Slope =	0.301	mA/mm
Hatch =	0.125		Y-intercept =	4.97	mA
	Current (mA)	Length (mm)	Velocity (mm/s)	Traverse	Energy
Full =	13.5	28.3	1677	7.4074892	3.86391493
3/4 =	11.375	21.225	1326	7.80656982	4.11902766
1/2 =	9.25	14.15	1015	8.96311837	4.37600099
1/4 =	7.125	7.075	547	9.66283863	6.25323785
Min =	5	1	364	45.4614583	6.5989964
				mm/s	J/mm2
4 x 28.3x28.3x13 mm Triangles			Temperature: 1025 to 1000 C		
3rd and 4thnd Tri (Hot)				Solid & Complex	
Min Current =	3	mA	PA	12.5	
Max Current =	9	mA	Prop_K	0.76170213	
Triangle Length =	28.3	mm	Scan_Ref	44.75	
SF =	120		Slope =	0.213	mA/mm
Hatch =	0.12		Y-intercept =	2.98	mA
	Current (mA)	Length (mm)	Velocity (mm/s)	Traverse	Energy
Full =	9	28.3	2012	8.5319788	2.23644157
3/4 =	7.5	21.225	1082	6.11684335	3.46607102
1/2 =	6	14.15	882	7.47561837	3.40328985
1/4 =	4.5	7.075	607	10.2961837	3.70647466
Min =	3	1	497	59.628	3.01871604
				mm/s	J/mm2

Figure 136. Screen capture of final process parameters of build E4.

4 x 28.3x28.3x13 mm Triangles			Temperature: 1025 to 1090 C		
1-4 Triangles for first 0.5 mm (Sweep)				Solid & Complex	
Min Current =	3	mA	PA	12.5	
Max Current =	9	mA	Prop_K	0.76170213	
Triangle Length =	28.3	mm	Scan_Ref	44.75	
SF =	120		Slope =	0.213	mA/mm
Hatch =	0.125		Y-intercept =	2.98	mA
	Current (mA)	Length (mm)	Velocity (mm/s)	Traverse	Energy
Full =	9	28.3	2012	8.88747792	2.14698391
3/4 =	7.5	21.225	1082	6.37171182	3.32742818
1/2 =	6	14.15	882	7.78710247	3.26715825
1/4 =	4.5	7.075	607	10.7251914	3.55821568
Min =	3	1	497	62.1125	2.8979674
				mm/s	J/mm2
Post Spot Melting Surface Sweeping					
1-4 Triangles after 1.0 mm (Sweep)				Solid & Complex	
Min Current =	3	mA	PA	12.5	
Max Current =	9	mA	Prop_K	0.76170213	
Triangle Length =	28.3	mm	Scan_Ref	44.75	
SF =	120		Slope =	0.213	mA/mm
Hatch =	0.125		Y-intercept =	2.98	mA
	Current (mA)	Length (mm)	Velocity (mm/s)	Traverse	Energy
Full =	9	28.3	2012	8.88747792	2.14698391
3/4 =	7.5	21.225	1082	6.37171182	3.32742818
1/2 =	6	14.15	882	7.78710247	3.26715825
1/4 =	4.5	7.075	607	10.7251914	3.55821568
Min =	3	1	497	62.1125	2.8979674
				mm/s	J/mm2

Figure 137. Initial and 'Sweeping' process parameters of build E5.

Dehoff Spot Melting					
Dehoff Fill 283 Solid T		Spot # 1	Dehoff Fill 283 Complx T		Spot # 2
Current =	18	mA	Current =	18	mA
px/mm =	6	#	px/mm =	6	#
on time =	0.25	ms	on time =	0.25	ms
Power =	1080	W or J/s	Power =	1080	W or J/s
Length =	28.3	mm	Length =	28.3	mm
Area =	400.445	mm^2	Area =	400.445	mm^2
# of Spots =	14416.02	#	# of Spots =	10000	#
Part time =	3.60	s	Part time =	2.50	s
Focus off =	2	mA	Focus off =	2	mA
Energy =	9.72	J/mm2	Energy =	6.74249897	J/mm2
New Fill Pattern					
Hfill 283 Solid T		Spot # 3	Hfill 283 Complx T		Spot # 4
Current =	16	mA	Current =	17	mA
px/mm =	4	#	px/mm =	4	#
on time =	0.25	ms	on time =	0.25	ms
Power =	960	W or J/s	Power =	1020	W or J/s
Length =	28.3	mm	Length =	28.3	mm
Area =	400.445	mm^2	Area =	400.445	mm^2
# of Spots =	13251	#	# of Spots =	8666	#
Part time =	3.31	s	Part time =	2.17	s
Focus off =	2	mA	Focus off =	2	mA
Energy =	7.94176479	J/mm2	Energy =	5.51843574	J/mm2

Figure 138. Dehoff and 'Hfill' process parameters of build E5.

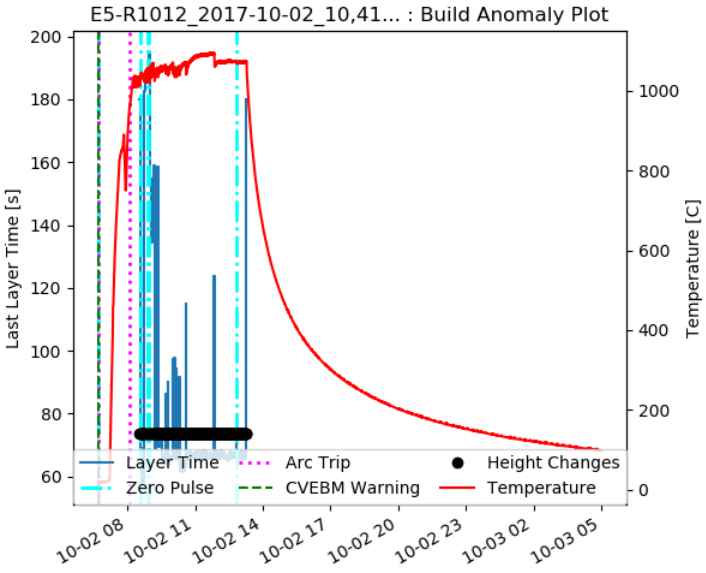

Figure 139. Build Anomaly Plot for build E5.

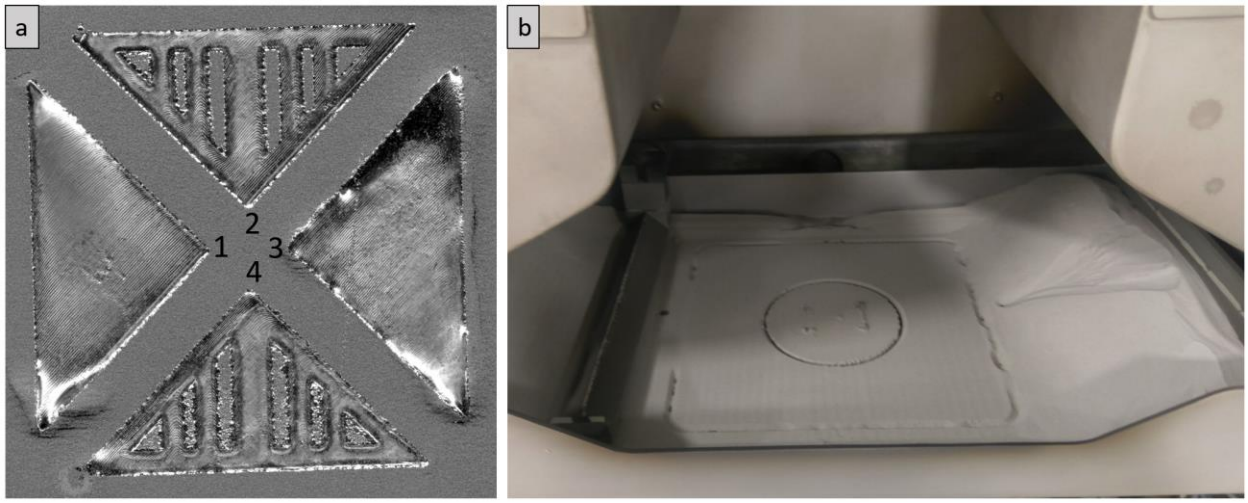

Figure 140. (a) Top surface scan of E5 and (b) image of the build and mound in the Arcam.

A.3.10 Build Set # 10: Ni-6Cr-6Al-6Ta Using MiniVat, F6.

Builds Set # 10 is made of a single build, F6, summarized in Table 11. Build F6 was performed at an elevated temperature near 1200 ºC using preheat parameters from build E2. An elevated temperature was chosen as a method for preventing cracking. By processing above the solvus temperature, no precipitation hardening would occur and cracking could be avoided. The initial drops and jumps in temperature were due to the thermocouple, which is placed at the bottom of the build plate, not being grounded properly.

When the beam was initially turned on, the temperature was not tracking with the orange to white glow of the build plate. When the build was stopped and filament turned off the temperature quickly jumped to match the glow of the base plate. After seeing this take place the build was restarted and the processes was started and stopped to check the preheat of the base plate. This can be seen in the early stages of the Build Anomaly Plot, Figure 141. Once the build was started it continued steady except for a few dips in temperature and long layer times a third of the way through.

The build began with process parameters from build E4 and reduced them over time to achieve a smooth top surface as seen through the leaded glass window. While doing so, swelling was appearing to occur in the 45 º corners. Process parameters are modified in this region by the speed function and changes to the rest of the part were not influencing the corners of the parts. Because of this the speed function was turned off and swelling in the corners disappeared. The top surface of all parts in Figure 142 are among the best top surface finishes achieved in this project. The process parameter used for this build were based on the runs performed with Ni106 prior to switching out the powder. The final process parameters can be found in Figure 143.

If there was one build to repeat, it would be build F6 with a new thermocouple. Due to the inaccurate temperature history it is unclear if the build temperature was above the precipitant solvus. The non-uniform structure precipitant structure that was observed could be better explained if an accurate grounded thermocouple was used.

Table 11. Overview of final build with Ni-6Cr-6Al-6Ta

Build	**Geometry**	**Height**	**Parts Characterized**	**Samples**	**Date**	**~ Temp.**
F6	4 Tri (28.3)	13 mm	1 – 4	Z-diag.	10/4/17	1200

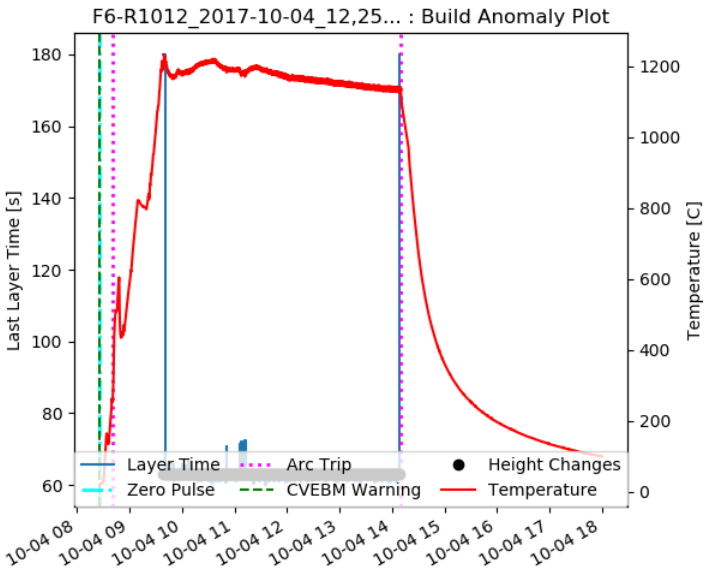

Figure 141. Build Anomaly Plot for build F6.

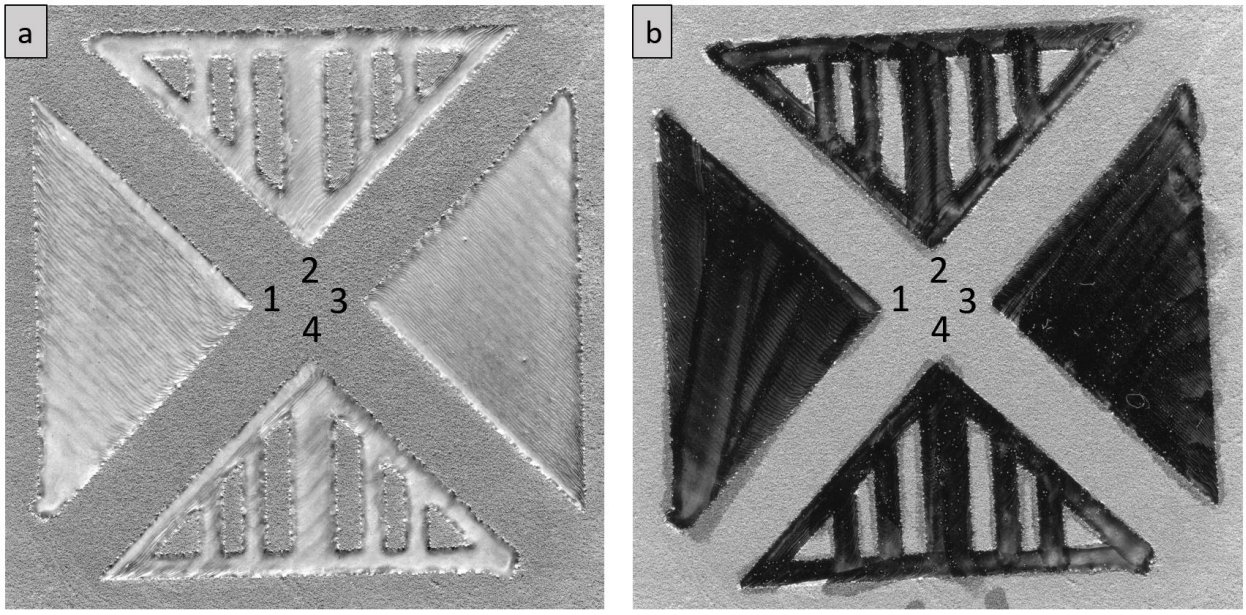

Figure 142. Top surface scan of build F6 with and without sharpie marker.

4 x 28.3x28.3x13 mm Triangles			Temperature: 1180 to 1220 C		
1st and 2nd Tri (Colder - SF)				Solid & Complex	
Min Current =	3	mA	PA	12.5	
Max Current =	9	mA	Prop_K	0.76170213	
Triangle Length =	28.3	mm	Scan_Ref	44.75	
SF =	170		Slope =	0.213	mA/mm
Hatch =	0.125		Y-intercept =	2.98	mA
	Current (mA)	Length (mm)	Velocity (mm/s)	Traverse	Energy
Full =	9	28.3	2843	12.5590769	1.52
3/4 =	7.5	21.225	1528	8.99734982	2.36
1/2 =	6	14.15	1244	10.9893993	2.32
1/4 =	4.5	7.075	857	15.1384717	2.52
Min =	3	1	702	87.7375	2.05
				mm/s	J/mm2
4 x 28.3x28.3x13 mm Triangles			Temperature: 1025 to 1000 C		
3rd and 4thnd Tri (Colder - Hatch)				Solid & Complex	
Min Current =	8	mA	PA	12.5	
Max Current =	9	mA	Prop_K	0.36028369	
Triangle Length =	28.3	mm	Scan_Ref	127	
SF =	120		Slope =	0.035	mA/mm
Hatch =	0.175		Y-intercept =	8.00	mA
	Current (mA)	Length (mm)	Velocity (mm/s)	Traverse	Energy
Full =	9	28.3	2012	12.4424691	1.53
3/4 =	8.75	21.225	1413	11.652925	2.12
1/2 =	8.5	14.15	1413	17.4793875	2.06
1/4 =	8.25	7.075	1413	34.958775	2.00
Min =	8	1	1413	247.333333	1.94
				mm/s	J/mm2

Figure 143. Screen shot of process parameters used in build F6.

VITA

Curtis Frederick was born a Buckeye in Columbus, Ohio, to parents Kathy and Greg Frederick who moved to North Carolina shortly after Curtis was born. After graduating from Hickory Ridge High School in May of 2009 he moved to Raleigh and attended North Carolina State University. After five years, he graduated with a Bachelors in Material Science and Engineering and decided to sign up for more classes on the other side of the Appalachian Mountains. Curtis joined Suresh Babu's group as a graduate research assistant at the University of Tennessee, Knoxville. He began work on an Air Force Research Laboratory project in January of 2015. The project focused on alloying rules for control of the Columnar to Equiaxed Transition in nickel-based superalloys processed by Selective Electron Beam Melting. Curtis presented at annual conferences during his time graduate studies and is currently publishing some of the work in Metallurgical and Materials Transactions A. While living in Knoxville, Curtis began to rock climb to conquer his fear of heights.